Defect Engineering in HfO_2/TiN based Resistive Random Access Memory (RRAM) Devices by Reactive Molecular Beam Epitaxy

TECHNISCHE UNIVERSITÄT DARMSTADT

Fachbereich Material- und Geowissenschaften

Genehmigte
Dissertation

zur Erlangung des akademischen Grades
eines Doktors der Ingenieurwissenschaften (Dr.-Ing.)

von

M.Tech. Sharath Sankaramangalam Ulhas

geb. in Kerala, Indien

Darmstadt 2018

D17

TECHNISCHE
UNIVERSITÄT
DARMSTADT

Genehmigte Dissertation von M.Tech. Sharath Sankaramangalam Ulhas aus Kerala, Indien.

Defect Engineering in HfO_2/TiN based Resistive Random Access Memory Devices by Reactive Molecular Beam Epitaxy

Defektkontrollierter HfO_2/TiN basierter resistiver Direktzugriffsspeicher hergestellt durch Molekularstrahlepitaxie

Referent: Prof. Dr. Lambert Alff
Zweitreferent: Prof. Dr. Thomas Schröder

Tag der Einreichung: 20.11.2017
Tag der mündlichen Prüfung: 31.01.2018

Darmstadt – D17

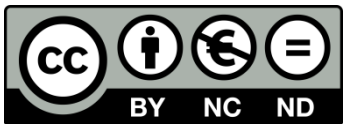

Erklärung zur Dissertation

Hiermit versichere ich, die vorliegende Dissertation ohne Hilfe Dritter nur mit den angegebenen Quellen und Hilfsmitteln angefertigt zu haben. Alle Stellen, die aus Quellen entnommen wurden, sind als solche kenntlich gemacht. Diese Arbeit hat in gleicher oder ähnlicher Form noch keiner Prüfungsbehörde vorgelegen.

Darmstadt, den 20.11.2017

_____

(Sharath Sankaramangalam Ulhas)

Dedicated to My Parents

Acknowledgements

First and foremost, I would like express my sincere gratitude to **Prof. Lambert Alff** for being a great mentor and giving me the opportunity to do research leading to my PhD thesis in the exciting scientific fields of thin film growth, oxide electronics and emerging memory technologies. I have been extremely lucky to have his tremendous support, patience and guidance throughout the course of my work. I truly appreciate his valuable inputs, open ear to discussion at all times and the degree of freedom that he has offered me in exploring own ideas. Moreover, his commitment to this work and encouragement allowed me to present our work at national and international conferences, where I became acquainted with the latest research and leading scientists and also helped in my personal and professional growth.

I also express my sincere thanks to my co-advisor **Prof. Thomas Schröder,** for his continuous support as well as for his many valuable inputs and discussions. I am extremely grateful for the facilities and resources provided during my multiple visits to his materials research group at IHP Microelectronics, Frankfurt (Oder) for measurements, as well as through the collaboration over the years, which was critical in the development of this work.

Besides my advisors, I would like to acknowledge **Prof. Wolfgang Donner** and **Prof. Klaus Hofmann** for their support by serving in my PhD thesis committee and related discussions. I thank **Prof. Wolfgang Donner** additionally for his suggestions and insightful inputs regarding XRD and crystallography over the last years. I would also like to thank **Prof. Hans-Joachim Kleebe** for facilitating TEM measurements in his labs.

I would like to wholeheartedly thank and express my debt to **Dr. Jose Kurian** for introducing me to this research topic on oxygen engineering and supervising me during my first two years of PhD. He was the one who taught me all the basics of thin film growth by MBE and further characterization. Moreover, this work would not have been possible without his continued mentorship, kind support through encouragement, scientific discussions and inputs as well as his help in correcting this thesis, even after leaving TU Darmstadt.

In addition, I would like to thank **Dr. Philipp Komissinskiy** for performing XPS measurements, related scientific discussions and his help towards device fabrication; **Dr. Erwin Hildebrandt** for sharing his expertise from his preceding PhD work on oxygen engineering and his continued support, and **Dr. Marton Major** for inputs and help with crystallography. I deeply appreciate the help and enthusiastic support of **Dr. Leopoldo Molina-Luna** and his colleagues in providing all the TEM based measurements presented in this work. I also want to extend my special appreciation to **Dr. Gennady Cherkashinin** for his help with XPS interpretation and related discussions as well as his support and friendship.

I would also like to express my gratitude to all the present and past scientific staff at IHP, who contributed to this work. My thanks are due to **Dr. Thomas Bertaud** for his collaboration in my first paper on RRAM: for helping me get started with learning resistive switching measurements as well as in realizing HAXPES measurements. I would also like to express my gratitude to **Dr. Christian Wenger** for inputs regarding QPC modelling and switching models; **Dr. Peter Zaumseil** for his help and inputs with XRD and XRR fitting; **Dr. Gang Niu**, **Dr. Pauline Calka** and **Dr. Christian Walczyk** for insight into HAXPES/XPS and electrical switching measurements.

I would like to especially acknowledge **Stefan Petzold (Vogel)** for the time spent working together in fabricating and characterizing RRAM devices as well as for all his help, friendship and fun. I owe a special thanks to **Alexander Zintler** for acquiring and analyzing TEM data of titanium nitride films, as well as **Dr. Michael Duerrschnabel** for analyzing TEM data of hafnium oxide films. I would also like to wholeheartedly thank **Merin Jissy Joseph** and **Michael Grigor'jan**, whom I provided guidance during their work and who in-turn helped me a lot.

I greatly appreciate the hard work and support of my past and present colleagues in the MBE sub-group over the years, who worked together frequently on Fridays to maintain the MBE unit. I would also like to wholeheartedly thank **Jürgen Schreeck**, **Gabi Haindl** and **Michael Weber** for their continued support in the laboratory, without which this work would not have been possible. The following people have supported my work in a significant way through science and friendship: **Dominik Gölden, Shalini Sharma, Daniel Bick, Dr. Arzhang Mani, Hardik Jain** and **Jonas Hunka.** I thank you all.

I would also like to thank **Dr. Stefan Flege** for his assistance with SIMS and DC sputtering, **Dr. Shunyi Li** for briefly facilitating electrical measurements and **Dr. Suman Narayan** for introducing and facilitating clean room usage for device fabrication.

Over the years, I have also gained a better scientific understanding about this work from the short interactions and fruitful discussions with leading researchers and collaborators. I am thankful to scientists at Forschungszentrum Jülich (FZJ), **Prof. Rainer Waser** and **Prof. Regina Dittmann** for their insight and inputs regarding resistive switching in oxides; **Prof. Krzysztof Szot** and **Dr. Christian Rodenbücher** for providing insights regarding XPS measurements; and **Prof. Marjana Ležaić** and **Dr. Konstantin Rushchanskii** for the theoretical insights regarding phase formation in hafnium oxide. I would also like to thank **Prof. Michael Lehmann** and **Dr. Tore Niermann** from TU Berlin, for their inputs from the work on TEM-holography.

Additionally, I want to thank all my past and present colleagues in advanced thin film technology (ATFT) division for their support and friendship. My time in Darmstadt was made enjoyable due to the many friends that became a part of my life. I want to thank the support and help I have received from **Dr. Vikas Shabadi, Marion Bracke, Dr. Deepu Babu, Jithin Abraham, Dr. Aldin Radetinac, Supratik Dasgupta, Dr. Mehran Vafaee, Patrick Salg, Eszter Piros, Benjamin Krah, Jan Preusker, Sareh Sabet, Lukas Zeinar, Uta Sitzler, Felix Vogel, Dr. Oleksandr Kovalenko, Sandeep Yadav, Tamal Roy and Vignesh Gurumurthy.**

Finally, I would express my deep gratitude to my parents, my parents-in law, my wife, my brother, my siblings-in law and my past teachers; whose constant support and encouragement keeps me motivated. I would not be the person I am without the never-wavering love and support of my parents, **Ulhas. P. R and Rajeswari. T;** and my brother **Sangeet S. U** who always encouraged and believed in me. My greatest thanks goes to my wonderful wife, **Divya Nair**, for her love and patience, for standing by me in the final years of PhD that we have been apart and for all the sacrifices she is making.

Preface

Recently, there has been huge interest in emerging memory technologies, spurred by the ever increasing demand for storage capacities in various applications like Internet of Things (IoT), Big Data, etc. CMOS based flash memory, the current mainstay of the memory technology, has been able to increase its density by scaling down to a 16 nm node and further implementation of 3D architectures. However, flash memory is expected to soon run into disadvantage due to challenges in further scaling. Therefore, extensive efforts are being made towards developing new devices for the next generation of non-volatile memories with the combined advantages of flash memory like non-volatility, high density, low cost and low power consumption as well as high speed performance of DRAM.

Among the many competitors, resistive random access memories (RRAM) based on resistive switching in oxides are promising due to its simple metal-insulator-metal (MIM) structure, fast switching speeds (<10 ns), excellent scalability (<10 nm) and potential for multi-level switching. RRAM devices based on the popular dielectric-metal gate combination of hafnium oxide (HfO_2) and titanium nitride (TiN), which is the subject of research in this work, are particularly interesting due to its compatibility with existing CMOS technology in addition to the aforementioned advantages. Though prototype RRAM chips have already been demonstrated, key problems for commercial realization of RRAM include large variability and insufficient understanding of the complex switching physics. Resistive switching mechanism in oxides is generally understood to be mediated via the transport of oxygen ions leading to the formation of a conductive filament composed of oxygen vacancy defects. Appropriate defect engineering approaches offer potential towards tailoring the switching behavior as well as improving the performance and yield of HfO_2-RRAM. In this thesis, the impact of pre-induced defects on the resistive switching behavior of HfO_2-RRAM is investigated in detail and our results are presented.

Defect engineered oxide thin films were deposited using reactive molecular beam epitaxy (RMBE) to fabricate metal oxide/TiN based devices. RMBE technique offers the unique possibility to precisely and reproducibly control the oxygen stoichiometry of the thin films in a wide range. Using RMBE, defects were introduced in polycrystalline HfO_x thin films intrinsically by oxygen stoichiometry engineering and extrinsically via impurity doping (trivalent lanthanum and pentavalent tantalum). Both the studies were performed at at CMOS compatible deposition temperatures (< 450 ^{o}C) with an eye on practical applications. Prior to tantalum doping in HfO_2, oxygen stoichiometry engineering studies were also performed in amorphous tantalum oxide (TaO_x) thin films to identify the oxidation conditions of tantalum metal. The density of oxygen stoichiometry engineered thin films of HfO_x and TaO_x could be tuned in a wide range from that of the bulk oxide density to close to metallic density. High degree of oxygen deficiency in oxides led to the formation of defect states near the Fermi level as well as multiple oxidation states of the metal, as observed by X-ray photoelectron spectroscopy (XPS). The pure stoichiometric hafnium oxide films crystallize as expected in a stable monoclinic structure (*m*-HfO_2) whereas, oxygen deficient HfO_x thin films were found to crystallize in vacancy stabilized tetragonal like structure (*t*-HfO_{2-x}). Impurity doping also led to the stabilization of higher symmetry tetragonal (*t*-Ta:HfO_x) or cubic structures (*c*-La:HfO_x) depending on the ionic radii of the dopant.

The growth of TiN thin films was also investigated using RMBE. The devices used for electrical studies in this work mostly involved deposition of oxides by RMBE on polycrystalline TiN/Si electrodes after *ex-situ* transfer for further deposition. Therefore, RMBE grown TiN thin film electrodes with similar or better quality would allow *in-situ* uninterrupted deposition of subsequent oxide layers in future to form cleaner interfaces. Optimized conditions for growth of epitaxial TiN films on the commercially relevant (001) oriented silicon and *c*-cut sapphire substrates were established, with focus on achieving smooth surfaces and low resistivity. High quality epitaxial TiN(111)||Al_2O_3(0001) and TiN(001)||Si(001) films with a low resistivity (20-200 $\mu\Omega$.cm) were achieved, in spite of the large lattice mismatch. Very low surface roughness, characterized by a streaky reflection high energy electron diffraction (RHEED) pattern during TiN film growth was additionally obtained, by tuning the Ti/N flux ratios.

Oxygen engineered HfO_x/TiN devices were further electrically characterized to obtain *I-V* characteristics during quasi-static DC switching. Usually, an initial electroforming step (high voltages) is required to obtain further reproducible switching operation (at lower voltages). High device to device variability in RRAM is typically associated with the stochastic nature of electroforming process which increases at higher forming voltages. Using highly oxygen deficient HfO_x and TaO_x films, the forming voltages were found to be reduced to levels close to operating voltages, paving the way for forming-free devices. However, the use of high defect concentration adds to increasing the complexity of the switching mechanism. This is reflected in the rather complex and dissimilar switching behaviors observed in the myriad of similar RRAM devices reported in the rapidly growing literature. Using model Pt/HfO_x/TiN-based device stacks; it is shown that a well-controlled oxygen stoichiometry governs the filament formation and the (partial) occurrence of multiple resistive switching modes (bipolar, unipolar, threshold, complementary). These findings fuel a better fundamental understanding of the underlying phenomena for future theoretical considerations. The oxygen vacancy concentration is found to be the key factor in manipulating the balance between electric field and Joule heating during formation, rupture (*reset*), and reformation (*set*) of the conductive filaments in the dielectric. While a bipolar switching occurs in all the devices irrespective of defect concentration, switching modes like unipolar and threshold switching is favored only at higher oxygen stoichiometry. This suggests the suppression of thermal effects via higher heat dissipation and lowered concentration gradient of oxygen vacancies in oxygen deficient devices. A qualitative switching model based on the drift, diffusion and thermophoresis of oxygen ions is suggested to account for the partial occurrence of various switching modes depending on the oxygen stoichiometry. Further, the evolution or drift of high resistance states during endurance test of the common bipolar operation is compared for HfO_2 and $HfO_{1.5}$ based devices and interpreted using the quantum point contact (QPC) model. Similar observations regarding switching modes were also obtained in oxygen engineered Pt/TaO_x/TiN devices, therefore allowing the findings to be generalized to other filamentary resistive switching oxides and contributing towards developing a unified switching model.

Besides finding application as non-volatile memory, RRAM devices are also promising for hardware implementation of neuromorphic computing. This is motivated by the possibility of multi-level switching or gradual (analog) modulation of resistance in an RRAM device which can emulate biological synapses. Defect engineering approaches have thus been investigated in Pt/hafnium oxide/TiN devices for tuning the DC *I-V* switching dynamics to

achieve multi-level or gradual switching electronic synapses. Higher contribution of thermal effects in pure stoichiometric HfO_2 typically results in a single sharp *set* process and abrupt sharp current jumps during the *reset* process during a conventional bipolar operation. By using ~18% La-doped HfO_x based device, a completely gradual *reset* behavior with a higher ON/OFF ratio could be achieved during the bipolar reset operation. This is likely related to filament stabilization around the dopant sites allowing a uniform rupture during *reset*. More interestingly, in oxygen deficient $HfO_{1.5}$ based devices, intermediate conductance states corresponding to integer or half-integer multiples of quantum conductance (G_0) was observed during both the *set* and *reset* operations at room temperature. These are related to the better stabilization of intermediate atomic size filament constrictions during the switching process. Occurrence of these intermediate quantum conductance states, especially during the typically abrupt *set* process, is likely aided by a weaker filament and better thermal dissipation in the highly oxygen deficient devices. These results suggest that a combination of doping and high oxygen vacancy concentration may lead to improved synaptic functionality with concurrent gradual *set* and *reset* behaviors.

Vorwort

Es gibt derzeit einen enormen Bedarf an digitalen Speichertechnologien, der durch die stetig zunehmende Nachfrage nach Speicherkapazität in verschiedensten Anwendungen, die durch Schlagworte wie Internet of Things (IoT), Big Data usw. umschrieben werden können, vorangetrieben wird. Bislang konnte diese Nachfrage durch Steigerung der Speicherdichte von CMOS (komplementärer Metalloxid-Halbleiter) basierten Flash-Speichern, die das derzeitige Rückgrat der Speichertechnologie bilden, durch fortschreitende Miniaturisierung bis in die 16 nm-Technologie und durch dreidimensionale Architekturen bedient werden. Man geht jedoch davon aus, dass eine weitere Skalierung aufgrund gravierender technologischer und physikalischer Schwierigkeiten nicht möglich sein wird. Deswegen werden derzeit große Anstrengungen unternommen, um alternative Bauteile für die nächste Generation nicht-flüchtiger Speicher zu entwickeln, die die Vorteile der Flash-Technologie wie Nicht-Flüchtigkeit der Information, hohe Speicherdichte, niedrige Kosten und niedriger Energieverbrauch mit den Vorteilen der hohen Geschwindigkeit von derzeitigem DRAM (dynamischer Direktzugriffsspeicher) verbinden.

Unter den zahlreichen Kandidaten für alternativen nicht-flüchtigen Speicher ist der resistive Direktzugriffsspeicher (resistive random access memory, RRAM), der auf widerstandsschaltbaren Oxiden basiert, aufgrund seiner geringen Schaltzeiten (unter 10 ns), der hoher Skalierbarkeit (kleiner als 10 nm) und des großen Potentials für Multizustandsschalten, ein herausragender Kandidat. RRAM auf Grundlage der Kombination des bekannten dielektrischen Gatteroxides Hafniumoxid (HfO_2) verbunden mit dem Elektrodenmaterial Titannitrid (TiN), die in dieser Arbeit untersucht wurde, ist neben den eben erwähnten Vorteilen wegen seiner erwiesenen Kompatibilität mit der CMOS-Technologie von besonderem Interesse. Obwohl hochintegrierte Schaltkreise mit RRAM-Prototypen schon hergestellt wurden, bestehen mit der hohen Bauteilvariabilität und dem unzureichenden physikalischen Verständnis des zugrundeliegenden Schaltverhaltens schwerwiegende Hindernisse für eine weitere Kommerzialisierung und Marktdurchdringung. Man geht generell davon aus, dass das resistive Schalten in Oxiden durch den Transport von Sauerstoffionen bedingt ist, der zur Bildung eines leitfähigen Filaments aus einer Agglomeration von Sauerstoffleerstellen führt. Geeignete Manipulation dieser Defekte bietet das Potential, das Schaltverhalten zu kontrollieren und die Leistungsfähigkeit und Effektivität von HfO_2-RRAM weiter zu steigern. In dieser Arbeit wurde der Einfluss von schon bei der Schichtsynthese induzierten Sauerstoffdefekten sowie zusätzlich eingebrachten Dotierstoffen auf das Schaltverhalten von HfO_2-RRAM detailliert untersucht.

Defekt manipulierte oxidische Dünnschichten wurden mittels reaktiver Molekularstrahlepitaxie (RMBE) abgeschieden, um Metalloxid/TiN basierte Speicherbauteile herzustellen. RMBE bietet die einzigartige Möglichkeit, die Sauerstoffdefektkonzentration in einem großen Bereich präzise und reproduzierbar einzustellen. Mittels RMBE wurden in polykristallinen HfO_x Dünnschichten Sauerstoffdefekte intrinsisch mittels Einstellung der Sauerstoffstöchiometrie und extrinsisch durch Dotierung bzw. Substitution mit trivalentem Lanthan und pentavalentem Tantal kontrolliert eingebracht. Diese Untersuchungen wurden jeweils bei CMOS kompatiblen Substrattemperaturen (unter 450 °C) in Hinblick auf die praktische Anwendung durchgeführt. Vor der Tantal-Studie wurde getrennt die Sauerstoffstöchiometrie in Tantaloxid (TaO_x) Dünnschichten untersucht, um das

Oxidationsverhalten von Ta zu verstehen. Die Dichte der Sauerstoff eingestellten Dünnschichten aus HfO_x und TaO_x konnte in dem vollständigen Bereich zwischen der Dichte des einkristallinen stöchiometrischen Oxids und der Dichte des Metalls kontrolliert werden. Die hohe Dichte an Sauerstofffehlstellen in den Oxiden führte zur Ausbildung von Defektzuständen am Fermi-Niveau und zu multiplen Valenzen des Metallions, die mittels Photoelektronenspektroskopie (XPS) untersucht wurden. Stöchiometrisches Hafniumoxid kristallisiert wie erwartet in einer stabilen monoklinen Struktur (*m*-HfO_2), während Sauerstoff defizitäre Schichten eine defektinduzierte tetragonale Struktur (*t*-HfO_{2-x}) ausbildeten. Die dotierten Schichten kristallisierten in Abhängigkeit vom Radius des Dotierelements ebenfalls in einer Struktur mit höherer Symmetrie, tetragonal im Falle des Tantals (*t*-Ta:HfO_x) bzw. kubisch im Falle von Lanthan (*c*-La:HfO_x).

Das Wachstum von TiN Dünnschichten mittels RMBE war ebenfalls Gegenstand der Untersuchungen. Die meisten der hier verwendeten elektronischen Bauteile besaßen als funktionale Schicht ein mittels RMBE auf TiN/Si Elektroden abgeschiedenes Oxid, wobei die Elektroden *ex situ* hergestellt wurden. RMBE gewachsene TiN Elektroden mit ähnlichen bzw. besseren Eigenschaften erlauben ein *in situ* Wachstum der Metall-Isolator-Metall-Struktur (MIM-Struktur), was zu einer Verbesserung der Grenzflächeneigenschaften führen würde. Daher wurden die Wachstumsbedingungen von TiN auf kommerziell relevanten Si (001) und *c*-geschnittenen Saphirsubstraten mit dem Ziel optimiert, möglichst glatte Oberflächen bei einem gleichzeitig niedrigen Widerstand zu erzielen. Dabei wurden trotz der sehr hohen Gitterfehlanpassung hochwertige epitaktische TiN(111)||Al_2O_3(0001) und TiN(001)||Si(001) Dünnschichten mit einem sehr niedrigen spezifischen Widerstand (20-200 $\mu\Omega \cdot cm$) erzielt. Durch geeignete Einstellung des Atomflussverhältnisses von Titan zu Stickstoff konnten Schichten synthetisiert werden, die zusätzlich eine sehr geringe Oberflächenrauigkeit aufwiesen, was durch streifenartige Reflektionsmuster in Hochenergie-Elektronenbeugung (RHEED) während des TiN Schichtwachstums nachgewiesen wurde.

Die Sauerstoff eingestellten HfO_x/TiN Bauteile wurden elektrisch durch Vermessung der Strom-Spannungs-Kennlinien während des quasi-statischen DC Schaltens charakterisiert. Üblicherweise ist das Bauteil zunächst durch einen sogenannten Elektroformierschritt bei hohen Spannungen zu aktivieren, um es anschließend bei niedrigeren Spannungen reproduzierbar zu schalten. Die hohe Variabilität der Kennwerte der (hoch)integrierten RRAM-Strukturen in einem Schaltkreis wird auf die stochastische Natur des Elektroformierschritts zurückgeführt, wobei die Variabilität bei hohen Spannungen zunimmt. Durch die Verwendung stark Sauerstoff defizitärer HfO_x und TaO_x Dünnschichten konnten die benötigten Formierspannungen in die Nähe der zum Schalten eingesetzten Spannungen reduziert werden, wodurch im Prinzip formierfreie, ohne den fehlerbehafteten Formierschritt hergestellte Bauteile möglich werden. Materialien mit hohen Defektkonzentrationen erhöhen andererseits die Komplexität der atomistischen Schaltmechanismen. Diese Tatsache spiegelt sich in den vielfältigen und stark voneinander abweichenden Schaltvorgängen wider, die in der enormen Vielzahl ähnlicher RRAM-Bauteile in der schnell wachsenden Literatur diskutiert werden. Durch die Verwendung der hier beschriebenen Modellstruktur Pt/HfO_x/TiN konnte gezeigt werden, dass die experimentell gut kontrollierten Sauerstoffdefekte die Filamentbildung und das (teilweise gleichzeitige) Auftreten der verschiedenen Schaltmodi (bipolar, unipolar, Schwellen artig, komplementär) bestimmen. Durch diese Beobachtung konnte ein besseres Grundlagenverständnis der dem resistiven Schalten zugrunde liegenden

atomistischen Phänomene für eine zukünftige detailliertere Modellbildung gewonnen werden. Die Sauerstoffdefektkonzentration im Dielektrikum ist der entscheidende Faktor, mit dem die Balance zwischen dem Einfluss des angelegten elektrischen Feldes und des durch Joulesche Wärme entstehenden Temperaturgradienten während der Filamentbildung, der Filamentunterbrechung (Reset) und Filamentneubildung (Set) gesteuert werden kann. Während bipolares Schalten unabhängig von der Defektkonzentration in allen Bauteile auftritt, wird unipolares und Schwellen artiges Schalten durch hohe Sauerstoffstöchiometrie begünstigt. Dies kann so interpretiert werden, dass thermische Effekte aufgrund der höheren Wärmedissipation und des niedrigeren Sauerstoffdefektgradienten in defizitären Bauteilen unterdrückt werden. Mit einem qualitativen, auf Drift, Diffusion und Thermophorese von Sauerstoffionen beruhenden Schaltmodell konnten die experimentellen Beobachtungen des (partiellen) Auftretens der verschiedenen Schaltmodi als Funktion der unterschiedlichen Sauerstoffdefektkonzentratio interpretiert werden. Zusätzlich konnte die Evolution des Driftverhaltens des Zustands mit dem höheren Widerstand während Dauerbeanspruchungstests im relevanten bipolaren Schaltmodus in HfO_2 und $HfO_{1.5}$ basierten Bauteilen durch ein Quantenpunktkontaktmodell (QPC) erklärt werden. Ein ähnliches Verhalten wurde auch in Sauerstoff eingestellten Pt/TaO_x/TiN Bauteilen beobachtet, was den Schluss nahelegt, dass das entwickelte Schaltmodell generell auf filamentäres Schalten in Oxiden verallgemeinert werden kann und so einen Beitrag zu einem universellen Schaltmodell leisten kann.

Neben der Nutzung als nicht-flüchtiger digitaler Speicher können RRAM-Bauteile auch als Computerteile (hardware) zur Implementierung von neuromorphen Rechnerarchitekturen verwendet werden. Dies liegt an der Möglichkeit des Schaltens zwischen mehr als zwei Zuständen (Multizustandsschalten) bzw. der graduellen, also analogen Modulation des Widerstands, mit der biologische Synapsen nachgebildet werden können. Der hier verfolgte Ansatz der Defektmanipulation wurde daher auch in Pt/Hafniumoxid/TiN Bauteilen hinsichtlich der Erreichbarkeit von multiplen Widerstandszuständen bzw. graduellem, synaptischem Schaltverhaltens verfolgt. Der hohe Anteil thermischer Effekte in rein stöchiometrischen HfO_2 RRAM-Bauteilen resultiert in einzelnen scharfen Set-Schaltvorgängen während einer konventionellen bipolaren Operation. In einem mit etwa 18% Lanthan dotiertem (Hf,La)O_x Bauteil wurde ein vollständig graduelles bzw. analoges Reset-Verhalten im bipolaren Modus mit einem hohen An/Aus-Verhältnis des Widerstands erreicht. Dies liegt sehr wahrscheinlich daran, dass das Filament während des Reset-Vorgangs durch die an den atomaren Dotierstellen stets gleichförmig erfolgende Unterbrechung stabilisiert wird. Interessanterweise wurden in Sauerstoff defizitären $HfO_{1.5}$ basierten Bauteilen intermediäre Leitungszustände bei Raumtemperatur beobachtet, die bei ganz- und halbzahligen Vielfachen des Leitfähigkeitsquantums (G_0) sowohl während des Set- als auch während des Rest-Vorgangs auftraten. Diese intermediären Zustände sind mit der bevorzugten Stabilisierung von Filamentanordnungen mit atomar begrenzten, quantisierten Leitkanälen während des Schaltvorgangs assoziiert. Das Auftreten der intermediären quantisierten Leitfähigkeitszustände während der typischerweise eher abrupten Set-Vorgänge wird durch schwächer ausgeprägte Filamente in einer Sauerstoff defizitären Matrix mit hoher thermischer Dissipation begünstigt. Die hier beschriebenen Ergebnisse legen nahe, dass eine geeignete Kombination von Dotierung und eingestellter Sauerstoffdefektkonzentration zu einer verbesserten synaptischen Funktionalität mit gleichzeitig auftretenden graduellen Set- und Reset-Vorgängen führen kann.

Contents

Abbreviations

AFM	atomic force microscopy
ALD	atomic layer deposition
AVD	atomic vapor deposition
BEOL	back end of line
BRS	bipolar resistive switching
CC	current compliance
cf8	counter figure eight-wise
CMOS	complementary metal–oxide–semiconductor
CRS	complementary resistive switching
CVD	chemical vapor deposition
DC	direct current
DFT	density functional theory
DRAM	dynamic random access memory
ECM	electrochemical metallization memories
EDS	energy dispersive spectroscopy
f8	figure eight-wise
FWHM	full width at half maximum
HAADF	high-angle annular dark-field
HAXPES	hard X-ray photoelectron spectroscopy
HRS	high resistance state
IMFP	inelastic mean free path
LRS	low resistance state
MBE	molecular beam epitaxy
MIM	metal-insulator-metal
MIT	metal insulator transition
NVM	non-volatile memory
PVD	physical vapor deposition
QPC	quantum point contact
RF	radio frequency
RHEED	reflection high energy electron diffraction
RMBE	reactive molecular beam epitaxy
RRAM	resistive random access memory
RS	resistive switching
RSM	reciprocal space mapping
SAED	selected area electron diffraction
SCLC	space charge limited conduction
STEM-	scanning transmission electron microscopy
TAT	trap assisted tunneling
TCM	thermochemical memories
TEM	transmission electron microscopy
TRS	threshold resistive switching
UHV	ultra-high vacuum
URS	unipolar resistive switching
VCM	valence change memories
XPS	X-ray photoelectron spectroscopy
XRD	X-ray diffraction
XRR	X-ray reflectivity

1. Introduction

Currently, the demand for memory for various applications is met individually using different silicon-based memories (SRAM, DRAM, Flash), each with its own complementary metal-oxide-semiconductor (CMOS) manufacturing technology. In today's computer architecture, a storage hierarchy, as shown in figure 1.1 is implemented based on different stand-alone volatile and non-volatile memories (NVMs) for optimal costs and high performance. Traditionally, the primary storage involves high-speed volatile memories, which remain closest to the processor core. They consist of registers, cache and the main memory which are fast, volatile and expensive and are often referred to as just the *'memory'*. Among them, static RAMs (SRAM) and dynamic RAMs (DRAM) functioning as the cache and main memory respectively have been in use for over 30 years. The secondary storage (or *'storage'*) is non-volatile, slower and inexpensive; and was initially dominated by the magnetic hard disk drives (HDD) for over five decades, and more recently by flash memories since the advent of portable electronics. However, the floating gate – based flash memories, the current mainstay of the non-volatile memory (NVM) market due to its high density, high performance and low fabrication costs, is expected to run in to disadvantages on further scaling of the CMOS process in the near future.

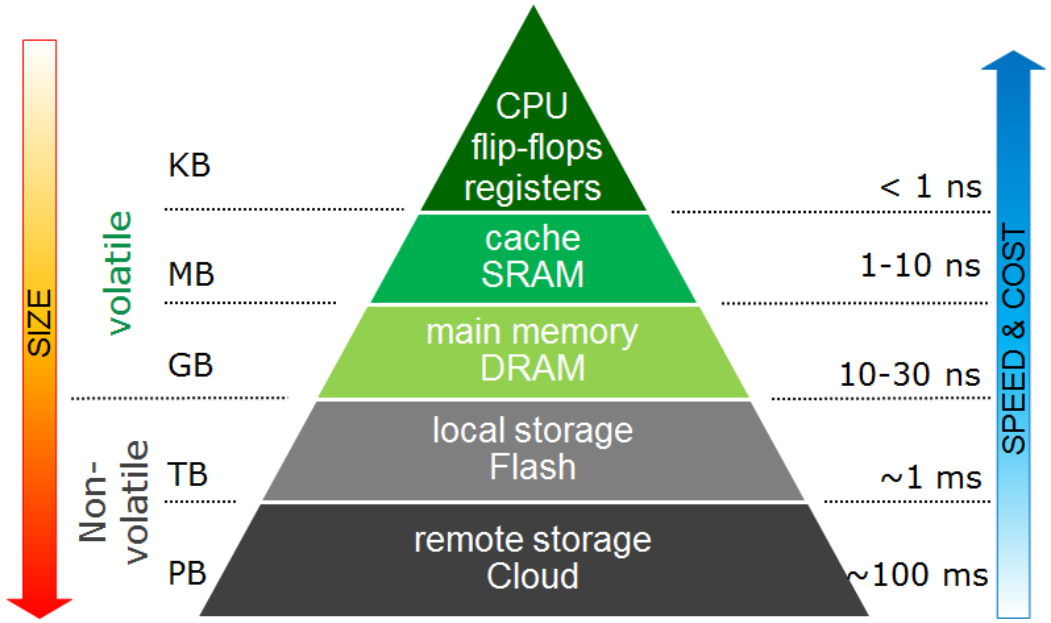

Figure 1.1: Typical schematic of memory hierarchy.

Among the emerging technologies for the next-generation of NVMs, resistive RRAM (RRAM) devices based on binary transition metal oxides (HfO_x, TaO_x, TiO_x, etc.) is presently considered to one of the most promising candidates, due to its high-speed (<10 ns), ultimate

scalability (< 10 nm), low-power consumption (~ 1pJ/bit), capability of multi-bit switching, potential for 3D integration and proven compatibility to CMOS technology.[1-3] Despite these advantages, for commercial realization of RRAM, concerns about reliability are yet to be fully addressed, for which a detailed understanding of switching mechanisms is necessary.

1.1. Emerging memories

A hypothetical 'universal memory' which has the combined requirements of low costs (DRAM), high speeds (SRAM), non-volatility (Flash) and infinite endurance, however remains out of reach. The search for a universal memory led to active research with focus on attaining non-volatile, high-speed, low-cost, high-density, low power consuming and reliable devices for future NVMs.[4] Therefore, in recent years, there have been several emerging NVM technologies under extensive research and development aimed at replacing or complementing the limitations of transistor based memories. They prominently include phase-change random access memory (PCRAM), spin-transfer torque magnetic RAM (STT-MRAM), ferroelectric RAM (FRAM), resistive RAM (RRAM or ReRAM) and conducting bridge RAM (CBRAM).[5] If many of these new memories are realized successfully, it could additionally pave way for novel future schemes of monolithic three dimensional integration of different memories and logic computation layers, thus eliminating the need for long distance data movement.[6]

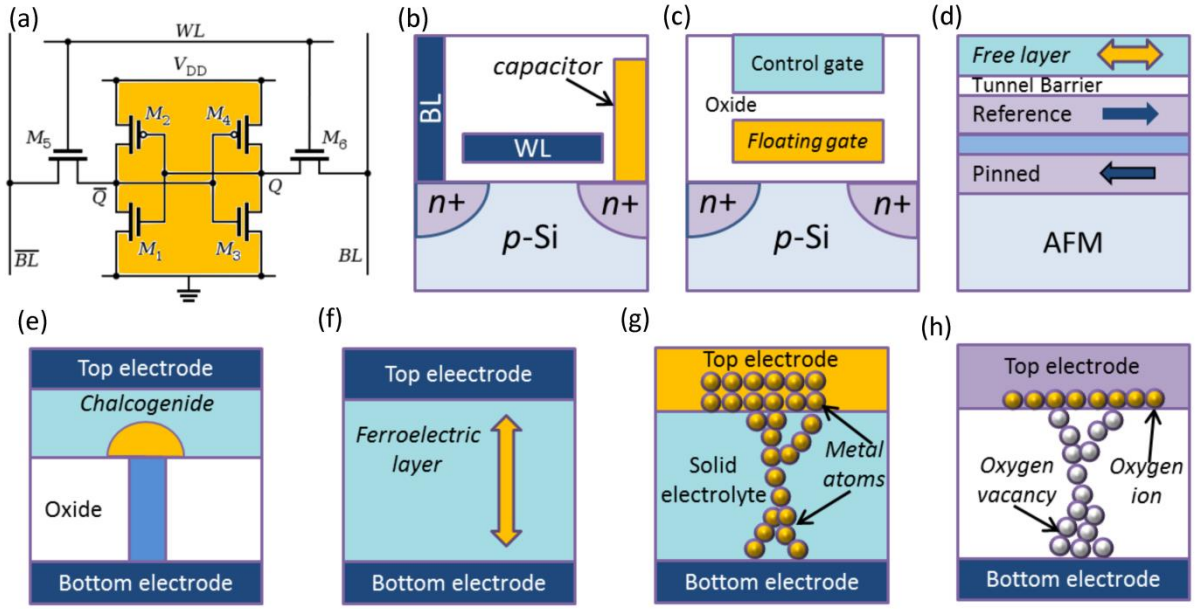

Figure 1.2: Schematic of memory elements in the current and emerging technologies (adapted from Wong and Salahuddin.[6]); (a) SRAM, (b) DRAM, (c) Floating- gate based Flash memory, (d) STT-MRAM, (e) PCRAM (f) FRAM (g) CBRAM and (h) oxide RRAM.

1.1.1. Physical Mechanisms

A robust understanding of the physical mechanisms involved in information storage in each of these emerging memories is necessary for their commercial realization. A schematic of various prominent memory devices are shown in figure 1.2. The current technologies of SRAM, DRAM and Flash memories use CMOS transistor technology. SRAM uses six transistors (6T) where the volatile information is stored like that in a flip-flop. DRAM and Flash devices can function with a single transistor, where a capacitor and floating gate, respectively are used in addition to store electronic charge. Among emerging memories, PRAM, RRAM and MRAMs are resistance based memories, while FRAM is based on capacitance.

Resistive switching refers to the physical phenomena where the resistance of a two-terminal device changes under the action of a strong electric field or current. In general, non-volatile and reversible resistive switching phenomenon has been observed under the influence of an electric field in various capacitors like switching cells. However, the taxonomy of RRAM in literature which is used to broadly categorize resistive switching devices usually excludes well defined switching phenomenon in magnetic (MRAM) and phase change (PCRAM) materials. In PCRAM, a chalcogenide glass material can be switched between its crystalline (conducting) and amorphous (insulating) phases by the use of a heating element or laser pulses. STT-MRAM relies on directing a spin polarized current to flip between parallel and anti-parallel configuration of two ferromagnetic layers separated by a thin tunneling insulator layer. FRAM on the other hand works on the principle of switching of the ferroelectric polarization states under the influence of sufficiently strong electric fields.

Resistive switching in oxide based RRAM devices, which is the subject of this work, is primarily due to generation and transport of defects (oxygen vacancies/ions) in transition metal oxides (HfO_x, TiO_x, TaO_x etc.). Based on the geometric nature and location of the switching event in these devices, filamentary (percolative paths) as well as homogeneous (interface type) switching has been defined in the literature.[7] Filamentary type switching is due to the formation and rupture of conductive filament between two electrodes. They can be further classified as cationic or anionic RRAM depending on the nature of the mobile species. This has sometimes led to a separate classification of conducting bridge RAM (CBRAM) within the larger class of RRAM, where the filaments are formed due to the migration of metal cations from the electrode material in to a thin film electrolyte.

1.1.2. Performance and scaling

Due to the different underlying physics of operation, the device performance characteristics are also different among emerging memory technologies. Table 1.1 compares

the optimal characteristics of these emerging and conventional memory technologies. The current DRAM and Flash memory technologies based on charge storage faces severe performance degradation on scaling below 21 nm. 3D stacking of NAND (Samsung, Intel/Micron) which drives further miniaturization will become unviable in future due to economic reasons and added complexity in lithography process. Besides limitations in scalability, energy efficiency is becoming increasingly important in mobile computer systems to extend its battery life. Replacement of DRAM with NVMs is touted to be ultimately necessary in order to save on storage energy. Flash based NVMs also faces other drawbacks like low endurance ($\sim 10^5$ cycles) and long write/erase times (0.1 ms) which make it unsuitable as the future NVMs.[5] Emerging memories are therefore under development with focus on scalability beyond DRAM/Flash and compatibility with the CMOS process flow.

A mature FRAM technology which is already established in niche markets is based on a 1T-1C (1 transistor-1 capacitor) configuration similar to DRAM. However, these FRAM devices which are prominently made up of perovskite family oxides like $Pb(Zr_xTi_{1-x})O_3$ (PZT) and $SrBi_2Ta_2O_9$ (SBT) face scaling issues below 130 nm limited by the available polarization charge.[8] The other possible use of perovskite oxides is in a 1T-1C configuration also called the ferroelectric FET (FeFET) with the prospect of 3D scalability. FeFET's has also been struggling with problems of low retention and very thick memory stacks arising from a low coercive field. In this regard, the discovery of ferroelectricity in HfO_2 in 2011 by Böscke *et al.* exhibiting very high coercive field´s (1-2 MV/cm) opens up future possibility of 3D scalable ferroelectric memories.

Table 1.1: Comparison of characteristics of existing and emerging memories. (adapted from Hwang[5])

	Existing memories			Emerging memories			
	SRAM	**DRAM**	**NAND-FLASH**	**FRAM**	**STT-MRAM**	**PCRAM**	**RRAM & CBRAM**
Cell Elements	6T	1T-1C	1T	1T or 1T-1C	1T-1R	1T-1R or 1D-1R	1T-1R or 1D-1R
Cell	Latch	Stack/ trench	Floating gate/ charge trap	Polarization change	Magnetic anisotropy	Phase change	Resistance change
Cell size	$140F^2$	$6\text{-}8F^2$	$4\text{-}5F^2$	$15\text{ -}34F^2$	$6\text{-}20F^2$	$4\text{-}10F^2$	$\leq 4F^2$ (3D)
Write/ Erase time	<1 ns / <1 ns	10 ns / 10 ns	1 ms / 0.1 ms	10 ns / 10 ns	15 ns / 3 ns	20 ns / 50 ns	5 ns / 5 ns
Energy per bit access	> 1 pJ	2 pJ	10 nJ	20 pJ check	< 1 pJ	100 pJ	2 pJ
Endurance cycles	$> 10^{15}$	$> 10^{15}$	$10^4\text{- }10^5$	$> 10^{14}$	$> 10^{15}$	$10^8\text{- }10^{15}$	$10^6\text{- }10^{12}$
Retention	Volatile		10 years	10 years	10 years at 85 °C	10 years at 85 °C	10 years at 85 °C

Among the other emerging memories (STT-MRAM, PCRAM and RRAM), excellent performance in terms of speed (~10 ns), energy consumption and endurance has been reported, when compared to NAND Flash. In RRAM/CBRAM devices, the resistive switching phenomenon and critical issues to be solved in terms of understanding the mechanism will be discussed in the subsequent sections. In terms of potential for scaling, high density RRAM chips have already been reported and RRAM remains competetive in the race towards the goal of ultimately replacing NAND Flash memory. The reported storage capacity of the emerging memories under developement in comparison to NAND flash is shown in figure 1.3.[9] Among the milestones, Samsung reported an unprecedented endurance of 10^{12} cycles in a Ta_2O_5/TaO_x stacked RRAM device.[10] In 2012, Panasonic realized an 8 Mbit memory embedded RRAM in a microcontroller unit using a resistive element of $TaN/TaO_2/Ta_2O_5/Ir$ in a 180 nm process.[11] A 32 Gbit RRAM was reported by Sandisk/Toshiba in a 24 nm process using a yet to be revealed metal oxide with the goal of ultimately competing with conventional storage class Flash memory.[12] Despite these advances, mass-production of a competeitive RRAM technology, needs identifying specefic applications where it can outperform an existing technology, and is still being expected to take some more years.

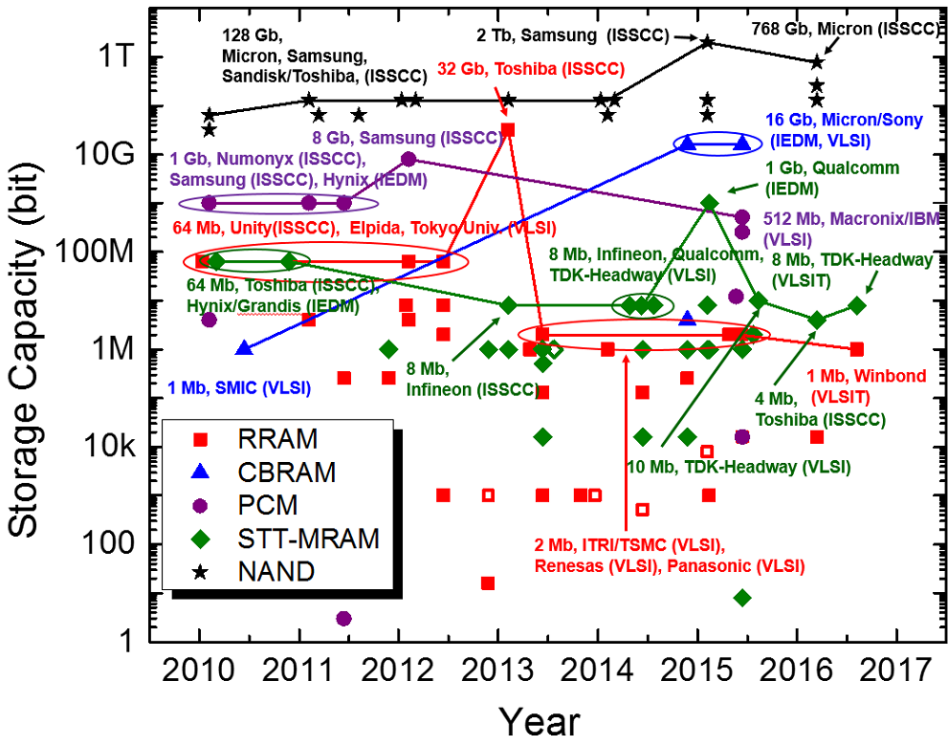

Figure 1.3: Storage capacity trend of emerging memories in comparison to NAND Flash. Wong *et al.* Stanford memory trends[9]

1.1.3. Potential applications of RRAM

RRAM technology, with its many advantages is currently being explored with the aim to address multiple applications, which are listed below.[13]

1. *Stand-alone mass storage*: The amount of data generated yearly is exploding at a pace significantly faster than the Moore's law. 40 Zetta bytes of new data is expected to be generated in 2020, which is a 500 fold increase from 2010.[14] This data explosion has created an ever increasing demand for lower cost and higher density digital memories. Though, 3D-NAND Flash has been able to increase its density by scaling down to a 16 nm node and further implementation of 3D architectures, scaling process is expected to become less viable in future. Therefore, 3D integration schemes of RRAM is being investigated as a direct replacement to stand alone 3D-NAND flash.

2. *Storage class memory*: RRAM, with its potential for high density due to its simple structure, and higher switching speed is promising to bridge the performance gap between 'memory' (DRAM: low density, high performance) and storage (high density, slow operation).[3] Combined with a low cost of fabrication, the so called 'storage class memory' (SCM) based on RRAM blurs the line between 'memory' and 'storage' and is expected to impact the design of computer systems. Moreover, SCM is being envisioned as a disruptive technology, where the need for flow or transfer of data between the volatile and non-volatile memories is minimized, thus overcoming the need for a conventional memory hierarchy.

3. *Embedded memory*: Recently, the ability of integrating 100's of millions of gates and cells on a chip meant that large subsystems are being integrated into a single chip. Therefore, *'embedded memory'* is becoming a large part of such embedded - system on chips (SoC) with emerging applications ranging from low-power internet of things (IoT) devices to high-performance engine control unit for autonomous driving in automobiles.[15, 16] Among the major drawbacks of the current Flash based embedded NVMs is that it adds costly processing step on top of the standard logic CMOS flow, which is becoming increasingly incompatible with advanced logic processes. Embedded RRAM is especially interesting due to its lower energy consumption and higher speed compared to Flash. Moreover, it can be easily integrated at low costs in the back end-of-line (BEOL) of a CMOS logic process.

4. *Programmable logic*: Fundamental Boolean logic operations have been demonstrated using RRAM devices, therefore allowing the same devices to be used simultaneously as memory

and logic.[17] This has led to the possibility of future novel paradigm of memory based computing.

5. *Neuromorphic applications:* RRAM devices are promising for hardware implementation of neuromorphic computing, due to its low power consumption and ability to store multiple-bits of data corresponding to changing strength of the nanoscale filaments.[18] Such an analog or gradual switching can thus be exploited to emulate biological synapses.

1.2. Resistive Switching: History, Materials and Mechanisms

There have been many excellent review articles in literature summarizing the resistive switching effects in different materials in the recent years.[5, 19-22] Thus, the section is only discussed concisely with main focus towards introducing aspects important to this work. Various physical driving mechanisms are responsible for these electrically induced resistive switching behaviors in different class of materials. Waser *et al.* classified the origin of various switching phenomenon as shown in figure 1.4.[1, 19] Among the more advanced memory device concepts are phase change memory and magneto resistive memory which was discussed in the previous section as PCRAM and MRAM, respectively.

Pure electronic or electrostatic effects can also lead to a change in resistance. This is commonly observed in charge trapping insulating materials resembling the popular floating gate-flash FET, where electrons can be trapped at defect sites or at metal nanoparticles within an insulator. In general, correlated electron systems exhibit interesting physical phenomena, such as metal-insulator transition (MIT) and high–T_C superconductivity. In these materials, the metal-insulator transitions can be categorized based on the dominant interaction that drives the material into the insulating phase. A dominant disorder-electron interaction, lattice-electron interaction and electron-electron interaction could induce Anderson localization, Peierls transition and/or Mott transition, respectively.[23] Mott type electronic switching, where charge injection results in a doping induced insulator metal transition is observed in perovskite oxides like PCMO and Cr:$SrTiO_3$.[24, 25]

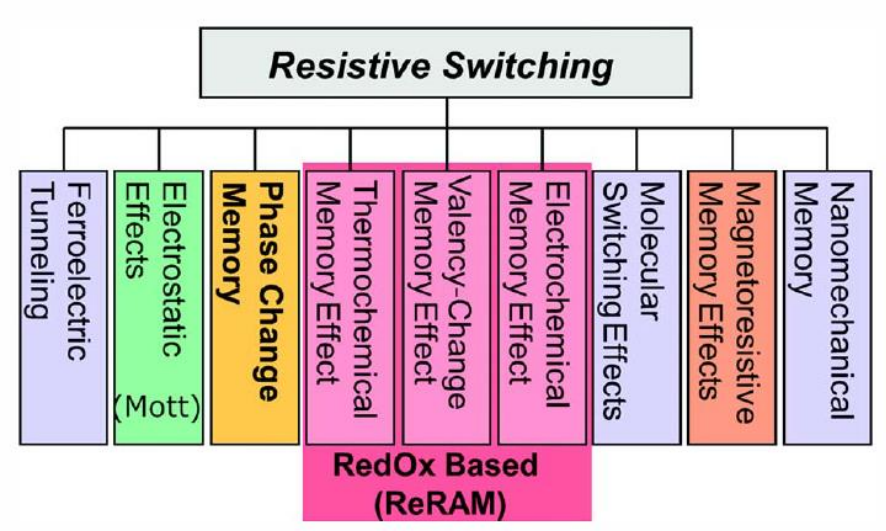

Figure 1.4: Classification of resistive switching mechanisms. From Wouters *et al.* [19]

The concept of a ferroelectric tunnel junction (FTJ) takes advantage of the ferroelectric polarization in a barrier material (eg. PZT) which leads to a change in resistance leading to different tunneling currents.[26] FTJ's are different from FRAM where the negative or positive (up or down) direction of the remnant polarization is the memory state. There also other phenomenon likes molecular switching typically in an organic molecule[27] or nano-mechanical memory effects which could become viable as memory devices in future.

1.2.1. Redox based resistive switching: A brief history

The earliest literature on resistive switching can be traced back to 1962 by Hickmott *et al.* in metal-insulator-metal (MIM) configuration of binary metal oxides like Al_2O_3, SiO_2 and Ta_2O_5.[28] More recently, in the 90's, the discovery of high temperature superconductivity in cuprates and colossal magnetoresistance in manganites [29] coupled with advancements in thin film deposition techniques led to much interest in the transport behavior of perovskite-like (ABO_3) complex oxide thin films. Consequently, Asamitsu *et al.*[24] reported the presence of a current driven resistive switching in $Pr_{0.7}Ca_{0.3}MnO_3$ (PCMO) in 1997. Following this, in 2000, the groups of Ignatiev[30] and Bednorz[31] reported reversible and reproducible resistive switching behavior in PCMO and $SrZrO_3$, respectively, creating renewed interest in oxide based restive switches for memory applications. Meanwhile, in the late 90's, Kozicki *et al.* contributed to advancing the concept of the resistive switching in MIM devices composed of chalcogenides with Group IB or Group IIB metals with an anode comprising of silver, where the switching takes place by growth and retraction of silver dentrites.[32] In 2008, Strukov *et al.*[33] from HP Labs suggested that the hysteretic current–voltage behavior observed in many of these oxides including TiO_x can be classified as a 'memristor'.[33] Memristor had been proposed

by L. Chua as the missing fourth fundamental circuit element in according to symmetry considerations for current (i), voltage (v), charge (q) and magnetic flux (φ).[34] Chua introduced memristance (M) linking magnetic flux and charge as $d\varphi = M dq$, similar to resistance ($dv = R di$), capacitance ($dq = C dv$) and inductance ($d\varphi = L di$). The concept of memristor has also been debated by others who claim that resistive switching is not a prefect memristor.[35] Nevertheless, resistive switching has since then been observed and studied in a wide variety of materials including binary oxides (NiO, HfO_2, Ta_2O_5, SiO_2, TiO_2 etc.), complex metal oxides (PCMO, $SrTiO_3$ etc.), organic materials, amorphous silicon and even carbon-based materials.[7]

Redox-related resistive switching: Classification of mechanisms

This work deals with reversible switching arising primarily due to the transport of ions, which can be categorized as redox-related memory, where the mobile ions (**cations** or **anions**) are oxidized or reduced thereby assisting in their ionic transport. Redox related switching phenomenon can be further classified as electrochemical metallization memories (**ECM**), valence change memories (**VCM**) and thermochemical memories (**TCM**).

1.2.2. Cationic memories

In **electrochemical memory (ECM)** devices, as shown in figure 1.2(g), an electrochemically active electrode metal (M) like Ag, Cu or Ni is used in combination with an electrochemically inert counter electrode (eg. Pt, Ir, W, Au etc.) to form a capacitor like structure. A thin solid film is usually used as an electrolyte (Ge-Se, Ge-S, (Zn,Cd)S, SiO_2 etc) which is an ionic conductor for the active metal cation. ECM memories, where the switching takes place by the motion of cations, are also described as conducting bridge RAM (CBRAM) or programmable metallization cells (PMC) in the literature. Here, the switching process can be described as taking place through redox reactions in an electrolytic cell. In the switching process, the *`set´* process is described by the anodic dissolution of the electrochemically active metal (M) from as M^{x+} cations into the electrolyte followed by its migration under the influence of the electric field towards the inert cathode where it is reduced and recrystallized. This results in the gradual formation a metallic dendrite like *`filament´* of the electrochemically active metal through the electrolyte, ultimately short circuiting the cell. The shorted state or the *`low resistance state´* (LRS) is described as the ON state or the logic `1`. The first step of forming the so called dendrite or filament is called *`electroforming´*. The voltage required for the set processes subsequent to this electroforming step is usually lowered. During the *`reset´* process, the dendrite can be dissolved from the inert electrode by applying a voltage of the opposite polarity to the active electrode thereby increasing the

resistance of the cell. This increased resistance state is referred to as the `*high resistance state*´ or OFF state (logic `0´). Such a formation and dissolution of the dendrite was reported first in 1976 by Hirose *et al.* in Ag/Ag-As_2S_3/Au system. The corresponding redox reactions can be expressed as:

$$M \rightleftharpoons M^{x+} + xe^{-}$$

1.2.3. Anionic memories

When transition metal oxides are typically used as the insulators in the absence of an electrochemically active metal electrode, the anions are often more mobile than the cations, hence called anionic memories. The switching effect in such anionic memories can be further classified according to the location of the switching event, which can either be localized to a conducting filament (CF) like region or can happen uniformly across the interface. As shown in figure 1.5, an *interface type switching* occurring uniformly across the entire area of interface can be typically distinguished by studying the electrode area dependence of the low and high resistance states. In the case of *filamentary switching*, it's very common that an initial `*electroforming*´ step happening at higher voltages becomes necessary. The electroforming step will be considered in detail in further sections. The switching mechanism in anionic memories can be further classified as valence change memories (VCMs) and thermochemical memories (TCMs).

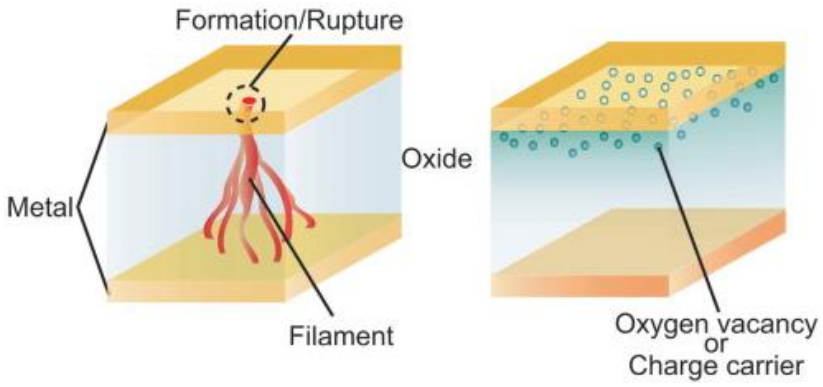

Figure 1.5:Proposed models of resistive switching by Sawa *et al.* [36] based on a filamentary conduction path (left) and interface type conduction path (right) in anionic oxide memories.

In the case of **valence change memories (VCM)**, the switching takes place *via* the field induced migration of anions (oxygen ions, O^{2-}), which are typically described by the motion of corresponding vacancies (oxygen vacancies, V_O), analogous to electrons and holes.[19] The loss of oxygen anion leads to a valence change in the corresponding transition

metal oxide sub-lattice, hence the name valence change memories (VCM). The resulting oxygen deficient lattice usually shows enhanced electronic conductivity and is thus the `*low resistance state´*. The anions can be usually driven back into the lattice, at least partially by applying an electric field of the opposite polarity which annihilates the vacancies, returning it to a higher resistance denoted as the `*high resistance state´*. The possibility to reversibly stabilize at least two resistance states qualifies the device to be used as RRAM. The switching process in VCMs usually takes place near the electrode-oxide interfaces. In the case of metal oxide VCMs, the redox reaction can be represented as follows:

$$O_O \rightleftharpoons \frac{1}{2}O_2\,(\mathrm{g}) + V_{\ddot{O}} + 2e^-$$

where, O_O and $V_{\ddot{O}}$ denote oxygen ions in the lattice and oxygen vacancies, respectively, according to Kröger-Vink notatation.[37]

In **thermochemical memories (TCM)** on the other hand, the resistance switching is primarily due to a voltage/current induced increase in temperature or Joule heating, leading to the formation of local conducting regions. The thermal breakdown involved in TCMs generally leads to a filamentary type switching after the typical high voltage electroforming process. Similar to filamentary VCMs, the physical switching mechanism in filamentary TCM's further involve growth and rupture of CFs, where the motion of mobility of ions dominated is by Joule heating in TCMs. However, unlike VCMs, the filament rupture does not necessarily take place near the electrode interfaces. The rupture location has been suggested in literature to be taking place away from the electrode to avoid heat loss and thus achieving improved efficiency of the thermal rupture of the filament.[38] It is also a matter of debate, whether the switching is mediated via the formation/rupture of a single filament or multiple filaments.

1.3. Basic resistive switching operation modes in MIM devices

In the case of transition metal oxides based capacitor like structures, switching phenomenon is due to one or a combination of effects of electronic charge trapping/detrapping, electric field induced drift of cations/anions and Joule heating induced migration of ions. Before going into detail, it becomes necessary to describe and classify the current voltage characteristics observed during switching, to help further understand and isolate the individual contributions of these effects and choice of materials.

Depending upon the nature of current-voltage characteristics, the observed switching modes in oxide thin films can be categorized into *'memory'* type non-volatile switching and *'selector'* type volatile switching.

1.3.1. Non-volatile memory: Bipolar and Unipolar switching

In non-volatile memory devices, the I-V characteristics of the device can be unipolar or bipolar depending on the operation scheme. As represented in figure 1.6(a), *unipolar resistive switching* (URS) involves set and reset processes which can take place in the same polarity. When the unipolar switching can take place in both polarities, the switching is also called *nonpolar* in nature. On the other hand, *bipolar resistive switching* (BRS) as shown in figure 1.6(b and c) requires the application of opposite polarities during set and reset. The bipolar switching can be further classified as *figure eightwise (f8)* or *counter figure eightwise (cf8)* depending on the nature of the I-V curve. This is helpful to distinguish between switching processes which can take place at opposite electrode interfaces in a similar device and even occur simultaneously or coexist.

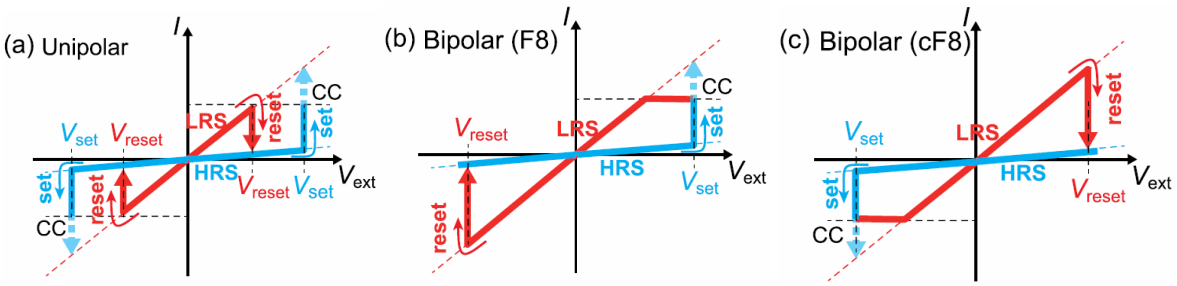

Figure 1.6: Operation modes of resistive switching (RS) for non-volatile memory applications: (a) Unipolar RS (b) figure eightwise (f8) type Bipolar RS and (c) counter figure-eightwise (cf8) type bipolar RS. Adapted from Lee *et al.*[21]

Current compliance (CC): During the set process, a hard breakdown is prevented by limiting the current flowing through the device, typically by the presence of an external *current compliance*. In a laboratory setting, the current compliance can be activated using the measurement system. In high density memory arrays, the current compliance is achieved by connecting a transistor in series to the memory device, which can then be operated in the saturation regime. It should be noted that, in some resistive switching devices, the compliance current is intrinsically present called the *self-compliance*. Such a self-compliance, typically due to a higher device resistance in series with the switching region, is desirable to reduce the complexity during manufacturing of large density arrays and remains of much interest.

1.3.2. Volatile selector-type Threshold and Complementary switching

Additional devices like transistors which are used to provide current compliance also play the role of access devices,[39] which are used to individually address devices without modifying the memory state of other devices in the larger memory array due to sneak path currents. Such access devices are thus called *selectors*. These selector devices are essentially non-linear devices which have high resistance at low bias voltages. A wide variety of selector devices (diodes, transistors etc) are available, the choice of which depends on the operating conditions of the individual memory and remains a large field of research by itself. The high resistance of the selector device when connected in series with the resistive switching device protects it from stray sneak path currents. At higher voltages, the selector devices have a very low resistance thus allowing the voltage to drop across the switching device.

Selector like behavior can otherwise be achieved by means of volatile switching which happens only at higher voltages. In filamentary resistive switching oxides, selector like switching behavior has been observed in threshold switching and complementary switching.

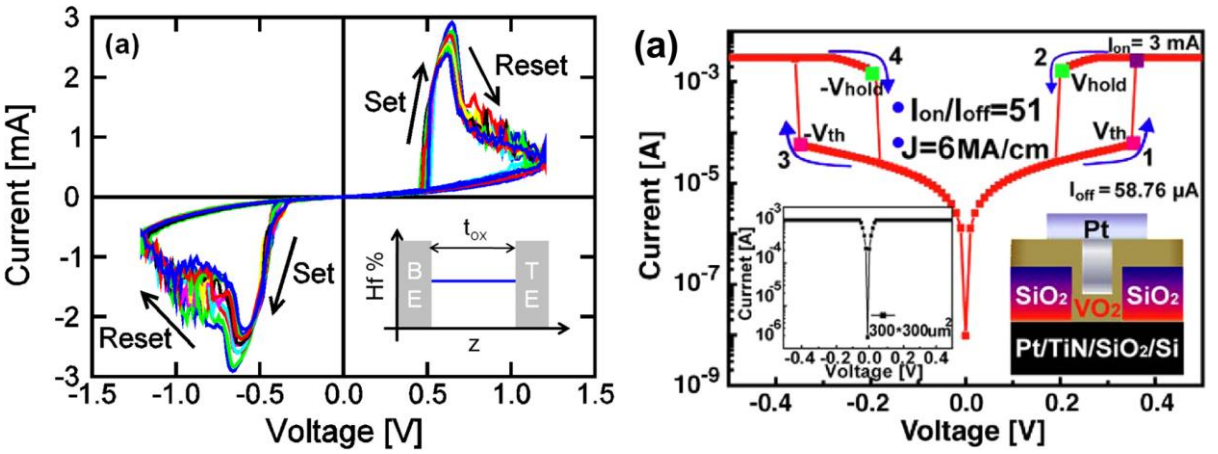

Figure 1.7: (left) Complementary resistive switching in a TiN/HfO_x/TiN device stack. From Nardi *et al.* [40] , (right) Threshold resistive switching in VO_2 . from Son *et al.*[41]

Complementary resistive switching (CRS) was initially proposed by Linn *et al.* in a configuration of two anti-serially connected bipolar resistive switching devices of Pt/GeSe/Cu,[42] thereby forming a symmetric device of Cu/GeSe/Pt/GeSe/Cu. Here, the two devices were switching independently such that the set process for individual devices occurs in the opposite polarity. Thus, at least one of the devices is in the HRS state at low voltage bias. On increasing the bias, the set process happens initially for the device in HRS which is followed by reset process of the other device in the same polarity. The CRS switch is in the LRS state only in the intermediate voltage range, when both the devices are in the LRS state. Nardi *et al.* demonstrated that a complementary switching behavior is also observed in a

single layer nonpolar RRAM device with a symmetric configuration of TiN/HfO_x/TiN,[40] as shown in figure 1.6(left). In such single layer devices, the CRS is understood to occur via filament rupture at the top and bottom electrode interfaces. Such a CRS operation can be understood to be due to the coexistence of *f8* and *cf8* bipolar switching modes in hafnium oxide.

In threshold switching, as shown in figure 1.7(right), an initial state of high resistance is turned into a low resistance state as soon as a threshold voltage is reached. Among oxides, threshold resistive switching has been reported in various oxides like NiO,[43] VO_2,[41] NbO_2,[44] TaO_x[45] etc. The mechanism behind TRS is being debated in individual oxides. A purely Mott-Peierls type MIT is believed to be the driving force in the case of a VO_2 based threshold switch. However, in the case of filamentary switching as in as in TaO_x and even NbO_2, Joule heating induced thermal runaway is believed to play the major role.[45 46]

1.4. Role of oxides and electrodes in resistive switching

Binary transition metal oxides, TaO_x, HfO_x, TiO_x, SiO_x, AlO_x, and NiO have raised much research interest for applications due to its simplicity and capability to be easily processed. For anionic memories, different non-electrochemically active materials like Ti, Hf, Pt, Zr, TiN, Ru, *etc* can be used as metal electrodes. Here, the ionic transport in mainly due to oxygen ion related defects which are more mobile than the corresponding transition metal cation.

Table 1.2 shows some examples of commonly studied oxide based device stacks with different reported switching modes and mechanisms classified according to the dominant mobile species as cationic/anionic and as filamentary/interface type based on the conduction path. Filamentary type-switching is observed in a wide variety of oxides, most commonly in binary metal oxides, which require an electroforming step. Interface-type RS is most commonly observed in oxides that are semiconducting or conducting in their pristine state, particularly in many ABO_3 ternary oxides with perovskite structure. Depending on the choice of MIM configuration, different resistive switching modes have been found in various configurations of the MIM devices. Oftentimes, multiple switching modes have even been found to coexist in a similar device configuration. The coexistence of these switching modes depend on multiple factors like operating conditions (current compliance, operation polarity and set/reset voltages), oxide properties (thermal conductivity, type of dominant carriers), electrode properties (work function, oxygen affinity, electrochemical activity), polarity of initial electroforming and the nature of interface. A quasi-static DC operation is thus commonly used to understand and distinguish between the resistive switching modes as well

as the resulting dynamics (abruptness/sharpness) and electronic transport in various device configurations.

Table 1.2: Examples of resistive switching in oxide based devices classified according to the reported switching mode and mechanism.

Device configuration	Switching modes	Mechanism	Remarks
$Hf/HfO_2/TiN$; [47] $Ti/HfO_2/TiN$ [48, 49]	*Bipolar*	*Filamentary (O^{2-}/V_O): VCM*	Implemented as *1T-1R* devices
$Pt/Ta_2O_{5-x}/TaO_{2-x}/Pt$ [10] $Pt/TaO_x/Pt$ [50]	*Bipolar*	*Filamentary (O^{2-}/V_O): VCM*	Ta_2O_5/TaO_2 based redox couple
$Ta/Ta_2O_5/Pt$; [51] $Ta/C/Ta_2O_5/Pt$ [51]	*bipolar* *bipolar*	*Filamentary (O^{2-}/V_O): VCM;* *Filamentary (Ta): ECM*	O^{2-} transport suppressed by amorphous carbon interlayer
$Cu/Cu:HfO_2/Pt$ [52]	*nonpolar type unipolar*	*Filamentary (Cu): ECM*	$R_{ON}/R_{OFF} > 10^7$
$Ag/HfO_2/p^+$-Si; [53] $Ag/ZrO_2/Pt$ [53]	*threshold, bipolar;* *threshold*	*Filamentary (Ag): ECM/Selector* *Filamentary (Ag): Selector*	threshold RS for $I_{cc}<100$ μA; Only threshold RS
$Pt/HfO_2/Pt$ [54] $Pt/TiO_2/Pt$ [55] $Pt/HfO_2/TiN$ [56]	*unipolar and bipolar*	*Filamentary (O^{2-}/V_O): Coexistence of VCM/ TCM;*	
$TiN/HfO_x/TiN$ [57]	*complementary bipolar, unipolar*	*Filamentary (O^{2-}/V_O): Coexistence of VCM/ TCM;*	
$Pt/NiO/Pt$ [43]	*unipolar, bipolar and threshold*	*Filamentary (O^{2-}/V_O): Coexistence of VCM/ TCM;*	threshold RS at high temperatures in NiO[43]
$TiN/TaO_x/TiN$ [45]	*Threshold*	*Thermal runaway (Hot filament- Joule heating)*	No ion transport, Formin-free
$Pt/Ti/Nb_2O_5/Pt$ [44]	*Threshold*	*Filamentary: Thermal runaway (NbO_2)*	Nb_2O_{5-x}/NbO_2 filament: forming
$Pt/VO_2/Pt$ [41]	*Threshold*	*Metal Insulator Transition (MIT)*	As selector device
$Pt/Ta_2O_5/HfO_{2-x}/TiN$ [58]	*Bipolar*	*Interface type :Charge trap/detrap in HfO_{2-x}*	self-rectification at Pt/Ta_2O_5 interface
$Sm/La_{0.7}Ca_{0.3}MnO_3/Pt$ [59]	*Bipolar*	*Interface type (O^{2-}/V_O): VCM*	Forming free
$Pt/Fe:SrTiO_3/Nb:SrTiO_3$ [60]	*Bipolar*	*Coexistence of Filamentary and Interface type: VCM*	
$Ag/Pr_{0.7}Ca_{0.3}MnO_3/Pt$ [61]	*Bipolar*	*Interface type: Charge trap/detrap*	

Some of the major factors affecting the switching behavior to be taken in to account for the material choice of oxide and electrode in the devices are described below:

a) Electrochemical activity (electrode): The use of electrochemically active electrodes (Ag, Cu etc.) more often results in filamentary type ECM devices like in the case of Cu/Cu:HfO_2/Pt.[52] In the case of electrochemically inactive electrodes (Ti, Hf, Ta, Pt, TiN) in MIM devices, a anionic type of switching is typically obtained. Interestingly, anionic (oxygen ion) transport was found to be suppressed in Ta/C/Ta_2O_5/Pt devices by the use of a thin amorphous carbon layer inserted at the Ta/Ta_2O_5 switching interface.[51] Consequently, the cationic transport was found to dominate, resulting in ECM type switching mediated via tantalum metal filament.

b) Work function and Oxygen affinity (electrode-oxide interface): The use of noble metals with lower affinity to oxygen or inert nitrides (TiN, TaN) result in the formation of a Schottky contact, whereas highly reactive electrodes like Ti, Hf, Ta, Al result in the formation of an ohmic contact. Unipolar resistive and threshold switching has been reported more often with inert electrodes and especially for symmetric devices (eg: Pt/NiO/Pt[43]), where Joule heating based TCM becomes dominant. Whereas, bipolar resistive switching is favored in asymmetric devices when a combination of Schottky and Ohmic electrodes are used as observed in Ti/HfO_2/TiN[49] and Ta/Ta_2O_5/Pt.[51] The presence of such high oxygen affinity electrode introduces an oxygen vacancy rich layer near the interface. These observations were confirmed in the TE/HfO_2/TiN configuration[62] as shown in figure 1.8.

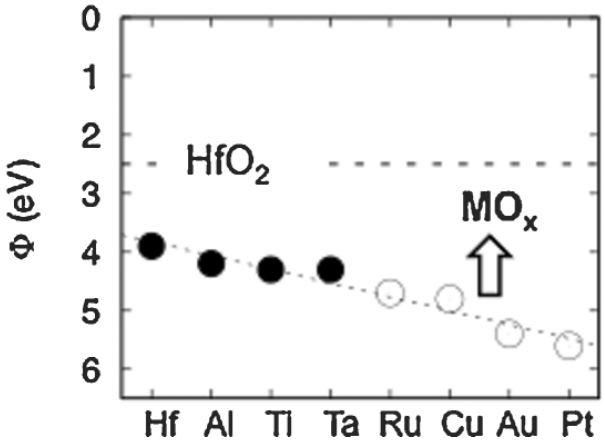

Figure 1.8: Instances of bipolar RS (solid circles) and unipolar RS (open circles) reported in literature for various top electrodes (TE) in a TE/HfO_2/TiN configuration; taken from Kamiya *et al.*[62]

The standard Gibbs free energy of formation (Δ_fG^o) of corresponding oxide can be used as an indication of oxygen affinity of a metal, where a lower Δ_fG^o corresponds to higher oxygen affinity. The Gibbs free energy of formation of prominent oxides are: $\Delta_fG^o(HfO_2)$= -1088.2 kJ/mol, $\Delta_fG^o((2/5)Ta_2O_5)$= -764.4 kJ/mol, $\Delta_fG^o(TiO_2)$= -888.8 kJ/mol.[63,64] A lower Δ_fG^o of a metal electrode would lead to the formation of thick interfacial layers, which will serve as reservoirs of oxygen ions or vacancies. It has been

suggested that electrode-oxide combinations with similar oxygen affinity like Ta/Ta_2O_5 and Hf/HfO_2 yields the highest endurance in the devices.[64]

c) Charge carrier type (oxide): In the case of interface type VCM's, the type of charge carriers play a role in determining the nature of the interface which is formed. Depending on the work function (φ_m) of the metal (M) electrode, an Ohmic contact (low φ_m) or rectifying Schottky contact (high φ_m) can form for electrodes in contact with *n*-type oxides. Vice versa is found to be true ion the case of p-type oxides, and it has been shown that the contact resistance of M/PCMO (*p*-type) interface decreases with φ_m, while that of M/Nb:STO (*n*-type) interface increases with increase in φ_m.[36] This is significant, since the switching in interface-type VCM devices normally takes place at the rectifying interface, which affects the directionality of switching process (counter figure eightwise vs figure eightwise) with respect to the anode and cathode.

d) Operating conditions

Current compliance: A higher current compliance (I_{cc}) leads to the formation of stronger conducting filaments. This is reported in the many cases where the filament is found to be non-volatile only when a certain level of compliance current is maintained, below which threshold switching is obtained.[53] In this case, very low current compliances form very weak filaments which readily dissolve at lower voltages. Too high of a current compliance would lead to hard-breakdown of the device. Varying the current compliance during operation can also be exploited to obtain various targeted switching modes. For example, $Pt/TiO_2/Pt$ devices was reported to exhibit both unipolar and bipolar types of switching with the determining factor of the switching type being the level of I_{cc} (low I_{cc} (<0.1mA) activates bipolar RS and high I_{cc} (>1mA) activates unipolar RS).[55] This can be interpreted to be due to the larger contribution of Joule heating at higher currents.

Temperature: RRAM devices are generally designed to function at room temperature and should also function without degradation up to 85 °C. Very high temperatures can sometimes lead to the gradual decay of the resistance state via ion diffusion. The switching behavior itself has also been found to depend on the temperature, for example in NiO_x based device where a unipolar switching observed at low temperatures (118 K) transformed to threshold switching mode at 300 K.[43] Such a behavior is again attributed to the level of heat dissipation which can be obtained in the devices. It is therefore important to appropriately choose the thermal conductivity of the oxide and electrodes in the RRAM device.

Voltage: The stop voltages during the set and reset voltages during device operation is generally significant in determining the degree to which the filament formation/rupture is

stronger or weaker. Though low voltages are preferred for low-power applications, increased operating voltages can be used to increase the ratio of R_{OFF}/R_{ON}. In cases, where multiple switching modes coexist, the stop voltages can also be varied to choose between an eightwise operation, counter-eightwise operation or complementary switching modes of operation.[57]

1.5. HfO_2/TiN based RRAM Devices

Hafnium oxide (HfO_2), as an insulting binary transition metal oxide initially gained attention following the Moore's law of scaling, when there was a need to ultimately replace SiO_2 (ε = 3.9) gate dielectric with other *high-k* dielectric oxides in CMOS field effect transistors. This became apparent when the SiO_2 layer became so thin (< 2 nm) that the leakage current due to direct tunneling through SiO_2 became very high (> 1A/cm^2 at 1V).[65] The use of new gate oxides with higher dielectric constants (ε) allowed the use of thicker ($t_{high\text{-}k}$) layer which can be compared 'equivalent oxide thickness' (EOT, $t_{eq.ox}$) of SiO_2 as follows:

$$t_{eq.ox} = EOT = \frac{3.9}{\epsilon} t_{high-k} \qquad \text{Equation 1-1}$$

Among the different high-*k* dielectrics, hafnium oxide (HfO_2) therefore attracted much interest due to its high dielectric permittivity (ε = 16-25), large band gap (5.7 eV) and high thermal stability ($T_{melting\ point}$ = 2780 °C). Additionally, it has a high thermodynamic stability and high energy barriers for electrons and holes when contacted with silicon.[66] This has led to the eventual replacement of SiO_2 (ε = 3.9) with dielectric based on HfO_2 as the gate oxide in CMOS field effect transistors and flash memory devices. In the recent years, HfO_2 was an attractive choice of material for RRAM devices due to its proven *compatibility to CMOS processing*. Additionally, due to the simple structure of RRAM, hafnium oxide based metal-insulator-metal structure could be integrated in the back-end-of-line integration scheme at very low costs for applications as embedded non-volatile memory.[67] This follows the *More-than-Moore* (MtM) approach where added values to existing devices are targeted by incorporating functionalities that do not necessarily scale with the Moore's law.

1.5.1. Hafnium Oxide: crystal structure and properties

The physical property parameters of HfO_2 are summarized in table 1.3. There are many polymorphic modifications for stoichiometric hafnium oxide (HfO_2) as summarized in table 1.4 and shown partially for the common phases in figure 1.9. The most stable structure of crystalline stoichiometric hafnium oxide in its pure form is a monoclinic phase (m-HfO_2,

$P2_1/c$) under standard atmospheric conditions. In the monoclinic phase, the oxygen ions are layered with alternating coordination to hafnium ions: three-coordinated (3C) and four-coordinated (4C). The hafnium ions are coordinated to seven oxygen ions (three of 3C and four of 4C). Other higher symmetry phases are also reported for HfO_2, which are either stabilized at high temperatures, higher pressures, under stress, via doping or at low crystallite sizes.

Table 1.3: Physical properties of stoichiometric hafnium oxide

Physical property	**HfO_2**
density	9.7 g/cm^3
melting point	2758 ^{o}C
boiling point	5400 ^{o}C
molar mass	210.49 g/mol
dielectric constant	16-25 (monoclinic)
band gap	5.3 – 5.8 eV
breakdown strength	~ 6 MV/cm

Table 1.4: Crystal structure and space groups of stoichiometric hafnium oxide

Structure	**Space group**	**Lattice parameters and stability**
Monoclinic *m*-HfO_2	*$P2_1/c$ baddeleyite*	a= 5.116 Å, b= 5.182 Å, c= 5.285 Å, $\alpha=\gamma= 90^o$, $\beta= 99.26^o$
Tetragonal *t*-HfO_2	*$P4_2/nmc$*	a = b = 3.5775 Å, c = 5.1996 Å, $\alpha = \beta = \gamma = 90^o$
Cubic *c*-HfO_2	*Fm3m (fluorite)*	a = b = c = 5.084 Å, $\alpha = \beta = \gamma = 90^o$ T > 2900 K
Orthorhombic *o*-HfO_2 (*OI*)	*Pbca*	*Higher pressure phase*
Orthorhombic *o*-HfO_2 (*OII*)	*Pnma (cotunnite)*	*Higher pressure phase*
Orthorhombic *o*-HfO_2 (*FE*)	*$Pca2_1$*	*Non – centrosymmetric Ferroelectric phase*

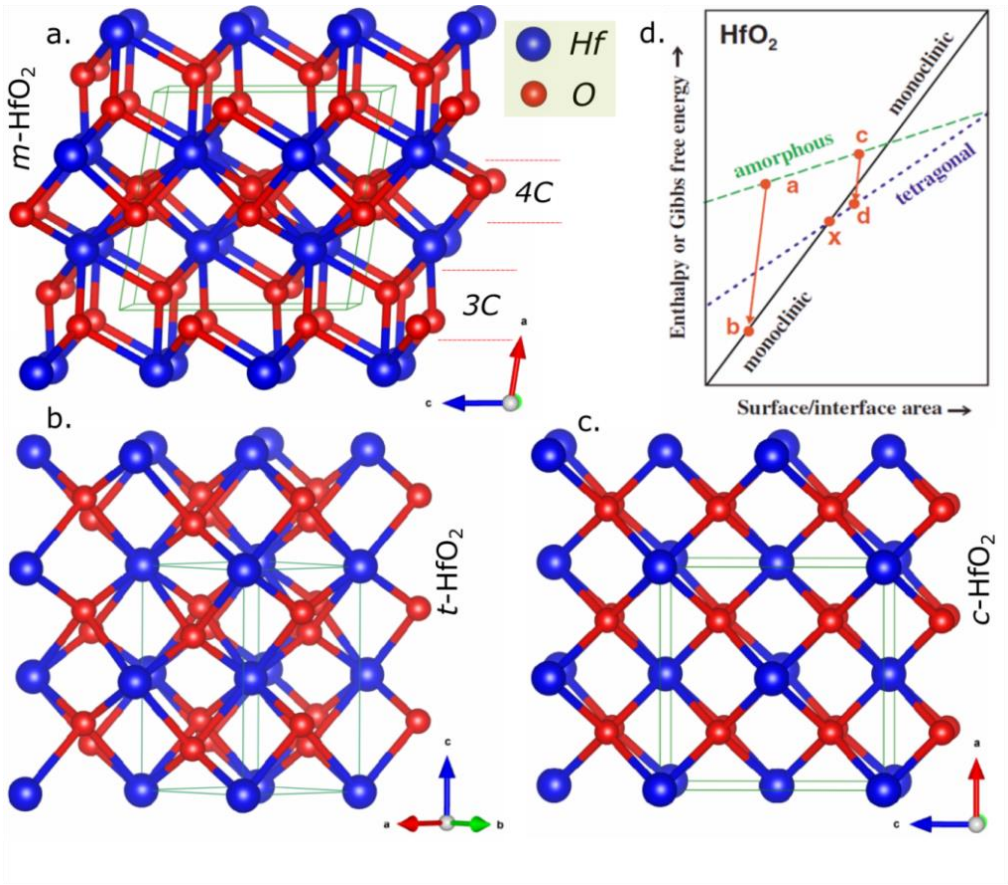

Figure 1.9: Crystal structure of hafnium oxide in the (a) monoclinic, *m*-HfO_2, (b) tetragonal, *t*-HfO_2 and (c) cubic, *c*-HfO_2, phases. (d) Schematic energy map for crystallization of hafnium oxide (reference) depending on the surface/interface area, where paths a-b and c-d corresponds to crystallization into monoclinic and tetragonal phases directly.

At higher temperatures, m-HfO_2 phase which is stable at room temperature undergoes transition to a tetragonal phase (*t*-HfO_2, $P4_2/nmc$) at 2000 K and a cubic phase (c-HfO_2, *Fm-3m*) transition occurs at 2900 K. These higher symmetry structures have an eight coordinated hafnium ion and four coordinated oxygen ion. The dielectric permittivity of crystalline phases is higher than that of the amorphous HfO_2. The cubic phase (ε = 27) has a higher dielectric permittivity higher than that of the monoclinic phase (ε = 16-25), and the tetragonal phase (ε = 35-70) shows the highest permittivity. On the other hand, at high pressure, *m*-HfO_2 phase transforms to orthorhombic phases: OI, *Pbca* initially and further to OII, *Pnma* phase at even higher pressures. Interestingly, ferroelectricity was discovered recently in hafnium oxide,[68] which could not be attributed to all these pre-mentioned centrosymmetric space groups. The ferroelectricity in pure HfO_2 was obtained up on annealing amorphous HfO_2 in the presence of a stress inducing top electrode. The most viable non-centrosymmetric orthorhombic phases responsible ferroelectricity in HfO_2 was identified to be $Pca2_1$ and $Pmn2_1$, using a first principles based search algorithm[69] and further confirmed as $Pca2_1$ using transmission electron microscopy.[70] After the discovery of ferroelectricity, there is much work going on

recently towards understanding the crystallization in HfO_2, which is now believed to be occurring via intermediate metastable phases. Amorphous hafnium oxide (*a*-HfO_2) is sometimes preferred for high-*k* applications to avoid higher leakage current and lateral non-uniformity associated with grain-boundaries.[71] Crystallization temperature of HfO_2 is very low ranging from 200 to 400 ^{o}C. Early studies also found that the crystallization of HfO_2 to a stable monoclinic HfO_2 occur via an intermediate tetragonal phase which was found to be stable at low crystallite sizes (< 5 nm). This was attributed to a higher thermodynamic stability of the tetragonal phase at high surface/interface area (figure 1.9(d)) at lower crystallite sizes.

Stoichiometry: Thermodynamic stability of the monoclinic HfO_2 phase is also likely limited by the stoichiometry of HfO_x. When the concentration of oxygen vacancy defects is increased, structural phase transitions from the most stable monoclinic phase to other phases are expected. McKenna *et al.* reported first principle based study of nucleation and growth of metal-rich precipitates under oxygen removal, which could serve as precursors for filament formation in hafnium oxide during electroforming.[72] Based on thermodynamic stability of the phases, a monoclinic phase was found to be stable at higher stoichiometry (x>1.25). The tetragonal structure of HfO_x was found to be stable in the narrow region of x = 1, below which a hexagonal metallic like phase (*hcp*-Hf) was found to be dominant.

Doping: The presence of impurities as dopants in HfO_2 can induce point defects in the crystal. Based on DFT calculations, Lee *et al.* found that dopants (Si, Sn, Ge, Ti, P, Al) with smaller ionic radii than Hf cation stabilized the tetragonal phase, while those with higher ionic radii (Y, Sc, Gd etc.) stabilized the cubic phase.[73] Additionally, it was found that ionized oxygen vacancies induced by trivalent dopants (Al, Y, Gd, etc.) play a role in stabilizing either cubic or tetragonal phases. Here, charged vacancies lead to 7-fold coordination of Hf atoms near the vacancy. Other oxygen ions are attracted towards the vacancy thereby screening the charge and better stabilizing the tetragonal and cubic structures.

1.5.2. Titanium Nitride electrode: crystal structure and properties

Titanium nitride (TiN) is a refractory metal showing a wide variety of interesting properties. Due to its high hardness, inertness, and diffusion barrier properties, TiN has now long since been the material of choice in diverse applications like protective coatings, medical implants and recently, and as metal gate electrodes in CMOS transistors. The successful combination of TiN and dielectric materials based on hafnium oxide (HfO_2) in CMOS FETs has led to a flurry of research in next generation devices like RRAM based on resistive switching in TiN/HfO_2 devices. Moreover, as a superconductor with bulk transition

temperature (T_c) of up to 6.0 K [74, 75] exhibiting low loss at microwave frequencies, TiN is also being investigated as electrode material in Josephson junctions and superconducting coplanar waveguides[76] and in microwave resonators for cubits. Recently, TiN has also gained significant interest in plasmonic and metamaterial applications in the visible and near-IR wavelength range.[77] The physical properties of TiN are summarized in Table 5.

Physical property	Titanium Nitride
density	5.2 g/cm^3
melting point	2930 °C
color	golden
resistivity (single crystal)	11.07 $\mu\Omega$.cm [78]
crystal structure	Cubic (Fm$\bar{3}$m)
work function	4.7-5.0 eV
superconducting transition temperature (T_c)	6.0 K

Table 1.5: (right) Physical properties of titanium nitride (TiN)

As shown in figure 1.10, TiN has a rock-salt crystal structure (Fm-3m) with a lattice constant of 4.24 Å. Here, the Ti and N atoms are arranged in a face-centered cubic (FCC) lattice, displaced with respect to each other along the <100> direction. This NaCl-type structure has been found to be present in the wide composition range of nitrogen from 30 to 55 at.% N. Therefore, there can be a high defect concentration in TiN films with vacancies and interstitials in the Ti as well as N sublattices. The lattice parameter of TiN has been reported to decrease in conditions of excess or deficient nitrogen.[79] Typically, a stoichiometry of 1:1 is desired for lowest resistivity and highest T_c.

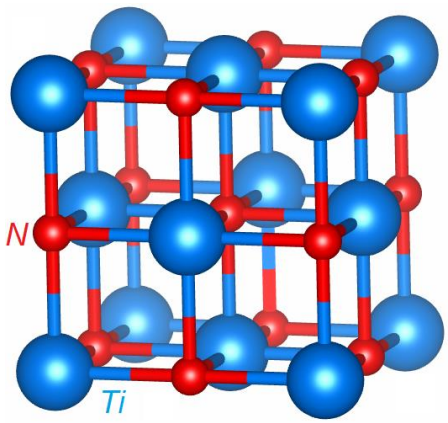

Figure 1.10: Cubic crystal structure of titanium nitride (TiN);

Polycrystalline TiN diffusion barrier layers, preventing the undesired interaction of contact metal (Al, W) and substrate material (Si, SiO_2) at high annealing temperatures up to 550-700 ^{o}C, are widely studied and reported in literature.[80] Polycrystalline TiN thin films are deposited either by deposited by physical vapor deposition (PVD) techniques like r.f. sputtering or chemical vapor deposition (CVD) techniques be it inorganic CVD or metal organic CVD (MOCVD). At room temperature, resistivity values as low as 25 $\mu\Omega$.cm and as high as 1000 $\mu\Omega$.cm have been reported for polycrystalline TiN in literature. Most commonly, these polycrystalline thin films of TiN exhibit a columnar type of morphology with grain boundaries running along the entire film thickness. Grain boundaries provide fast diffusion pathways for some metals (Cu) and are thus undesirable for efficient diffusion barrier performance.[80] On the other hand, the presence of defects like nitrogen vacancies and grain boundaries in TiN has been reported to assist in storing oxygen at the HfO_2/TiN interface during resistive switching.[81]

Epitaxial or singly oriented growth of TiN is also reported in literature using dc reactive sputtering,[82] pulse laser deposition (PLD)[83] and plasma assisted molecular beam epitaxy (MBE).[76] High quality epitaxy leads to very smooth film surfaces and lower defect densities. Thus, it is also highly desirable for superconducting and plasmonic applications, better diffusion barriers and as epitaxial buffer electrodes. In the work by Krockenberger *et al.*, TiN growth on MgO substrates by plasma assisted MBE with T_c up to 5.25 K and resistivity in the range of 10-15 $\mu\Omega$.cm was reported.[76] The highest surface quality and superconducting transition temperature of 5.25 K was obtained for films grown at 720 ^{o}C. Superconductivity was found to disappear at lower growth temperatures presumably due to changes in nitrogen content in the films. In the recent thesis work by Olson,[84] plasma MBE based growth of TiN on MgO, Si and sapphire substrates were investigated for low-loss superconducting quantum circuits. A superconducting T_c as high 6.1 K, closest to bulk TiN was reported by Olson for thin films grown at temperatures close to 1000 ^{o}C.

We have made investigations of TiN growth by plasma assisted MBE with focus on obtaining surfaces of high surface quality and low resistivity. This would in turn allow clean *in-situ* growth of subsequent hafnium oxide layers by MBE in future. High surface quality is obtained relatively easily for TiN (001) films grown on MgO (001) substrates due to very low lattice mismatch (0.7 %). However, it is preferable to obtain TiN films on more industrially viable and cheaper silicon and sapphire substrates. But, growth of atomically flat surfaces of TiN film on silicon and sapphire substrates is expected to be difficult due to higher lattice mismatches. The lattice constant of Si is 5.431 Å, leading to a lattice mismatch of ideally 25%

which is typically too high for epitaxial TiN(001) growth on Si(001) surface. However, Narayan *et al.* reported the epitaxial growth of TiN on Si (001) substrates by pulsed laser deposition, which was suggested to occur via a domain matching epitaxy.[85] Here, four of the TiN (001) unit cells can be considered to fit on three unit Si (001) unit cells with a lattice mismatch of less than 4%. Talyansky *et al.* first reported the epitaxial growth of TiN (111) film on c-cut sapphire or Al_2O_3 (006) substrates with resistivity as low as 13 $\mu\Omega$.cm and an rms surface roughness (5 × 5 μm^2) of 0.6-1.0 nm.[78] A high lattice misfit of 8.75% was calculated considering a rhomb-on-rhomb growth on the sapphire substrate. Though epitaxial growth has been reported to be possible on silicon and sapphire substrates, the growth mechanism with focus on improved smoothness and epitaxy for electrode applications is currently not well investigated in literature.

1.5.3. State of the art in HfO_2/TiN based RRAM

In addition to its pre-established CMOS compatibility, HfO_2/TiN based RRAM is especially popular due to its fast speed (<10 ns)[48], low power switching (1 pJ/bit)[47], high endurance (10^9 cycles)[86] and excellent scaling capability down to 10 nm.[47] Figure 1.11(a) shows the TEM cross section of commonly studied device of TiN/Ti/HfO_2/TiN. The Ti buffer layer acts as oxygen scavenging layer causing a possible reaction at the interface between Ti and HfO_2 during an annealing process.[87] The interfacial layer thus formed acts as an oxygen reservoir and series resistor during the switching process. Most commonly, a bipolar resistive switching behavior as shown in figure 1.11(b) is observed for TiN/Ti/HfO_2/TiN devices. The thickness of Ti buffer layer is critical to the performance of the devices and can be chosen so as to control the dielectric breakdown strength and therefore the forming voltage of the HfO_2 layer.[67, 88] It was found that the forming voltage can be reduced from 3.6 V (without Ti buffer) to nearly 1.8 V (10 nm Ti) in a TiN/Ti/(5.5 nm)HfO_2/TiN device. However, a very high thickness of the Ti buffer layer causes a highly oxygen deficient hafnium oxide layer to form at the interface. This was found to lead to reduced performance due to fast degradation of the HRS, where surrounding excess vacancies would move into the ruptured high resistance region. A thickness ratio of 1:1 for Ti:HfO_2 has been suggested for optimal performance of the devices.[89] A lowered thickness of Ti layer (3 nm) compared to 5.5 nm HfO_2 was found to lead to a complementary resistive switching in TiN/Ti/HfO_2/TiN devices, as has also been found in symmetric TiN/HfO_2/TiN devices,[57, 88] which can be used as selector devices.

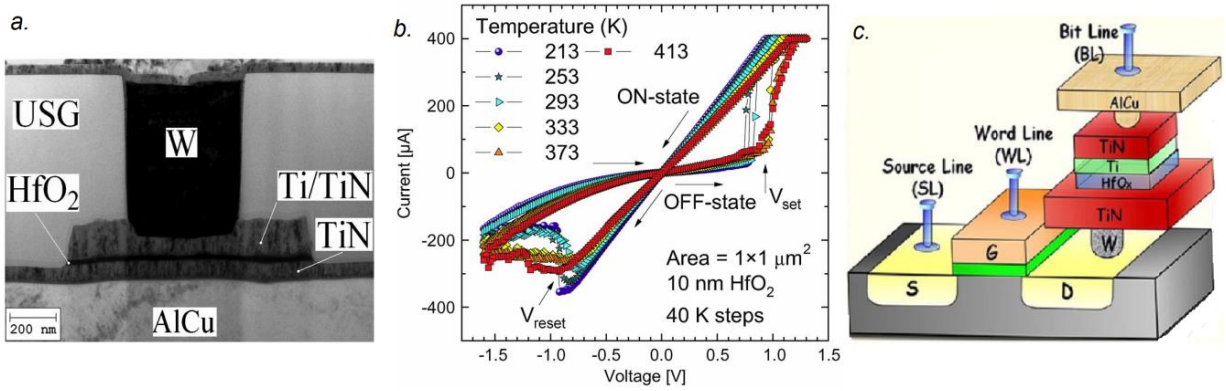

Figure 1.11: (a) cross sectional TEM of TiN/HfO2/Ti/TiN device of area 1 x 1 μm^2 from Walczyk *et al.*[67] (IHP GmbH, Germany); and (b) corresponding I-V characteristics during bipolar switching operation at different temperatures; (c) 1T-1R series configuration of TiN/HfO2/Ti/TiN devices from Rahaman *et al.*, [88] (ITRI, Taiwan).

For application as embedded NVM, such a TiN/Ti/HfO_2/TiN device stack is very promising, since it can be easily be integrated in the back-end-of-line (BEOL) process of CMOS in a 1T-1R configuration as shown in figure 1.11(c), where the device (R) is in series with the CMOS transistor (T), which plays the role of an access device and also provides current compliance for set operation.[88] A very high performance and yield has been reported in 1 kb array devices based on 30 × 30 nm^2 devices with good endurance (10^6 cycles), where a high device yield (~100%) was achieved using verification methods to overcome soft errors.[90] This 1T-1R HfO_x device design, which is not highly scalable due to lateral spacing between the transistor and memory element is however especially well-suited to embedded-NVM focusing on low-power applications, where the scalability is not critical.

In terms of scalability which is important for storage class memory, a minimum RRAM cell size of 10 x 10 nm^2 was achieved in a cross-point configuration of Hf/HfO_2/TiN device.[47] Recently, NAND based flash technology has overcome the lateral scaling limitations (< 18 nm) arising due to quantum tunneling by the way of 3D stacking. However, the relatively simpler structure coupled with further scalability still gives certain advantages for RRAM over NAND. Similar to NAND based flash, different integration schemes have been envisioned for oxide based RRAM.

Stacking of the 2-D cross point arrays as shown in figure 1.12(a) is one way of achieving 3D RRAM of the highest density, where the intermediate electrode is shared.[1] The array is obtained by perpendicular conductive wordline electrodes (rows) and bitline electrodes (columns) with the memory element existing at the intersection. The memory can be read and written by biasing the corresponding wordline and bitline. Such a dense packing of wordlines/bitlines allow for an extremely small bit area of only $4F^2$, where F is the

minimum feature size accessible by lithography. However, such a stacking requires a good selector element in series to the memory element, which remains an intensively investigated topic in itself. One other approach of 3D stacking is by using vertical electrodes called V-RRAM as shown in figure 1.12(b).[91] Here the resistive element is sandwiched vertically between pillar electrodes and multilayer plane electrodes. A similar technology is currently already being used in V-NAND devices. V-RRAM brings down the requirements for critical patterning steps and is highly promising in terms of cost-effectiveness. However, realization of V-RRAM technology requires several challenges to be resolved. One of the challenges is to identify RRAM devices with built-in self-selection properties since additional selector element cannot be introduced inside the vertical configuration. Moreover, deposition technology also remains an issue where PVD techniques allowing for good control over stoichiometry have been found to be incompatible. Figure 1.12(c) shows such a TEM cross section of a double layer TiN/HfO_x/Pt V-RRAM device fabricated by Yu *et al.*[92] The HfO_x layer is deposited on the sidewall of a predefined trench by atomic layer deposition (ALD).[93] A number of stacked devices can be defined by layers of Pt electrode separated by an insulating layer (SiO_2). Moreover, a TiON interfacial layer which formed was suggested to be additionally responsible for non-linear I-V characteristics, thus opening up possibility of selector-less arrays.

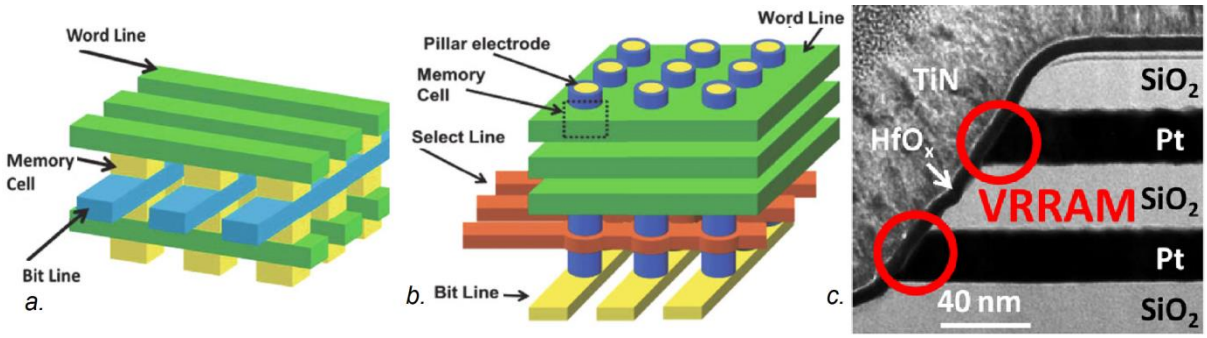

Figure 1.12: Typical 3D architectures for RRAM from Hudec *et al.*[91] (a) cross-point architecture in case of horizontal RRAM; the memory element is sandwiched between perpendicularly accessed bitlines and wordlines; (b) vertical pillar based stacking called V-RRAM, Here, the memory cell is vertically aligned to the side wall of the pillar, (c) TEM of the a two-layer Pt/HfO_x/TiN based vertical RRAM fabricated by Chen *et al.*[92]

1.6. Defect physics in hafnium oxide

Thin films of hafnium oxide usually contain many defects which affect its electronic transport and optical properties. These defects act as electron and hole traps, thereby significantly affecting the functionality of the devices. In a high-*k* dielectric, traps play an adverse role by capturing electrons injected into the oxide layer and increase the leakage current. On the other hand, Flash memories work on the principle of charge storage by electron localization at

these traps. In this case, a trap density of $N \geq 10^{19}$ cm^{-3} is ideal for a high resistance window between the logical '0' and '1'. Moreover, sufficiently high ionization energy (≥ 1 eV) is necessary for high retention (≥ 10 years at 85 °C) of these non-volatile memories.[94] Therefore, it is important to have a good understanding of the atomic and electronic structure of oxygen vacancies. Oxygen vacancy defects can be formed in HfO_2 *intrinsically* during synthesis of thin films by (1) a non-stoichiometric growth or (2) via impurity necessitated charge compensation. Oxygen vacancies can also be created *extrinsically* by breaking the Hf-O bonds by (1) high electric field and temperatures, (2) chemical reactions with adjacent highly reactive contact metals or by (3) irradiation of stoichiometric hafnium oxide with inert gas ions or other heavy ions.

1.6.1. Defect states and energy levels: theory

Optical band gap of stoichiometric HfO_2 has been experimentally reported to be 5.7-5.8 eV. The electronic states near the valence band are formed by the *d* orbitals of the hafnium ([Xe $4f^{14}$ $5d^2$ $6s^2$]) ions, with minor contribution of *p* states from oxygen ([He] $2s^2 2p^4$). The conduction band is formed mainly formed by *p* states of oxygen atoms with very minor hafnium contribution. Currently, oxygen vacancies are recognized as the most thermodynamically stable point defects in hafnium oxide.[94] In monoclinic HfO_2, oxygen vacancies can be three (V_{III}) or four (V_{IV}) coordinated according to the local structure of hafnium oxide. Additionally, depending on the number of trapped electrons, oxygen vacancies can be double/single positively charged (V_O^{+2},V_O^{+1}), neutral (V_O) or double/single negatively charged. (V_O^{-1}, V_O^{-2}). Other possible defects in HfO_2 include hafnium vacancies and interstitials of oxygen. In comparison to the formation of an oxygen vacancy in a monoclinic structure, which required the breaking of three or four Hf-O bonds, a hafnium vacancy would require breaking seven such bonds and are thus less energetically favorable. The presence of interstitial oxygen has also been suggested in the case of oxygen excess or during diffusion, which will be discussed in the section 1.8 on ionic transport.

Theoretical calculations have been performed by several researchers to ascertain the stability and energy levels of these defects in HfO_2. Xiong *et al.* adjudged that the formation of oxygen vacancies were more thermodynamically stable than interstitials using density functional methods based on screened exchange (sX) method and weighed density approximation (WDA).[95] The authors found that oxygen vacancies provided trap energy levels below the conduction band lying above the Si conduction band in *cubic*-HfO_2/Si, as shown in figure 1.13(a).[95] Thus, vacancies are ideal for easier electron transitions to Si channels compared to interstitials (I_O), which were found to form trap energy levels just above the

valence band of hafnium oxide.[95] Gavartin *et al.* calculated the position of trap levels for the five different charge states of vacancies in monoclinic-HfO_2 as shown in figure 1.13(b). Positively charged (V_O^{+2},V_O^{+1}) were found to be more stable in 3-fold coordinated sites, whereas, neutral and negative vacancies were found to be favored in 4-fold coordinated sites. Positive and neutral vacancies lie deeper in the band gap, thus requiring activation for electron capture to the conduction band. However, negatively charged vacancies causes the formation of shallow traps (close to conduction band) which was suggested to be responsible for threshold-voltage instability in MOS transistors. Ramo *et al.* reported that neutral and double positively charged vacancies (V_O, V_O^{+2}) are the stable charge states of vacancies under thermodynamic equilibrium.[96] The other charge states have been suggested to occur under non-equilibrium conditions. Therefore, it can be assumed that charge trapping and detrapping occurring in these in these vacancies during electronic transport in the presence of an applied bias can lead to the stabilization of the other charge states of vacancy. Moreover, Hf-V_O bond lengths are affected according to the charge state of the vacancies. Neighboring hafnium atoms have been found to be displaced in the presence of charged vacancies by 11% and 8% away from V_O^{+2} and V_O^{+}, respectively.[97] Similarly, negatively charged V_O^{-2} and V_O^{-} shift the Hf atoms towards the vacancy by 8% and 4%, respectively. Neutral vacancies resulted in a very negligible shift of neighboring hafnium atoms.[97]

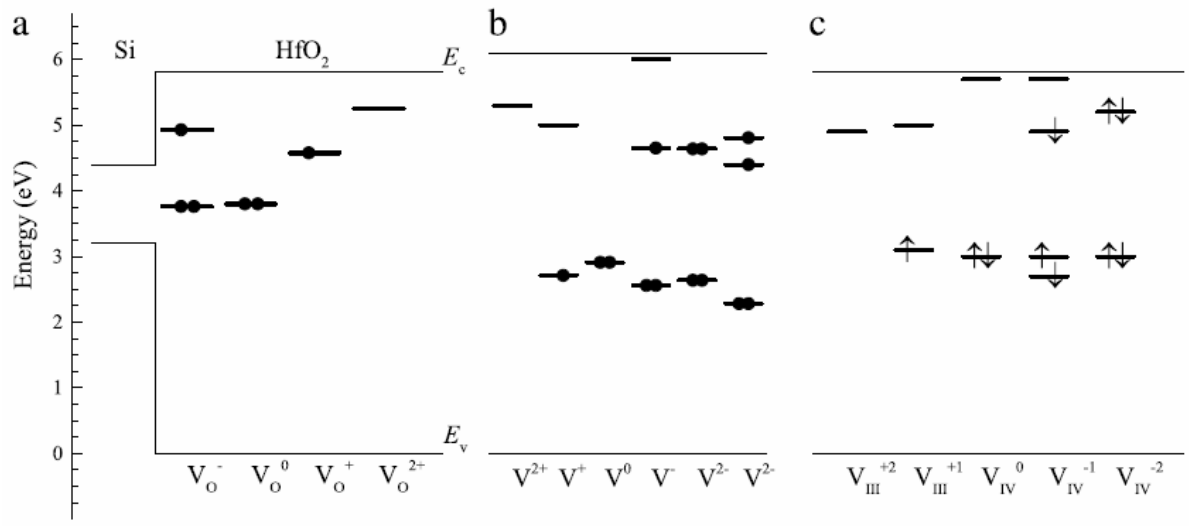

Figure 1.13: Defect state energy levels induced the band gap of hafnium oxide due to oxygen vacancies with different charge states and coordination as summarized in Gritsenko *et al.* from different works.

1.6.2. Metal insulator transition in HfO_2: Theory and Experiments

In hafnium oxide based resistive switching devices; a **local** insulator metal transition (IMT) in HfO_2 is achieved via the local clustering of high concentration of vacancies forming conducting filamentary pathways. Therefore, appropriately controlling and identifying the nature and density of oxygen vacancies in HfO_2 has turned out to be necessary for optimization of RRAM devices. Perevalov *et al.* performed ab initio numerical simulations of poly vacancies in HfO_2 and found that, as more vacancies are generated in hafnia, the defect induced trap levels or peaks merely grow in amplitude and the position of the defects or trap levels remain similar to mono-vacancies.[98]

In a different scenario, Hildebrandt *et al.* reported a very higher oxygen vacancy concentration induced **global** IMT in HfO_{2-x}. In this case, uniformly distributed vacancies across the bulk of the film were achieved in thin films grown by reactive molecular beam epitaxy (RMBE).[99, 100] As shown in figure 1.14(a), the resistivity of the as-grown films was found to change several orders or magnitude spanning from a typical insulating (10^{18} μΩ cm) down to metallic (10^{2} $\mu\Omega$ cm) nature by tuning the oxygen stoichiometry. Moreover, the appearance of the films grown on transparent sapphire substrates changed from a typical transparent film (2 sccm; high oxidation conditions) to darker films with a golden shine (0.3 sccm; low oxidation conditions) at lower oxygen flows. The optical band gap of the oxygen deficient thin films was found to decrease by more than 1 eV figure 1.14(b), which has not been reported in theoretical calculations. At very high oxygen content (HfO_{2+x}), oxygen interstitials or hafnium vacancies were suggested as the likely defects inducing further lowering of the band gap. Taking into account that the golden shine requires an absorption edge of about 2 eV, a band structure (figure 1.14(c)) was suggested by the authors to explain the observed optical transition and metallicity. A single negatively charged vacancy (V_O^-) was proposed to be the dominant defect in highly oxygen deficient films with Fermi level placed near the conduction band near the half-filled defect band. Additionally, *p*-type conductivity was also observed in these highly oxygen deficient films, which was suggested to arise from the more than half-filled second defect band.[99] Considering a lowered band gap of ~4.5 eV, electronics transitions (~ 2 eV) between the fully occupied mid gap defect states (arising from V_O^-) and the conduction band was suggested to be the cause of the golden shine. The ability to tune the oxygen concentration in oxides using RMBE, as reported in this study forms the basis of continued work reported in this thesis.

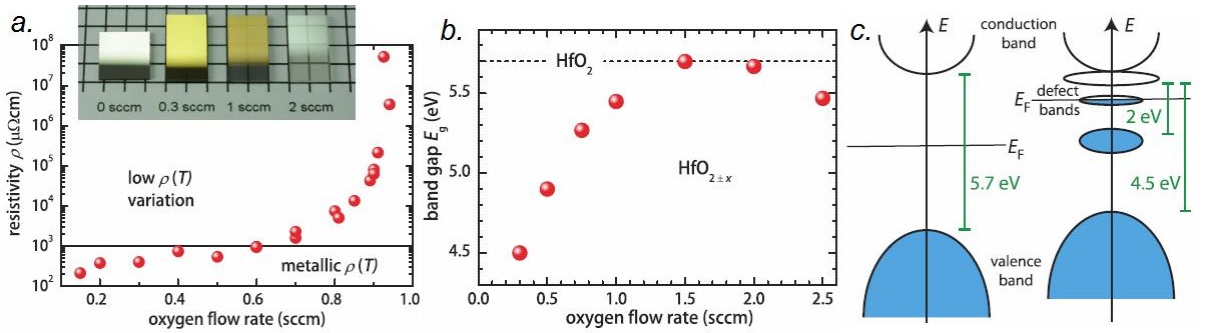

Figure 1.14: Resistivity as a function of oxygen flow rate for HfO2-x thin films grown on *c*-cut sapphire by reactive molecular beam epitaxy from Hildebrandt *et al.* [99, 100]

1.7. Electronic transport in oxide RRAM

Electronic transport mechanisms in oxide based MIM structures can be classified as electrode-limited conduction mechanisms and bulk limited conduction mechanisms, as summarized in literature.[101, 102] A schematic representations of major conduction mechanisms is shown in figure 1.15(a). Among the electrode limited conduction mechanism are: (1) Schottky emission (SE), Fowler-Nordheim tunneling (FN) and (3) direct tunneling. The bulk limited conduction mechanisms are (4) Poole-Frenkel (PF) emission, hopping conduction: (5a) nearest neighbor hopping (NNH) and (5b) variable range hopping (VRH), (6) trap assisted tunneling, (7) ohmic conduction and space-charge limited conduction (SCLC) (not shown). In bulk-limited conduction mechanism, traps in the form of point and extended defects in the oxide layer play a major role in assisting and providing pathways for the transport of electrons.

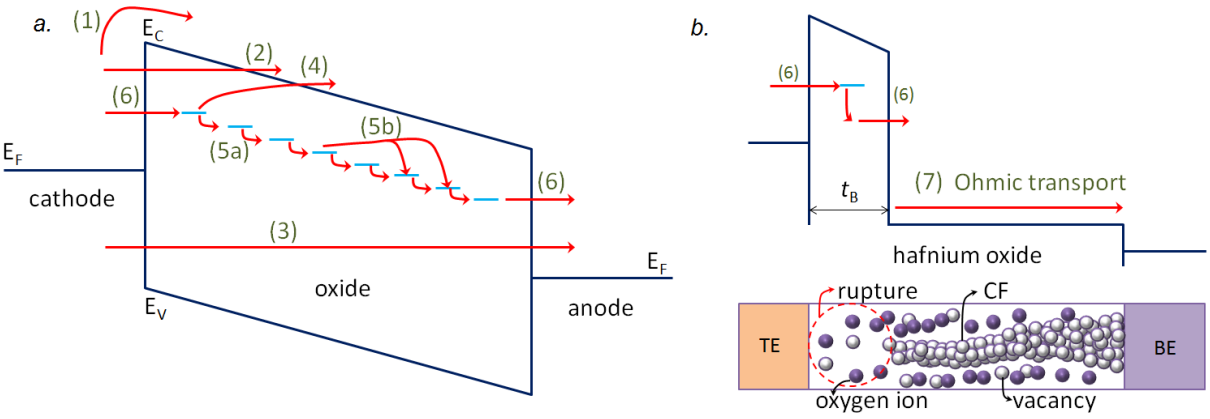

Figure 1.15: Schematic diagram showing (a) the electronic transport (1-6) mechanisms in a metal-oxide-metal devices adapted from Bagdzevicius et al.[22] and (b) Typical conduction in a filamentary HfO_x based device, where the conduction is Ohmic (7) in the filamentary region.

Table 1.6 summarizes the expressions relating the electric field (E) and current density (J) of these conduction mechanisms. The electronic conduction mechanism in RRAM devices is typically confirmed by comparing the field as well as temperature dependence of current-voltage characteristics to the relevant equations of various mechanisms. However, this does not necessarily provide a clear answer, as it is usual that multiple conduction mechanisms may occur simultaneously in devices. In HfO_x RRAM devices, as shown in figure 1.15 (b), high resistance state constitutes a partially ruptured filament configuration. The conduction mechanism is typically reported to be Ohmic in nature for a fully cohesive filament in the low resistance state. A interface limited trap assisted tunneling (TAT) has been reported more often in the ruptured or high resistance state of HfO_x.[103-105] As observed by Yu *et al.*[104] in a TiN/HfO_x/Pt based device, though the current voltage characteristics could fit well to a Poole-Frenkel (PF) emission transport at higher voltages (> 0.2 V) showing a linear behavior of ln(I/V)-$V^{1/2}$, it was ruled out due to unrealistic values of the extracted trap energy and dielectric constant. By similarly eliminating other mechanisms, TAT was found to be the most probable conduction mechanism. Temperature dependent investigation of electronic hopping transport in the similar TiN/HfO_x/Pt based device also revealed a transition from nearest neighbor hopping to variable range hopping below 77 K due to lowered thermal energy of electrons.[106] A qualitative statistical model based on multi-phonon TAT (MPTAT) was used by Bersuker *et al.* in a TiN/HfO_x/TiN device,[103] taking into account lattice relaxations due to electron-phonon coupling and defect movement by ionic transport.

Padovani *et al.* presented a comprehensive model describing the electroforming and switching operations at microscopic level in a TiN/Ti/HfO_2/TiN. Electronic transport was modeled in the framework of a multiphonon TAT theory, using a statistical kinetic Monte Carlo approach(kMC) to account for randomly distributed oxygen vacancies.[107] When high defect densities are reached, electron drift becomes dominant in the presence of defect sub-bands, with a critical defect density of $N_{CRIT} \sim 1.7 \times 10^{22}$ cm^{-3}, corresponding to defect-to-defect distance of 3.5 Å. The charge trapping-hopping at defect sites is associated with energy release at the defect sites, leading to local increase of temperature to up to 900 K.[103] The power is dissipated microscopically through phonon emission at defect sites and also at the electrodes. A 3D map of the temperature profile, T(x,y,z) during switching can be obtained by solving the Fourier's heat flow equation for power dissipation, P(x,y,z).

$$P(x,y,z) = k_{TH}\nabla^2 T(x,y,z) \qquad \text{Equation 1-2}$$

where k_{TH} is the thermal conductivity of HfO_2.

Table 1.6: Equations for field dependence of various conduction mechanisms (Adapted from Lim *et al.*[101])

Conduction mechanism	Current Density (J) – Electric field (E) expression
Schottky Emission (SE)	$J_{SE} = \frac{4\pi q m^* (kT)^2}{h^3} \exp\left[\frac{-q(\phi_B - \sqrt{qE/4\pi\varepsilon})}{kT}\right]$
Fowler-Nordheim (F-N) Tunneling	$J_{FN} = \frac{q^2}{8\pi h \phi_B} E^2 \exp\left[\frac{-8\pi\sqrt{2qm^*}}{3hE} \phi_B{}^{3/2}\right]$
Direct Tunneling	$J_{DT} \approx \exp\left[\frac{-8\pi\sqrt{2q}}{3h} (m^* \phi_B)^{1/2} k.\, t_{ox,eq}\right]$
Poole-Frenkel (PF) Emission	$J_{PF} = q\mu N_C E \exp\left[\frac{-q(\phi_T - \sqrt{qE/4\pi\varepsilon})}{kT}\right]$
Nearest Neighbor Hopping (NNH)	$J_{NNH} = \sigma_0 exp\left(\frac{-T_0}{T}\right).E$
Variable Range Hopping (VRH)	$J_{VRH} = \sigma_0 exp\left(\frac{-T_0}{T}\right)^{\frac{1}{4}}.E$
Trap-assisted Tunneling (TAT)	$J_{FN} = A \exp\left[\frac{-8\pi\sqrt{2qm^*}}{3hE} \phi_T{}^{3/2}\right]$
Ohmic Conduction	$J_{Ohmic} = \sigma E = q\mu N_C \exp\left[\frac{-(E_C - E_F)}{kT}\right]$
Space-Charge Limited Conduction (SCLC)	$J_{SCLC} = \frac{9}{8}\varepsilon_i \mu\theta \frac{V^2}{d^3}$ *(At high fields only, Ohmic at low field)*

m*: electron effective mass in oxide; k: Boltzmann constant, T: absolute temperature, h: Plank's constant, ϕ_B: Junction barrier height, ε: dielectric permittivity, $t_{ox,eq}$:equivalent oxide thickness, μ: electron mobility, ϕ_T: trap energy w.r.t to conduction band (E_C), N_c: density of states in E_C, σ_0: Electrical conductivity at T_0, θ: ratio of free and shallow trapped charge, V: voltage, t: oxide thickness, E_F: Fermi level, A: constant

1.7.1. Quantum point contact (QPC) model

The filament size or the degree of rupture and cohesion of the filament is modulated during the set and reset processes. This leads to an intermediate transport regime of conductance quantization in point contact configurations of the filament. Observation of quantum conductance steps in a SiO_x based RRAM during the break down or set process is shown in figure 1.16(a).[108] The corresponding filament geometry evolution is shown on the top of figure 1.16(a), where the filament can be understood to evolve gradually from a fully ruptured to a point contact to thicker filament composition. Here, conductance steps corresponding integer and half-integer multiples of G_0 is observed in the current-voltage characteristics during the set process. $G_0 = 2e^2/h$ is the quantum conductance with a value of 12.9 $k\Omega^{-1}$ or 77.5 μS, where e is the electronic charge and h is the Planck's constant. Such quantum conductance steps were first observed in 1988 by Van Wees *et al.* in ballistic point

contacts in the 2DEG (two dimensional electron gas) of high mobility GaAs-AlGaAs heterostructures. [109]

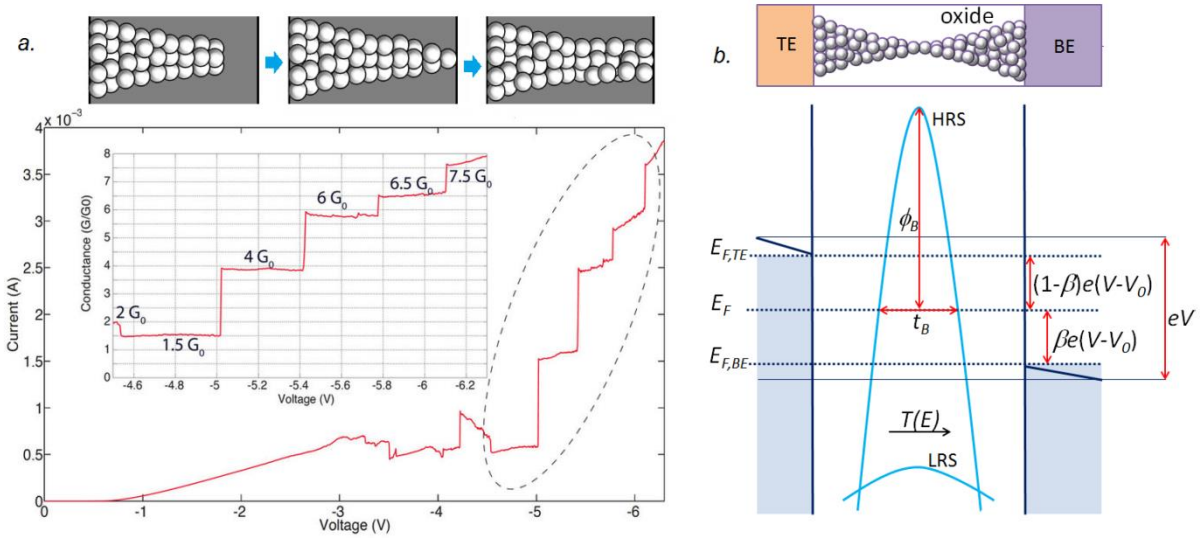

Figure 1.16: (a) Observed quantum conductance steps in a SiO_x based RRAM during the set process in Mehonic *et al.*[108] The filament configuration is shown on the top where an oxygen vacancy – filament ruptured filament transitions from a ruptured to a point contact to thicker filament compose dof multiple channels. (b) The energy level diagram showing parabolic potential barrier corresponding to high resistance state configuration for a narrow constriction with a barrier height, Φ_B. and thickness, t_B. V: applied voltage, V_0 is the voltage dropped across ateh the TE and BE, β is the voltage asymmetry parameter.

According to Datta,[110] quantization phenomenon of conductance is observed when the dimension of the conductor is smaller than any of the three characteristic length scales: (1) de Broglie wavelength of electrons; (2) mean free path of electrons and (3) phase relaxation length of electrons. This leads to a ballistic transport of electrons in the case of a narrow filament, where the electrons are not scattered. In a ruptured filament configuration, the conductance is lower than G_0, when at least one re-oxidized vacancy exists in the ruptured CF region. In the filament formation process during set, the current can be considered to be flowing through multiple discrete channels, each of which contributes a maximum amount of one G_0. The conductance of the conductor can be described by the Landauer formula, $G = G_0\Sigma_i T_i$, where T_i is the transmission probability of individual channels, which is determined by conductor geometry and electronic structure of the material. Suñé and Miranda used the Quantum point contact (QPC) model based on Landauer formalism to describe the post breakdown conduction process in gate dielectric of FET, considering the breakdown path as narrow constrictions.[111]

Consequently, the QPC model can be used to model the conduction process in the high and low resistance states of RRAM devices, where the narrowest part of CF is considered an atomic contact[112] as shown in figure 1.16(b). This thinnest part of the filament constituting of

one (or few) atoms is modeled as a potential barrier with quantized sub-bands. The quantum transport through the constriction can be modeled as a simple 1D tunneling behavior. Using Schrodinger equation, which can be split into transverse and longitudinal equations, the dispersion curve of the electronic sub-bands can be obtained as: [113]

$$E(k_z, z) = \epsilon_n(z) + \frac{\hbar^2 {k_z}^2}{2m} \qquad \text{Equation 1-3}$$

where, z and k_z are the real and k-space coordinates in the direction of the constriction, respectively; m is the electron mass and $\hbar$ is the reduced Planck constant. For a rectangular confinement[114] with dimensions L_x and L_y of the constriction,

$$\epsilon_n(z) = \frac{\hbar^2 {k_z}^2}{2m}\left(\frac{n_x^2}{L_x(z)^2} + \frac{n_y^2}{L_y(z)^2}\right) \qquad \text{Equation 1-4}$$

Here, n_x and n_y are integers. Therefore, discrete parabolic sub-bands can be obtained from the dispersion relationship (E-k_z). In real space, the dependence of energy levels can be represented as arch-spaced curve as shown in figure 1.16(b). In case of thick filaments, L_x and L_y becomes larger thus lowering the energy band spacing and this leads to weak confinement or a 3D bulk energy band. Here, for the low resistance state (LRS) the sub-bands are in deep energy levels. For a narrow or disrupted filament, the bottom of the sub bands will be lifted as represented for HRS.

The quantum point contact (QPC) model of the conducting filament based on the Landauer-Büttiker formalism can be used to model electronic transport through the constriction as a transmission problem for electrons at the Fermi level. The injected electrons under a potential drop eV can travel with a transmission probability, T(E) across the barrier. Depending on the nature and position of the constriction, $\beta \in [0,1]$ is the potential drop at the side of the voltage source. The sub-band has a barrier height represented by Φ_B and a width represented by barrier (rupture) thickness, t_B at E=0. For negligible electrode resistances, the potential drop almost entirely happens across the filament. The current flowing through the device can be derived as:

$$I = \frac{2e}{h} N_{ch} \int_{-\infty}^{\infty} T(E)[f(E - \beta eV) - f(E + (1-\beta)eV)]dE \qquad \text{Equation 1-5}$$

where, E – energy, f is the Fermi-Dirac distribution function and N_{ch} is the number of open 1D vacancy channels. Assuming an inverted potential barrier, the transmission probability can be obtained as follows:

$$T(E) = \{1 + \exp[-\alpha_B(E - \Phi_B)]\}$$ Equation 1-6

Where, α_B is the curvature parameter which is related to the inverse of the [potential barrier curvature and proportional to barrier thickness and effective electron mass, m* as given by:

$$\alpha_B = \frac{t_B \pi^2}{h}\sqrt{\frac{2m^*}{\Phi_B}}$$ Equation 1-7

Inserting the transmission probability into the integral, the expression for current can be obtained as follows:

$$I = \frac{2e}{h}N_{ch}\left\{eV + \frac{1}{\alpha_B}Ln\left[\frac{1 + \exp\{\alpha_B(\Phi_B - \beta eV)\}}{1 + \exp\{\alpha_B[\Phi_B + (1-\beta)eV]\}}\right]\right\}$$ Equation 1-8

At low resistance state or a very thick filament, the barrier is assumed to play no role at all and the above equation converges to linear I-V expression as follows,

$$I_{LRS} \cong N_{ch}\beta G_0 V$$ Equation 1-9

Considering a simplified treatment of the constriction as a hard-wall lateral confining potential, from the first eigen value of a circular infinite well, the radius r_B of the constriction can be approximated as:

$$r_B = \frac{hz_0}{2\pi\sqrt{2m^*\Phi_B}}$$ Equation 1-10

where, $z_0 = 2.404$ is the first zero of the Bessel function J_0.[112]

First principle calculations based on the density-functional theory (DFT) using Green's function based transmission probability performed by Cartoixa *et al.* for a crystalline HfO_2 matrix found that a single oxygen vacancy channel can display quantization effects. Using the QPC model, Miranda *et al.* extracted parameters of barrier thickness and radius in the HRS of a Pt/HfO_2/Pt device which was found to be in the nanometer range.[112] Bipolar resistive switching in devices with non-similar electrodes (Ti/HfO_2/Pt) have been modeled with an asymmetric (conical) filament (β= 0 or 1) where the switching proceeds via the oxidation/reduction of the tip of the conducting filament near the active interface.[115]

Conductance quantization phenomenon has been reported to be observed in the set/reset process of a many oxide devices. However, in HfO_x based VCM or TCM's, step wise quantization phenomenon involving integer or half-integer steps of G_0 has been reported at room temperature and shown to occur statistically only in the reset I-V curves of Pt/HfO_2/Pt

devices.[54] In another work, gradual bipolar reset was found to change to a step-wise reset behavior in the region close to $G=G_0$ at low temperature in a Ti /HfO_2/TiN device.[116] Highly controlled occurrence of individual quantized steps yet remains out of reach, since each of the cycles involves high fluctuations. In the present study described in this work, we have investigated and found a dependence of existence of quantized conductance states on the oxygen stoichiometry.

1.8. Ionic transport in anionic RRAM: electroforming and switching

As described in the previous session, the electronic transport typically observed at low voltages in an oxide is strongly influenced by the presence of oxygen vacancies. In this section, the transport of ions which occur at high voltages is considered.

1.8.1. Forces driving ionic transport

Electric field: In the presence of an electric field, oxygen vacancies will be driven towards the cathode and oxygen ions will move towards the anode, parallel to applied field. In a crystal lattice, the ionic motion can be imagined as a hoping process in a periodic potential. The ion hopping rate, r_{hop} in the presence of an electric field, E is given by: [21]

$$r_{hopping} = ve^{-(E_a - qaE)/k_BT}$$

For oxygen ions/vacancies, the attempt frequency and activation energy are $\nu \sim 10^{13}$ Hz and $E_a \sim 1.0$ eV, respectively. At room temperature, $k_B \sim 25$ meV, where k_B is the Boltzmann constant. Considering double positively charged oxygen vacancies ($V_{\ddot{O}}^{2+}$) with a charge state of q=2 and a hopping distance of a= 0.5 nm, under an electric field of E = 0.1 V/nm, the hopping rate $r_{hopping}$ is $\sim 10^{-4}$ s^{-1} (one hop per hour). This would mean a very long retention time ($t_{retention}$) for the memory state, however a very slow switching process during the write process of set/reset. In metal oxide based RRAM devices, a fast switching speed of below 10 ns has been achieved.[2] This implies an acceleration of switching kinetics by more than 10^{12} ($t_{retention}/t_{read}$) when the voltage increases by a factor of 10, (V_{write}/V_{read}). Such a high intrinsic non-linearity in the switching process has been termed *'voltage-time dilemma'*.

Based on the highly non-linear kinetics of the ionic transport, the fast switching speeds achieved cannot be described by just the typical field induced drift of oxygen vacancies or ions at 300 K. The additional accelerating forces facilitating fast switching have been suggested to be due to thermally assisted transport by Joule heating, quicker transport along extended defects (dislocations, grain boundaries etc.), and very high fields at switching interfaces.[19] Such a combination of accelerating forces has been suggested to increase the ion mobility by

over 12 orders of magnitude.[117] The resulting field is usually sufficiently large approaching the breakdown field of materials.

A more simplistic picture to understand the ionic transport processes including the additional effect of Joule heating involved in anionic RRAM was suggested by Strukov *et al.* Here, the switching process was modeled to proceed via the combined action of the driving forces arising from the presence of a concentration gradient ($\nabla\eta_v$), electric field ($\nabla\varphi$) and temperature gradient (∇T).[118] The corresponding ionic flux in one dimension, as represented in figure 1.17, arising from these driving forces of Fick diffusion, drift and Soret themophoresis, the can be individually approximated as:

$$J_{Fick} \approx -D_V \frac{dn_V}{dx}$$

$$J_{Drift} \approx D_V n_V \frac{qE}{k_B T}$$

$$J_{Soret} \approx -D_V S_V n_V \frac{dT}{dx}$$

where n_V, T are the density of vacancies and local temperature and diffusion factor of vacancies respectively, as functions of x. D_V and S_V are position dependent diffusion factor and Soret coefficients for vacancies, respectively.

$$D_V = f_{esc}\, a^2 \exp\,[-U_A/k_B T]\,;$$

where f_{esc} is the effective vibrational frequency of the vacancies, U is potential barrier height.

Soret force: Thermophoresis or Soret force as an additional microscopic force was initially suggested to explain the set process in unipolar devices, where a continuous ionic motion in the direction of just the electric field would lead to accumulation and loss of ions and cannot explain the observed long cycling endurance.[118] Thermophoresis is the temperature gradient (∇T) driven oxygen ion transport from a hotter region to a cooler region, due to higher energy of ions in the hotter region. This leads to clustering of oxygen vacancies during the set and forming processes. Considering a typical cylindrical nature of the filament connecting the electrodes, a temperature gradient will appear perpendicular to the axis of the filament due to Joule heating caused by electronic transport. This would therefore drive a lateral motion of oxygen ions or vacancies, i.e. perpendicular to the electric field.

Fick force: Diffusion of ions in the direction opposite to the Soret force plays an important role during the reset process, restoring the oxygen-vacancy rich filament to its original location. In the presence of a high concentration gradient ($\nabla\eta_v$) of vacancies, ions will diffuse to minimize the free energy, thus maximizing the entropy. Here again, Joule heating is

the driving force moving the oxygen ion from oxygen-rich to oxygen poor filament regions, thus rupturing the filament. The net ionic motion is determined by a competition between all the driving forces. Moreover, the actual geometry of the filament is not cylindrical, and Joule heating is higher at narrow constrictions in the filament, which determines the actual location of the switching event.

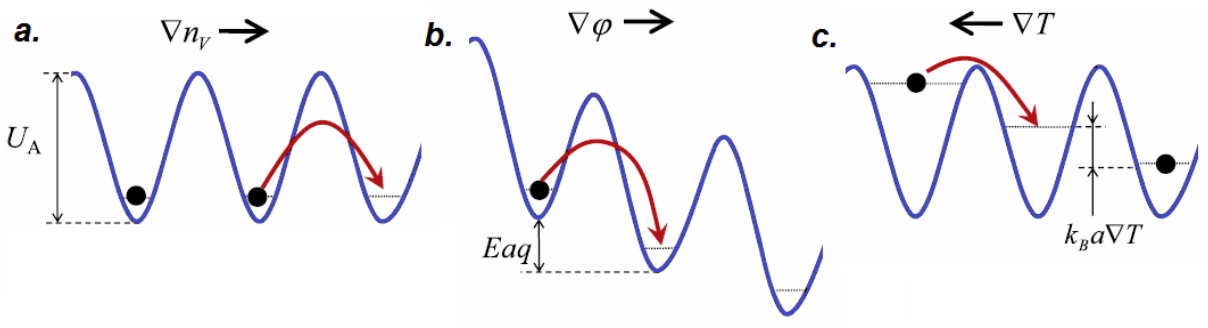

Figure 1.17: Schematic of the driving forces for oxygen anion transport: (a) Fick diffusion due to concentration gradient ($\nabla\eta_v$), (b) Electric potential gradient ($\nabla\varphi$) and (c) Temperature gradient (∇T). From Strukov *et al.* [118]

1.8.2. Effects of ionic transport in HfO_2: Electroforming and Switching

The local enrichment and depletion of oxygen ions during switching, and the resulting changes in electronic conductivity have been investigated thoroughly in some materials like epitaxial thin films and single crystals of $SrTiO_3$. However, such studies are lacking in prominent binary metal oxides like TaO_x and HfO_x which are commonly found to be amorphous or polycrystalline under CMOS processing conditions, where the understanding of ionic transport is still lacking. There have been progress in the understanding of ionic transport in HfO_2 based MIM devices by visualization of conducting filamentary regions using various probing methods and theoretical calculations.

Conducting filament characteristics: Surface studies based on CAFM and tip contact potential difference (CPD) maps obtained using Kelvin probe force microscopy (KPFM) have shown higher leakage currents at the grain boundaries in crystalline HfO_2. This is suggested to be due to segregation of positive charged vacancies at the grain boundaries.[103] From breakdown measurements using CAFM, the breakdown region was found to occur at GBs, however with a size of ~ 10 nm in diameter, which was larger than the GB cross section of around 1-2 nm. This suggests that CF formation happens with GBs acting as precursors and also consuming the grains. In another work, a scalpel- scanning probe microscopy-LCAFM combination was used to create a 3D filament tomography of a Hf/HfO_x bilayer RRAM, where the electrode and oxide can be gradually removed by using the SPM tip after switching and

then mapped electrically. [119, 120] At an operation current of 100 μA, the filament constriction size was found to be below 10 nm x 10 nm irrespective of the device size, indicating good scalability of VCM devices. Recent studies using synchrotron transmission X-ray microscopy (STXM) observed the O-K edge spectrum around CF region in a Pt/HfO_x/TiN device. A ring like region of oxygen excess was found around the filament suggesting lateral movement of oxygen due to thermophoresis/diffusion during switching.[86] Further microscopic studies have involved imaging using *in-situ* transmission electron microscopy (TEM)-holography to observe the structure of the filaments to identify the rupture location in a Pt/AlO_y/HfO_x/TiN device. The filament rupture in this case was found to occur at HfO_x/TiN interface after a reset operation with TiN acting as the cathode.[121] However, this is in disagreement with other bodies of works, where the rupture during reset is assumed to take place at Pt anode.[56,122] The rupture location and its dependence on devices with varying electrodes remains a matter to be understood. Moreover, microscopic nature of the filament in hafnium oxide is yet to be fully understood.

Mobile species: As shown in table 1.7**,** it is currently understood that, oxygen interstitial ions O_i^{2-} have a lower diffusion barrier of ~0.5 eV compared to that of 0.69 eV for positively charged oxygen vacancies and are thus the mobile species in hafnium oxide.[123] Neutral vacancies on the other hand have diffusion barrier of ~ 2.38 eV. In polycrystalline HfO_x, oxygen vacancies are more stable at the grain boundaries by more than 0.8 eV compared to the grain, thereby causing its segregation at grain boundaries.[103] During electroforming, there are multiple possible coexisting processes: (1) oxygen Frenkel pair emission in HfO_2 layer (2) oxygen vacancy transport involving exchange between the anode and HfO_2 and (3) radial migration of oxygen ions. In the first case, the breaking of Hf-O bond creates a Frenkel defect pair consisting of an oxygen interstitial and oxygen vacancy.[123] Since immediate neighbor intimate Frenkel pairs (IFPs) are thermodynamically unstable,[124] well separated 'extended Frenkel pairs' (EFPs) arising from diffusion of oxygen interstitials is understood to play the major role in electrofroming.[125] In the presence of pre-existing vacancies, it is possible that oxygen vacancy transport is more dominant over EFP emission[125] as has been shown to be energetically favorable in some cases like in the case of a reactive electrode.[125, 126] Negatively charged oxygen ions are driven by the electric field towards the anode. Initially and at low fields, the generation of vacancies happens uniformly across the dielectric. In the presence of GBs, the vacancies are clustered around GBs enhancing the current and local temperature, thus creating more defects. The formation energy of IFP is presumably further lowered near oxygen vacancy clusters due to a weak attraction of oxygen vacancies thus promoting easier clustering and filament growth.[125] At high fields, when the

generation rate of defects is higher than the time taken to diffuse away, Coulombic repulsion between O^{2-} ions and high local temperature promotes radial migration (thermophoresis) of ions.[103] Recent studies have also revealed that the Hf cation might also be mobile during the electroforming, where an amorphous carbon layer can be used to suppress the oxygen migration.[67] Otherwise, under normal conditions, oxygen interstitials/vacancies are understood to be more mobile than the Hf cation.

Table 1.7: Diffusion barrier of various defects in hafnium oxide.

Species	Diffusion barrier
V_O (neutral vacancies)	2.38 eV
V_O^{2+} (positive charged vacancies)	0.69 eV
O_i^{2-} (oxygen via interstitials)	0.5 eV

Phase formation: In a pristine oxide of HfO_x and TaO_x, high voltages during the electroforming step results in the formation of a conducting filament via the current compliance limited soft break-down of the oxide. The non-stoichiometry in the resulting oxygen deficient region of the filament can be very large leading to thermodynamic instability of the pristine phase. It is therefore likely that the further switching process involves the oxidation and reduction of a sub-stoichiometric phase, perhaps a metastable one in the filament region. Such a process has been reported for a $Pt/TaO_x/Pt$ based device where the switching occurs via the change in stoichiometry between TaO_2 (conducting) to Ta_2O_5 (insulating) through a redox reaction. In HfO_x based devices as well, the switching behavior is understood to be mediated by oxygen deficient filaments, the oxygen deficient phase and stoichiometry yet remaining speculative. The most stable phases of Hf-O system are suggested to be monoclinic HfO_2 and hexagonal Hf. X-ray photoelectron spectroscopy (XPS) studies of oxygen deficient thin films suggest the presence of at least one metastable phase, corresponding to an intermediate oxidation of the local structure of hafnium metal.[127, 128] A nominal oxygen containing phase like Hf_6O[129] and $HfO_{0.2}$[72] has also been suggested to relatively stable based on theoretical calculations using first principles. Existence of semi-metallic Hf_2O_3 also has been suggested based on DFT calculations.[130] Various other stoichiometry's like Hf_3O, Hf_2O Hf0, Hf_4O_7 etc. also have been considered in theoretical calculations. [131] An optimal stoichiometry of x=1.5-1.75 in HfO_x was suggested by McKenna et al. for efficient nucleation and growth of Hf-rich clusters.[72] In most likelihood, the oxygen deficient phase in the filament is a mixture of different stable and metastable phases.

1.9. RRAM based Synapses for Neuromorphic computing

Today's CMOS transistor based von Neumann digital computing has inherent bottleneck for advanced computing due to gap between the performance of cache (SRAM) and NVM.[132] In contrast, bio inspired brain-like neuromorphic computing works on mass parallelism of distributed computing and is attractive for correlated input of huge amount of data for applications like image or speech recognition. Currently, advanced neuromorphic computing is implemented using artificial neural networks (ANNs) in software. Alternatively, a hardware approach may physically reproduce the mass parallelism. A large scale hardware system would require technologies which support high density scaling and low energy consumption. Therefore, RRAM devices with these specific advantages are being envisioned as potential candidates for large-scale demonstration of neuromorphic systems.

Synaptic behavior in HfO_2 based filamentary devices are being investigated due to its demonstrated multi-level[133] as well as gradual resistance modulation capability,[134] corresponding to different degrees of filament rupture and cohesion. As shown in figure 1.18(a),[132, 135] in an analogy, biological synapse lies at the junction of two neurons and allows an electric or chemical signal to be passed from one to other. It is also understood to play a role in storing memory by modulating the strength of the connection between neurons. It does so by changing its conductance by potentiation/depression, i.e. activating or deactivating ion channels between the membrane and the synaptic junction when an action potential arrives from pre-synaptic and post-synaptic neurons coherently. The oxide synaptic device changes its resistance by generation and migration of the oxygen vacancies when the programming voltage pulse that is larger than a threshold is applied in either polarity. Such a potentiation/depression operation is shown in figure 1.18(b) where the application of pulse trains of constant amplitude allows the conductance to be modulated in a $Al/HfO_2/Ti$ device[136] with a typical bipolar switching operation (figure 1.18(c)). For multi-level switching, bipolar RS, where the set and reset processes happen in opposite voltage polarity is more frequently used; as has been commonly observed for HfO_2 in contact with Ti/TiN or Pt metal electrodes. Synaptic plasticity is typically realized by programming either by controlling I_{CC}, set and reset voltages during a DC operation, or more commonly by applying pulse ramps/trains of varying amplitude and width.[137] Filamentary synaptic devices typically exhibit gradual RESET but abrupt SET characteristics as shown for a $Pt/HfO_x/TiN$ device in figure 1.18(d). However, a gradual modulation of resistance in the reset as well as set process without using I_{CC} is preferable for easier hardware implementation of synaptic potentiation/depression.[137] The sharp nature of the set process is understood to be due to a positive feedback loop which exists during the breakdown process. Here, as the filament starts

to grow quickly in HfO_2 at near to breakdown voltages, the rise in current causes a rise in in temperature by Joule heating, which causes further increase in current. This positive feedback shows up as steep slope in the I-V characteristics during switching.[138] the reset process can be more gradual due to a negative feedback between the pace of filament rupture and the lowering of Joule heating by drop in current.[132] Though concurrent gradual nature of set as well as reset sometimes called 'analog switching' has been achieved using doping [139] and various electrode-oxide combinations as shown in figure 1.18(c), it usually involves very low switching ratios and the material aspect of achieving this is not well understood. It therefore becomes necessary to understand and control the dynamics of switching in HfO_2 based filamentary devices also to improve its dynamic range of operation and reliability of multi-level states.[140] In this, thesis, the impact of defects on the nature of switching dynamics in HfO_2 is investigated.

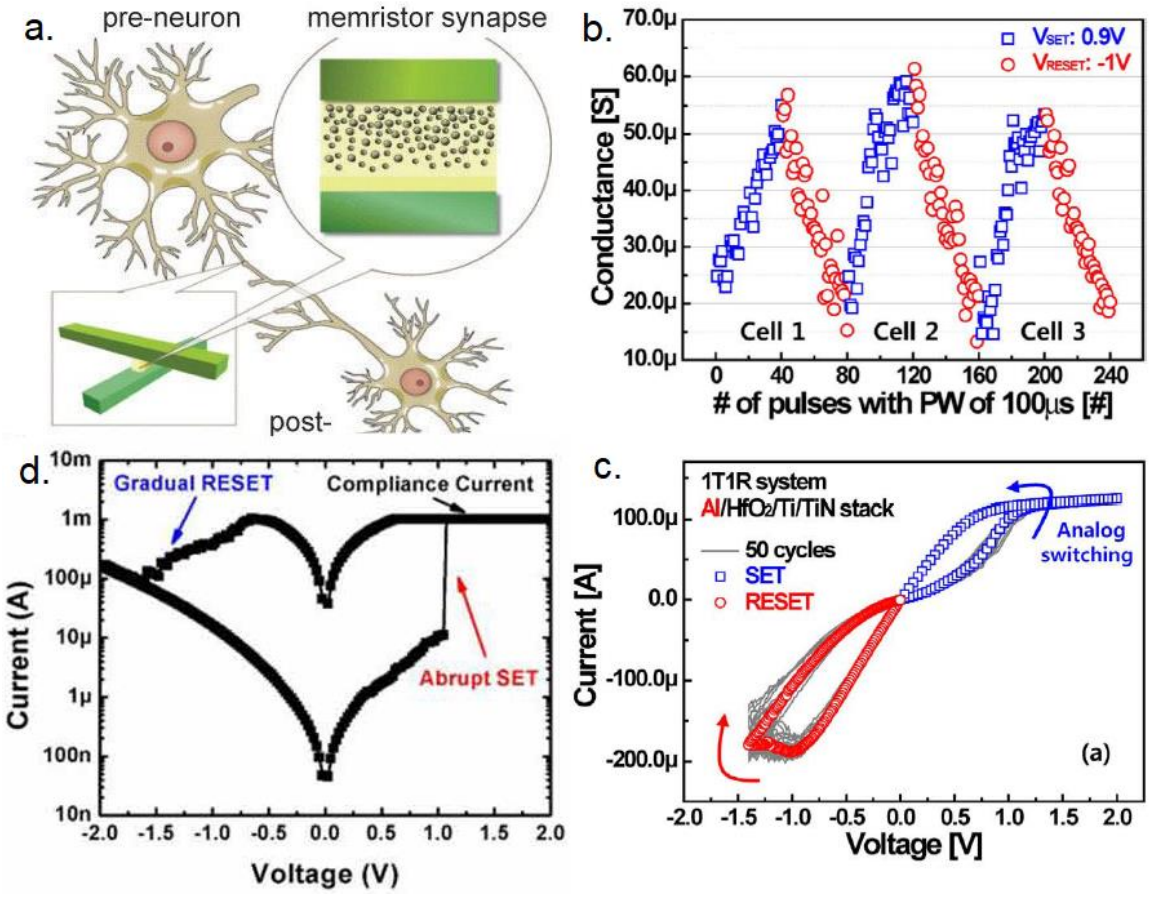

Figure 1.18: (clockwise) (a) Synaptic behavior analogy of an RRAM device,[135] (b) potentiation and depression achieved in an RRAM device by applying a train of pulses of constant amplitude (0.9 V and −1.0 V) and width of 100 μs from Woo *et al.*[136] (c) Analog bipolar switching involving gradual set as well as reset in a Al/HfO_2/Ti/TiN device. (d) Typical bipolar switching in a TiN/HfO_x/TiO_x/HfO_x/TiO_x/Pt device stack involving gradual reset and abrupt set, by Yu *et al.*[132]

1.10. Challenges and Motivation

Filamentary type oxide based resistive switching devices have been found to be promising for applications ranging from: non-volatile memories (embedded or stand-alone), selector devices for memories (complementary, threshold switching) and as electronic synapses in neuromorphic computing. In spite of the advances, there are problems impeding the realization of RRAM technology. Among the major challenges that have been identified to be resolved to enable RRAM devices are:[1] (1) Variability (2) Forming and (3) Selector devices. Moreover, the physics of switching at the microstructural level remains to be fully understood.

Though RRAM with such multi-functional capabilities is highly promising, lowered device yield arising from inter-cell and intra-cell variability and switching instability in RRAM devices remains of concern.[141] Such variability is intrinsically present in HfO_x RRAM due to the atomic configuration of the filament which can vary from cycle to cycle and from device to device.

Cycle to cycle variability is dominant at low operating currents where current jumps associated with quantum-mechanical conduction are dominant at low operating currents (< 100 μA). [142] Even at higher operating currents, degradation associated with gradual reduction in resistance ratios is observed, which has been associated with loss of oxygen further away from the filament.[86] One other aspect is the presence of impurities or dopants like carbon which might adversely affect the device performance and variability.[143] If the cycle to cycle variability due to device degradation is high, higher resistance ratios are required to sustain the operation window of the device.

Device to device variability is usually reflected in the initial forming conditions which differ from device to device. In this case, the microstructure of the film as well as stochastic nature of forming process plays a very significant role. Higher forming voltages are associated with current overshoots[144] associated with parasitic capacitance and higher Joule heating leading to the formation of stronger filaments. This leads to high device to device variability in the reset currents ($I_{reset,\ max}$) required to rupture the filaments. Under electroforming conditions with a single step DC electroforming; only a yield of less than 90% could be achieved in a 4 kbit array.[145] Though higher yields can be achieved using pulse forming and verification algorithms, this is time consuming and too costly. **Electroforming-free devices** or at least lower forming voltages are therefore necessary to achieve a higher effective yield of a high density one transistor-one resistor (1T-1R) RRAM array. From the point of view of

implementation of stand-alone memory (1S-1R), appropriate selector devices with good scalability (10 nm) and high non-linearity have also not yet been demonstrated.

1.10.1.Defect engineering in HfO_2/TiN based RRAM by RMBE

In this work, we first try to address the high forming voltages in HfO_x/TiN based RRAM devices. Lowered forming voltages or forming-free HfO_x devices have been proposed to be achieved by different approaches in literature: (1) lowering the oxide thickness, (2) use of highly reactive oxygen scavenging electrodes and (3) defect engineering. Electroforming voltage is typically found top scale with oxide thickness.

In the former approach, reducing the oxide thickness (usually less than 3 nm) reduces the forming voltages, which becomes equal to the set voltage at one point.[146] However, this has been suggested to lead to new filament formation on each switching cycles adding to the variability.[1] The latter approaches involve introducing defects in the HfO_x layer to reduce the breakdown strength. This common second approach used in industry, as shown in figure 1.19(left), involves deposition of an oxygen scavenging layer like Hf, Ti, Ta etc. The scavenger electrode introduces oxygen vacancies in the oxide layer through oxygen extraction after an annealing process, thereby creating an oxygen reservoir layer close to the switching layer.[87, 147] In the third defect engineering approach, oxygen vacancies or defects are introduced directly in oxide layer. Defect engineering in hafnium oxide can be achieved either intrinsically via (1) **oxygen stoichiometry engineering**, extrinsically by (2) **impurity doping** or even (3) ion bombardment or implantation. In this work based on direct defect engineering in HfO_x, as shown in figure 1.19(right), an inert Pt top electrode has been chosen so as to separate the effect of highly reactive scavenging layer, thus enabling to isolate and investigate the impact of defects introduced directly and uniformly in the oxide layer.

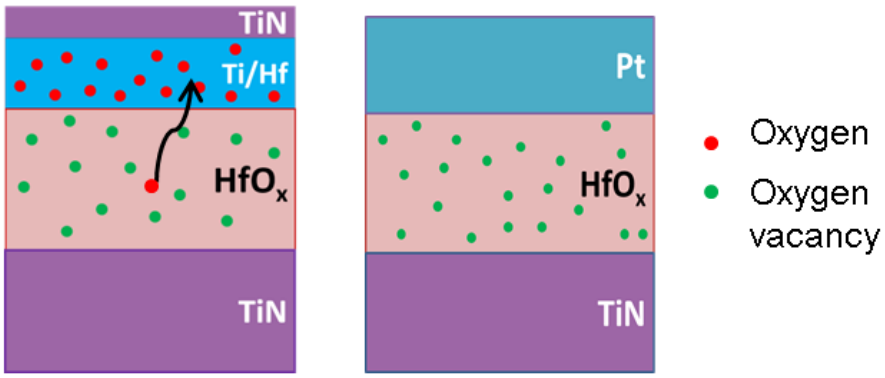

Figure 1.19: (left) Traditional defect engineering approach involving the use of a scavenger electrode layer like Ti, Hf in HfO_x/TiN based RRAM, (right) Direct defect engineering via oxygen stoichiometry engineering or impurity doping in Pt/HfO_x/TiN configuration used in this work.

Reactive molecular beam epitaxy deposition tool allowing for controlled doping and stoichiometry control in a wide range has been used to grow defect engineered oxide thin films. Conventionally, a CVD technique like atomic layer deposition (ALD) is used in industry scale deposition of hafnium oxide. However, CVD techniques are limited in its ability to deposit sub-stoichiometric films which usually lead to residual carbon content in case of incomplete oxidation. RMBE technique offers the unique possibility to precisely and reproducibly control the oxygen stoichiometry of the thin films in a wide range. In a work preceding this thesis, Hildebrandt *et al.* reported an insulator to metal transition in oxygen engineered hafnium oxide thin films grown on sapphire substrates at 700 °C by tuning the oxygen flow in RMBE.[100] Such a wide tunability in the resistivity by many orders of magnitude (10^{15}) has not been demonstrated prior in hafnium oxide films by other deposition techniques. Moreover, using RMBE, high degrees of oxygen deficiency can be achieved in combination with high purity, making it suitable to isolate the effect of oxygen deficiency on resistive switching behavior in HfO_x based RRAM. In this work, defect engineered HfO_x thin films have been grown at CMOS compatible temperatures of less than 450 °C on titanium nitride substrates, aiming to investigate HfO_2 with crystallinity similar to practical applications.

1.10.2. Resistive switching modes and dynamics in Pt/HfO_x/TiN devices

The model device of HfO_2 (or TaO_x) using Pt and TiN electrodes, used in this study to investigate the impact of pre-induced defects, has been reported to exhibit reliable switching in several publications. In addition, Pt/HfO_x/TiN device type is particularly interesting due to multiple coexisting switching modes and polarities,[56, 122, 148] as well as a large possible resistance window of operation, making it promising as multi-bit synaptic devices in neuromorphic computing.[133] However, a clear material oriented understanding of the reasons for the existence and partial coexistence of different switching modes in the same device configuration is lacking.

In the Pt/HfO_2/TiN device configuration, with applied bias to Pt electrode, a stable *cf8*-BRS mode has been most often reported. This *cf8*-BRS mode of operation is typically characterized by a sharp set under negative bias to Pt followed by a progressive (deep) reset process which allows for high resistance ratios (> 10^3).[149, 150] A unipolar resistive switching (URS) sometimes coexists with this *cf8*-BRS, where the reset process which is common to both modes is possible only when Pt acts as the anode.[151] Adding to the more frequently observed *cf8*-BRS mode, a lower-bias voltage *f8*-BRS mode (reset process with TiN as anode) with lower resistance ratios (≤ 10) was also observed in similar devices.[152] This *f8* operation was

further found to coexist with a complementary resistive switching (CRS) operation.[122, 148] Despite these various observations, the nature of partial coexistence of various switching modes remains to be understood. Thus, oxygen engineered thin films allow to investigate the impact of oxygen stoichiometry on resistive switching modes in addition to electroforming.

Moreover, the material conditions for the controlling the switching dynamics in hafnium oxide based RRAM is also not well understood. The deep reset process common to bipolar and unipolar switching in Pt/HfO_x/TiN has been reported in literature to sometimes exhibit gradual switching dynamics,[56] which is more desirable for adaptive learning in synaptic devices based on Pt/HfO_x/TiN.[133, 149] On the other hand, in other HfO_x based unipolar devices like Pt/HfO_2/Pt,[54] sharp transitions between discrete quantized conductance states were observed during the deep reset process, where the resistance corresponds to multiples of the quantum of conductance ($G_0 = 2e^2/h$). However, conductance quantization has not been reported before during the set process which is typically sharp and abrupt in hafnium oxide based RRAM. Moreover, even in devices where quantization phenomenon was observed, the practical application of quantized states for multibit memory remains elusive, partly due to large fluctuations from cycle to cycle.[113] Therefore, the impact of oxygen stoichiometry and doping (La, Ta) on switching dynamics and occurrence of conductance quantization phenomenon is studied in Pt/HfO_x/TiN based RRAM devices.

1.11. Outline of the work

Chapter 2 discusses briefly the experimental techniques used in this work starting from thin film growth and material characterization to device fabrication and electrical characterization.

In **Chapter 3,** reactive molecular beam epitaxy deposition allowing for controlled doping and stoichiometry control in a wide range has been used to grow defect engineered oxide thin films. Oxygen engineering (HfO_x, $0<x<2$), P-type trivalent doping (Lanthanum) and N-type pentavalent (Tantalum) doping were investigated in polycrystalline hafnium oxide thin films. Oxygen engineering was also studied in tantalum oxide thin films, initially motivated by the need to identify the oxidation conditions required for tantalum doping in hafnium oxide. A major part of the work on defect engineering in oxide thin films were performed on *ex-situ* grown polycrystalline titanium nitride (TiN) films deposited on Si wafers by sputtering. A part of the thesis also focuses on growth and optimization of *in-situ* grown TiN films on silicon, sapphire and magnesium oxide substrates by RMBE to allow future *in-situ* depositions of hafnium oxide for cleaner interfaces.

Chapter 4 deals with the investigations of resistive switching in a Pt/metal oxide/TiN device configuration. The physics of switching in HfO_x/TiN based RRAM remains to be fully understood and defect engineering which has become necessary to reduce electroforming voltages adds to increasing the complexity. Therefore, we have investigated the influence of direct oxygen engineering and impurity doping on resistive switching in transition metal oxide based RRAM using a model device configuration with the Pt and TiN electrodes, which are both rather inert. This chapter aims at contributing towards further understanding of resistive switching in HfO_x/TiN devices in the presence of preexisting defects (oxygen vacancies/dopants), with primarily focus on the following properties: electroforming, occurrence of resistive switching modes, quantum effects and switching dynamics. Additionally QPC model was used to study the evolution of resistance states in oxygen engineered RRAM devices. Further a simple model has been developed depending on the oxygen stoichiometry to account for all the different switching modes based on electric field, Soret and Fick forces.

Chapter 5 summarizes the major results in this work and gives a brief future outlook.

2. Experimental Methods

The various experimental techniques used in this work starting from thin film growth and material characterization to device fabrication and electrical characterization is briefly described in this chapter. First, the important aspects of thin film growth, reactive molecular beam epitaxy and *in-situ* characterization techniques with focus on the MBE growth of oxide and nitride thin films are discussed. Afterwards, the wide range of *ex-situ* material and electrical characterization techniques employed for the nitride and oxide thin films are introduced. Moreover, the device fabrication and electrical characterization of Pt/metal oxide/TiN based devices is also discussed.

2.1. Thin Film Growth and *In-Situ* Characterization

In today's technology, thin films constitute most of the active and passive layers in electronic devices. A major aspect of thin film growth is the control of the kinetic and thermodynamic conditions under which they are deposited to yield desirable properties.[153] Various growth techniques are used to grow complex oxide and nitride thin films. Although atoms can be provided for the thin film material from solid or liquid phases, most common approach is to provide them through a vapor phase. This vapor phase of atoms to be supplied in the film can be provided by physical or chemical means, thus classified as physical vapor deposition (PVD) and chemical vapor deposition (CVD), respectively.[154] PVD techniques usually involve vaporization using heat (evaporation) or high energy impact of particles to cause ionization (sputtering). CVD techniques, on the other hand, require gaseous materials under the conditions in the chamber or reactor.

In the growth of oxide or nitride thin films, gas sources are additionally used to obtain the required oxidation or reaction at the thin film growth surface. These gas sources can be provided either as molecules (O_2, N_2), activated radicals (O*,N*), ozone (O_3) or as ions (O^{x-}) are commonly used. The **vapor pressure**, p_v determines the technique using which atoms or molecules can be delivered to the deposition chamber.[153] For the case of low pressure deposition as is the case in PVD, molecular form of gases are insufficient to promote complete oxidation or nitridation of the films, prompting the use of ozone or radical sources.[155] Materials having $p_v < 1$ mbar at the temperature T_w of the deposition chamber can be physically deposited by evaporation or sputtering. Thus PVD usually involves low pressure operation and a 'line of sight' deposition due to condensation of the material at the chamber walls. In CVD process, materials with $p_v > 1$ mbar are typically used which can be deposited even at close to atmospheric pressure.[153] The background pressure during thin film growth

determines the average distance travelled by the particle. Using kinetic theory, the mean free path (λ) of the vapor particles can be obtained as:

$$\lambda = \frac{k_B T}{\sqrt{2}\pi d^2 P} \qquad \text{Equation 2-1}$$

Where, k_B is the Boltzmann constant, T is the temperature, d is the diameter of the particle and P is the pressure. At ultra-high vacuum (UHV) conditions (P< $\sim 10^{-9}$ mbar), the mean free path of the particle reaches values close to 10^6 cm, which is several order of magnitude greater than the dimensions of the deposition unit.

2.1.1. Physics of thin film growth

The film growth process on a substrate, as shown in figure 2.1(a), involves condensation or adsorption of vapor, surface diffusion, desorption or re-evaporation, reaction or nucleation to form the film, and coalescence of the materials leading to growth of the films.

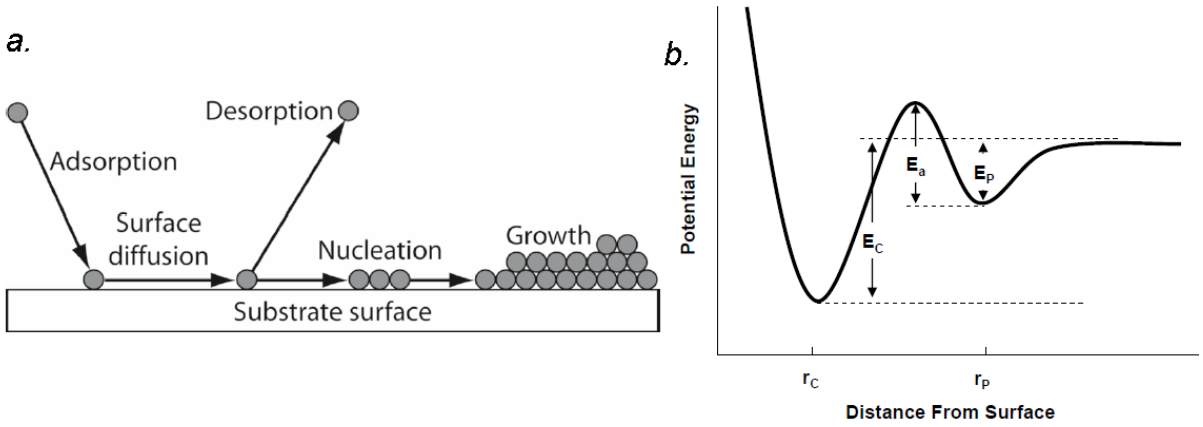

Figure 2.1: (a) Schematic of the events during the thin film growth process; (b) Interaction potential energy diagram as a function of distance of the approaching atom or molecule from the surface, the potential barrier for chemisorption, and physisorption are represented (right).

At first, an approaching atom or molecule can be adsorbed or reflected from the substrate. Depending on the energy of the atom, the adsorbed particle may be physisorbed or chemisorbed as shown in energy-distance relationship in figure 2.1(b). Physisorption (E_p ~0.25 eV) is caused by van der Waals force which is weak allowing adatoms to diffuse easily on the surface, whereas chemisorption (E_c:1-10 eV) involves the sharing of electrons and the formation of a stronger new chemical bond. Therefore, a physisorbed particle requires overcoming an activation energy barrier of E_a to be chemisorbed and to become part of the film. This activation energy can be acquired from heat transfer from the surface. The adsorbed particle may also be desorbed depending on the amount of incoming atoms or flux and the temperature. It is therefore typical to define a 'sticking coefficient' as the probability of a

particle to remain and become part of the films. If the thermal energy acquired by the atom is lower than the activation energy for chemisorption, the adatom is able to diffuse on the surface to lower the surface energy.

The process is further followed by nucleation of atoms to form clusters. Considering a homogeneous nucleation, the free energy associated with the formation of a solid spherical cluster of radius r can be given as:

$$\Delta G = \pi r^2 \gamma_S + \frac{4\pi r^3 \Delta G_V}{3} \qquad \text{Equation 2-2}$$

where, γ_S is the interfacial energy per unit area and ΔG_V is the volume free energy. Surfaces formation is usually unfavorable (positive γ_S) with increasing energy ($\sim r^2$). Since, volume expansion is favorable, ΔG_V is negative. The situation is shown in figure 2.2(a), where the total energy increases initially for smaller r and then reaches a maximum after which it drops and converges towards r^3. An expression for the critical size (r^*) is derived by setting $d(\Delta G_V)/dr = 0$, yielding $r^* = -2\gamma_S/\Delta G_V$. The cluster formed is stable only when $r > r^*$. The nucleation barrier (ΔG^*) can be obtained by substituting r^* in to Equation 2.2. However, in thin film growth, the growth typically happens through heterogeneous nucleation on a surface aided by defects. These defects may also have a repulsive interaction with the adsorbates. Here, the mean-free path during surface diffusion is close to or larger than the average distance between point or line defects.[156] Atomic sized steps observed in various substrates are examples of line defects, where surface adatoms are aggregated during film growth. As shown in figure 2.2b, during film growth, a part hemispherical island structure (with area A) is formed during clustering. Under surface energy considerations, a contact angle of θ is observed based on the interface energies (γ_i) between the film and the substrate and the surface energies of the substrate (γ_S) and film (γ_F). The total free energy change associated with a change in surface area ΔA of this island is expressed as:[154]

$$\Delta G_{surface} = \Delta A \gamma_F cos(\theta - \Delta\theta) + \Delta A(\gamma_i - \gamma_S) \qquad \text{Equation 2-3}$$

Under equilibrium conditions, equation 2.3 can be given under limits of small ΔA *and* $\Delta\theta$ as follows:

$$\frac{dG}{dA} = \gamma_F cos\theta + (\gamma_i - \gamma_S) = 0 \qquad \text{Equation 2-4}$$

Equation 2.4 can be considered to be like a force balance equation, where the vector sum of the surface energies becomes zero.

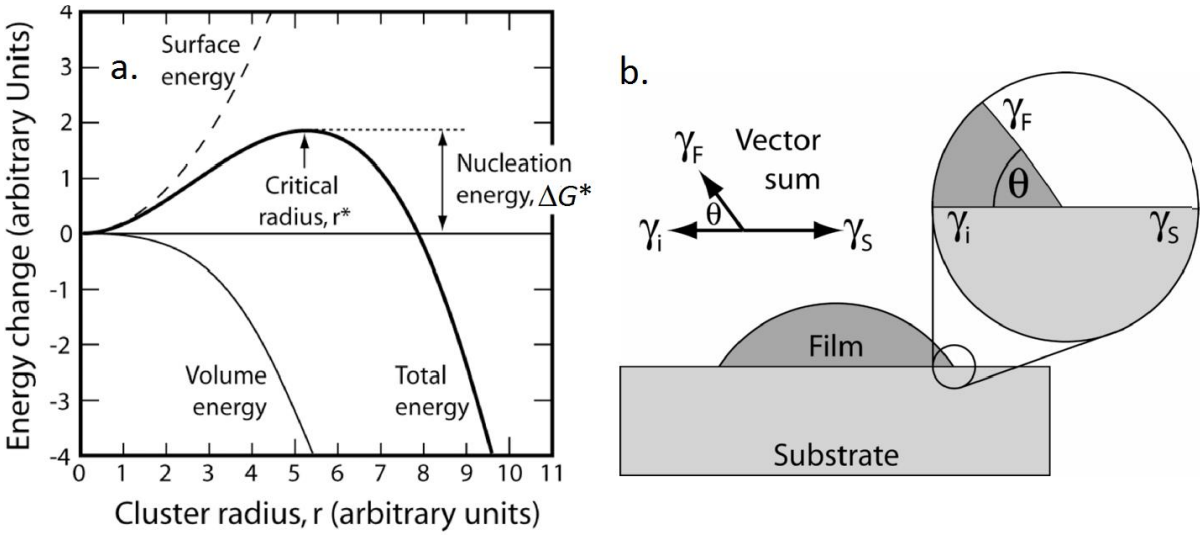

Figure 2.2: (a) Energy change associated with the formation of clusters during homogeneous nucleation in dependence of radius of the cluster (b) Schematics of the island formation geometry involving the surface energies of the substrate, film and resulting interface. Images form Rockett *et al.*[154]

Based on variations in above mentioned surface energies during growth, three basic modes of growth are envisioned for growth of thin films on single crystal substrates, as shown in figure 2.3:

(1) Volmer-Weber or island-like growth, $\theta>0 \Rightarrow \gamma_S < \gamma_F + \gamma_i$

In this case, the interaction between the adatoms is stronger than that between the adatom and substrate. This results in clustering or 3D-island like formation of adatoms. This is usually the case when the thermal energy provided at the substrate is insufficient for diffusion of adatoms.

(2) Frank and van der Merwe or layer-by-layer growth, $\theta=0 \Rightarrow \gamma_S \geq \gamma_F + \gamma_i$

In this case, the film wets the substrate well and thus the growth results in 2D high quality single crystal thin films. This is aided by a fast surface diffusion of surface adatoms.

(3) Stranski-Krastanov growth (layer-by-layer followed by island),

Here, the growth proceeds initially via 2D growth and then transitions to 3D island formation as surface energies change after a critical thickness of the film.

The growth on single crystal substrates is additionally affected by the lattice parameter mismatch between the substrate (a_s) and the film (a_f), given by $(a_f - a_s)/a_s$ as well as the surface energy parameters which change during the course of the growth. Misfit introduces strain in the film, wherein the strain energy is released through the formation of defects like dislocations.

In case of a polycrystalline or amorphous substrate, the growing film is unable to make any alignment to the substrate lattice. The growth, thus proceeds either by trying to align to individual grains of the substrate or in a way to reduce the surface energy of the film. If the grains of the substrate are randomly oriented, the former results in polycrystalline films. In the latter case, to reduce the surface energy of the film, the atoms try to arrange themselves as close to each other to maximize the bonding. This usually result in preferentially orientation or texture of the film, where closed packed planes like (111) in case of fcc (face centered crystal) structures and (110) for bcc (body centered crystal) structures are obtained.

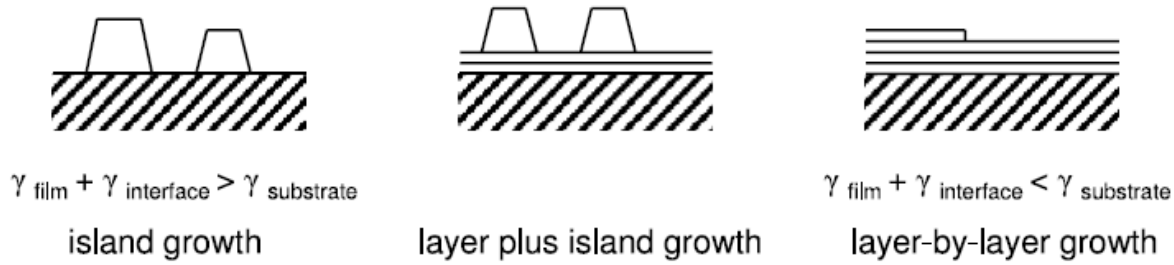

Figure 2.3: Schematic of thin film growth modes on a single crystal substrate from Kowarik *et al.*[157]

2.1.2. Reactive Molecular beam Epitaxy

Molecular Beam Epitaxy (MBE) is a vacuum deposition technique in which one or more thermal beam of atoms or molecules react at a crystalline surface under ultra-high vacuum conditions to produce an epitaxial film. Originally developed in the 1970s for the growth of GaAs and (Al,Ga)As, MBE distinguished itself from other vacuum deposition techniques due to its extraordinary control over growth conditions and fluxes yielding high quality epitaxial films.[158] In combination with *in-situ* characterization during growth, MBE was further adapted for the growth of other semiconductors, metals and insulators. Typically, thermal sources are used to produce beams of atoms or molecules which are directed towards a heated substrate. In addition, the introduction of gas fluxes facilitating composition control for the growth of complex oxides and nitride thin films have been generally categorized as reactive MBE.[159] [155] With appropriate flux control combined with *in-situ* reflection high energy electron diffraction (RHEED), MBE allows to reproducibly grow films with high quality and precise stoichiometry. There are two approaches used in MBE: (1) shuttered MBE: where, different atomic layers are deposited sequentially. This is achieved via mechanically driven shutters for each individual elemental source. (2) co-evaporation of various sources, where two or more elemental sources are simultaneously deposited on the substrate, with controlled individual fluxes to attain a specific stoichiometry. A schematic of the MBE unit based on co-evaporation, used in this work is shown in figure 2.3.

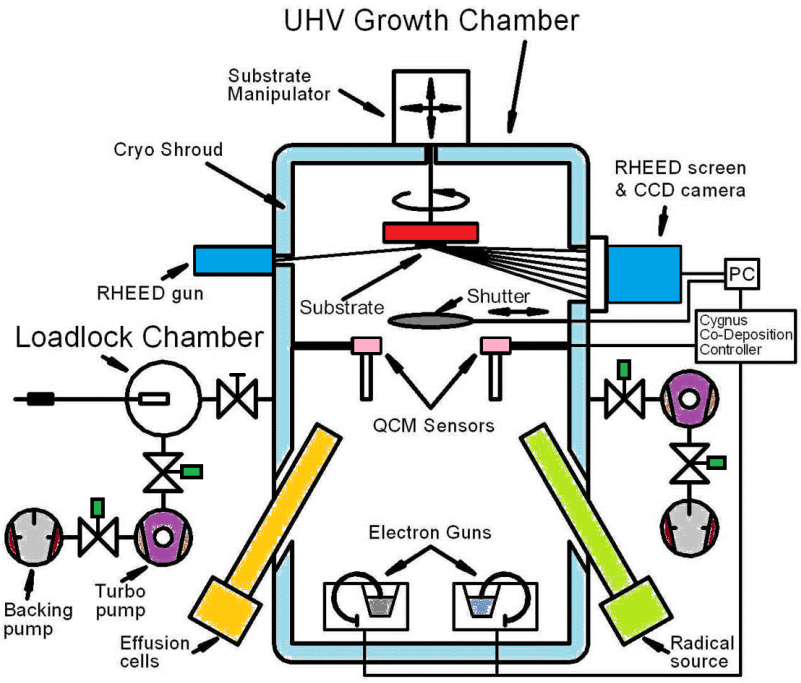

Figure 2.4: Schematic of the reactive molecular beam epitaxy (RMBE) setup used in this work adapted from Buckow *et al.*[160]

The RMBE unit used in this work, as shown in figure 2.4, consists of a custom designed UHV growth chamber with a base pressure of up to 10^{-9} mbar and a load lock (for substrate transfer) separated by a gate valve. Material for film growth is introduced in the chamber via three different electron-beam evaporation sources (Hanks HM^2 single crucible e-guns, Thermionics), an effusion cell and two radio frequency (RF) activated gas radical sources (HD25, Oxford Applied Research). These are individually equipped with integral water cooling shrouds. Quartz crystal monitors (QCM) in combination with a co-deposition controller (Cygnus) were employed for real time atomic flux monitoring and control. Here, collimated QCMs placed directly above a source were used for individually monitoring the rate of each of the evaporated sources. Further, a RHEED setup was used for *in- situ* growth monitoring. Mass flow controllers (MFC) allowed controlling the flow rates of oxygen (99.995% purity) or nitrogen (99.995% purity) to the radical sources. A cryoshroud, which can be filled with liquid nitrogen (LN_2) is employed on the outer walls around the growth chamber to achieve UHV conditions by adsorbing the residual gases and impurities to the chamber walls. A substrate manipulator fitted with a pyrolytic graphite heater allows substrate heating (up to 800 °C) and rotation during the growth to ensure lateral uniformity. Different chucks of sample holders made of stainless steel were used allowing deposition on up to 2" diameter wafer substrates or multiple smaller substrates. A pneumatically controlled shutter attached to the front of the substrate holder can be used to block line of sight to the atomic fluxes. A thermocouple between the sample holder and heater was used to maintain

the growth temperature. An optical pyrometer was used to calibrate the substrate temperature. A computer interface using custom LabView program was used during film growth. The RMBE setup coupled with *in-situ* flux and growth monitoring enabled the growth of high quality oxide and nitride thin films.

2.1.3. Electron Beam Evaporation

The single crucible e-gun setups for e-beam evaporation used in this work were capable of delivering a maximum power of 10 kW, the schematic of which is shown in figure 2.5(a). It consisted of a filament (tungsten) placed underneath a crucible containing the elemental sources which was heated by applying a very high voltage (up to 10 kV). This, in turn, emits electrons which are bent by 270° and focused on to the source surface using deflecting magnets. The kinetic energy of the electrons is transferred to the source material, thus locally heating and eventually evaporating the material into the vapor phase. The crucible is simultaneously cooled under water flow. This allows direct transfer of energy to the source during heating, allowing evaporation of high melting point metals like hafnium, tantalum. Sweep coils, which are located near located close to the crucible pocket can be used to position and scan the electron beam on the material. The e-beam can scanned be over the material by applying a suitable waveform to the sweep coil, allowing for more uniform evaporation from the material surface. Water flow interlock, pressure interlock (which cease e-beam operation above 10^{-5} torr) and cabinet interlock together ensures its smooth functioning. In this study, e-beam evaporation setup was used to evaporate elemental sources of titanium (99.99 %, Chempur), hafnium (99.9% pure except Zr, MaTecK), lanthanum (99.9%, Lesker), and tantalum (>99.9%, Evochem).

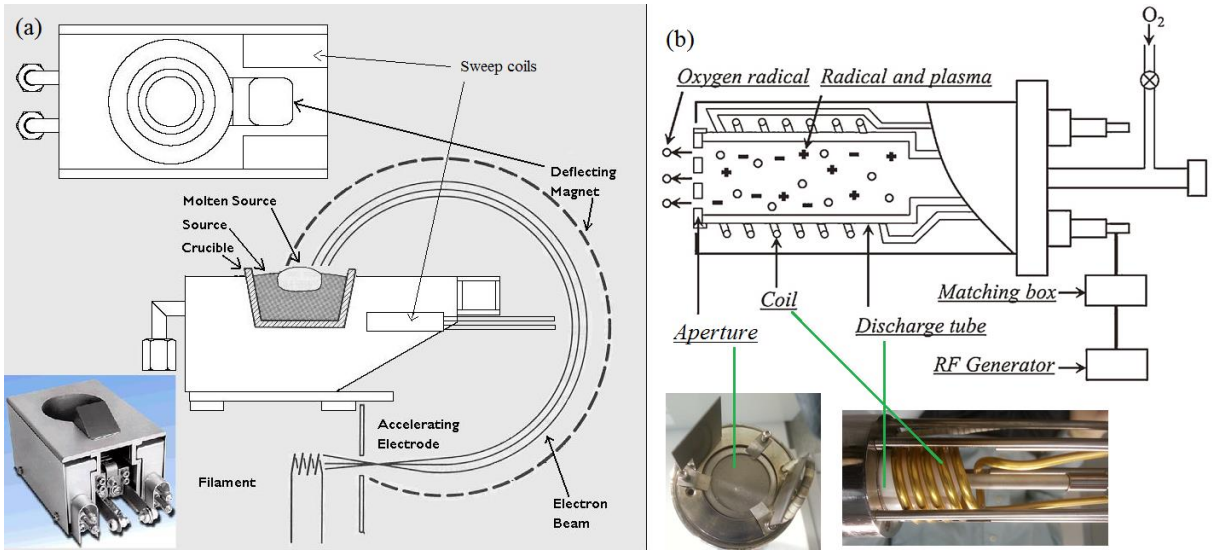

Figure 2.5: (a) Schematic of an E-beam evaporator[161] where the inset (left, bottom) shows the HM[2] Thermionics E-gun[162]; (b) Schematic[163] and corresponding images (bottom) of an RF plasma source (Oxford Applied Research, HD25)

2.1.4. RF Plasma sources

Oxygen/nitrogen radicals obtained using RF plasma sources (Oxford Applied Research, HD25) were used as the source of oxidation/nitridation in our experiments. As shown in the in figure 2.5(b), RF plasma sources works on the principle of plasma discharge in a discharge tube created from inductively-coupled RF excitation at 13.56 MHz. An auto-tune unit allows tuning the impedance of the discharge tube cavity to match with the output resistance of the RF-generator automatically. The discharge tubes used in the work were made of quartz (oxygen or nitrogen) or pyrolytic boron nitride (PBN) tube (used for nitrogen only). The molecular gas flow rate (standard cubic centimeters per minute, sccm) is controlled using a mass flow controller (MKS) in the range of 0.1-2.5 sccm. Up on reaching the RF discharge tube, the gases are cracked into highly reactive atomic oxygen or nitrogen and released into the growth chamber through a beam exit aperture. It has been reported that that OAR HD25 sources have a high atomic content in the discharge.[164] A deflection plate which can be charged (0-1000 V) allows deflection of higher energy ionic species away from the direct line of deposition discharge. Different tubes with varying aperture areas to control the oxidation/nitridation conditions were tested over the course of the work, with most of the work performed with a quartz based aperture with an area of 4.65 mm^2 (37 holes each with a diameter of 400 μm). The source is also equipped with an optical emission detector to monitor the intensity of plasma emission, which gives a measure of the amount of radicals generated. For oxygen plasma,[165] the strong emission at 777 nm, corresponding to the oxygen atom transition O ($3p^5P \rightarrow 3s^5S^0$) can be monitored. In case of nitrogen plasma,[166] the line at 746.8 nm corresponding to the emission line of N ($3s^4P \rightarrow 3p^4S^0$) was monitored.

The two parameters controlling the oxidation or nitridation conditions are: (1) applied RF power (0-400 W) and (2) gas flow rate (0-3 sccm) controlled with MFC. The amount of gas radicals reaching the surface is roughly proportional to the optical emission intensity of the plasma discharge monitored using an optical detector. At too low flow rates (< 0.2 sccm), it is usually difficult to maintain a stable plasma. The range of operation conditions depends directly on the tube aperture area, where smaller aperture areas can be used to operate at further lower oxidation conditions. At low RF power conditions (< 200 W), a low-brightness mode of plasma can be obtained, which is significantly capacitively coupled and contains higher energy ions and lower atomic content. At slightly higher RF powers (200-350 W), a stable nitrogen or oxygen plasma of high-brightness is obtained, which is inductively coupled. The high-brightness mode consists of dominantly atomic radical species (O*, N*) and is thus

typically used during growth. At very high RF powers (> 350 W), higher amount of ions may be produced typically causing more defects in the films.

The broad range of operating conditions under low pressure conditions allow fine tuning of the stoichiometry of the thin film with good quality. In order to grow oxygen or nitrogen deficient thin films, the shutter is closed and the plasma switched off immediately after growth, so as to minimize any possibility of further oxidation or nitridation. Contamination of layers by source materials (quartz, PBN), possible surface damage by energetic particles and eventually, the degradation of discharge tube due to high reactivity of radical species are some of the drawbacks of this technique.

2.1.5. Reflection High Energy Electron Diffraction

Reflection High energy electron diffraction (RHEED) is a powerful *in-situ* non-destructive technique for monitoring growth of thin films surfaces in vacuum. In this method, high energy (5-40 keV) monochromatic electron beam is focused on to the surface of the sample at glancing angle (< 3^{o}). The grazing incidence together with strong electron-substrate interactions keeps the penetration depth of incident electrons to a few monolayers. This also leads to surface irradiation area of 1-3 mm, thus giving information from a large area. The beam is reflected and scattered from the surface-most layers of the sample and impinges on a visual fluorescent screen. According to the lattice periodicity (d) of the surface atoms, diffraction can occur. According to the well-known Bragg's law, $\lambda = 2d \sin\theta$ relates the wavelength, λ of the electrons and the diffraction angle, θ. In the reciprocal space, the possible diffraction condition can be set such that, the wave vectors of the incident (k_0) and diffracted wave (k_{ij}) differ by a reciprocal lattice vector. The surface of the sample in reciprocal space can be transformed into an array of reciprocal lattice points, when viewed from the top of the sample, as shown in the top view figure 2.6(a). Considering elastic scattering only, this can be cast into the geometrical construction of the Ewald sphere in reciprocal space, where the incident and diffracted wave vectors form the radius of the sphere. Considering the side view, the reciprocal space consists of vertical lines called reciprocal lattice rods. The conditions for constructive interference for diffraction are met at the points where the reciprocal lattice rods cross the Ewald sphere. These appear as diffraction spots on the RHEED screen and lies on concentric circles called Laue zones.

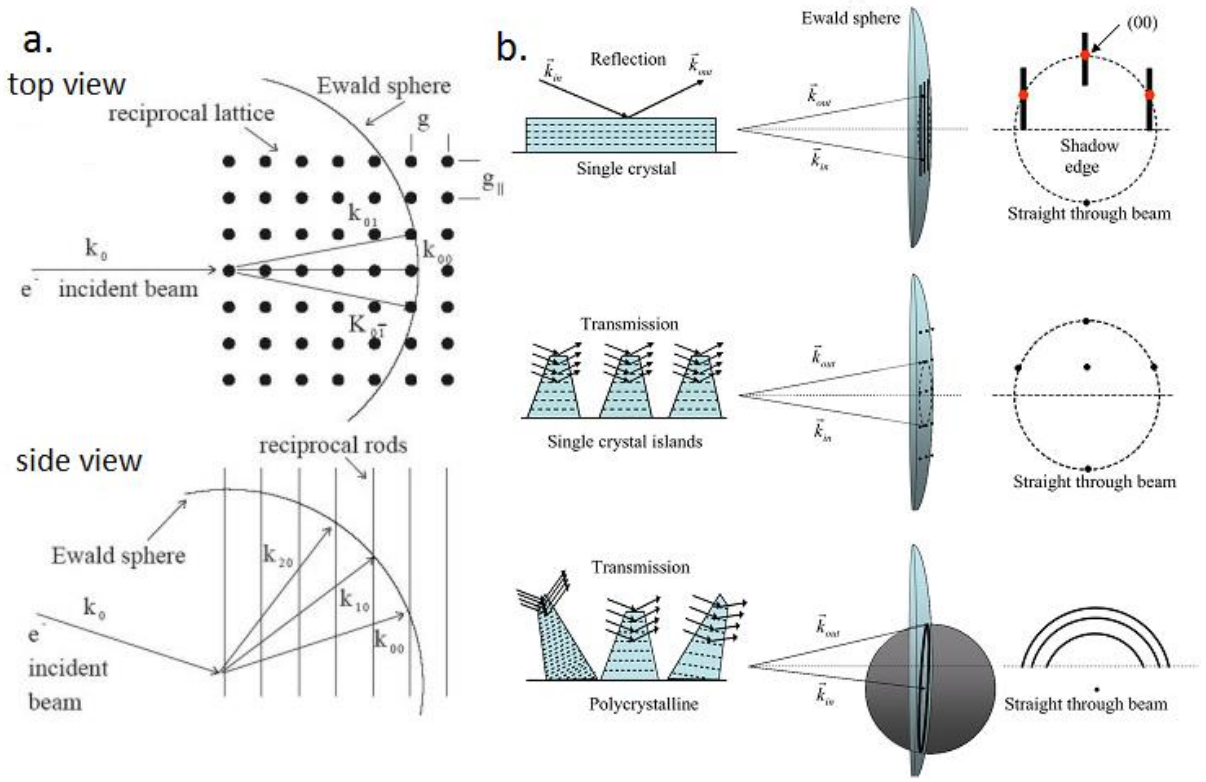

Figure 2.6: (a) Representation of the Ewald sphere construction and RHEED diffraction from both the top and side view with respect to the sample and the electron beam (b) Schematic of RHEED pattern resulting from different surface geometries of the sample from Tang *et al.*[167]

The RHEED pattern can be used to understand the surface morphology of the sample. As shown in figure 2.6(b), RHEED patterns observed for various surfaces range from diffuse rings to spots to streaks.[167] In an atomically flat perfect single crystalline sample, only diffractions spots or dots corresponding to sharp reciprocal lattice rods will be observed. This is typical of single crystal substrates of high quality. However, in real thin films, the rods are broadened and have a finite width due to imperfections and/or finite instrument response of the RHEED. These small imperfections act as out of phase domains with a size shorter than the coherence length of the electron beam. Here, the intersection between the reciprocal rods and the Ewald sphere become large ellipses, resulting in elongated spots called streaks in the RHEED pattern.[168] In general, streaky RHEED pattern is interpreted as due to a smooth surface of good crystalline perfection. As the surface roughens, it becomes possible for the beam to transmit though the individual 3D islands leading to conventional diffraction pattern of many spots on the screen. A pattern of spots thus either point to a rough surface and/or a highly faceted surface. In polycrystalline films, the islands with their own crystalline orientations are randomly oriented. The sum of individual contributions from different grains results in a reciprocal space with set of concentric circles. In the presence of a texture, these rings are sometimes broken into individual arcs. The presence of layers without long-range order lead to highly diffused rings in the RHEED pattern. The spacing of RHEED diffraction pattern can

be used to obtain information about the surface lattice spacing and arrangement of the atoms. Moreover, analysis of periodic variations in the intensity of the diffraction spots, called RHEED oscillations can give information regarding the surface coverage of a growing layer enabling monolayer control over film growth. A detailed explanation of the use of RHEED in further evaluation of thin films is beyond the scope of this thesis and can be found in literature.[169, 170]

2.1.6. Substrate preparation and handling

A variety of substrates were used in this work as summarized in Table 2.1. TiN was always used as the bottom electrode of choice, in order to fabricate metal oxide/TiN devices. TiN films were either deposited by MBE or acquired from IHP GmbH. Oxide thin films were grown by MBE on TiN films for device fabrication and on different oxide substrates for comparison as well as for material characterization.

Polycrystalline TiN electrodes grown on Si(001) wafers, provided by IHP GmbH, was deposited by atomic vapor deposition (AVD) in a clean room environment on a Si(001) wafer with a diameter of 200 mm. After *ex-situ* transfer to TU, Darmstadt under atmospheric conditions, TiN/Si wafer was cut into sizes of 5x5 mm^2 or 10x10 mm^2 using a Loadpoint Microace Series 3 dicing machine for further deposition of oxides by MBE. The substrates were further cleaned in an ultrasonic bath at 40 °C in distilled water, double de-ionized (DI) water and acetone respectively for 15 minutes each. Before deposition, the polycrystalline TiN substrates were always subjected to the deposition temperature (typically ≥ 300°C) for 30 minutes under UHV conditions.

Substrates Used	Thin Films grown
Polycrystalline TiN on Si(001)	Oxygen engineered HfO_x, TaO_x and doped (La/Ta) HfO_2
c-plane sapphire, Al_2O_3(0001)	TiN, Oxygen engineered HfO_x, TaO_x
MgO (001)	TiN
Si (001)	TiN
Y:ZrO_2 (001)	La doped HfO_2

Table 2.1: List of substrates used in the current work.

For the growth of TiN thin films by MBE for further *in-situ* deposition of oxides, many substrates were considered: sapphire (*c*- plane oriented), Si(001) and MgO(001). *c*-plane sapphire was also used as substrates for direct deposition of oxides for thickness calibration as well as for visual of oxygen engineered thin films. Sapphire substrates were mostly used as directly received from CrysTec GmbH, where an annealing procedure at the film growth

temperature was sufficient to remove organic residue and obtain clean surface, as evidenced from RHEED. MgO substrates were annealed at 1000°C for 12 hours in an oven under ambient before being introduced into MBE deposition unit.

In case of silicon, 2" wafers of Si(001) were first cut into sizes of 5x5 mm^2 or 10x10 mm^2 using the dicing machine and further cleaned in acetone and DI water for 15 minutes each in an ultrasonic bath at 40 °C. Since the MBE heater unit was limited to 800°C, which was insufficient for flash removal of SiO_2 from the substrate surface which is possible at higher temperatures, chemical etching followed by quick *ex-situ* transfer into the load lock of the MBE unit had to be employed. For native removal of the oxide layer as well as any contamination, a 15-60 second dip in 1:20 HF:DI water was performed, which was followed by a strong rinse in DI water.

Y:ZrO_2 (001) substrates were used for epitaxial growth study of doped hafnium oxide thin films. They were first cleaned in acetone and DI water for 15 minutes each in an ultrasonic bath at 40 °C. Further, a Piranha cleaning process was used to remove organic residues and oxidize the surface. A fresh 3:1 solution of H_2SO_4:H_2O_2 was prepared. This was followed by immersing the substrates into the solution and kept for 10 minutes in ultrasonic bath. The substrates were further rinsed thrice in DI water and dried with a nitrogen gun.

2.2. *Ex-situ* characterization

The many *ex-situ* methods used in this study ranging from material characterization to device fabrication to electrical characterization are summarizes in this section. The section does not delve into the fundamentals, but rather briefly summarizes the techniques employed with focus on the property of interest. Among material characterization techniques, a combination of (high resolution) X-ray diffraction and X-ray reflectivity is used widely after MBE film growth in this work for obtaining information regarding crystal structure, thickness, density, surface and interface roughness etc. of the thin films. X-ray photoelectron spectroscopy and optical absorption measurements were used to understand composition and defect physics of the thin films. Transmission electron microscopy based measurements were employed to gain further insight about the structure and chemistry of the as-grown thin films. In some cases, where possible, atomic force microscopy was used to obtain information regarding surface morphology. Four probe measurements were performed to analyze the resistivity of the TiN electrodes. The Pt/metal oxide/TiN devices were fabricated initially by evaporation of Pt electrodes using shadow masks and later via photolithography and lift-off process. Electrical characterization was performed using a Keithley-4200 semiconductor characterization system.

2.2.1. X-Ray diffraction and X-Ray reflectivity

There are many ways in which X-rays can be used to characterize thin films. X-ray diffraction is a well-known technique with several advantages like capability of non-destructive analysis in varying conditions (atmospheric conditions, high temperature, high pressure), low radiation damages, ability to characterize buried interfaces etc. to name a few. X-ray diffraction can be used to obtain information on crystal structure and phases in thin films with focus on lattice constants, crystal orientation and symmetry, crystallite sizes etc. Similar to electron diffraction in RHEED described in a previous section, the elastic scattering of X-rays occurring in the bulk of the crystal due to periodicity of lattice (planes) is made use of in the structural investigations by X-ray diffraction. Here, the Bragg's diffraction condition is satisfied which can be expressed as: $n\lambda = 2d_{hkl} \sin\theta$, relating the wavelength, λ of the X-ray's, the diffraction angle, θ and the d_{hkl} is the interplanar spacing of adjacent (hkl) lattice planes. An in depth discussion of the technique can be found in several works. [171, 172]

In this work, a Rigaku SmartLab X-ray diffractometer (9 kW rotating anode) using Cu-$K_{\alpha\alpha}$ radiation (λ= 1.54059 Å) was employed with the capability of several kinds of measurements. The diffractometer was mainly used in a parallel beam geometry by employing various divergence limiting slits and monochromators: incident Ge(220) 2-bounce monochromator for very high resolution (0.01°) and graphite monochromator at the detector side for medium resolution measurements. A four-circle goniometer composed of four axes: the ω-axis (sample rotation axis), the φ-axis (in-plane rotation axis), the χ-axis (tilting axis) and the 2θ-axis for scanning the detector forms the basis of the various measurement techniques as depicted in figure 2.7.[173] In a typical out-of-plane diffraction using parallel beam geometry, a symmetric 2θ-θ scan gives information regarding the set of planes which are parallel to the surface of the sample. In a polycrystalline sample, the grains being randomly oriented have multiple orientations parallel to the surface of the sample, leading to the observation of multiple peaks in the XRD pattern. In an epitaxial/textured thin film or a single crystal, planes perpendicular to out-of-plane orientation are additionally useful to determine the symmetry and strain in lattice of the films. In such cases, the scattering vector lies perpendicular to the surface of the thin film and can be measured by using the $2\theta_\chi$-φ in-plane axis of measurement. Other planes lying at an angle to the surface can be accessed in a configuration of asymmetric reflections of 2θ-ω in combination with tilt (χ) and rotation (φ) of the sample. Control of the axes was done using the SmartLab guidance software during various measurements which were either controlled automatically or manually.

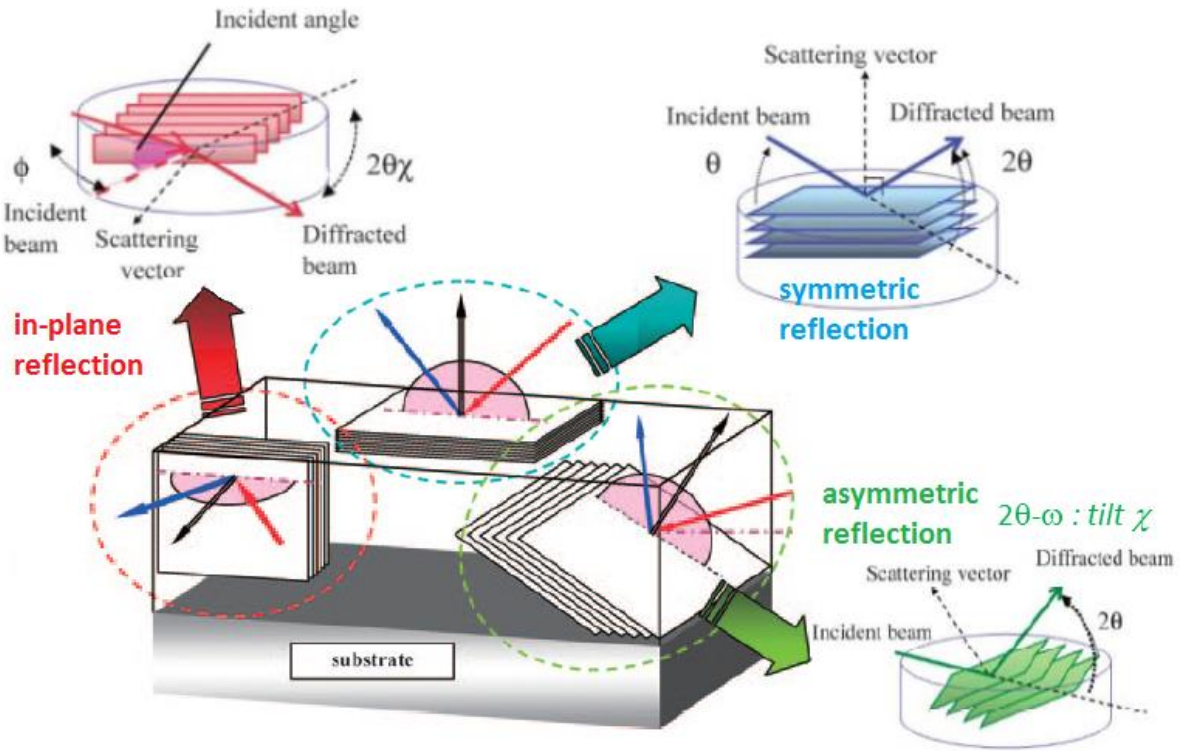

Figure 2.7: Geometry of reflection to access different planes in an epitaxial grown thin film from Inaba et al.[173]

Rocking curve measurement is a technique used to obtain information regarding the crystal quality or mosaicity (misorientation) of a sample. It involves a ω-scan or rocking motion such that the 2θ is fixed to a reflection of interest. The broadening in the peak width is quantitatively described by full-width at half-maximum (FWHM). The broadening is typically a mixture of effects due to misorientation of crystallites and effects from strain relaxation, which are difficult to separate.

Phi-scan (φ) is a similar in-plane measurement with sample rotation performed under set conditions of a particular Bragg diffraction peak (2θ) in an asymmetric or in-plane geometry. Here, the broadening or FWHM of the peak again reflects the in-plane mosaic spread of the crystallites. Phi scan spanning a wider range of angle can give information regarding the symmetry (n- fold) of that particular peak with respect to the rotating axis.

Reciprocal Space Mapping (RSM) is a technique to map the region around reciprocal lattice spots, which can reveal additional information beyond that provided by single line scans such as high-resolution rocking curves. RSM can be acquired by scanning the region near a particular Bragg diffraction peak (2θ-ω) in steps of 2θ-ω or ω. The data was analyzed in the reciprocal space using the Rigaku 3D Explore software. RSMs are useful to aid in the interpretation of peak displacement arising from epitaxial strain related effects, peak broadening or peak overlap.

In addition, X-ray reflectivity (XRR) measurements performed under grazing incidence can be used to determine density, thickness, roughness etc. of single or multilayered thin films, independent of its crystallinity. The refractive index of materials in the case of X-ray tend to be slightly less than 1, leading to total external reflection at small angles (θ) of X-ray incidence less than a critical angle (θ_c). The reflectivity of X-ray decreases rapidly with increasing angles of incidence higher than θ_c. The incident X-rays which penetrate the topmost layer are typically incident at the next interface at lower angles and undergo further reflection. This leads to interference occurring between the X-rays reflected from the surface and those reflected at the interfaces. The resulting oscillations, as shown in figure 2.8, which are superposed on the attenuating intensity of reflected X-rays with increasing 2θ, are called Kiessing fringes.[174] Figure 2.8 summarizes the many effects of thin film properties like thickness, surface and interface roughness, layer densities on the X-ray reflectivity curve. A change in electronic density of the different layers is reflected in the XRR profile. The period of oscillations in the XRR profile is related to the individual layer thickness. The critical angle of total reflection and amplitude of the oscillation depends on the density and differences in electronic density of films. Higher the surface and interface roughness of the films, higher is the attenuation rate of the XRR curve intensity. In this work, the individual layer thickness, density and roughness associated with different thin films grown by MBE was calculated by fitting the XRR profile, using a RCREFSIM software package[175].

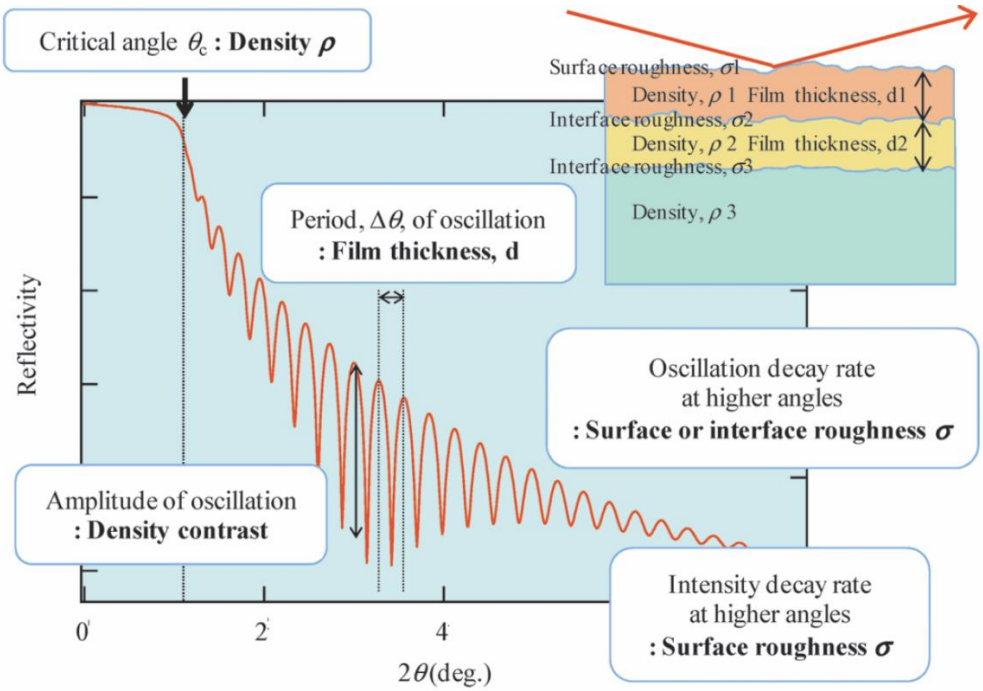

Figure 2.8: A typical X-ray reflectivity profile and the associated information from Yasaka *et al.*[174]

2.2.2. (Hard) X-ray photoelectron spectroscopy

X-ray photoelectron spectroscopy (XPS) is based on the photoemission process. On irradiating a sample with X-rays, the electrons in the core level of surface atoms absorb the photon energy (hν). On overcoming the binding energy (E_B) of the core electrons, the electrons are emitted out of the surface into vacuum with a kinetic energy E_{kin}, as shown in figure 2.9(a). This can be described by the following relation:

$$E_B = h\nu - E_{kin} - \Phi \qquad \text{Equation 2-5}$$

where Φ is the work function induced by the analyzer. The kinetic energy of the emitted electron is measured by the analyzer, thus making it possible to determine the binding energy of core electron level. This number of emitted electrons plotted as a function of binding energy gives the XPS spectra as shown for a HfO_2 sample in figure 2.9(b). XPS can provide both elemental and chemical information. The binding energy of the core level is characteristic of each element allowing determining the chemical compositions. Additionally, the binding energy is shifted according to changes in electron density of the atom which allows the determination of further local chemical information regarding bonding and oxidation states. Analysis of XPS spectra involves identifying all the peaks, their position and features, which could originate from and be affected by different physical phenomenon, the most common of which are briefly described below: [176-178]

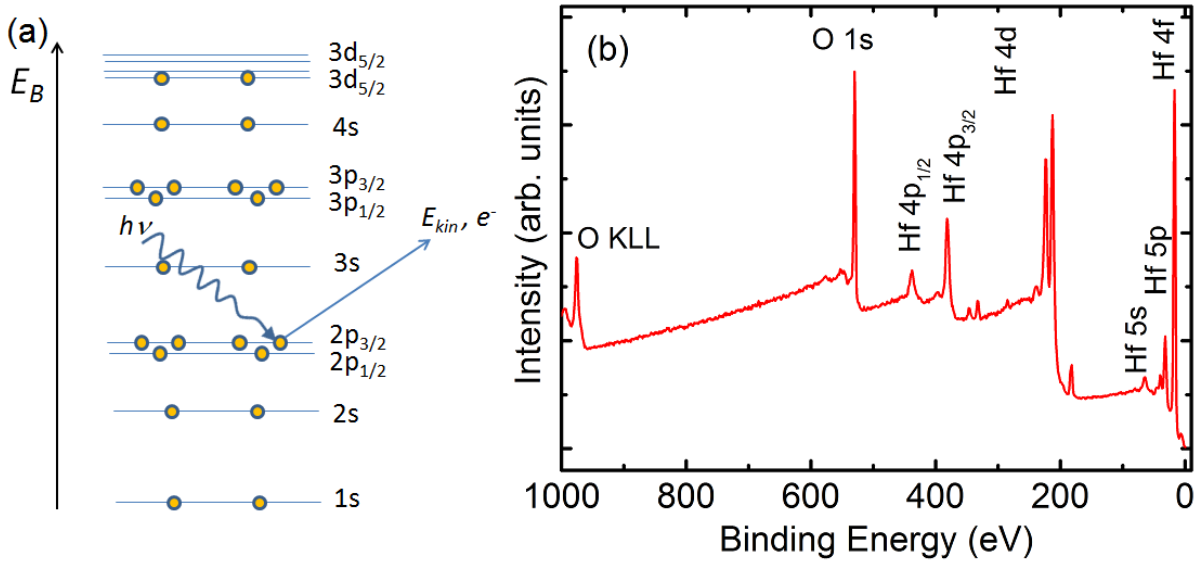

Figure 2.9: (a) Schematic of a photoelectron emission event from a core level due to an incoming photon. (b) Typical survey spectrum obtained from X-ray photoemission spectroscopy (XPS) of a HfO_2 sample.

Main lines: They are due to due to photoelectrons emitted from any core level or valence band, when the energy of X-ray is higher than that of core electron energy. Eg: Hf 4f, Hf 4p lines.

Spin orbit splitting: The main lines can split into a doublet peak due to energy level splitting arising from the electron spin angular momentum (s) and orbital angular momentum (l). eg: Hf 4f is split into Hf4$f_{7/2}$ and Hf4$f_{5/2}$. All core levels except s-levels ($l=0$) forms a doublet ($l \pm s$), with specific area ratios based on the degeneracy of each spin state.

Chemical shift: Any change in the oxidation state or the local chemical environment of an atom will be reflected in the binding energy of core electrons. The binding energies are shifted to higher values, higher the positive oxidation state due to extra coulombic interaction between the ion core and the core electron. This is usually the case when an atom is bonded to another atom of higher electronegativity. This shift in binding energies called the chemical shift is characteristics of the local environment.

Auger lines: They originate from a three electron process involving (1) electron emission from a core level, (2) electron form a higher core level fills the hole created in the first step and (3) the gained energy is transmitted to another electron which is emitted from the atom. Eg: O-KLL

Satellite peaks (shake processes): Shake-up peaks appear for main peaks at higher binding energies, where extra energy is spent in midst of the electron ejection to excite the ion from the zero loss state to an excited state. In shake-off events, electrons are ejected during photo-ionization to the unbound continuum states, leading to broader structures at higher binding energies.

There are also additional features observed in XPS spectra like (1) X-ray satellite peaks arising due to non-monochromatic radiation, (2) inelastic scattering background, (3) multiplet splitting in the presence of unfilled shells containing unpaired electrons and (4) plasmon peaks associated with loss of energy of photoelectrons via inelastic scattering to outer shells. A detailed discussion of XPS and its peak features can be found in literature.[176, 177]

Probing depth: Probing depth during XPS is controlled by the inelastic mean free path (IMFP) of electrons, where only those electrons with energy sufficient to escape the sample contribute to the XPS spectra. IMFP (λ) is defined as the length within which the photoemission intensity decays to 1/e times the original intensity from the point of origin. IMFP depends on the material in which electrons are traversing and the kinetic energy of photoelectrons, which is characteristic of a particular core level as well as the incident X-ray energy. In this work, we

have considered energy dependent IMFPs according to the TPP-2M formula as calculated by Tanuma *et al.*[179] Therefore, the intensity electrons emitted from a depth (d) reaching the surface (I_S) of a material is attenuated exponentially according to the Lambert-Beer law as follows: [180]

$$I_S = I_0 e^{-d/\lambda sin\alpha} \qquad \text{Equation 2-6}$$

where, I_0 is the initial electron intensity, λ is the IMFP and α is the electron take-off angle. With a path length of λ, 63% of all electrons are scattered. Therefore, the probing depth in XPS is typically taken to be 3λ, which accounts for close to 95% of the signal intensity. Typically, α is taken to be close to 90°, i.e. perpendicular to the surface to probe the maximum depth of the surface. In angle dependent XPS studies, lower take-off angles are used to obtain more surface sensitive signal. Using laboratory based XPS equipment using Al K_α or Mg K_α based X-ray sources, the kinetic energy of the photoelectrons is low (< 2 keV). This typically results in a probing depth of approximately 6 nm ($\lambda \sim$ 2nm), where the majority of the signal is acquired from the top layers. The probing depth can be increased by up to an order of magnitude by using higher energy photons (5-15 keV) called hard X-rays, which are typically available at synchrotrons.

In the current work, photoelectron spectroscopy measurements of metal oxide/TiN devices were performed using either of the following equipment:

(1) a laboratory based XPS with a PHI Versaprobe 5000 spectrometer employing monochromatic Al K_α (1486.6 eV) or Mg K_α (1253.6 eV) radiation. The spectrometer was calibrated with respect to the Ag Fermi edge and Ag $3d_{5/2}$ emission of the reference sample. During XPS, TiN bottom electrode was grounded. To prevent charging of the sample surface, an integrated argon ion neutralizer was additionally used. XPS spectra were collected at electron take-off angles of 20, 45 or 75°. The collected spectrum was corrected for any charging related peak shifts using the adventitious carbon peak of C1s at 284.8 eV. [181]

(2) a synchrotron based hard X-ray HAXPES located at the P09 beamline of the Positron Electron Tandem Ring Accelerator – PETRA III storage ring at DESY (Deutsches Elektronen-Synchrotron, Hamburg, Germany). The HAXPES equipment has the possibility measuring of photoelectron kinetic energies up to 15 keV using a SPECS Phoibos 225 HV hemispherical analyzer. The schematic and details of the setup can be found in Gloskovskii *et al.*[182] In this work, hafnium oxide thin films deposited under different oxidation conditions was probed using HAXPES, with photon energy of 8 keV, thus allowing probing deeper into the thin films.

Deconvolution of individual spectrum obtained from XPS/HAXPES and elemental quantification has been performed using the CASA XPS software.[178] Before peak fitting and integrating the area under the spectra, background has to be subtracted. In this work, two kind of commonly used background, Shirley and Tougaard has been used for quantification.[183] The peak shapes corresponding to various oxides were fitted considering mixed Gaussian-Lorentzian(30%) functions. In the case of metallic contributions, photoelectrons typically lose energy during interaction with conduction electrons, and thus were modeled based on asymmetric Doniach-Sunjic profile.[178] In order to obtain the chemical composition of elements which are homogeneously distributed in the probed area, quantification of the spectral intensity (area) of individual elemental peaks gives a measure of its concentration. The spectral intensity (area), is dependent on a number of geometric and physical parameters, which can be expressed as:

$$I = nf\sigma y\theta\lambda AT \qquad \text{Equation 2-7}$$

where *I* is the number of photoelectrons per unit of time in a specific spectral peak related to '*n*' number of atoms per volume of the sample from area '*A*'. Here, *f* is the X-ray flux in photons/area per unit of time, σ is the photo emission cross-section for the atomic orbital of interest and θλ is the IMFP. θ, y and T are efficiency factors related to the electron-take-off angle, probability and efficiency of photoionization and analyzer transmission, respectively.

The concentration, n of an element can be determined as n = I/S, where the dependent factors are assigned to a common atomic sensitivity factor 'S'. The built-in sensitivity factor in the PHI spectrometer software and CASA XPS software package was used for elemental quantification in this work. In general, the elemental fraction of an element in a compound can be determined as, $(I_i/S_i)/\sum (I_i/S_i)$.

2.2.3. Transmission electron microscopy

Transmission electron microscopy (TEM) is a microscopy technique, where an image is obtained by the interaction of an electron beam which is transmitted through a very thin sample. TEM is based on a high voltage electron gun (to produce electron beam), apertures (to limit beam diameter), condenser lenses (to collimate beam), objective lenses, specimen holders and detectors.[184] With the introduction of aberration correction, the resolution of TEM has been pushed below 0.2 nm. A number of imaging techniques can be carried out by changing the lens strength or by deactivating the lens. TEM setup also makes it an ideal platform for other techniques based on interaction of electrons with the sample.

In conventional Imaging, the images are either produced from attenuated beam which passes through directly (bright field TEM) or from only the diffracted beam (dark field TEM). Both these modes are very useful in producing complementary information. In bright field images, regions of higher atomic number appear darker. Dark field images can be useful for information like particle size and phase analysis.

High resolution TEM (HRTEM) is based on the phase contrast due to the phase modulation of the electron waves by the periodic crystal lattice. Phase interference between diffracted and transmitted electrons is utilized to image the crystal lattice at an atomic scale. A Fourier transform is often used to calculate the contrast in high resolution images.

In a Scanning TEM (STEM) mode, the electron optics focuses the beam into a narrow spot which is scanned over the film in a raster pattern. Using a high-angle detector, incoherent high angle electrons instead of the coherent elastically scattered electrons is measured. This high angle scattering is due to Rutherford scattering, where heavier elements with higher atomic number (Z) lead to brighter regions in images. This technique is called high-angle annular dark-filed (HAADF) imaging or Z-contrast imaging and can form atomic resolution images, where the contrast is directly related to the atomic number. However, this has certain drawbacks like beam damage and/or contamination from long exposure, difficulty in imaging low-atomic number elements and drifting induced reduction in image quality.

Diffraction: TEM samples can be tilted to different angles to get Bragg's diffraction form different planes. The beam size and shape can be additionally controlled precisely using condenser lenses leading to selected area electron diffraction (SAED) and convergent beam electron diffraction (CBED)

Energy dispersive spectroscopy (EDS) is one such additional chemical analysis technique that allows the determination and mapping of composition of the sample across the film and interfaces. Fundamentally, this is based on emission and detection of X-rays, which are characteristics of a particular element. This is based on emission of photoemission of core level electrons from an atom in the presence of high energy electrons creating a hole. To compensate for the hole that is left behind, an outer shell electron jumps down to a lower level, thus losing energy, which is emitted as X-rays. The wavelength of the X-ray emitted is characteristic of a particular element allowing for chemical identification.

In this work, for the analysis of TiN thin films, a JEOL JEM-2100F microscope was employed with an electron acceleration voltage of 200 kV to acquire bright field and dark field TEM images, SAED patterns as well as EDS profiles. In case of oxide device stacks, a

JEOL-ARM 200F scanning transmission electron microscope, operated at 120 kV was used to acquire TEM and STEM images. Spatially resolved STEM-EDS images was obtained using a JEOL EDS-system JED-2300T system provided with a 50 mm^2 light-element-sensitive X-ray detector, a digital pulse processor for high speed accumulation and Be double tilt holder. The STEM-EDS maps acquisition was done using Digital Micrograph (DM) software, and spatial drift correction was applied.

2.2.4. Atomic force microscopy

Atomic force microscopy (AFM) is a type of scanning probe microscopy, where surface morphological information is gathered with resolution up to a fraction of nanometers. In the current work, AFM measurements were carried out using a VEECO Dimension 3100 AFM using a Nanoscope IV controller for understanding the surface morphology and roughness of TiN thin films. Samples were placed on a rotating table which can be controlled in translation by stepper motors. A tip made of antimony doped silicon (Bruker, model 13100-10) with a resonant frequency of 525 kHz was used to acquire the AFM images. AFM was operated in the tapping mode in order to avoid surface damage. Here, a scanning tip is attached to a cantilever arm and scanned over a sample surface. Cantilever oscillates with a constant frequency close to its resonant frequency. Changes in the amplitude and phase of the oscillation can be transformed into variations in height signal. A feedback loop is implemented during the scan for readjusting the height of the tip from the surface using a piezo-motor. The acquired images were processed using Nanoscope Analysis software.

2.2.5. Four probe resistivity measurements

Electrical transport measurements were performed to acquire the resistivity-temperature dependence and superconducting transition temperature of TiN thin films deposited by MBE. A four probe technique was implemented, for which four straight contact pads of silver were thermally evaporated through a shadow mask. The electrode pads were deposited on TiN films post transfer through atmosphere after MBE deposition. After electrode deposition, a custom designed dipstick to which the sample was electrically attached was used for temperature measurements. During measurement, a constant current (typically 100 μA) was passed through the outer pads and the voltage drop was measured across the inner contacts (which were separated by 2 mm). Keithley 6221 model current source and Keithley 2182A model nanovoltmeter were used for sourcing current and measuring voltage, respectively. The temperature was measured using a calibrated Lakeshore silicon diode sensor (model DT-670D-SD), placed in contact with the sample stage. The voltage measured in the diode was calibrated to the temperature. A pre-written Labview program interface was used for data

recording of current-voltage-temperature. The dip stick was inserted manually into a liquid helium dewar, where the temperature could be lowered from room temperature (300 K) gradually down to 4.2 K by controlling the distance of the sample head from the level of liquid helium surface. In case superconducting transition was not obtained down to 4.2 K, an Oxford cryostat was used for reaching temperatures as low as 1.5 K using the same dip stick set up.

2.3. Device Fabrication

After MBE deposition and characterization of metal oxide/TiN stacks, device stacks of Pt/metal oxide/TiN configuration were fabricated and studied. First generation devices were made using shadow masks and the newer devices fabricated were using a photolithography-lift off process.

In the first generation devices, platinum top electrode (15 nm) was evaporated followed by reactive sputtering of TiN capping layers (15 nm) through a shadow mask. The top TiN capping layer played the role of a hard surface to reduce scratch damage during contact. As shown in figure 2.10(a), top electrode of 100, 200 and 300 μm were targeted using shadow masks. Bottom electrode opening of 250x250 μm^2 was created using time of flight – secondary ion mass spectroscopy (SIMS), where oxide layer was removed until a TiN signal was detected. Though the fabricated Pt/metal oxide/TiN devices were found to be functioning,[152] the devices suffered from high non-reproducibility, therefore making it difficult to understand the switching mechanism. A careful look at the as-deposited top electrode in figure 2.10(a) shows ring shaped regions around the electrode. This ring-like appearance was due to lower thickness region at the outer regions of the electrode. This could be attributed to shadow effects during deposition due to the thickness of the shadow mask. Moreover, in smaller devices (middle, 100 μm), the devices were often more elliptical, suggesting vibration related drift of the samples or shadow mask during electrode deposition. The high degree of non-reproducibility from device to device could be related to easy oxygen escape to atmosphere at the edges where the top electrode thickness was found to very low ($\sim$ 5 nm). Such a lowering of yield was reported by Goux *et al.*,[150] by lowering the Pt electrode thickness to lower than 50 nm.

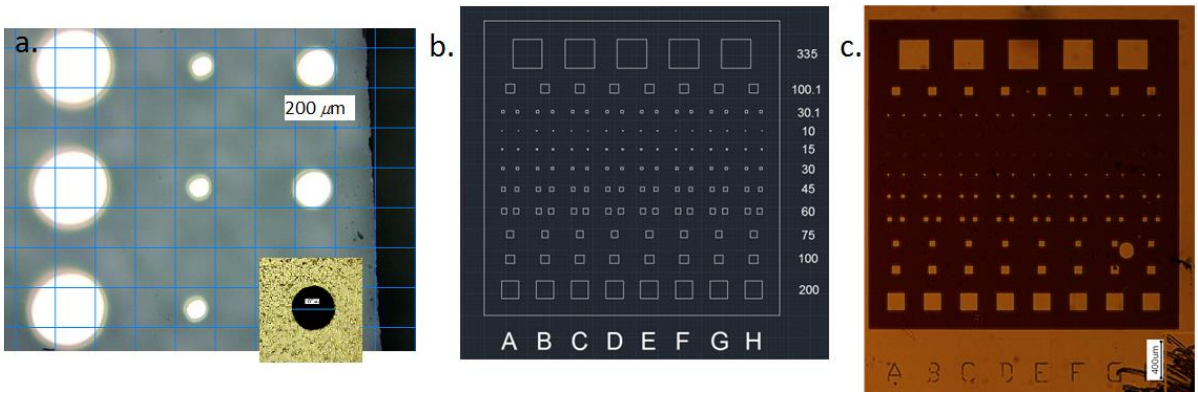

Figure 2.10: (a) Microscope image of top electrodes deposited through a shadow mask with varying diameter. Inset shows a corresponding region of the hole in the shadow mask. (b) Mask design for photolithography and lift-off based top electrode deposition.(c) Actual mask design transferred to a sample.

Therefore, to mitigate the disadvantages, in the second generation devices, a thicker top electrode (100 nm Pt followed by 300 nm of Au) was deposited via a photolithography-lift-off process. In this process, as shown in figure 2.11, a pattern can be transferred to a photosensitive polymer layer (called photoresist) via exposure of light through an optical mask. Figure 2.10(b) shows the optical mask that was designed for the purpose. Devices of square shape with sizes ranging from 10, 15, 30, 45, 60, 75, 100, 200 and 335 μm were targeted. The optical mask is made up of a transparent substrate (quartz) and consists of a pattern (chrome) made up of transparent and opaque regions. An exposure to UV radiation, typically g-line (435 nm) or *i*-line (365 nm) of the mercury lamp, increases or decreases the solubility of the photoresist. In case of a negative photoresist, the transparent regions in the pattern determine the remaining region after development. After development, a subtractive (etching) or additive (deposition) technique can be implemented to transfer the pattern into a device material. The feature of the remaining photoresist, in the form of an undercut, is most desirable in achieving 'lift-off' when using additive deposition of top electrode Pt metal. The undercut allows easier removal of the photoresist layer via a narrow access region available after metal deposition.

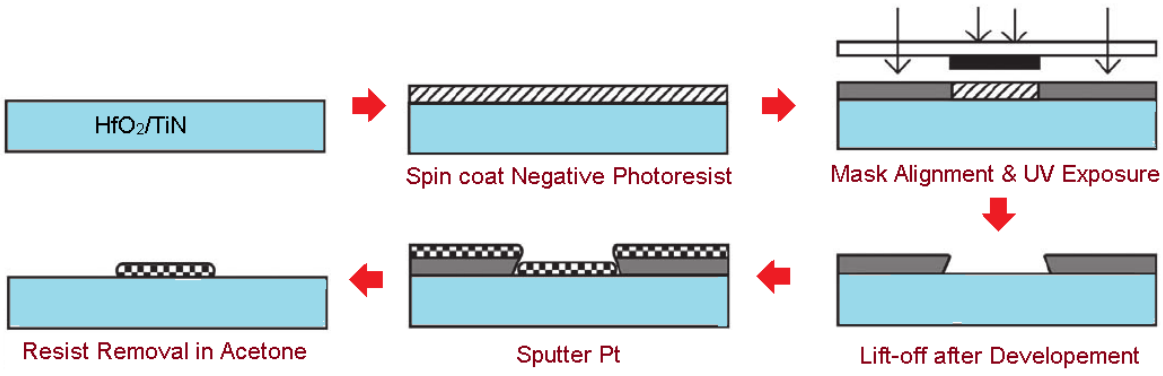

Figure 2.11: Process flow (clockwise) for top electrode deposition to fabricate Pt/metal oxide/TiN devices, image adapted from Zaouk et al.[185]

The steps involved in the processing (figure 2.11) of device fabrication and the optimized process parameters are shown in table 2.2, is described below:

(a) Photoresist coating: Here, sample oxide/TiN/substrate was attached to spin coater vacuum chuck and coated with negative photoresist (ma-N 1420, Microresist Technology) in clean room environment. The spin coating was performed by spinning at high speeds of 3000 rpm for 30 seconds. The residual ridges of resist which accumulated at the edges were removed manually.

(b) Prebake: Excess solvent remaining in the resist (typically 20-40%) was removed by a baking process. This leads to better adhesion of the resist and makes the resist less susceptible to sticking to the masks. Baking was performed for 120 seconds using a hot plate preheated to 100°C. After prebake process, a typical resist thickness of 1.5-2 μm was observed.

(c) UV Exposure: The mask was aligned to the photoresist coated sample using a SUSS Microtech (MJB4) mask aligner and the sample was contacted in a soft contact mode. The sample was then exposed to UV radiation (365) for 17 seconds.

(d) Development: the resist was further developed in a developer solution (ma-D 533/S, Micro resist technology) for 110 seconds to obtain the pattern of the mask onto the substrate, with suitable undercut features.

(e) Electrode deposition: Finally, the top electrodes were defined by deposition of 100 nm thick Pt top electrodes followed by 300 nm of Au by DC sputtering. Sputtering was carried out using Quorum technologies Q150T turbo pumped sputter coater. Pt and Au sputter targets were loaded simultaneously and were sputtered one after the other. Thickness of the platinum and gold were aimed for 100 nm and 300 nm respectively. The optimized parameters used for sputtering are specified in table 2.2.

(f) Lift-off: After, metal deposition, the resist was removed using further lift-off process under an acetone bath (40 °C) for 5 minutes.

Process Steps	**Parameters**
Photoresist coating	3000 rpm, 30 s
Prebaking	100 °C, 120 s
Exposure	Soft contact mode, 17 s
Development	110 s
Sputter deposition	Pt (30 mA, 413 s): 100 nm Au (30 mA, 103 nm): 300 nm
Resist removal	Acetone, 5 minutes

Table 2.2: Optimal process parameters used during the device fabrication of Pt/metal oxide/TiN devices using a photolithography-lift off process.

2.4. Electrical characterization

The resistive switching measurements of first generation devices were conducted initially at IHP GmbH using a Keithley 4200 SCS (semiconductor characterization system) and at TU Darmstadt using Agilent 4156 SCS. Later on, for second generation devices fabricated using lithography lift-off, all measurements have been performed at TU Darmstadt using a Keithley 4200 SCS in combination with a Lakeshore TTPX cryogenic probe station, which was set up and initialized as shown in figure 2.12(a) during the course of this work.

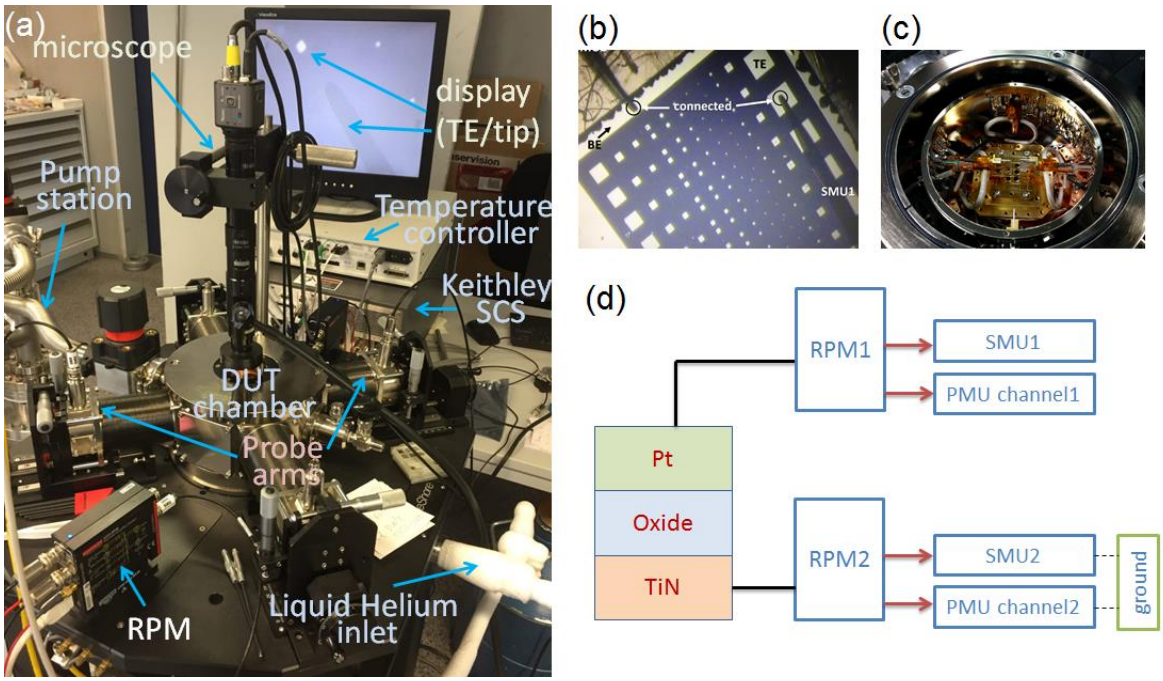

Figure 2.12: (a) The experimental setup showing the electrical characterization system attached to the probe-station, (b) image of a sample with devices contacted by tips. (c) The sample chamber in the probe station showing the probe arms. (d) Diagram showing the connections to the device for measurement in DC or pulse modes.

The Keithley 4200 SCS was equipped with two source measure units (named SMU1 and SMU2) capable of sourcing as well as measuring current and voltage simultaneously. The SCS was operated with the aid of Keithley interactive test environment (KITE) software. The electrodes were contacted as shown in figure 2.12(b) using CuBe tips or spring based W-tips for temperature based measurements. In quasistatic DC switching measurements of Pt/metal oxide/TiN devices, current compliant DC voltage sweeps were applied using SMU1 on the top Pt electrode, with the bottom TiN electrode grounded using SMU2. Pulse measurements, (single pulse, pulse trains and pulse ramps) were performed with model 4225 PMU (pulse measure units) equipped with 2 channels each capable of pulsing with simultaneous V and I measurements. Remote amplifier switch (4225-RPM), as shown in figure 2.12(d), was used to switch between SMU and PMU for dc and pulse measurements as well as for reducing the noise arising from long lengths of the wires. Most measurements were performed under

atmospheric conditions at room temperature. Probe station is also capable of low temperature measurements, which were performed under high vacuum conditions in the sample chamber. The probe station was used in combination with a Lakeshore model 336 temperature controller to control the temperature. The chamber containing the sample stage (figure 2.12(c)) was pumped down to high vacuum conditions and liquid helium was used to cool the probe station sample stage to as low as 5 K.

3. Molecular Beam Epitaxy (MBE) Growth and Characterization

In this chapter, focus is on growth and characterization of thin films by MBE. At first, the growth and characterization of titanium nitride (TiN) thin films on various substrates is discussed. Epitaxially grown TiN electrodes have been compared to polycrystalline TiN electrodes provided by IHP GmbH. The chapter further covers the growth and characterization of oxygen engineered thin films of hafnium oxide (HfO_x) and tantalum oxide (TaO_x). The effect of p-type (lanthanum) and n-type (tantalum) doping on crystallization of polycrystalline hafnium oxide thin films is also discussed briefly. All the oxide thin films were deposited at CMOS compatible temperatures (typically less than 450 ^oC).

3.1. Growth and characterization of titanium nitride thin films

Due to its many potential applications, the growth of high quality epitaxial TiN films with low resistivity and good surface properties on substrates suited for electronic applications becomes increasingly relevant. The nature and quality of surfaces and interfaces play an important role in the performance of devices and heterostructures grown on TiN. TiN has a cubic crystal structure (space group *Fm-3m*) with a lattice constant of 4.242 Å. In this study, we compare the growth of epitaxial TiN thin films on MgO(001), *c*-cut sapphire or Al_2O_3(0001) and silicon (001) substrates by nitrogen plasma assisted Molecular Beam Epitaxy. TiN film growth on MgO(00l) is considered due to a low lattice mismatch as well as to act as a benchmark for surface quality and resistivity. Growth of epitaxial TiN thin films on silicon and sapphire substrates are especially interesting due to its commercial relevance.

3.1.1. TiN thin films on MgO (001) substrates

High quality epitaxial TiN (001) films have been reported to be grown using different deposition techniques like by MBE,[76] PLD[83] and sputtering[186] on MgO (001) substrates, owing to a near perfect lattice match. MgO has a cubic lattice with a lattice parameter of 4.212 Å leading to a mismatch of ~0.7% in the [001] in-plane direction. In this work, growth of TiN on MgO substrates was performed at a low Ti evaporation rate of 0.2 Å/s, keeping the oxidation conditions constant at 1.0 sccm nitrogen flow and 200 W RF power. Growth was performed at various temperatures: 620 ^oC, 660 ^oC, 690 ^oC and 750 ^oC . As shown in the symmetric 2θ scans in figure 3.1(a), all the as-grown thin films with a thickness of ~ 30 nm showed TiN (002) peaks with observed Laue oscillations irrespective of the growth temperature. Moreover, the RHEED patterns (figure 3.1(b,c)) of the as-gown films was found to be streaky. RHEED pattern additionally had the presence of Kikuchi lines as well as diffraction spots on first Laue zone. These are indicative of a high crystalline quality and coherent interfaces of the as-grown epitaxial thin films. A careful look at the XRD pattern

indicate lower amplitudes of Laue oscillations for TiN film grown at the lowest temperature of 620 °C. Correspondingly, there is a slight broadening of the RHEED pattern in figure 3.1(b) in comparison to figure 3.1(c). Asymmetry in the Laue oscillations might be related to a slight non-uniformity in the nitrogen profile across the film due to reaction at the interface.

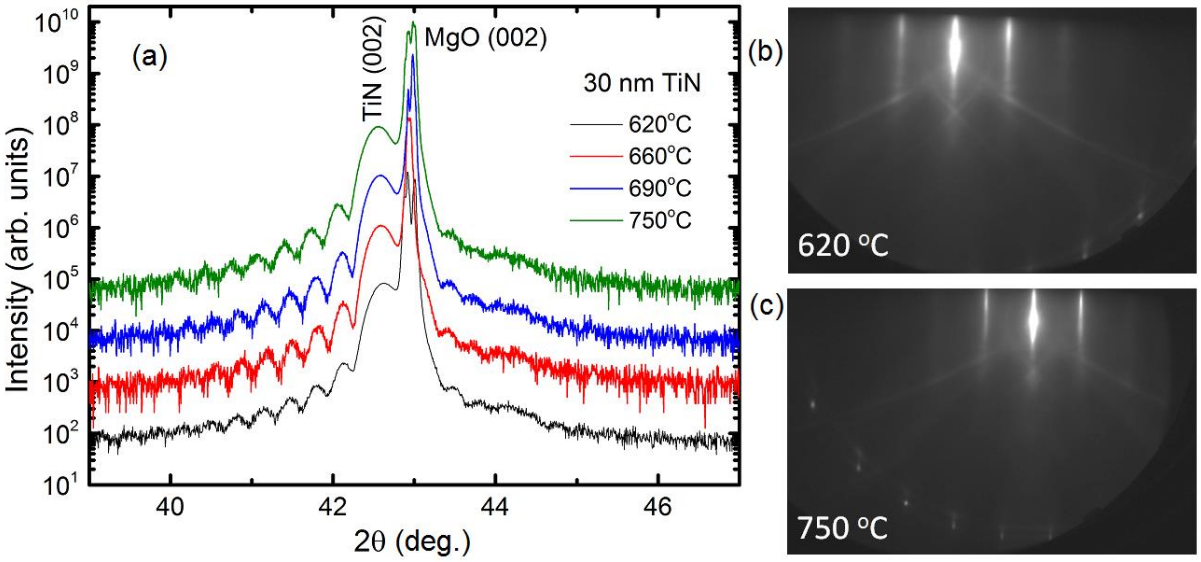

Figure 3.1: XRD patterns of the epitaxially grown TiN films on MgO (001) substrates at various temperatures; RHEED pattern of the as-grown TiN films at deposition temperatures of 620 °C (b) and 750 °C (c).

To get an idea regarding the interface quality, X-ray reflectivity measurements were performed as shown in figure 3.2(a). The XRR results show oscillations well beyond 7°, suggesting that the interface is rather smooth. Using GXRR3 software of Rigaku Corporation, a Fourier transform based analysis of the prominent oscillations yielded a thickness of ~ 30 nm for all the films. A careful look at XRR data of the TiN film grown at 620 °C indicate modulations in the amplitude of oscillations, where the amplitude is increasing from 0 to 4°, which is found to decrease beyond 4°. This is due to the superposition of another oscillation corresponding to a thinner layer with slightly different density, which is likely present at the interface. This superposed oscillation is found to reduce in its period at higher temperatures, suggesting increase in the interface layer thickness. Existence of undamped XRR oscillations, even if there is an interface layer formation, suggests that the interface layer is likely due to thermally driven nitrogen–oxygen exchange to a lesser extent at the interface. This could explain the slight asymmetry observed in the Laue oscillations, which was also observed by Krockenberger *et al.*[76] Reciprocal space mapping of the (113) reflex of the TiN film grown at 750 °C, as shown in figure 3.2(b), show the vertical alignment of the (113) peak of the TiN and MgO. This suggests a pseudomorphic growth of TiN, where the in-plane lattice constant of TiN is identical to that of MgO. Therefore, the TiN thin film grows in a strained manner with a cube-on-cube epitaxial relationship: TiN(001)[100]||MgO(001)[100]. The principal

113 diffraction peak of the TiN film is located at Q_Z = 0.705 Å^{-1}and Q_{110} = 0.337 Å^{-1} giving an out-of-plane and in-plane lattice constants of 4.25 Å and 4.20 Å, respectively. This difference is due to a compressive in-plane strain leading to an elongation of the lattice in the z-direction. The out-of-plane lattice constant is nevertheless very close to the bulk value of 4.24 Å.

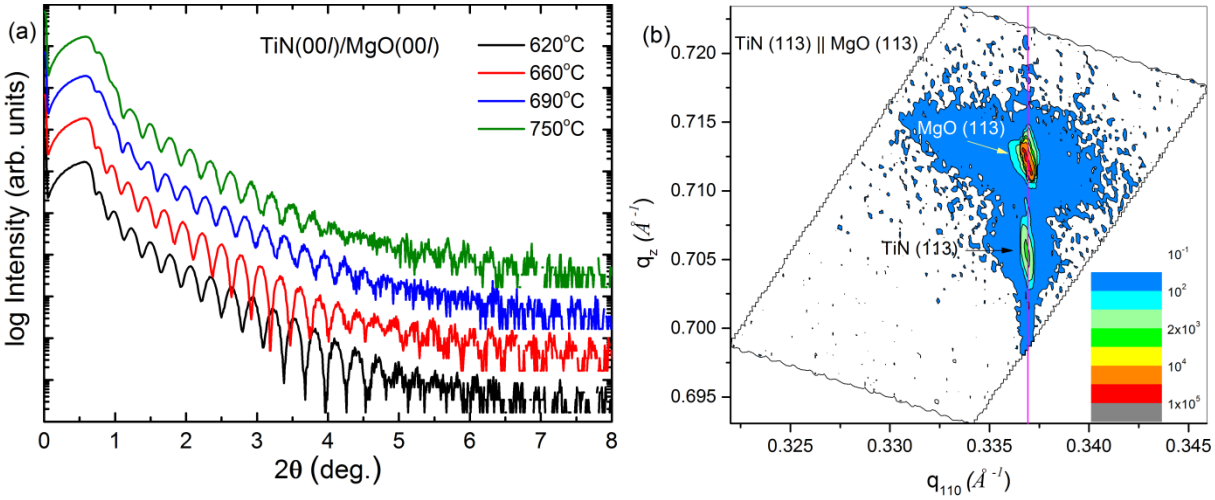

Figure 3.2: (a) X-ray reflectivity profile of TiN thin films grown on MgO (001) substrates at various temperatures. (b) Reciprocal space map near the (113) peak of TiN film grown at 750 °C on MgO (001) substrate.

The electrical resistivity of TiN films was estimated using four probe resistivity measurements. Figure 3.3(a) shows the temperature dependence of resistivity, ρ(T) of TiN thin films grown at various temperatures down to 1.5 K as well as the superconducting transition (T_c, figure 3.3(b)) occurring at lower temperatures. The resistivity of the as-grown thin films decreased from 38 $\mu\Omega$.cm to 25 $\mu\Omega$.cm, when the deposition temperature increased from 620 °C to 750 °C. The highest residual resistance ratio (RRR), ρ(300 K) /ρ(6 K) of 2.5 was obtained for 750 °C. All the films showed superconducting behavior with superconducting transition temperatures of ~4.4 K at the highest deposition temperature and 4.1 K at the lowest deposition temperature. This lower T_c observed in our films compared to the bulk transition of 6.0 K might be related to nitrogen vacancy related defects.[76, 187] Further increase in T_c and RRR is presumably possible by increasing the growth temperature.[84] Interestingly, the superconducting transition was found to be more gradual or step-like at higher deposition temperatures, suggesting a significant role of thermally activated nitrogen diffusion leading to regions with different nitrogen concentration. Nevertheless, the presence of superconductivity suggests near stoichiometric epitaxial TiN films with high crystal quality. The deposition conditions of TiN films on MgO substrates were further used as starting points for further studies on silicon and sapphire substrates.

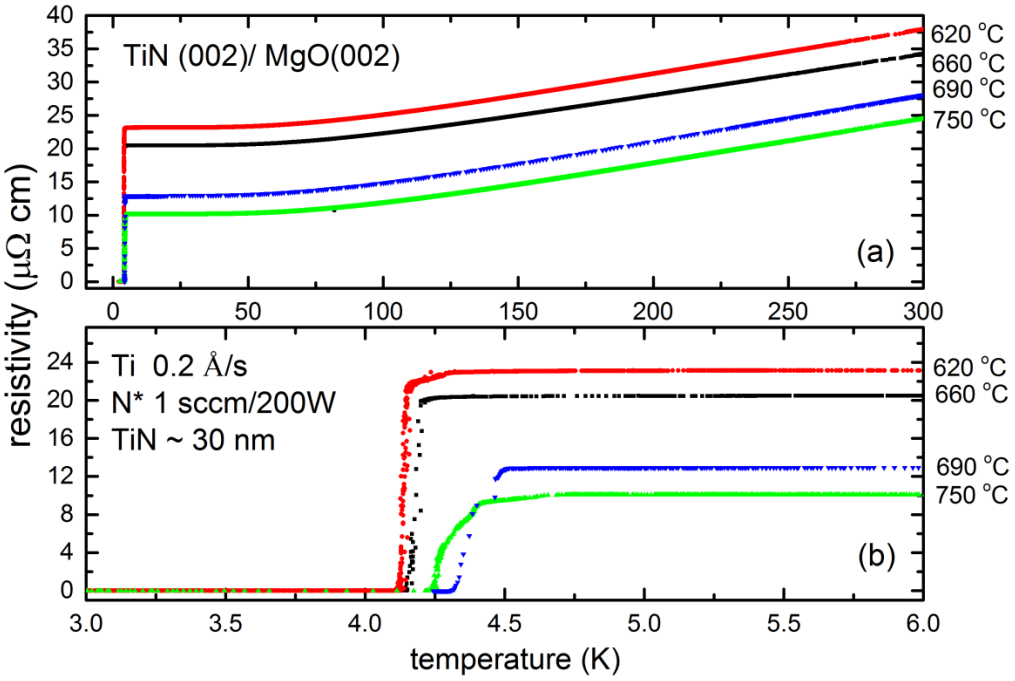

Figure 3.3: Plots of resistivity vs temperature for TiN thin films grown on MgO(001) substrate at various temperatures (top); and the bottom Plot showing the enlarged portion near the superconducting transition region.

3.1.2. TiN thin films on Si (001) substrates

The growth of epitaxial TiN (001) on Si (001) substrates has been reported prior by PLD even with high misfits of 24.6 %. Chowdhury *et al.* explained the epitaxy of TiN films grown at 600 °C on Si (001) by means of a 4-on-3 domain match epitaxy.[188] Later, Willmott *et al*. reported that TiN (001) growth on Si (001) transitions from a Volmer–Weber type (3D) 4-on-3 cube-on-cube mode at temperatures below 550 ± 50 °C to a Stranski–Krastinov 5-on-4 cube-on-cube type at higher temperatures.[189] Though, growth of TiN thin films using nitrogen plasma assisted MBE technique as used in this work was reported recently in the thesis work by Olson, epitaxial growth was not reported.[84] In Olson's work, focus has been to grow highly crystalline thin films with increased superconducting transition. Though, a superconducting transition as high as 6.0 K (close to the bulk) has been obtained at deposition temperatures close to 1000 °C, there is little focus on epitaxial growth. The challenge in growing epitaxial layers of oxides or nitrides on silicon mainly arises from amorphous layer formation prior to growth as well as reaction of titanium and nitrogen with silicon. The native oxide layer can be removed either by flash heating at very high temperatures (above 1050 °C) or via HF treatment. To grow epitaxial layers, it must be taken care to avoid further formation of amorphous layers, which might happen as nitrogen is introduced into the UHV deposition unit, especially when the silicon substrate is heated to high growth temperatures.

In this work, we are limited by the deposition temperature, which has been limited to a maximum of 760 °C during growth to protect the heater. Therefore, *ex-situ* HF treatment of Si(001) substrate was performed to remove the native oxide layer and obtain hydrogen terminated surfaces. Figure 3.4(a) shows the typical RHEED pattern of HF etched silicon (001) substrates heated to 660°C after hydrogen desorption. It is expected that further improvements can be made adopting the approach of flash removal of native oxide using strontium interlayers or flash heating thereby obtaining reproducible surface construction. Introduction of nitrogen gas directly after hydrogen desorption hampered epitaxy likely due to the formation of amorphous or polycrystalline silicon nitride interlayer. Therefore, in order to obtain epitaxial growth of TiN, an intermediate thin layer of Ti with a thickness of 4 Å was deposited followed by quickly switching on the nitrogen plasma source. Figure 3.4(b) shows the changed RHEED pattern obtained after nitrogen exposure, corresponding to ~1-2 monolayers of TiN. Further growth process of TiN was carried out by heating the sample to an ideal growth temperature. Figure 3.4(c) shows the RHEED pattern of an epitaxially grown TiN thin film grown at optimized conditions (650 °C) leading to a streaky RHEED pattern.

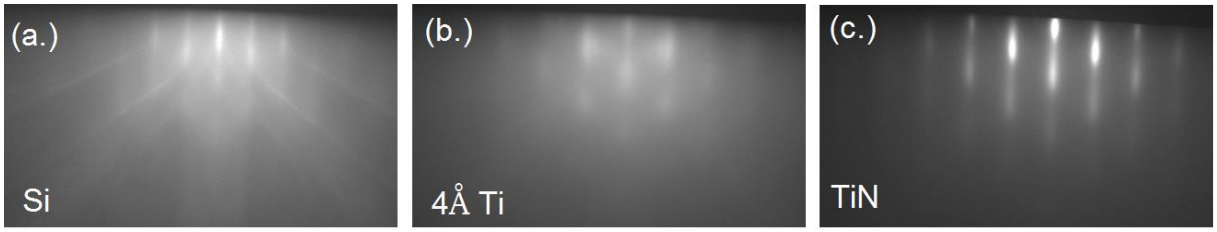

Figure 3.4: RHEED patterns of (a) HF etched Si(001) substrate along [110] azimuth heated to 650 °C, (b) after deposition of 4 Å Ti followed by nitrogen exposure and (c) TiN film (50 nm) thickness at optimized conditions.

To be able to grow epitaxial TiN films on silicon with rather smooth surfaces, as indicated by a streaky RHEED pattern, unlike MgO substrates, appropriate choice of deposition parameters was paramount. The RHEED patterns of TiN films at various deposition conditions during growth (obtained after ~ 400 Å Ti deposited in QCM), reflecting the many ways in which the growth could proceed, is shown in figure 3.5(a-d). A streaky RHEED pattern, as shown in figure 3.5(a and d), was usually obtained at higher flux rates of titanium and nitrogen. Here, a Ti evaporation rate of 1.0 Å/s and nitrogen flow rate of 2.0 sccm and 300 W RF power was used. The streaky RHEED pattern persisted during the entire film growth up to an end thickness of ~90 nm. Higher flux rates of nitrogen likely plays a role in reducing the deposition time, which might reduce reaction and inter-diffusion with the substrate. Through a streaky RHEED pattern could be obtained at a deposition temperature of 760 °C, ring like features usually corresponding to polycrystalline grains were also superposed on the streaky RHEED pattern. The ring-like features disappeared when the deposition

temperatures were lowered to 650 °C. It must be noted that, at the chosen high deposition temperatures, TiN diffusion barrier can fail. Therefore, it could be assumed that the ring like features is perhaps caused by silicon inter-diffusion and reaction leading to Ti-Si-N related phases. However, it is notable that the streaks were much broadened at lowered deposition temperatures (650 °C), indicating increased disorder and lower crystalline quality of the surface. On lowering the nitrogen flux from 2.0 sccm/300 W to 1.5 sccm/200 W (figure 3.5(b)), at the same deposition temperature (760 °C) and Ti flux rate (1.0 Å/s), the RHEED pattern evolved to become more spotty. Further decrease of the Ti flux from 1.0 Å/s to <0.6 Å/s led to further degradation of surface crystal quality as indicated by the formation of mixed spots and rings (figure 3.5(c)). During this deposition process, (<0.6 Å/s Ti) as shown in figure 3.5(c), the Ti evaporation rate was increased from 0.2 to 0.6 Å/s after deposition of first 100 Å of Ti. However, once spots and rings appeared in the RHEED pattern, they remained throughout the deposition process. This suggests that, the epitaxial formation of initial layers achieved by high initial flux rates is necessary. Therefore, comparatively high flux rate of nitrogen as well as titanium are required to be able to grow epitaxial TiN thin films on silicon.

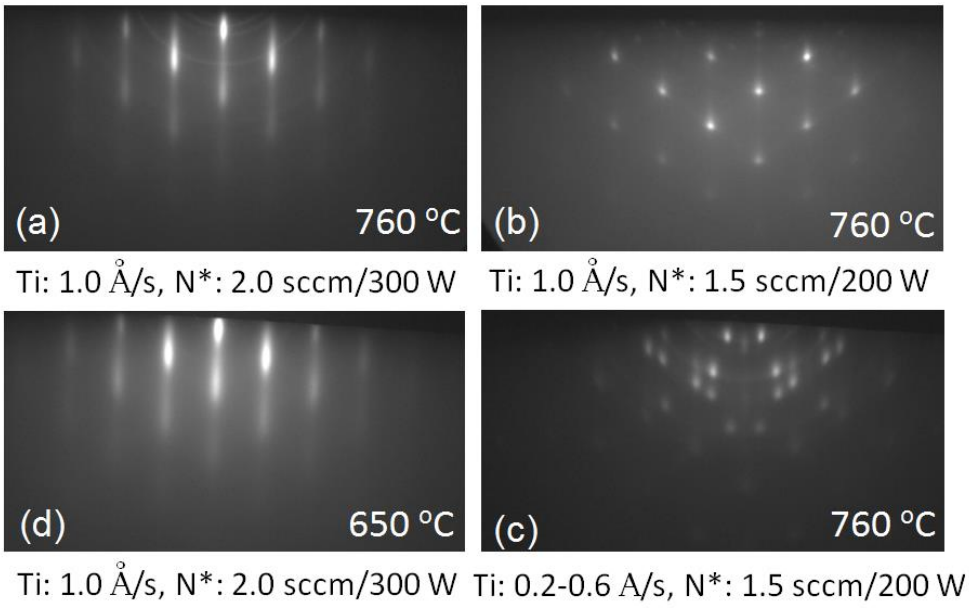

Figure 3.5: (clockwise) RHEED pattern of as-grown TiN thin films under different deposition conditions. High flux conditions lead to a streaky RHEED pattern (a and d),

As-grown thin films of TiN were characterized using XRD and XRR. The XRD pattern of a TiN film with a streaky pattern, acquired using high-resolution optics, is shown in figure 3.6(a). Only the TiN(002) peak at $2\theta = 42.6^{o}$ and the silicon substrate peaks corresponding to the (002) and (004) lattice planes were observed. This suggests texture of the TiN films with TiN(001) planes aligned along Si(001) planes. The observation of Si(002) planes is due to

multiple diffraction, the intensity of which depends on sample rotation angle (φ).[190] In order to determine the in-plane alignment of the films, phi scans were performed for the 111 peaks of Si and TiN at a sample tilt angle of 54.7 deg. As shown in figure 3.6(b), it is clear that that both Si and TiN have four 90°-distanced 111 peaks, indicating the epitaxy of TiN thin film on Si with a cube-on-cube relationship of TiN(100)||Si(100) and TiN[100]||Si[100]. The combination of XRD, RHEED and phi-scans suggests that TiN can be epitaxially grown on Si (001) substrates using nitrogen plasma assisted MBE, similar to the deposition using PLD.[85] To determine the interface quality, XRR measurements were performed as shown in figure 3.6(d). The XRR results show oscillations up to 4°, suggesting a rather smooth interface even though inter-diffusion is expected at the interface. It is likely that a higher crystal quality with as indicated by the streaky RHEED pattern keeps any inter-diffusion to minimum. Fitting of the XRR data using RCRefSim software, assuming a single layer of TiN yielded a thickness of ~ 92 nm and an interface roughness of ~ 0.9 nm.

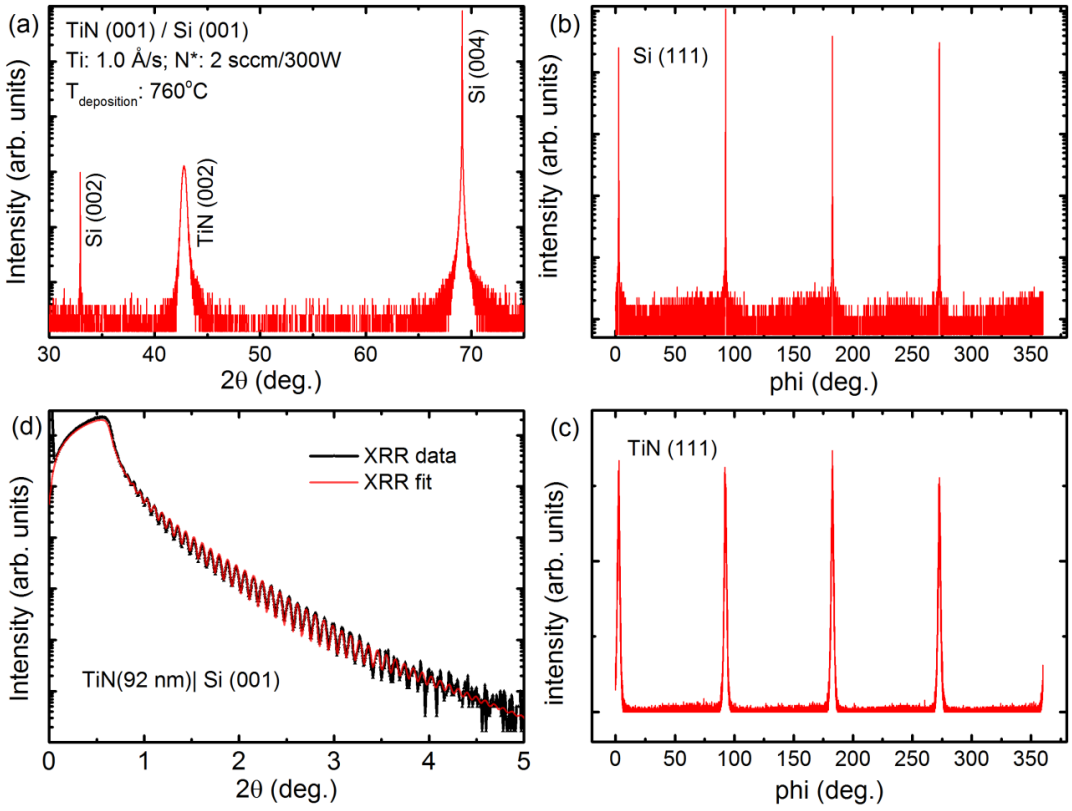

Figure 3.6 (a) XRD pattern of an as-grown TiN thin films grown on Si(001) at optimized deposition rates at a temperature of 760 °C. (b) and (c) show the phi scans of the (111) peak of Si and TiN, respectively. (d) XRR and fitting of the data for film corresponding to (a).

The electrical resistivity of TiN films with thicknesses of ~80-90 nm was estimated using four probe resistivity measurements. Figure 3.7(a) shows the temperature dependence of resistivity, ρ(T) of TiN thin films grown at different deposition conditions down to 1.8 K as well as the superconducting transition (T_c, figure 3.7(b)) occurring at lower temperatures.

The resistivity of the as-grown thin films strongly depended on the deposition conditions as well as crystallinity. At low flux rates, (0.2 Å/s Ti, N*: 1.0 sccm/200 W), the thin films were typically non-epitaxial with high surface and interface roughness. The resistivity of these low flux films at room temperature decreased from 87 to 21 $\mu\Omega$.cm by increasing the deposition temperature from 650 to 760 ^{o}C. Simultaneously, the onset of superconducting transition temperature increased from 2.7 K (650 ^{o}C) to 5.1 K (760 ^{o}C). At the same deposition parameters, increase in temperature can be understood to lead to increased crystal quality and higher superconducting transition temperature. At increased or high flux (1.0 Å/s Ti, N*: 2.0 sccm/300 W) rates, keeping the substrate temperature at 760 ^{o}C, an increased resistivity of 81 $\mu\Omega$.cm was obtained. This could be due to a higher crystal quality of the films as indicated by RHEED (figure 3.5(d)), where nitrogen incorporation becomes difficult, leading to sub-stoichiometry in the films. The highest onset of superconducting transition of 5.32 K was obtained at intermediate flux (0.2-0.6 Å/s Ti, N*: 1.5 sccm/200 W), corresponding to lower crystal quality (see RHEED pattern in figure 3.5(c)). Interestingly the superconducting transition has a two-step character, with transition onsets happening at 5.32 K and 4.90 K. The origin of multistep character remains unclear. This might be related to an increase in the Ti deposition rate from 0.2 to 0.6 Å/s in midst of the deposition process, leading to more inter-diffusion and inter-dispersed regions of different stoichiometry.

In this study, we demonstrate the possible epitaxial growth of TiN thin films on Si (001) substrates for the first time using nitrogen plasma assisted MBE, with the objective of using them as electrodes for resistive switching. Optimal conditions for growing epitaxial TiN films with low surface as well as interface roughness was obtained, as seen from a streaky RHEED pattern and observed XRR oscillations. For epitaxial films, a low resistivity of ~80 $\mu\Omega$.cm and a superconducting transition temperature T_c of ~3.0 K was obtained. The best resistivity of ~20 $\mu\Omega$.cm and a highest T_c of 5.32 K was obtained in thin films with lowered crystal quality. It is expected that, even higher crystal quality and lowered resistivity can be obtained from further studies with *in-situ* processing of silicon.

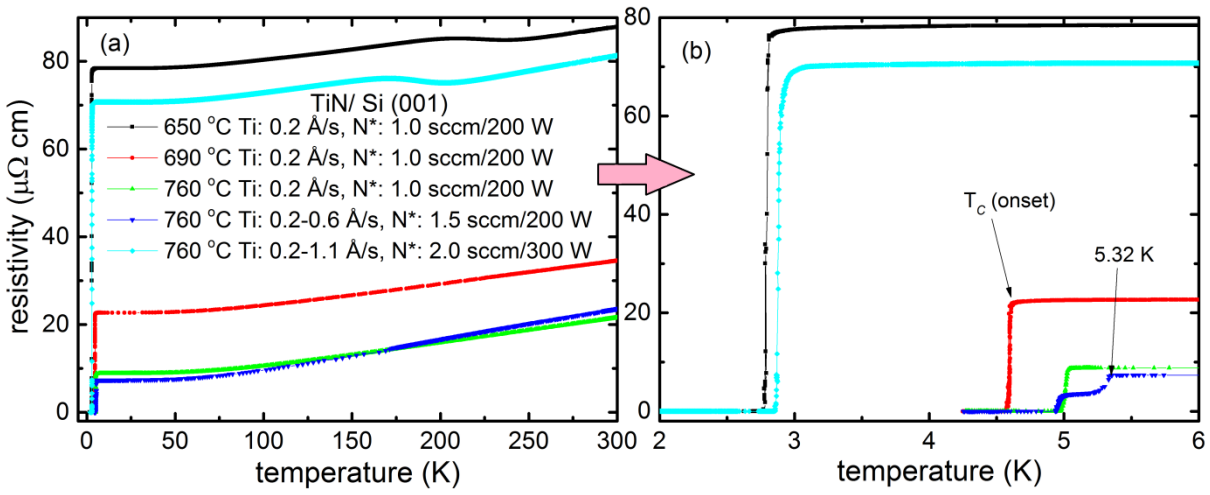

Figure 3.7: Resistivity –temperature dependence (a) and superconducting transition (b) of TiN thin films grown on Si(001) substrates grown at different deposition conditions.

3.1.3. TiN thin films on Al_2O_3 (0001) substrates

The epitaxial growth of TiN thin films on Al_2O_3 (0001) substrates was previously reported using PLD,[78] sputtering[77] and recently using MBE by Olson *et al.*[84] However, there is no report or study regarding the influence of nitrogen stoichiometry on the surface properties as well as epitaxy. Unlike growth on Si substrates, the growth processes on sapphire substrates were found to be straight forward. The as-grown thin films were found to grow epitaxial TiN at higher temperatures in a wide range of deposition conditions. However, at deposition conditions suited to highly stoichiometric TiN as used for MgO substrates, the as-grown films were rough, as indicated by the RHEED pattern. Therefore, further deposition conditions at various flux rates of titanium (0.2-1.0 Å/s) and temperatures (620-750 °C) and were investigated keeping the oxidation conditions constant at 1.0 sccm nitrogen flow and 200 W RF power.

Typical XRD, XRR and RHEED pattern of a TiN film grown at optimized deposition conditions is shown in figure 3.8. Here, growth of TiN films on sapphire substrates was performed at an intermediate Ti evaporation rate of 0.6 Å/s, 1.0 sccm nitrogen flow, 200 W RF power and a deposition temperature of 750 °C. As shown in the symmetric 2θ scans in figure 3.8(a), all the as-grown thin films with a thickness of ~ 25 nm showed TiN (111) peaks with observed Laue oscillations. The peaks position of (111) peak at 2θ = 36.832° corresponds to an interplanar spacing of d_{111} = 2.438 Å. This is slightly lower than the bulk TiN cubic lattice constant of d_{111} = 2.449 Å, either due to strain related effects or nitrogen non-stoichiomerty. To determine the interface quality, XRR measurements were performed as shown in figure 3.8(e). The XRR results show oscillations beyond 6°, suggesting a rather

smooth surface and interface for a 25 nm film. The rocking curve of TiN (111) peak shows a sharp Bragg feature with a FWHM of the ~ 0.3 as shown in figure 3.8(f). The superposed broader region is typically due to defects like dislocation in the films.[191]

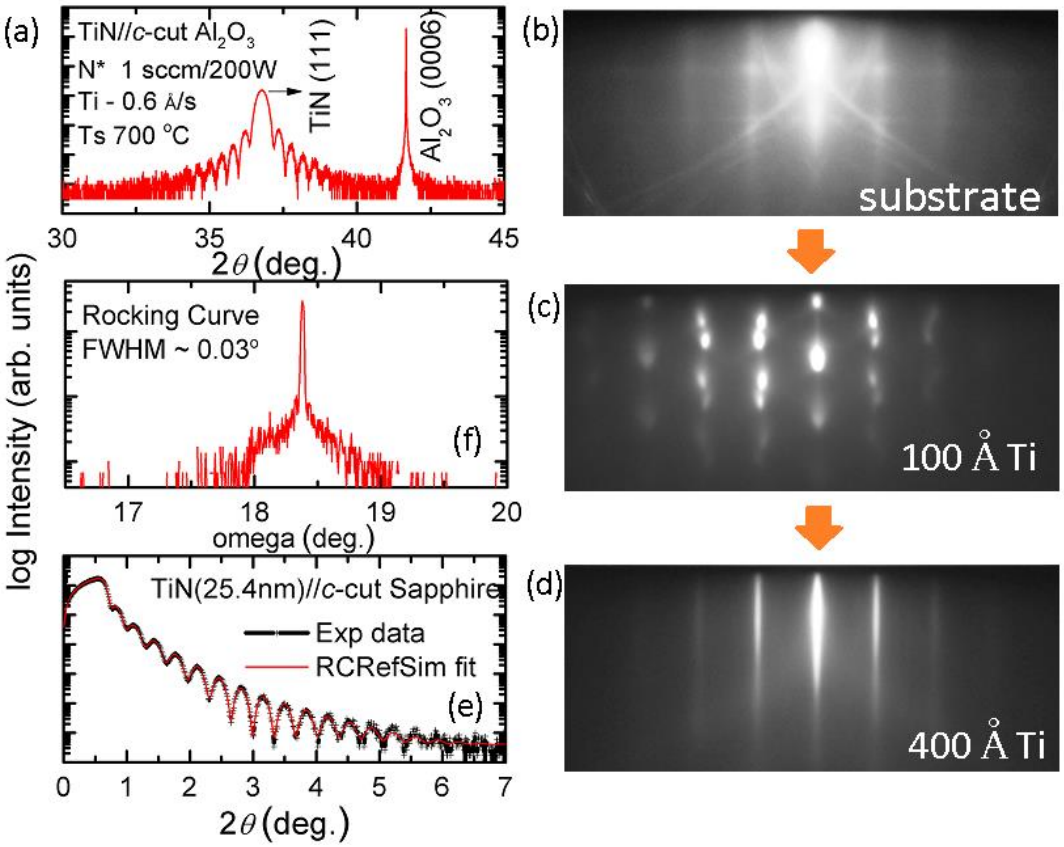

Figure 3.8: (clockwise) (a) XRD pattern of a TiN film grown epitaxially on *c*-cut sapphire; RHEED patterns of (a) Al_2O_3 (0001) substrate along [11-20] azimuth, (b) after 100 Å Ti deposition and (c) after 400 Å Ti deposition; (d) XRR data and (e) rocking curve of TiN (111) peak of the film corresponding to (a).

The RHEED pattern of the *c*-cut sapphire along the [11-20] azimuth is shown in figure 3.8(b). The RHEED patterns of as-grown TiN film were found to very sensitive to the Ti evaporation rates at a constant nitrogen flux. At the optimized growth conditions (0.6 Å/s), the RHEED pattern was found to initially consist of larger spots, as shown in figure 3.8(c), corresponding to 3D-island like growth of TiN. In midst of the growth process, up on increasing thickness, the RHEED pattern was found to gradually transform to a streaky pattern, as obtained at 400 Å Ti thickness as shown in figure 3.8(d). Such a transformation from 3D to 2D growth is usually unexpected. Moreover, if was further found that at low deposition rates (<0.6 Å/s), the RHEED remained spotty similar to figure 3.8(c), throughout the deposited thickness (upto 1000 Å Ti). The 3D to 2D growth mode transition was found to occur at a lower Ti deposited thickness (< 50 Å Ti), when a higher deposition rate of Ti (>0.7 Å/s), was chosen. Interestingly, a recent theoretical work by *Edström et al.* performed DFT calculations to understand the diffusion of TiN_x admolecules on a TiN(001) surface

during homoepitaxy.[192, 193] They found that the growth mode was strongly influenced by the N/Ti flux ratio, where a lower N/Ti adsorption ratio (slightly greater than 1) was optimal for layer-by-layer 2D growth.[192] This was found to be due to higher mobility of Ti adatoms, TiN dimers and TiN_2 trimers in comparison to TiN_3 tetramers formed at higher N/Ti flux, which were nearly immobile thus initiating island-like growth. A similar study on TiN (111) surfaces is currently non-existent in literature. But it can be expected that, such a TiN_x ad-molecule dependent mobility plays a similar role in influencing the growth modes on TiN. At optimized growth conditions, the observed streaky RHEED pattern, Laue oscillations and Keissig fringes are indicative of a good crystal quality and coherent epitaxial thin films.

In order to determine the in-plane alignment of the films, phi scans were performed for the TiN 002 peaks of TiN and Al_2O_3 (-102) peaks by tilting the sample. As shown in figure 3.9(a), it is clear that TiN (111) has six 002 peaks separated by 60°, which are located at ±30 with respect to Al_2O_3 (-102) peaks. This is indicative of the presence of two kind of domains which are rotated at 60° with each other, as reported previously for epitaxial TiN(111) films.[78] [194] Here, the equivalent TiN(111) domains can be understood to fit to the hexagonal atomic arrangement of Al_2O_3 (0006) surface, but forms twins with different stacking arrangement. The epitaxial relationship can be expressed as: TiN(111)||Al_2O_3 (0001) and TiN[110],[101] twins||Al_2O_3 [10-10]. AFM images acquired for a 1μm x 1μm region, as shown in figure 3.9(b) shows the presence of interlocked grains which are likely individual domains with grain sizes of 0.1-0.5 μm. An rms roughness of ~0.43 nm (1μm x 1μm) was obtained for the films with a streaky RHEED pattern. The combination of XRD, RHEED and phi-scans suggests that TiN can be epitaxially grown on Al2O3 (0001) substrates with smooth surfaces by changing the Ti/N flux ratio during nitrogen plasma assisted MBE.

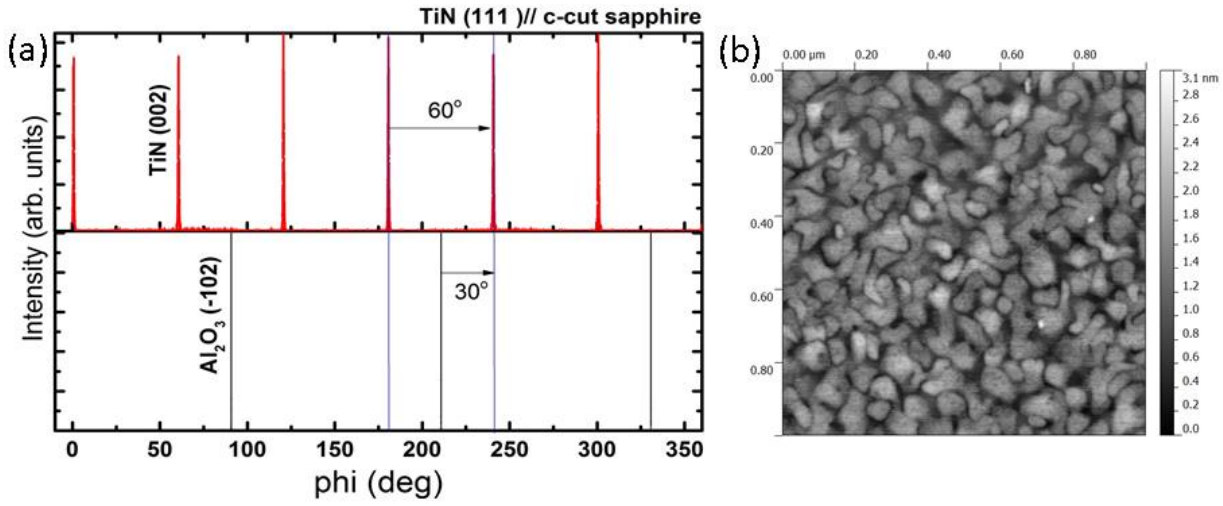

Figure 3.9: (a) Phi scan of TiN (002) and Al_2O_3 peaks, (b) AFM image of the corresponding TiN film surface characterized by a streaky RHEED pattern.

Figures 3.10(a) and 3.10(b) shows the TEM images and SAED pattern of the as-grown TiN thin films. Bright field TEM image corresponding to non-diffracted beam is shown on the top with the TiN film region indicated as #1. The corresponding dark-field (DF) TEM image (middle) acquired showed the presence of a brighter region in the middle due to an oriented grain with respected to the beam direction. This orientation is represented by the #2. On tilting the beam, it could be directed such that the diffraction primarily takes place from the differently oriented grains (#3). Due to the presence of multiple orientations of the grains, the obtained SAED pattern was found to be dependent on the grain to which the beam was focused. The SAED pattern obtained at the grain boundaries showed the diffraction spots corresponding to both grains (#2 and #3) as well as the direct beam spot (#1). The SAED pattern was found to match well with the RHEED pattern obtained previously in transmission for the initial 3D-island like growth mode.

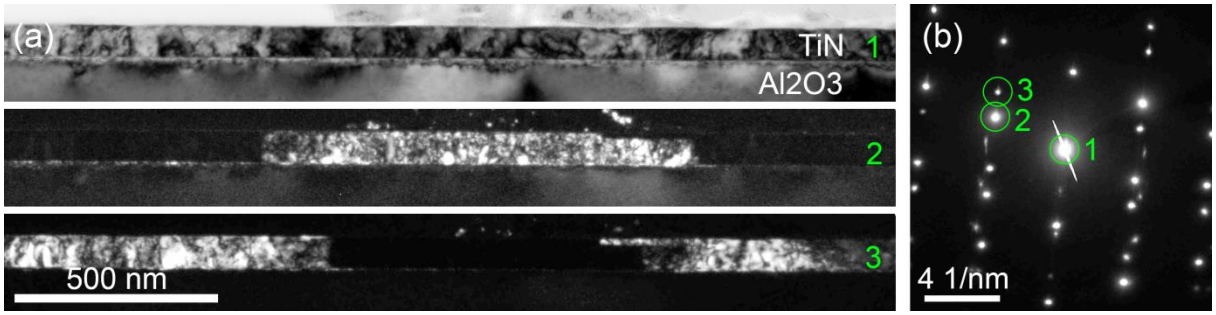

Figure 3.10: (a) Bright field (top) and Dark field TEM images for the two possible TiN grain orientations of the MBE sample, (b) corresponding SAED pattern acquired at the grain boundary between the TiN grains.

The bright field TEM images (figure 3.10(a)) showed a change in contrast in the region of the substrate near the films. This might be use due to inter-diffusion, which can occur at high deposition temperatures especially in the presence of non-stoichiometry in TiN films. To investigate the effect of formation of possible inter-diffusion phases, we compare the TiN thin films grown at the highest deposition temperature of 750 °C, where the titanium evaporation rate was increased from 0.2 (low) to 0.6 (intermediate) to 0.8 Å/s (high), at constant 1.0 sccm nitrogen flow and 200 W RF power. Figure 3.11(a) and 3.11(b) compares the XRD and XRR of the corresponding films, respectively where 1000 Å of Ti was deposited. At lowest Ti evaporation rate of 0.2 Å/s, the XRD pattern only shows the TiN (111) peak in the 2θ range from 10° to 43°. At the optimal deposition condition of 0.6 Å/s, there is a small background appearing in the region of 10-20°. The RHEED pattern changes from spotty to streaky, when the evaporation rate is increased from 0.2 to 0.6 Å/s. This is reflected in the XRR, where the intensity was found to drop quicker for 0.2 Å/s film than for 0.6 Å/s film, corresponding to increased surface roughness. The relatively good XRR pattern for the 0.6 Å/s film suggest that the inter-diffusion indicated by the diffraction background occurring at lower 2θ angles in

XRD in minimal. However, as soon as the Ti evaporation rate is increased to 0.8 Å/s, the XRD pattern changes with the occurrence of four additional peaks. These peaks can be attributed to the new phases of $Ti_2Al(O,N)$ and Ti_2O which form due to the reaction between nitrogen deficient TiN_x and Al_2O_3 substrate, as observed by Persson *et al.*[195] This is due to the diffusion of Al and O atoms into the sub-stoichiometric TiN_x films during deposition, causing an interface reaction. The formation of new phases near the interface is associated with increased interface roughness as indicated by XRR, even though the surface is probably smooth as indicated by streaky RHEED pattern.

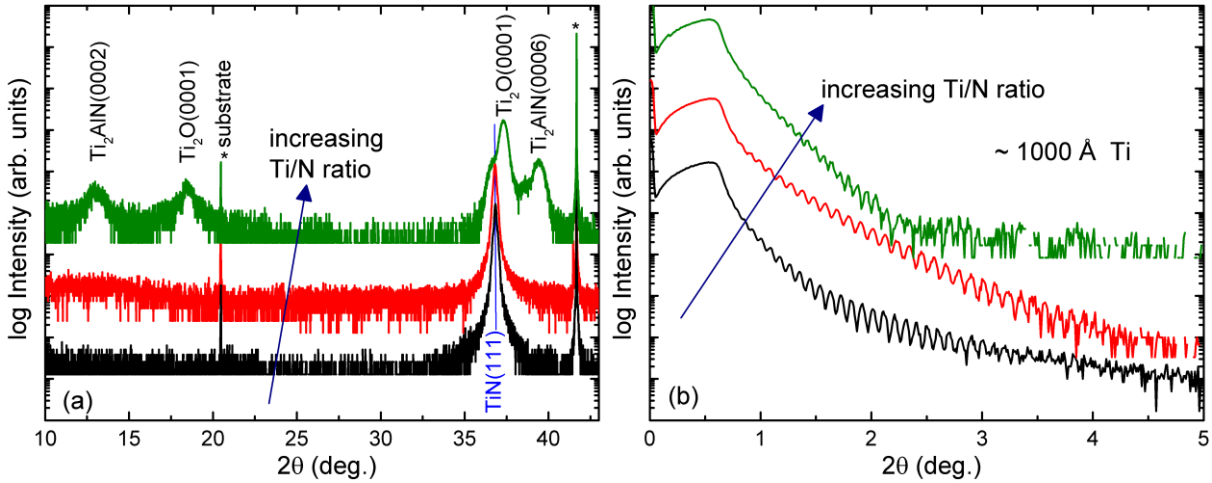

Figure 3.11: (a) XRD and (b) XRR patterns of as-grown films grown on Al_2O_3 (0006) substrates with 1000 Å Ti deposited at increasing Ti rates (0.2, 0.6 and 0.8 Å/s) at constant 1.0 sccm nitrogen flow and 200 W RF power.

Since the optimized growth conditions is such that the Ti evaporation rate falls at an intermediate value between low rates (3D growth mode in RHEED) and high rates (inter-diffusion phase observed by XRD), it becomes necessary to confirm the composition of the as-grown nitrogen deficient film across the bulk and interfaces. Figure 3.12 shows the acquired (a) STEM and (b) EDS images of an ~85 nm TiN (111) film grown epitaxial on Al_2O_3 (0001) at optimized growth conditions. The STEM images show a relatively uniform bulk TiN film. The corresponding EDS mapping of individual elements (Al, O, Ti, N) suggest relatively sharp interfaces. However, the oxygen signal shows moderate drops at the interface as well as small peak at the surface marked by arrows. The drop in intensity at the interface suggests a loss of oxygen towards the film, which is possibly the reason for the contrast difference observed in STEM images near the interface. The small peak at the surface might be related to TiON formation when the surface is exposed to ambient, due to the slight nitrogen deficiency in the as-grown TiN films at optimized growth conditions.

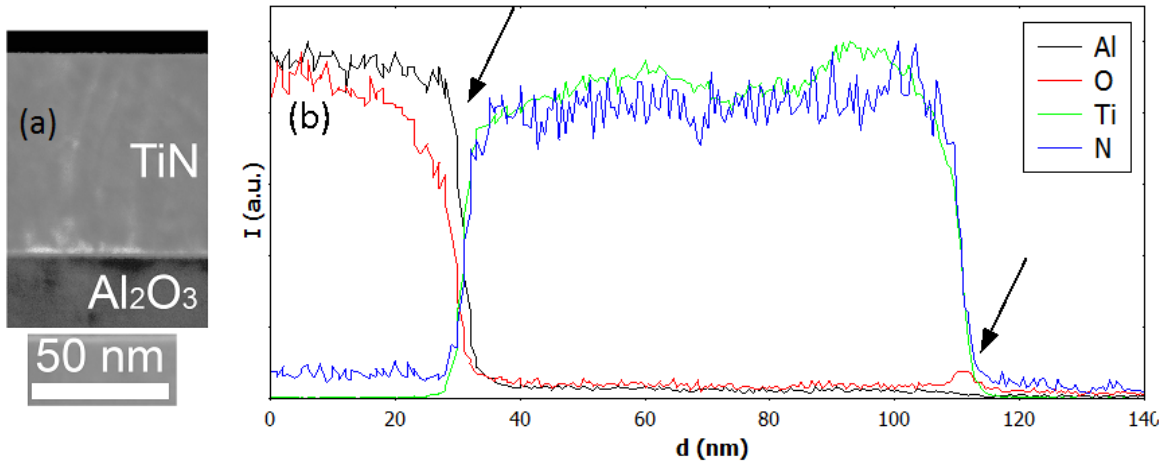

Figure 3.12: (a) STEM and (b) EDS pattern of the TiN film grown on at optimized growth conditions to achieve low surface roughness.

The electrical resistivity of the as-grown TiN films was investigated using four probe resistivity measurements, as shown in figure 3.13(a). Figure 3.13(a) shows the temperature dependence of resistivity, ρ(T) of TiN thin films grown at different deposition conditions down to 4.2 K as well as the superconducting transition (T_c, figure 3.13(b)) occurring at lower temperatures. The resistivity of the as-grown thin films strongly depended on the deposition conditions particularly Ti/N ratio determined by the Ti evaporation rate at constant nitrogen flow parameters. At low flux rates, (0.2 Å/s Ti, N*: 1.0 sccm/200 W), the thin films were typically epitaxial growing in the 3D-like Volmer-Weber growth mode. The electrical resistivity of these TiN films with thicknesses of ~30 nm decreased from 59 to 21 μΩ.cm by increasing the deposition temperature from 620 °C (#1) to 760 °C (#4). Simultaneously, the onset of superconducting transition temperature increased from 4.4 K (620 °C) to 4.9 K (750 °C). At increased Ti flux (0.6 Å/s Ti, 30 nm TiN, 750 °C) rates, the resistivity was found to increase to 90 μΩ.cm, likely due to nitrogen deficiency or sub-stoichiometry. Interestingly growth of a thicker film (80 nm TiN) at optimized growth conditions further increased the resistivity to 140 μΩ.cm. It is to be noted that, the initial growth at optimized conditions proceeded in a 3D island like growth mode. At higher thicknesses it is possible that the relatively low oxygen inter-diffusion which might be present plays a role in increasing the resistivity.

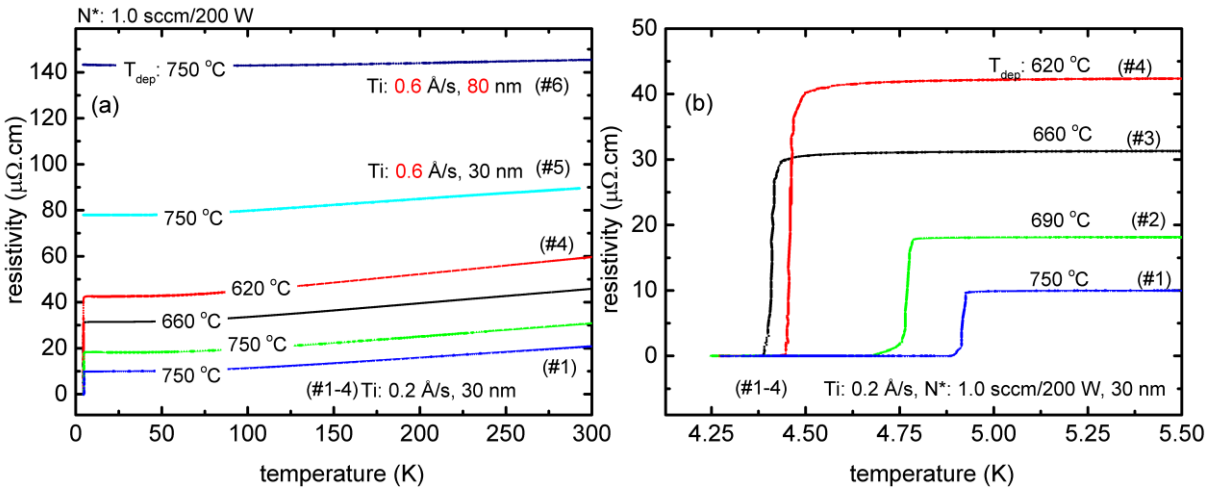

Figure 3.13: Resistivity –temperature dependence (a) and superconducting transition (b) of TiN thin films grown on Si(001) substrates grown at different deposition conditions.

In this study, we demonstrate the possible epitaxial growth of TiN (111) thin films on *c*-plane sapphire or (0001) substrates using nitrogen plasma assisted MBE, with the objective of using them as bottom electrodes for HfO_2 based RRAM. At optimal (slightly nitrogen deficient) conditions for growing epitaxial TiN(111) films, low surface/interface roughness was obtained, as seen from XRR, streaky RHEED pattern and observed XRR oscillations. The presence of twin domains rotated at 60° to each other was confirmed by RHEED, XRD phi scans and TEM. Most interestingly, we were able to obtain a 2D growth mode indicated by a streaky RHEED pattern, which has not been reported before for TiN growth on sapphire substrates. This transition from 3D to 2D growth mode was aided by a higher Ti/N flux ratio during growth possibly aided by the formation of ad-molecules which are more mobile. For epitaxial films, however showing a 3D-island like growth, a best resistivity of ~21 μΩ.cm and T_c of ~4.9 K was obtained for films grown at 750 °C. The conductivity and superconducting transition temperature is expected to be further improved at higher deposition temperatures. At optimal nitrogen deficient conditions (smooth surface with good conductivity), where 2D growth was observed, a slightly higher resistivity (80-150 μΩ.cm) was observed.

3.1.4. Summary of TiN electrodes and Remarks

In this study, most oxide devices used for electrical characterization were deposited on polycrystalline TiN electrodes which were obtained from IHP GmbH. TiN films were grown on SiO_2/Si(001) substrates by reactive sputtering. Figure 3.14 shows the bright field (BF), annular dark-field (ADF) and high-angle ADF (HAADF) STEM mapping of these polycrystalline TiN films. The TiN films had a thickness of ~ 72 nm. A thin interface layer (~ 2 nm) of amorphous SiO_2 is also visible. By comparing the contrast difference of BF and ADF images, there are regions which appear darker/brighter in BF/DF. This corresponds to grains

with lattice planes which are preferentially oriented along the beam direction for diffraction. The grain sizes in the TiN films are of the order of ~ 10 nm. HAADF STEM images appear to be darker due to the presence of lighter ions (Si, Ti, N, O) which does not cause enough high angle scattering. By four probe measurements, a resistivity of ~ 190 $\mu\Omega$.cm and T_c of ~4.13 K was determined (as shown in figure 3.15), which were sufficiently good for electrode applications.

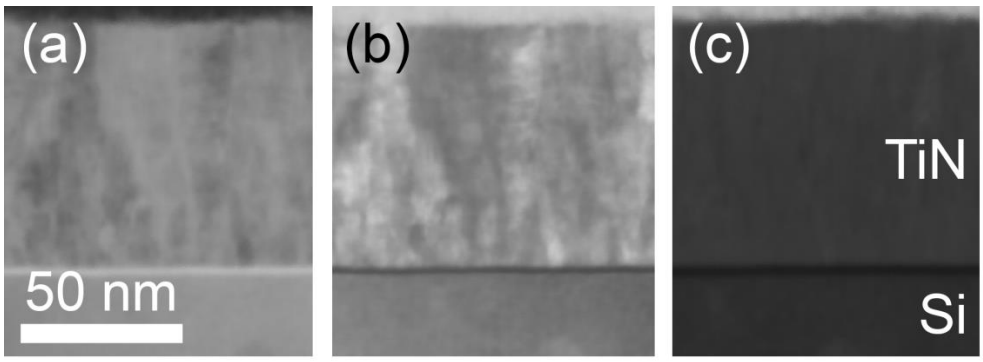

Figure 3.14:(a) BF, (b) ADF, (c) HAADF STEM mapping of the polycrystalline TiN films from IHP GmbH (Si substrate, TiN electrode and HfO2 oxide). (image courtesy: Alexander Zintler)

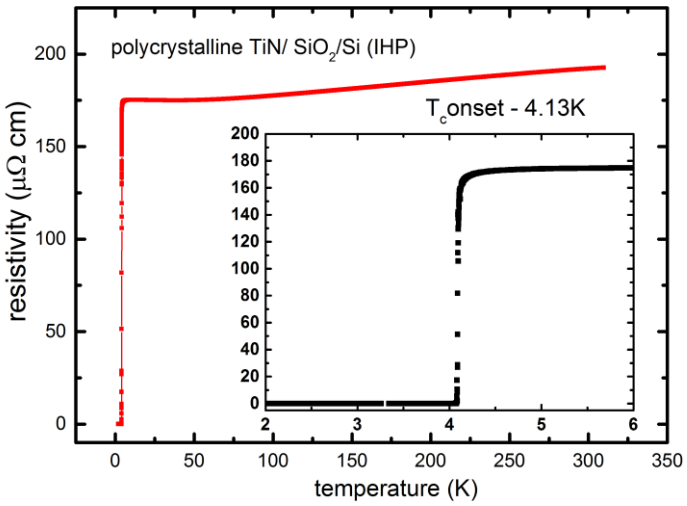

Figure 3.15: Resistivity–temperature dependence and superconducting transition (inset) of polycrystalline TiN thin films used in this study.

In the case of polycrystalline TiN films from IHP, hafnium oxide thin films were further deposited after *ex-situ* transfer of these TiN films through ambient to the MBE deposition unit. Under non-clean room conditions, it was found that device yield was not sufficiently high (20-30 %). This might be related to the presence of particulates on the TiN film. This affects the device characteristics, especially due to the chosen MBE technique, which is a line of sight deposition technique with less coverage and shadow regions of lower thicknesses are expected to form around particulates. Therefore, for yield enhancement, TiN films were grown

epitaxially using MBE to be used as electrodes for future *in-situ* growth of hafnium oxide thin films for RRAM device applications.

In summary, TiN films were grown epitaxially by MBE on commercially relevant sapphire and silicon substrates as well as MgO(001) substrates for comparison. In spite of a high lattice mismatch for sapphire and silicon substrates, smooth surfaces (streaky RHEED and XRR oscillations) as well as low resistivity (<150 μΩ.cm) were achieved for epitaxial TiN films, thus making them suitable for electrode applications. A superconducting transition temperature (3- 5 K) in the as-grown TiN films is characteristic of high quality of the as-grown films. The results of MBE grown films with the best parameters are summarized in Table 3.1.

TiN Film	Remarks	Resistivity $\rho_{(RT)}$ (μΩ - cm)	Superconducting Transition onset $T_{C,\,ONSET}$ (K)
TiN|SiO_2|Si (001) : IHP	Polycrystalline	190	4.13
Nitrogen plasma assisted reactive MBE			
TiN(111)||Al_2O_3 (0001)	Epitaxial (2D), **Streaky RHEED**	140	-
TiN(111)||Al_2O_3 (0001)	Epitaxial (3D), Spotty RHEED	**21**	4.9
TiN(001)||Si (001)	**Epitaxial, Streaky RHEED**	90	3.1
TiN||Si (001)	Polycrystalline, high roughness	**21**	**5.3**

Table 3.1: Summary of the TiN films grown with the best parameters of surface quality (roughness) or resistivity as grown by MBE (to enable further *in-situ* oxide growth) in comparison to polycrystalline TiN films received from IHP GmbH. (*ex-situ* oxide deposition)

3.2. Oxygen engineering in HfO_x

Oxygen stoichiometry was engineered systematically with high reproducibility in hafnium oxide thin films by varying the hafnium evaporation rate as well as the oxygen flow and RF power. Two discharge tubes made of quartz were used over the course of the work: DT#1 with an aperture area of 4.65 mm^2 (37 holes each with a diameter of 400 μm) and DT#2 with an aperture area of 3.48 mm^2 (197 holes each with a diameter of 150 μm). DT#1 allowed operation in the 0.15-2.5 sccm regime and DT#2 allowed operation at further lower oxidation

condition regime of 0.05-0.5 sccm. The hafnium oxide films were grown on *c*-cut sapphire substrates as well as polycrystalline and epitaxial TiN films.

3.2.1. Effect of oxidation conditions

Table S1 shows the typical deposition conditions used for stoichiometry control of as-grown HfO_x thin films in a wide range which was possible using the discharge tube #2. The hafnium oxide films were simultaneously grown on TiN films and *c*-cut sapphire substrates. The RF discharge tube was operated at low oxygen flows thus realizing very low oxygen partial pressures (10^{-7}-10^{-5} mbar) corresponding to low oxidation conditions. The RF power applied to the discharge tube was maintained constant at 200 W during growth. The substrates, TiN and sapphire was maintained at a CMOS compatible temperature of 320 °C. The thin films for X-ray characterization were labeled HfO #1, 2, 3, 4 and 5 each deposited under increasing oxidation conditions (HfO#1 was grown under lowest and HfO#5 under highest oxidation conditions). For the films HfO#1-3, the hafnium evaporation rate was maintained at 0.9 Å/s and the oxygen flow was increased from 0.1 sccm to 0.5 sccm. Further increase of oxidation conditions required the rate of hafnium evaporation to be lowered to 0.5 and 0.1 Å/s for the growth of samples HfO#4 and HfO#5, respectively.

Sample ID	Hf evaporation rate (Å/s)	Oxygen flow (sccm)
HfO #1	0.9	0.1
HfO #2	0.9	0.3
HfO #3	0.9	0.5
HfO #4	0.5	0.5
HfO #5	0.1	0.5

Table 3.2: Growth parameters used for the deposition of HfO_x thin films at 320 °C by MBE, RF power applied to the plasma source was maineteined at 200 W.

Figure 3.16(a) shows the X-ray diffraction patterns of all films grown on TiN/Si substrates, obtained using medium resolution optics. At highest oxidation conditions (#5), the films crystallize as expected for fully stoichiometric samples in a monoclinic structure (*m*-HfO_2). The predominant peaks of $(-111)_m$ and $(111)_m$ for the monoclinic phase are located at 2θ = 28.33° and 31.66°, respectively (JCPDS 00-034-0104). On reducing the oxidation conditions, the films show a transition to predominantly tetragonal-like phase of hafnium oxide (*t*-HfO_x), as indicated by the appearance of a peak located at 2θ = 30.30°, corresponding to $(101)_t$ (JCPDS 01-078-5756). On further reduction of the oxidation conditions, a reflection belonging to hcp-HfO_x appears (the structure of metallic Hf). Ideally, hcp-Hf has the strongest (101) peak at 2θ = 37.03° (JCPDS 04-003-5555). This peak,

however, is shifted to larger lattice spacing likely due to the presence octahedral interstitial oxygen. Theoretical calculations have suggested that it is thermodynamically favorable for phase separation of sub stoichiometric HfO_x to a mixture of *m*-HfO_2 and hcp-$HfO_{0.2}$, also suggesting a tetragonal phase to be stable only in a narrow window near x = 1.[72] Oxygen vacancies induced by doping in hafnium oxide is known to stabilize tetragonal and monoclinic phases. Previous reports also indicate a similar stabilization of oxygen deficient hafnium oxide phase with tetragonal symmetry unlike its high temperature structure obtained by varying the ion energy in ion beam assisted deposition.[196] DFT calculations have also shown that the presence of oxygen vacancies usually arising to neutralize dopants in HfO_x greatly stabilize the higher symmetry tetragonal and cubic structures of hafnium oxide.[73] Based on previous theoretical suggestions and photoelectron spectroscopic evidences of hafnium sub-oxides,[130, 152, 197] it is likely that the predominantly tetragonal HfO_x thin films are a mixture of major part oxygen vacancy stabilized *t*-HfO_{2-x} mixed with contributions from hcp-HfO_x, and sub-oxides. Figure 3.16(b) shows the optical appearance of the HfO_x thin films grown on sapphire substrates which are transparent under visible light to the alphabetic letters underneath at highest oxidation conditions. The HfO_x films turn gradually more greyish with reduced O/Hf ratio, indicative of the oxygen deficient nature of the hafnium oxide films similar according to an earlier study.[99] Post-exposure to ambient atmosphere, X-ray reflectivity (XRR) measurements were performed on the films grown on Al_2O_3 substrates. The onset of the critical angle for total reflection is plotted in Figure 3.16(c). With increasing oxidation conditions, the critical angle is found to consistently shift to lower angles, thus, indicating decreasing density of the HfO_x films. A more quantitative analysis was performed by refining the data using RCRefSim [175] as shown in Figure 3.16(d). The XRR data fitting of the highest oxidized film (#5) yielded a density of 9.4 g/cm^3 slightly lower the expected bulk density at stoichiometric conditions of 9.6 g/cm^3. The lower than bulk density is probably due to slight over stoichiometry in the as-grown films under high oxidation conditions. At lower oxidation conditions, the density is found to increase up to 12.12 g/cm^3 which is still considerably lower than the known density of Hf metal (13.3 g/cm^3). The wide tunability of density and the control of crystallization demonstrate the feasibility of oxygen stoichiometry engineering across the entire stoichiometry range of hafnium oxide using reactive MBE as the foundation of this study.

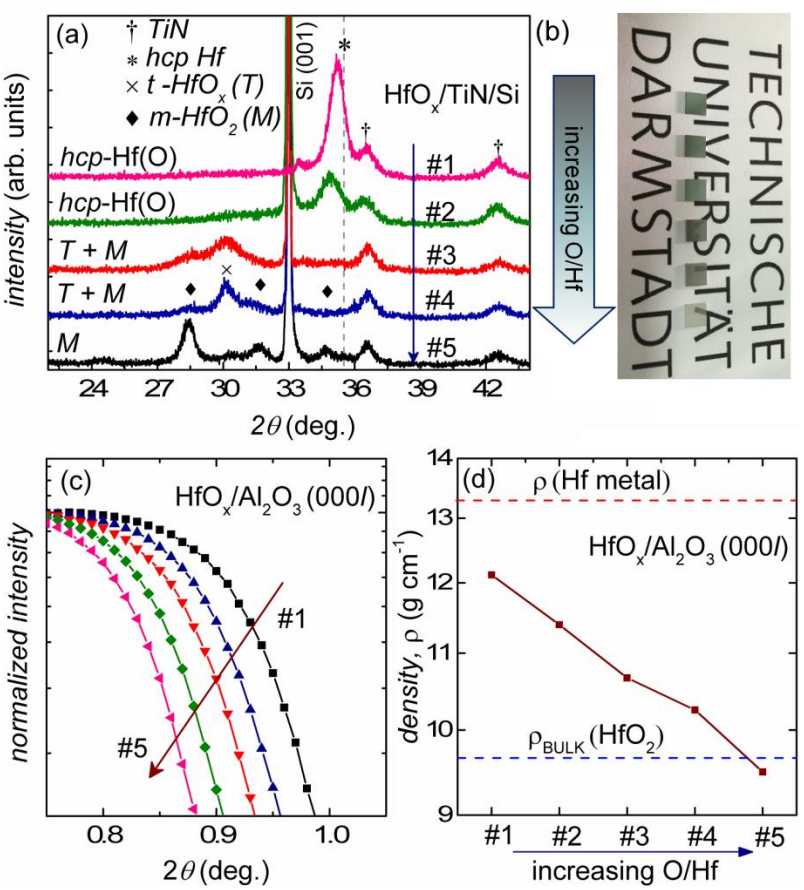

Figure 3.16: (a). X-ray diffraction patterns of 20 nm thick HfOx films grown at 320°C on TiN/Si electrodes under increasing (#1 - #5) oxidation conditions. (b) The image shows the optical appearance of 20 nm HfOx thin films grown simultaneously on sapphire substrates changing from a greyish (top) to transparent (bottom) film with increasing oxidation. (c) XRR measurements, showing the dependence of the critical angle on oxidation conditions of hafnium oxide films grown on sapphire substrates; (d) extracted density from XRR fitting vs. increasing oxidation conditions.

The thicknesses of the oxide layer in HfO_2/TiN device stack were obtained by fitting the grazing incidence X-ray reflectivity data using RCRefsim software. As shown in figure 3.17, XRR measurements of a device stack with aimed 20 nm thickness of hafnium oxide layer grown on polycrystalline TiN electrode typically results in oscillations up to 3°. A proper fit of the data gives good estimations of the thickness with an error of < 0.25 nm. The roughness estimates given by XRR fitting indicate a surface rms roughness of 1.83 nm and an interface roughness of 1.54 nm. The surface and interface rms roughness of all the oxide layers in the device stacks obtained in this study is less than 2 nm. It must be noted that XRR fitting gives macroscopic roughness and values may have significant discrepancies compared to actual roughness as measured by AFM, and thus have to be considered carefully if taken to be the actual roughness. Also, it was usually observed that the error in the XRR fitted roughness values may be significantly high, when multiple layers are considered for fitting. The discrepancies which might arise in XRR fitted roughness is reported in literature,[198] where the error is found to be lower for very smooth surfaces or interfaces.

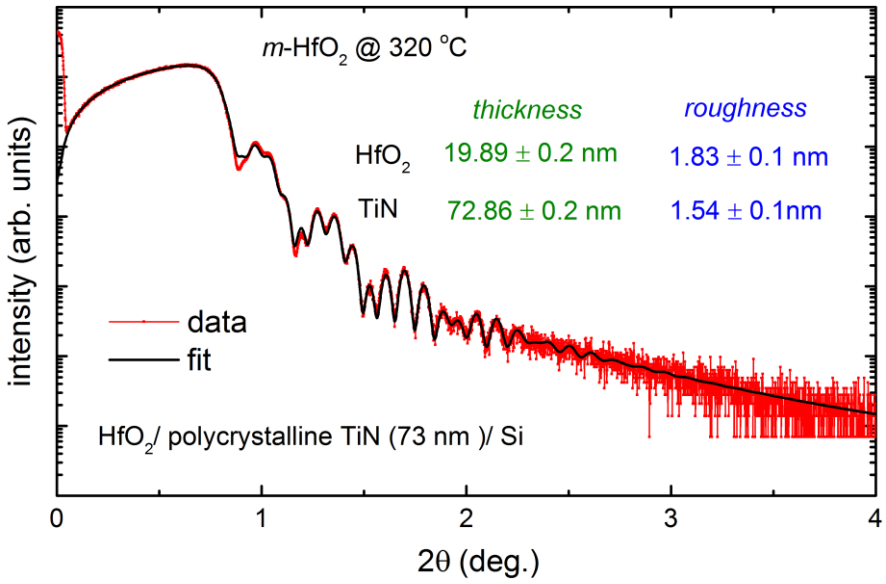

Figure 3.17: Typical XRR data and fitting of hafnium oxide thin film grown on TiN thin film electrodes

Growth was further performed on epitaxial TiN(111) thin films grown on Al_2O_3 (0001) substrates. Figure 3.18(a) shows the XRD pattern of 40 nm hafnium oxide films grown on epitaxial TiN(111)/ Al_2O_3 (0001) stack at 320°C, at close to oxygen deficient conditions. The growth parameters employed for the stoichiometric films were constant hafnium evaporation rate of 1.0 Å/s and 350 W RF power. The oxygen flow was changed form 0.16 sccm to 0.2 to 0.4 sccm, using the discharge tube (DT #1). As seen in the XRD pattern, at the lowest flow rate the predominant peak at $2\theta = 30.72^{o}$ is shifted to higher angles from the expected (101) peak position for the tetragonal phase at 30.3^{o}. This might be due the highly oxygen deficient nature of the film, leading to a compression in the lattice. It is to be noted that the peak is very broad which could be attributed to the formation of nano-crystalline grains. Therefore, in addition to oxygen vacancies, the smaller grain sizes also likely plays a role in stabilizing the tetragonal phases of hafnium oxide, as already reported in literature. The broad feature at lower angles (~28.3) and the background observed at higher angles (~34-35^{o}) can be attributed to the sum contribution of multiple broadened peaks of the monoclinic (-111,111, 200, 020 and 200) and tetragonal phase (110). At increased oxygen flow of 0.2 sccm, the XRD pattern remains relatively unchanged. However, at the highest oxygen flow of 0.4 sccm, the contribution from the tetragonal peak intensity is found to diminish and (-111) peak of the monoclinic phase appears as the strongest peak. Further increase on the oxygen flow rates lead to the formation of a purely monoclinic phase, as expected (not shown). Figure 3.18(b) shows the RHEED pattern of the TiN (111) films. Interestingly, the RHEED pattern of an as-grown film oxygen deficient (15 nm thickness) with dominant tetragonal-like phase (0.2 sccm) exhibited broad streaky features. This streaky pattern suggests the presence of preferential orientation of tetragonal phase. However, the diffused background intensity

suggest a low crystallinity, likely arising from the nano-crystalline monoclinic phase which is additionally present. At higher thicknesses, (> 20 nm) it was found that the diffused streaks were found to change to a spotty pattern with appearance of additional rings. As for the 15 nm hafnium oxide film grown at higher oxidation conditions with a predominantly monoclinic phase, the RHEED pattern exhibited multiple spots, suggesting the presence of grain texture. It can be concluded that, tetragonal phase of hafnium oxide can be stabilized at lower oxidation conditions and a substrate temperature of 320°C irrespective of the crystallinity of the TiN substrate.

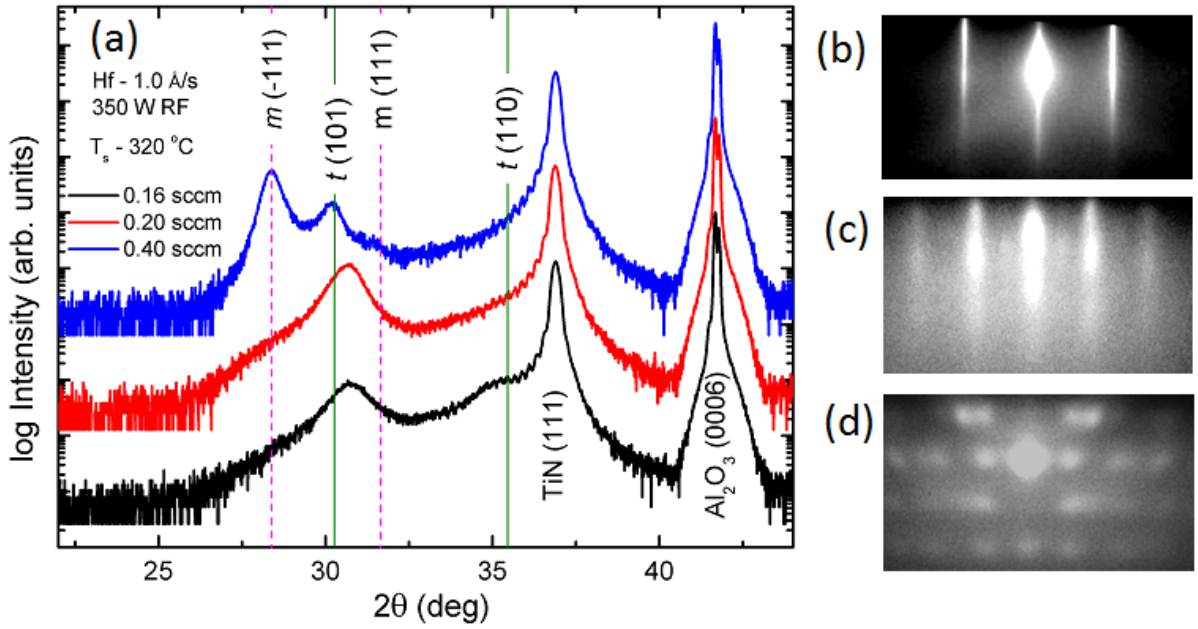

Figure 3.18: (a) XRD pattern of as-grown thin films with a thickness of ~ 40 nm on HfO_2 epitaxial TiN(111) films, with varying oxidation conditons (0.16, 0.2,0.4 sccm) at 350 W RF power. Hf evaporation rate of 1.0 Å/s as well as temperature (320°C) were maintained constant; RHEED pattern of the TiN (111) film along [11-20] azimuth of *c*-plane sapphire (b), as well as the hafnium oxide films (15 nm) grown undere oxygen deficient (c) and stoichiometric (d) conditions are additionally shown.

3.2.2. Effect of temperature and RF power

Figure 3.19(a) and 3.19(b) illustrates the XRD patterns of stoichiometric hafnium oxide films grown on polycrystalline TiN at 320 °C and RT, respectively. The growth parameters employed for these stoichiometric films were hafnium evaporation rate of 0.2 Å/s with oxygen flow of 1 sccm and 200W RF power, using the discharge tube (DT #1). The absence of any characteristic reflections of HfO_2 in the XRD pattern indicates that the films grown at RT are amorphous whereas the HfO_2 films deposited at 320°C are polycrystalline and belong to the monoclinic symmetry. Hafnium oxide growth was further performed on epitaxial TiN(001) thin films grown on Si (001) substrates. Figures 3.19(c) and 3.19€ shows the XRD pattern of oxygen deficient and stoichiometric hafnium oxide films, respectively, grown on epitaxial TiN(001)/Si(001) stack at 320°C. Here, the oxygen deficient films were

grown at a Hf rate of 0.7 Å/s, an oxygen flow of 0.2 sccm and 350W RF power. The crystallization remained similar to growth on polycrystalline TiN as well as epitaxial TiN(111), where the stoichiometric hafnium oxide films crystallize in a monoclinic symmetry and the oxygen deficient hafnium oxide films grown showed a tetragonal like phase of hafnium oxide. The phase formation under oxygen deficient conditions was found to be controllable with the applied RF power. The films grown at lower RF power (250W) and same oxygen flow rate (0.2 sccm) resulted in a mixed tetragonal-like and monoclinic phases, as shown in figure 3.19(d).

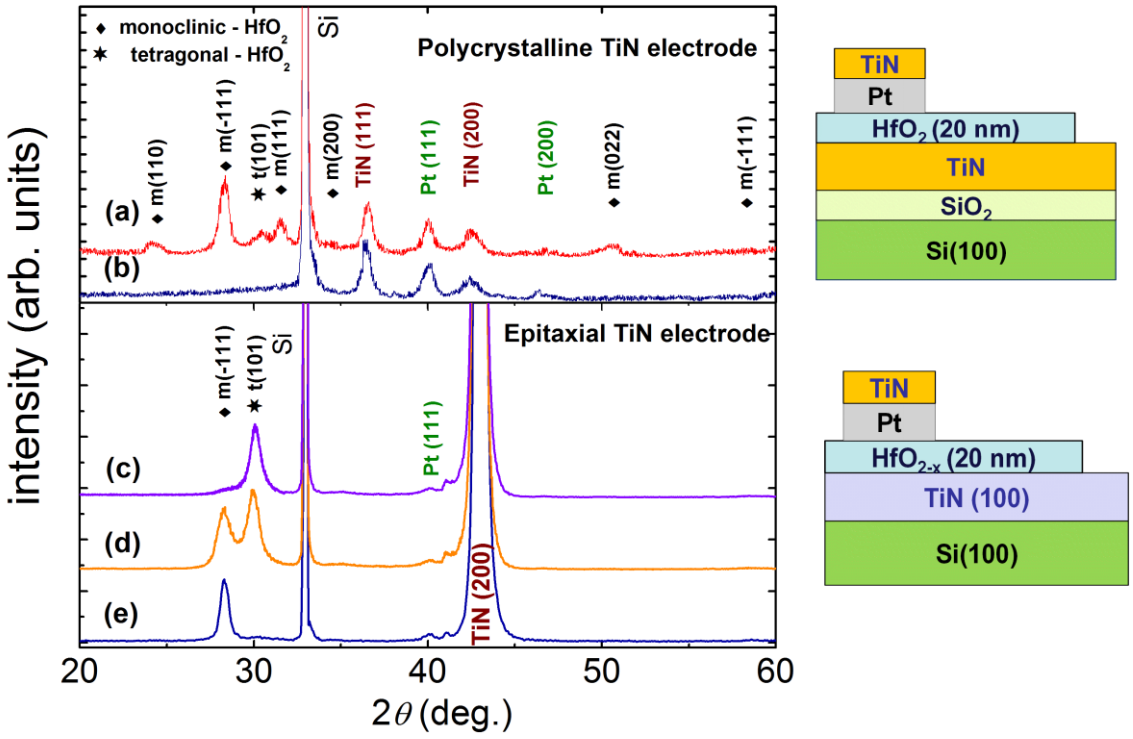

Figure 3.19: X-ray diffraction pattern of Pt/HfO_2(20 nm)/TiN//Si stack. HfO_2 films were deposited on polycrystalline TiN substrates at (a) Room temperature (amorphous HfO_2) and (b) 320°C (polycrystalline HfO_2). Oxygen deficient HfO_x films were grown at 320°C on epitaxial TiN substrate at Hf evaporation rate = 0.7Å/s and 0.2 sccm flow at RF powers of (c) 350 W (*t*-HfO_x) and (b) 250 W (mixed phase). Stoichiometric HfO_2 shows a monoclinic symmetry (e) at deposition conditions of 0.2Å/s Hf rate and 1 sccm oxygen flow at 250 W RF power.

Figure 3.20(a) illustrates the impact of higher temperature on the phase formation of oxygen deficient hafnium oxide films grown on TiN (111) films. The growth parameters employed for these oxygen deficient thin films were hafnium evaporation rate of 1.0 Å/s and an oxygen flow of 0.2 sccm (using DT #1) and 350W RF power, suitable for crystallization in the predominantly tetragonal phase at 320 °C. At higher substrate temperatures (420 °C and 520 °C), it is found that crystallization in the monoclinic phase is favored. At 420 °C, a mixed tetragonal and monoclinic phase is observed, whereas at 420 °C the films already crystallize in the monoclinic-HfO_{2-x} phase. Also, under similar growth conditions, Hildebrandt *et al.* previously reported that the growth of oxygen deficient hafnium oxide thin films at

temperatures as high as 700 °C resulted in oxygen deficient monoclinic phase of HfO_{2-x}.[199] At higher temperatures, thermodynamics can be understood to increase the reaction between oxygen and hafnium as well as lead formation of larger grains, thereby favoring crystallization in the monoclinic phase. Based on the XRD results, an empirical phase diagram (figure 3.20(b)) can be suggested to account for the different observations of crystallization in oxygen deficient hafnium oxide. Formation of metallic *hcp*-Hf is at extremely low oxidation conditions (typically HfO_x, $x<0.5$) is not represented. It is clear that the tetagonal-HfO_{2-x} phase is formed at lower oxidation conditions and lower growth temperatures (close to 320°C). At very low temperatures close to room temperature, amorphous hafnium oxide is formed. Intermediate growth temperature and oxidation conditions lead to the formation of mixed tetragonal and monoclinic structures.

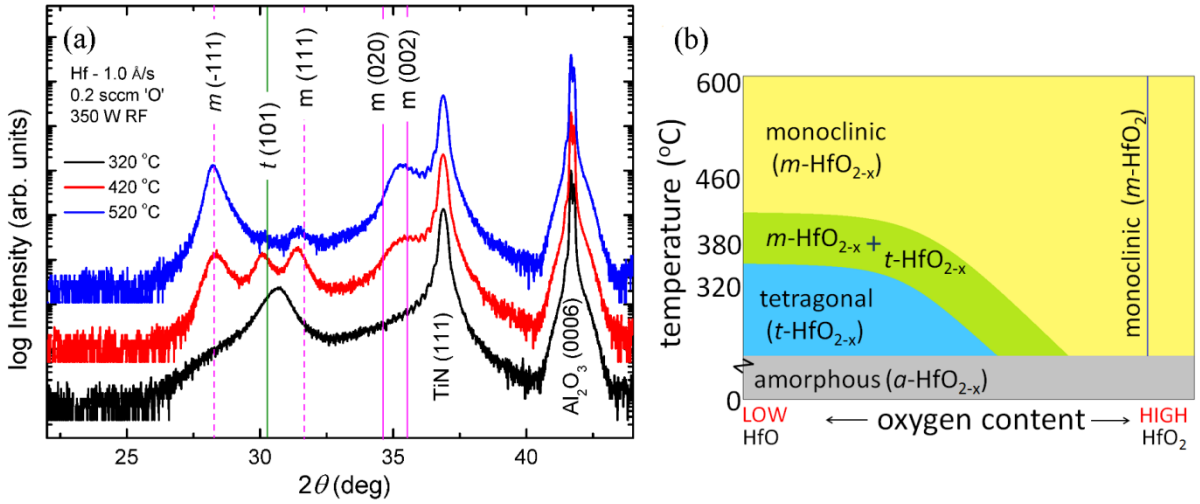

Figure 3.20: (a) XRD pattern of as-grown oxygen deficient hafnium oxide thin films with a thickness of ~ 40 nm on epitaxial TiN(111) films at different growth temperatures (320, 420 and 520 °C). The deposition parameters were maintained constant at 0.2 sccm oxygen flow,350 W RF power and Hf evaporation rate of 1.0 Å/s . (b) Phase diagram of the Hf-O showing crystallization under different temperatures and oxidation conditions.

3.2.3. Effect of oxide thickness

The impact of oxide thickness on crystallization in hafnium oxide films grown on polycrystalline TiN as well as epitaxial TiN (111) films were further investigated by XRD. The oxidation conditions for stoichiometric monoclinic phase and the tetragonal oxygen deficient phases were chosen for comparison. The growth parameters employed for the growth of stoichiometric monoclinic-HfO_2 films was hafnium evaporation rate of 0.2 Å/s with oxygen flow of 1.0 sccm and 200W RF power, whereas oxygen deficient tetragonal-HfO_x films were grown at a Hf flux of 1.0 Å/s, an oxygen flow of 0.2 sccm and 350 W RF power.

XRD patterns obtained for a typical stoichiometric and oxygen deficient hafnium oxide films grown on TiN (111) for increasing thicknesses from 10 nm to 200 nm are depicted in

figures 3.21(a) and 3.21(b), respectively. In case of oxygen deficient films with thicknesses greater than 20 nm, a predominantly tetragonal like peak at ~30.72 was observed. At the lowest oxide thickness of 10 nm, the broad peak at ~28.3 ° corresponding to nano-crystalline grains of the monoclinic phase was found to be more dominant. This corresponds to a diffused streaky RHEED pattern as observed initially for lower oxide thicknesses (<20 nm) as shown in figure 3.18(c), which transforms to a more spotty pattern with rings at higher thickness. It can be assumed that the strain arising from the TiN(111) films play a role in stabilizing the monoclinic phase at lower thicknesses. In case of growth under stoichiometric conditions, the XRD patterns indicate crystallization in the monoclinic symmetry with different orientations of the grains. The monoclinic phase was found to stable for thicknesses upto 200 nm.

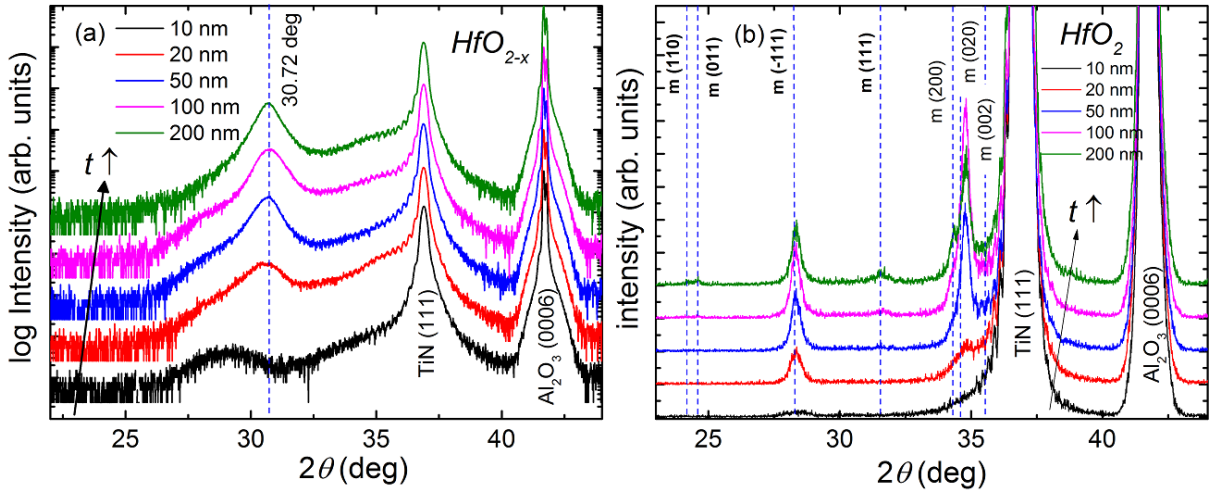

Figure 3.21: XRD pattern of as-grown (a) oxygen deficient and (b) stoichiometric hafnium oxide thin films on epitaxial TiN(111) films with increasing thicknesses from 10 nm to 200 nm. The deposition for both the of films were performed at 320 °C, however at different oxidation conditions to achieve stoichiometric and oxygen deficient films.

The XRD patterns obtained for a typical stoichiometric and oxygen deficient film grown at same conditions on polycrystalline TiN for thicknesses of 200 nm are depicted in figure 3.22(a). Similar to growth on TiN(111), the tetragonal-HfO_x structure stabilized at lower oxidation conditions and lower growth temperatures (320 °C) are observed to be unaltered even up to higher film thicknesses of about 200 nm. Interestingly, the maximum of peak position is located at ~30.35° which is closer to the (101) peak position of the tetragonal phase. The corresponding bright-field TEM images of the stoichiometric *m*-HfO_2 (right) and oxygen deficient *t* -HfO_x (left) films grown on polycrystalline TiN is shown in figure 3.21(b). Both the films have clearly demarcated interfaces, suggesting the formation of well-defined films at 320 °C. The *m*-HfO_2 film shows grains with different orientations, which are found to exhibit grain orientations similar to the TiN film beneath suggesting a transfer of texture from

TiN film to the *m*-HfO_2 film. On the other hand, *t*-HfO_x appeared to be darker due to higher concentration of heavier hafnium atoms. Grain orientation in *t*-HfOx film was not as clearly visible in comparison to *m*-HfO_2, possibly due to nano-crystalline nature of the grains.

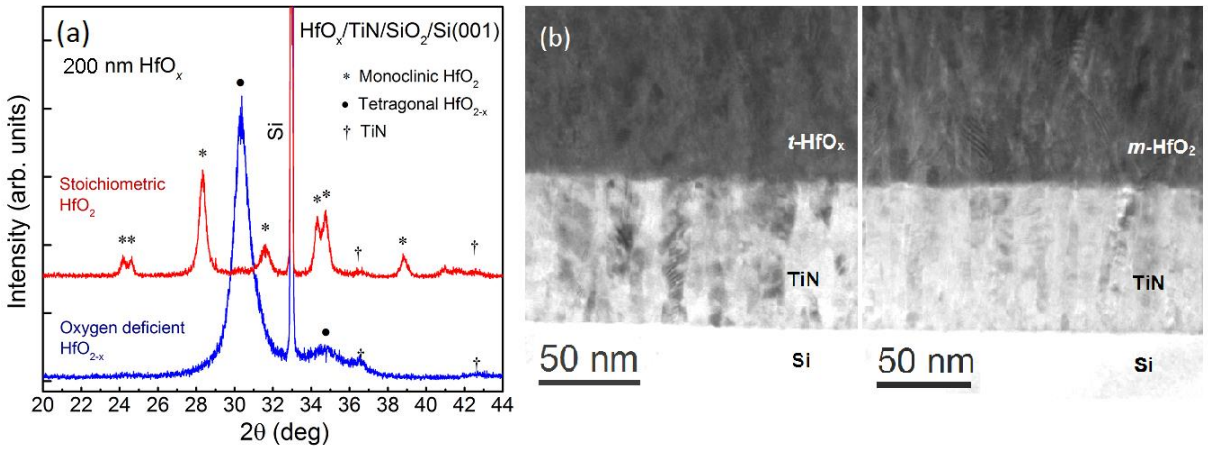

Figure 3.22: (a) 2θ-θ X-ray diffraction patterns of HfO_2 (200 nm)/TiN/SiO_2//Si stack films grown at 320 °C: (top) stoichiometric *m*-HfO_2 and (bottom) oxygen deficient *t* -HfO_x. (b) Bright-field TEM images of the stoichiometric *m*-HfO_2 (right) and oxygen deficient *t* -HfO_x (left) films grown on polycrystalline TiN.

3.2.4. Monoclinic - HfO_2 vs Tetragonal - HfO_x

Electrical characterization of Pt/HfO_x/TiN devices was performed with focus on polycrystalline films with a clear difference in stoichiometry and crystal structure. This was expected to allow a clear demarcation of the effects of oxygen deficiency on the resistive switching behavior. Keeping this in mind, stoichiometric monoclinic-HfO_2 (*m*-HfO_2) and oxygen deficient tetragonal-HfO_x (*t*-HfO_x) were further characterized by TEM and XPS. Here, hafnium oxide thin films grown on polycrystalline titanium nitride substrates at 320 °C were considered.

In order to quantify the stoichiometry of the HfO_x samples, STEM-EDS measurements were performed to compare the stoichiometric *m*-HfO_2 and oxygen deficient *t*-HfO_x thin films. Figure 3.23(a) 3.23(b) show *Z*-contrast scanning transmission electron microscopy (STEM) images and corresponding spatially-resolved STEM-EDS maps of 100 nm thick (c) *t*-HfO_x and (d) *m*-HfO_2 films grown on TiN/Si. Both films are polycrystalline, but compared to *m*-HfO_2, we observe a smaller grain size and sharper interface in the *t*-HfO_x film, suggesting negligible oxidation of titanium nitride due to the reduced oxygen flow rates during growth of *t*-HfO_x. The STEM-EDS elemental maps are color-coded as RGB images corresponding to red (Hf-M), blue (O-K), green (Ti-K). The quantification of the O signal is usually very prone to systematic errors and noise, making the quantification of light elements very demanding. Therefore, we recalibrated the results assuming an O/Hf ratio of 2 for the stoichiometric *m*-HfO_2 layer. The

weighted average of the O/Hf ratio of the non-stoichiometric *t*-HfO_x layer obtained in this way is 1.6. Even though the statistical error is lower, we estimate this result to be only correct within 10% due to systematic errors. The results were also found to be in close agreement with the stoichiometry of 1.5 obtained from electron energy loss spectroscopy (EELS) based quantification.[200]

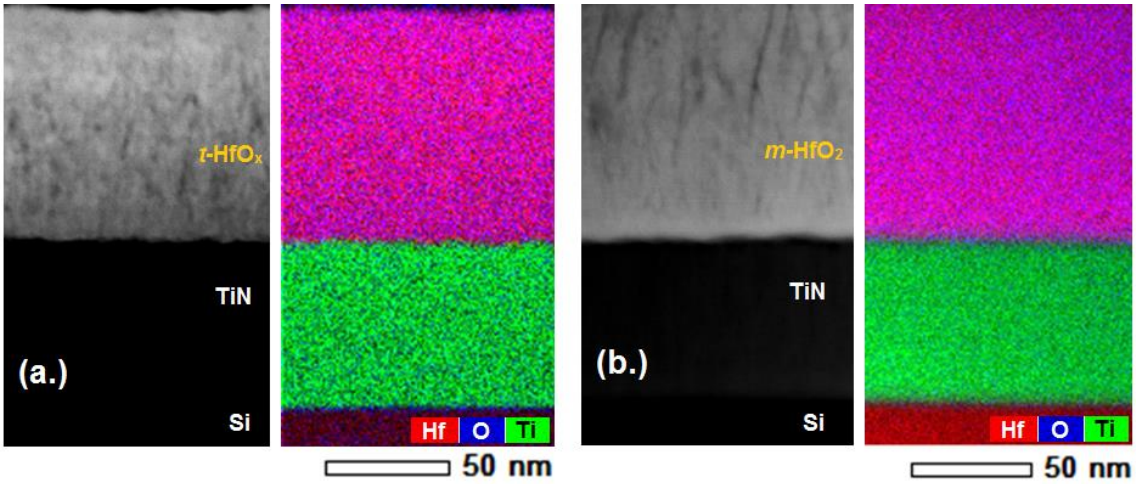

.

Figure 3.23: Z-contrast images and corresponding spatially-resolved STEM-EDS maps of 100 nm thick *t*-HfO_x (a) and *m*-HfO_2 (b) films grown on TiN/Si.

The stoichiometric *m*-HfO_2 and oxygen deficient *t*-HfO_x thin films with thicknesses of about 20 nm were then analyzed by HAXPES, which allows probing the bulk of the film. Photoelectrons were excited at photon energy of 8 *k*eV and the energy was calibrated with respect to $4f_{7/2}$ signal from a gold reference sample. The bottom electrodes are grounded to minimize charging effect. The Hf *4f* signals were compared for stoichiometric and deficient samples as shown in figure 3.24(a) and 3.24(b), respectively. There were considerable differences observed in the spectra. For peak deconvolution, Shirley background was removed from both the spectra and the oxide related peaks were modeled with Gaussian-Lorentzian peak functions. The metallic hafnium peak was however modeled based on Doniac-Sunjic function. The intensity ratio of the components of the Hf *4f* doublet and the spin-orbit splitting were fixed at 0.75 and 1.67 eV respectively. The stoichiometric sample was fitted with a single peak attributed to Hf^{4+} state of full width at half maximum (FWHM) = 1.08 eV and a spin orbit splitting of 1.67 eV. In comparison, the deficient samples could only be fitted with three different peaks attributed to full oxide (Hf^{4+}), a sub-oxide (Hf^{x+}) and metallic hafnium (Hf^0). The peak with the highest binding energy Hf^{4+} and the metallic state $Hf^{(0)}$ were fitted with $4f_{7/2}$ binding energies of 17.73eV and 14.22 eV respectively with corresponding FWHM's being 1.31 eV and 0.92 eV. These were in agreement with the previously reported values of 17.93 eV and 14.31 eV respectively.[197] The increase in FWHM

of the full oxide peak could be due to the presence of higher degree of disorder in the deficient films or as a result of coexistence of monoclinic and tetragonal phases with small differences in binding energy. A satisfactory fit could only be obtained considering the presence of a sub-oxide peak of binding energy 15.65 eV. The chemical shift for the sub-oxide (Hf^{X+}) peak was 1.23 eV in comparison to 1.19eV obtained before in the study of hafnium metal oxidation. [127] The sub-oxide could be attributed to the theoretically predicted semi-metallic Hf_2O_3[130] which might be responsible for oxygen deficient conducting filaments in resistive switching. The valence band spectra for the stoichiometric and oxygen deficient films are shown in figures 3.24(c) and 3.24(d), respectively. The presence of extra defect states in the valence band spectra near the Fermi level were observed in oxygen deficient hafnium oxide films in comparison to the stoichiometric film. This could also be indicative of the oxygen vacancy stabilized defect states as proposed previously in literature.[98, 100, 201]

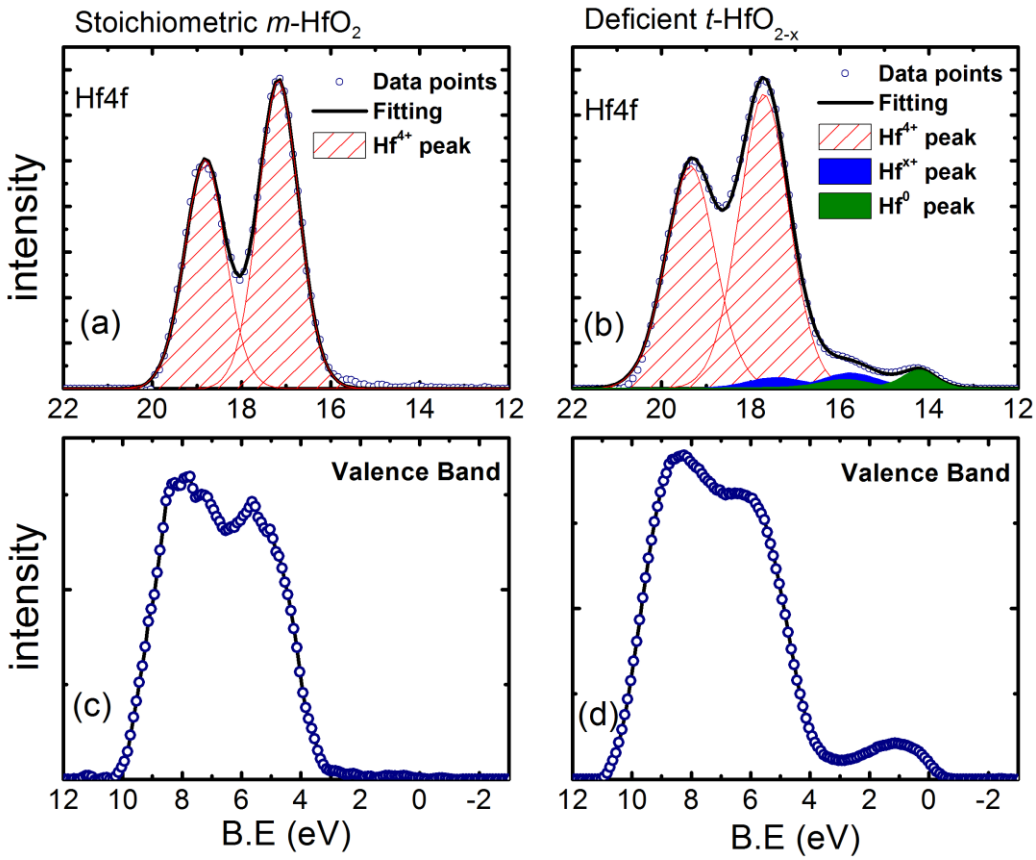

Figure 3.24: Hf*4f* HAXPES spectra of as- prepared hafnium oxide thin films under (a) stoichiometric and (b) oxygen deficient conditions. The corresponding valence band spectra are plotted below as (c) and (d).

The films were further characterized using laboratory based XPS to obtain information regarding the surface region. The oxygen deficient films were exposed to ambient conditions after deposition, raising the scenario of oxidation at the surface. In order to verify this scenario, we have carried out angle dependent XPS of stoichiometric and oxygen deficient

samples. The binding energies were calibrated with respect to C 1s peak value of 284.6 eV. Electron and Ar cation irradiation was used to minimize charging effect by neutralization of the surface. Initially, the 20 nm thick films of *m*-HfO_2 and *t*-HfO_x were characterized using XPS at photoelectron take-off angle of 75 degrees. The Hf 4*f* and valence band spectra obtained were compared for stoichiometric *m*-HfO_2 and oxygen deficient *t*-HfO_x films after removing a Shirley background. The Hf 4*f* spectrum for both stoichiometric and oxygen deficient thin films was similar to that obtained using HAXPES and is not shown. Figure 3.25(a) illustrates the valence band (VB) spectra of *m*-HfO_2 and *t*-HfO_{2-x} films acquired at an angle of 75°. The VB spectra acquired at 75° take-off angle shows the appearance of a defect band near the Fermi level in *t*-HfO_x (absent in m-HfO_2) suggesting the presence of a conducting matrix in the film. However, in-plane conductivity could not be observed on the surface of the *t*-HfO_x film by direct two probe contact method after exposure to ambient conditions. Therefore, 20 nm thick *t*-HfO_x films were further analyzed by angle dependent XPS at photoelectron take-off angles of 20°, 45° and 75°. , as shown in figure 3.25(b). In comparison to defect band observed in the VB spectra at 75 degrees, these states were found to reduce (45°) and disappear at 20 degree (i.e. towards the surface). This confirms the presence of an oxidized surface layer on *t*-HfO_x films, which is expected to affect the electroforming characteristics, which will be discussed in the next chapter. The inelastic mean free path (λ) of valence band photoelectrons is determined to be 2.2 nm using TPP-2M equation.[179] Therefore, the escape depth ($3\lambda.\sin\varphi$) of valence band photoelectrons at probing angles (φ) of 45° and 20° can be determined as 4.6 and 2.2 nm, respectively. The oxidized layer thickness can therefore be estimated to be < 4 nm. The results suggest that the top electrode should be deposited without breaking vacuum after the deposition of oxygen deficient hafnium oxide. However, patterning of such devices requires etching process in combination with lithography, for which equipment was not available and is envisioned in the near future.

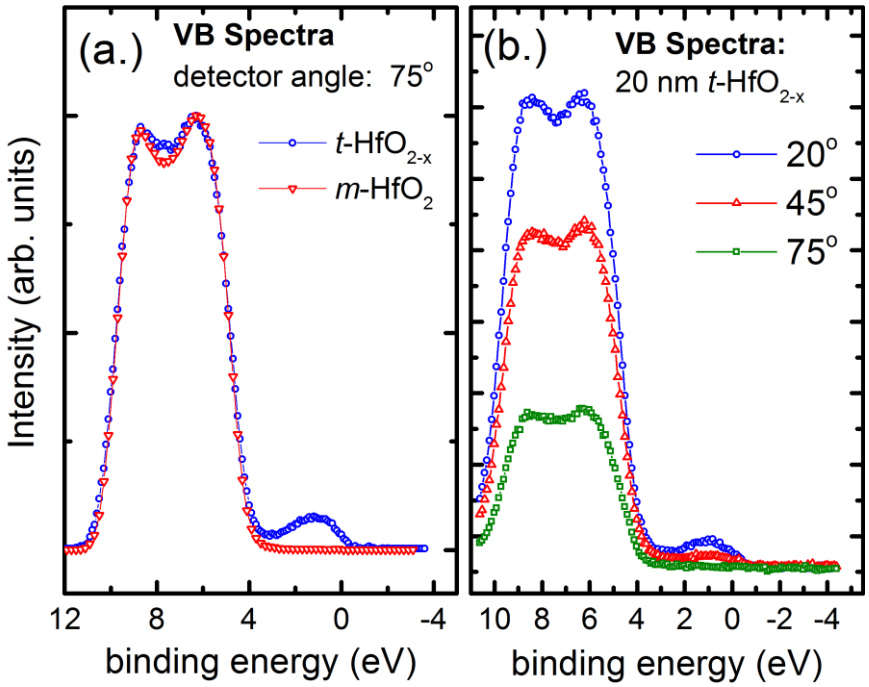

Figure 3.25: (a) Valence band (VB) spectra of *m*-HfO_2 and *t*-HfO_{2-x} films acquired at an angle of 75° (b) Angle dependence XPS of valence band of *t*-HfO_{2-x} thin films with 20 nm thicknesses obtained at photoelectron take-of angles of 75, 45 and 20 degrees.

3.3. Oxygen engineering in amorphous TaO_x thin films

Similar to oxidation study in hafnium oxide, oxidation stoichiometry engineering was also performed for Ta-O system with multiple objectives. First, TaO_x is also an attractive choice of insulator in RRAM devices and has been widely investigated. In this study, both TaO_x and HfO_x have been studied and compared in Pt/metal oxide/TiN device configuration. This was expected to enable further understanding of the influence of oxygen stoichiometry in general. Second, tantalum was envisioned to study the impact of pentavalent doping in hafnium oxide. For this, oxidation parameters required for oxidation of Ta metal had to be established for further co-evaporation of Hf and Ta metals by MBE.

The tantalum oxide films were deposited at various oxidation conditions on polycrystalline titanium nitride and *c*-cut sapphire substrates by varying the oxygen flow rate (0.2 to 2.5 sccm) while maintaining the RF power (applied to the radical source) constant at 350 W. Ta evaporation rate was also maintained constant at 0.15 Å/s. The substrate was heated to 440 °C. The absence of any peaks related to the oxide in XRD pattern (not shown) suggested the formation of amorphous TaO_x thin films, irrespective of the oxygen stoichiometry. This is consistent with the high temperature (> 850 °C) which has been reported to obtain crystalline tantalum pentoxide. [202] First, we consider tantalum oxide thin films with thicknesses of nearly 21 nm grown initially on *c*-cut sapphire substrates. Similar to HfO_x, transparent films were obtained at 2.5 sccm oxygen flow rate which gradually turned

greyish at lower oxygen flow rates (down to 0.2 sccm). It has to be noted that at similar evaporation rate of Hf (0.15 Å/s), much lower oxidation conditions (0.8 sccm oxygen flow at 200 W RF power) was sufficient to obtain stoichiometric or high band-gap transparent films of hafnium oxide.

Grazing incidence XRR measurements were further performed to estimate the density and thicknesses of the as-grown films on sapphire after exposure to ambient. Further analysis was performed by simulating and fitting of the data using RCRefSim.[175] Figure 26(a) and 26(b) shows the XRR data and simulated fitting for the films grown at 2.5 sccm and 1.5 sccm, respectively. The XRR data of the highest oxidized film (2.5 sccm) could be fitted with a single layer of $Ta_2O_{5-\delta}$. Whereas, appropriate fitting of the XRR data at lower flows could only be performed assuming an additional oxidized surface layer as shown for 1.5 sccm. At 2.5 sccm, a thickness and density values of 21 nm and 9.0 gm/cm^3 were obtained, respectively. The density of the visibly transparent films is found to be more than the bulk density of 8.2 gm/cm^3 of Ta_2O_5. This implies a slight sub-stoichiometry of these films, even though a surface oxidation layer could not be detected due to the vanishing electronic density difference probed by XRR. In contrast, at lower oxygen flows, the data was simulated assuming a configuration of Ta_2O_{5-y}/TaO_x /Al_2O_3 where Ta_2O_{5-y} is considered to be the surface oxidation passivation on the as deposited TaO_x post exposure to the ambient. The densities obtained for the TaO_x layer as well as the thickness of surface oxidized layer are shown in figure 26c. The density of the films is found to increase from 9.0 up to 12.4 gm/cm^3 on decreasing the oxygen flow. At 0.2 sccm, the obtained density of 12.4 gm/cm^3 is considerably lower than the density of tantalum metal (16.6 gm/ cm^3). The oxidized surface layer of Ta_2O_{5-y} was fit with a constant density of 8.2 gm/ cm$^{3.}$ Thickness of the surface $Ta_2O_{5-\delta}$ layer was found to decrease from 1.2 nm (at 0.2 sccm) to 0.46 nm (at 2.0 sccm). This is less than the typical surface oxidation observed of less than 20 Å for tantalum metal at low temperatures, as also described by the Cabrera-Mott theory of oxidation.[203] An *ex-situ* annealing step of the TaO_x films at 440 ^oC under ambient conditions for 2h reduced the density to the bulk value of 8.2 gm/ cm^3 and thus fully oxidized the films to stoichiometric Ta_2O_5.

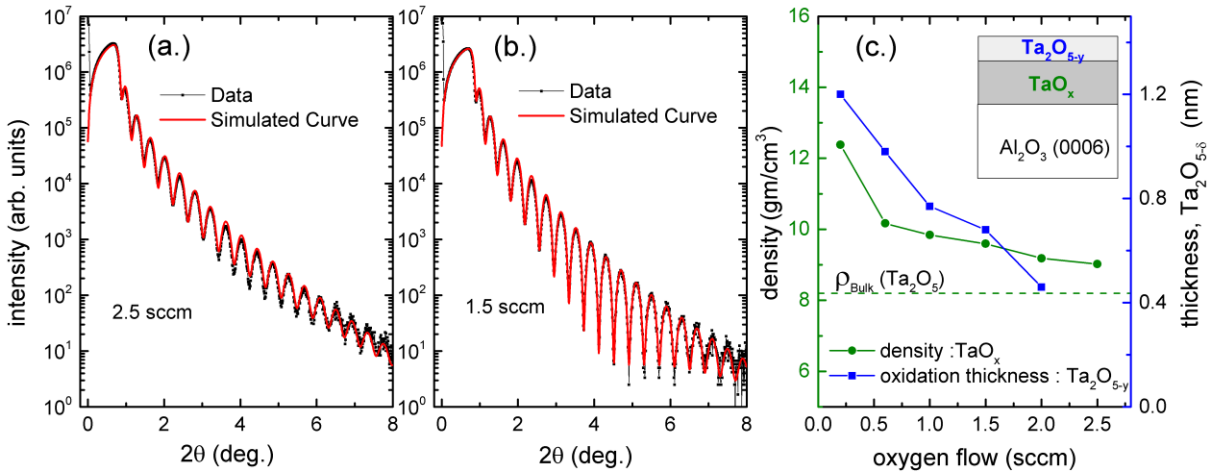

Figure 3.26: XRR data and simulation post exposure to ambience under the deposition conditions of (a) 2.5 sccm and (b) 1.5 sccm. (c) The density of the as deposited TaO_x films and corresponding surface oxidation thickness under ambience, Ta_2O_{5-y} (as depicted in the inset) under different deposition conditions.

The tantalum oxide layers of Ta_2O_{5-y} (2.5 sccm) and Ta_2O_{5-y}/ TaO_x (0.2 sccm) grown on polycrystalline TiN electrode was further analyzed *ex-situ* by XPS. The inelastic mean free path ($\lambda\varphi$) of the photoelectrons in the valence band of Ta_2O_5 is calculated as 2.22 nm using TPP-2M equation[179], giving an escape depth of 6.4 nm ($3\lambda.\sin\varphi$) for the VB photoelectrons. The lower thicknesses (t < 1.3 nm) of oxidized layer (determined by XRR) compared to the escape depth allows probing of the bulk TaO_x as well as the interface of the oxidized Ta_2O_{5-y} and the TaO_x. The valence band spectra for the films obtained at 75° take–off angle is shown in figure 3.27(a). In comparison to the 2.5 sccm, we clearly see the appearance of conducting states near the Fermi level in the 0.2 sccm film. This is indicative of the nature of the conducting states of oxygen deficient TaO_x lying beneath the oxidized surface as expected in the visibly darker films. The Ta *4f* signals were further compared for the oxygen deficient Ta_2O_{5-y}/TaO_x stack (0.2 sccm) and the oxygen rich $Ta_2O_{5-\delta}$ (2.5 sccm) as shown in figure 3.27(b) and 3.27(c), respectively. There were considerable visible differences obtained in the Ta *4f* spectra. A systematic peak fitting procedure developed by Brumbach *et al.*[204] for the deconvolution of the Ta *4f* spectra found that the distribution of oxidation states can be different even with the same Ta/O stoichiometry. Keeping this in mind, this same procedure has been adopted for the fitting of the Ta 4f spectra. A Shirley background was removed from spectra and the higher oxidation and metallic peak were modeled with Gaussian-Lorentzian and asymmetric Gaussian-Lorentzian functions. The spectra were fitted considering the binding energies for the different oxidation states of Ta (5+, 4+, 3+, 2+, 1+ and metal) as 26.94, 25.64, 25, 23.7, 22.54 and 21.78 eV respectively. The full widths at half maxima of the peaks were fixed at 1.1 eV, 1.39 eV and 1 eV respectively for the Ta^{+5}, intermediate oxidation states and metallic peaks. This indicates the oxygen deficient nature of a bulk phase present

below the interface of the passivation layer. The higher FWHM of the intermediate oxidation states can be attributed to the lower crystallinity of these metastable oxides, which might exist as small clusters within the oxide. Other XPS studies of surface passivation of tantalum metal have conjectured similar observations of the presence of multivalent sub-stoichiometric oxides also suggesting island like clustering within a Ta_2O_5 layer.[205] In comparison, the 2.5 sccm stack was fitted with a Ta 4f doublet attributed to the oxidation states of +5, +4, +2, +1 and metal with highest contribution from the 5+ valence state corresponding to $Ta_2O_{5-\delta}$, also suggesting incomplete oxidation as indicated by the density. The inset of figure 3.27(c) shows the fitting at lower binding energies. These are also in agreement with the multiple states as observed in other literature.[206] The binding energy of the higher oxidation states were kept the same, whereas the binding energy of the metal peak was lowered to 21.42 eV, as has been constrained in Brumbach *et al*. This could be due to larger crystallite size of the Ta metal precipitates in oxygen deficient TaO_x, thus changing its local surrounding to become more metallic. Theoretically studies have suggested such a stable existence of metallic tantalum in the form of Ta-Ta dimer in highly oxygen deficient TaO_x films, thus also contributing to the conduction path within a conducting filament of the RRAM device.[207] In comparison, hafnium in oxygen deficient hafnium oxide thin films exhibits a much less pronounced tendency to form multiple intermediate valence states, where XPS fitting could be satisfactorily performed assuming just one intermediate state.

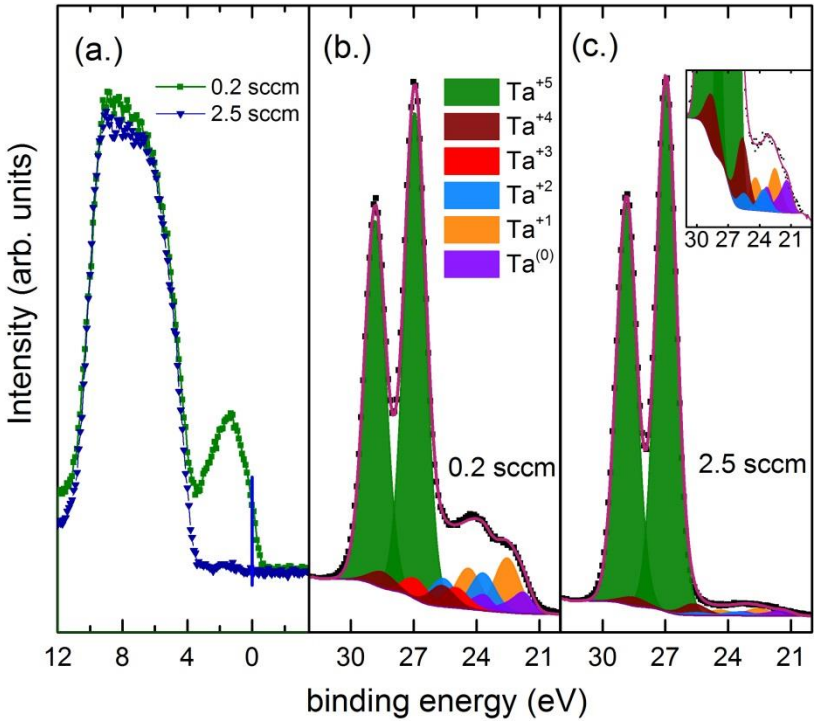

Figure 3.27: (a) XPS valence band spectra of TaO_x deposited at 0.2 sccm and 2.5 sccm. (b) Ta 4*f* XPS spectra of the as prepared TaO_x film on TiN/Si substrate at 0.2 sccm flow. (c) Ta 4*f* XPS spectra of the as prepared TaO_x film on TiN/Si substrate at 2.5 sccm flow. The inset shows enlarged region of the fit at lower binding energies).

3.4. Lanthanum and tantalum doping in HfO_x thin films

The growth of lanthanum doped hafnium oxide thin films was carried out by co-evaporation of hafnium and lanthanum on polycrystalline TiN as well as Y:ZrO_2(001) substrates. The evaporation rate of Hf was fixed 0.2 Å/s, while that of La was varied as 0, 0.015, 0.030, 0.045, 0.06 and 0.084 Å/s. The oxygen flow rate and the RF power (applied to the radical source) were fixed for all films at 1.2 sccm and 200 W respectively. The as-grown films with thicknesses of ~16 nm were deposited with the substrate temperatures maintained at 440 °C. Figure 3.28(a) illustrates the XRD patterns of La doped HfO_2 films grown on Y:ZrO_2(001) substrates. All the as-grown thin films with a thickness of ~ 16 nm showed only single peaks with observed Laue oscillations irrespective of the doping concentration. Then corresponding out-of-plane lattice constants are plotted vs the La/Hf evaporation rate ratio, as shown in figure 3.28(b). The undoped films are expected to crystallize in a monoclinic symmetry. However, the lattice constants of 5.227 Å doesn't correspond to any of the lattice constants of the monoclinic phase (*m*-HfO_2, $P2_1/a$) likely due to the presence of lattice strain. At a nominal lanthanum doping rate of 0.015 Å/s, the peak is found to shift to larger lattice spacing corresponding to expansion of the lattice due to the incorporation of the larger lanthanum atom. However, further increase of the rate to 0.03 Å/s lowered the lattice parameter to 5.149 Å. This is possibly due to a cubic structural transformation occurring due to the larger ionic radii dopant, when a threshold doping concentration is reached.[73] Further increase in La evaporation rates lead to a linear increase in the *c*-lattice constant, corresponding to a uniform expansion of the lattice. Figure 3.29 shows the RHEED pattern of the Y:ZrO_2(001) substrate and as-grown films at various lanthanum evaporation rates. The RHEED pattern is found to be streaky for undoped and nominally doped (0.015 Å/s) films, suggesting 2D growth of the films. At higher evaporation rates of lanthanum, the RHEED pattern was found to change to a spotty pattern corresponding to increased roughness due to 3D island like growth. This might be due to higher crystallization temperature typically required for lanthanum doped hafnium oxide, as reported in literature. It is expected that the 2D growth can be achieved at higher deposition temperatures. Nevertheless, the XRD results suggest that lanthanum is incorporated into the hafnium oxide crystal via substitutional doping. The trivalent lanthanum dopant is expected to create oxygen vacancies in the lattice for charge compensation.

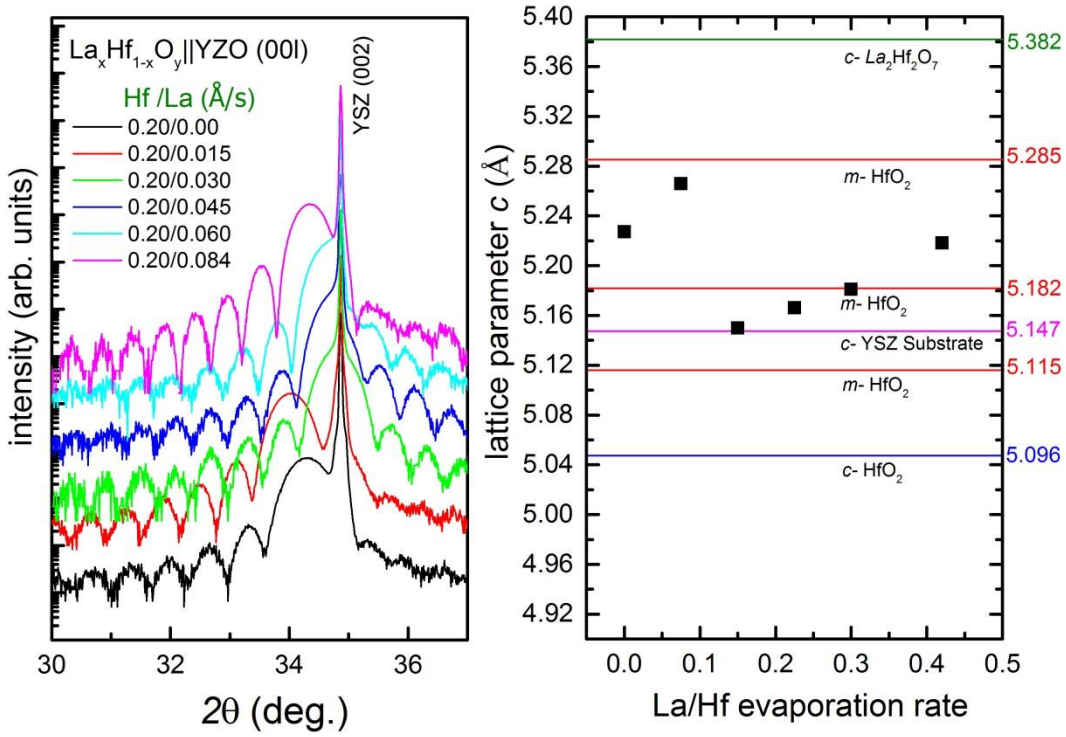

Figure 3.28: (a) XRD pattern of lanthanum doped hafnium oxide thin films grown on Y:ZrO_2(001)substrates at 440 °C , where Hf evaporation rate was fixed 0.2 Å/s, while that of La was varied as 0, 0.15, 0.30, 0.45, 0.6 and 0.84 Å/s. (b) Corresponding out of plane *c* - lattice constants obtained from the XRD pattern.

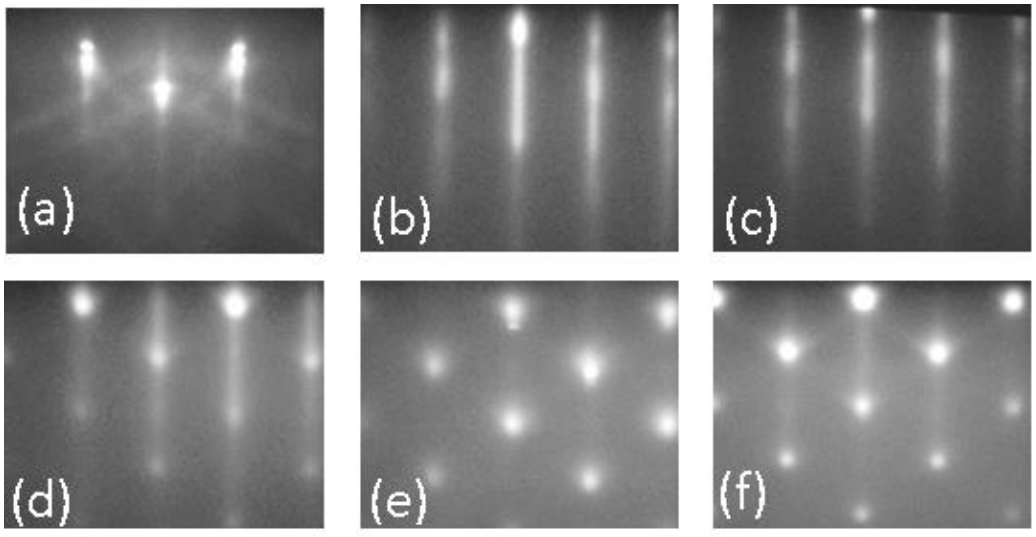

Figure 3.29: RHEED pattern of (a) Y:ZrO_2(001) substrates and as-grown lanthanum doped hafnium oxide films with lanthanum evaporation rates of (b) 0 Å/s , (c) 0.015 Å/s, (d) 0.030 Å/s, (e) 0.045 Å/s, and (d) 0.084 Å/s.

Figure 3.30 illustrates the XRD pattern of La doped HfO_2 films grown simultaneously on polycrystalline TiN/Si substrates. The TEM cross section of a film grown at La rate of 0.03 Å/s is shown in the inset of the figure. Non-doped films crystallize as expected in a monoclinic symmetry (*m*-HfO_2, $P2_1/a$) as proven by the (-111) reflection at 28.3°. At a nominal lanthanum doping rate of 0.015 Å/s, there is a peak appearing at higher angle corresponding

to a (111) reflection arising from a transition to cubic structure of hafnium oxide (*c*-HfO_2). This is consistent with the larger ionic radii of La^{3+} (1.1 Å) in comparison to Hf^{4+} (0.76 Å) and previous reports of cubic structural transformation on larger ionic radii dopants in HfO_2. Here, the oxygen vacancies induced by doping is known to play a stabilizing role in the cubic phase of hafnium oxide.[73] Interestingly, the cubic transition at nominal rate of 0.015 Å/s is unlike the growth on Y:ZrO_2(001) substrate, where the structure remained unchanged with only lattice expansion observed, possibly due to strain. Further increase in doping leads to a shift in peak position to lower angles due to further expansion of lattice. Vegard's law was applied to estimate the doping assuming a solid solution of cubic HfO_2 (fluorite, Fm-3m, a = 5.096 Å) and cubic La_2O_3 (bixbyite, Ia-3, a = 11.327 Å), since a fluorite MO_2 structure can be transformed to a bixbyite M_2O_3 structure by doubling of the unit cell and removing one-fourth the oxygen atoms along the intersecting <111> directions. Consequently, the doping concentration was estimated as 4.37, 7.07, 8.08, 12.12 and 18.18 % for La rates of 0.015, 0.03, 0.045, 0.06 and 0.084 Å/s, respectively from the peak positions.

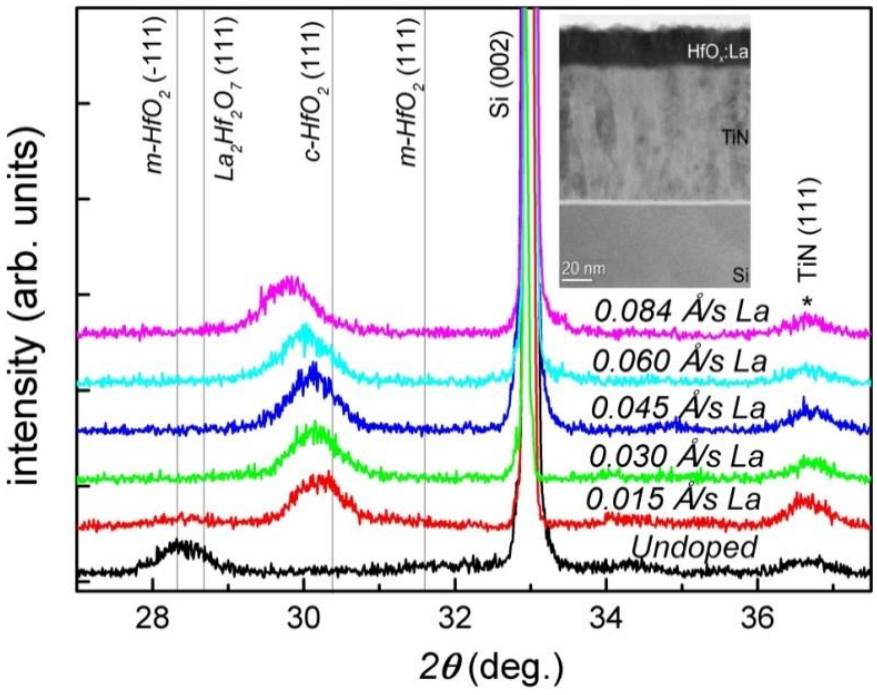

Figure 3.30: XRD pattern of lanthanum doped hafnium oxide films grown on polycrystalline TiN/Si(100) substrates at 440°C by increasing the la evaporation rates, keeping a constant Hf evaporation rate and oxidation conditions. Inset shows the bright filed TEM image of the film grown with La evaporation rate of 0.06 Å/s.

The films grown at lanthanum rates of 0, 0.03, and 0.084 Å/s on TiN electrodes were further analyzed by XPS *ex-situ*. The spectra (Hf 4f and La 3d) as shown in figure 3.30 were obtained at a take-off angle (φ) of 75°. The peak positions were corrected using adventitious carbon C1s peak at 284.8 eV. A Tougaard background was removed from the spectra and the peaks were modelled with Gaussian-Lorentzian function using the Casa-XPS software. Figure

3.30(a) shows the fitted peaks of the Hf 4f doublet with a spin-orbit splitting of 1.67 eV. The peaks were fitted with $4f_{7/2}$ binding energies of 17.95 eV corresponding to 4+ oxidation state of hafnium. The peak shifts which might arise due to doping were negligible falling within the instrument resolution (< 0.1 eV). However, the full widths at half maxima (FWHM) of the peaks were found to increase as 1.11 eV, 1.19 eV and 1.25 eV with increasing lanthanum concentration. The increase in FWHM of the full oxide peak could be due to the presence of higher degree of disorder in the oxide. The deconvolution of La 3d spectrum as shown in figure 3.30(b) were performed after subtraction of the superposing La $M_{4,5}N_{4,5}N_{4,5}$ Auger spectra as described by Sunding *et al.* using Mg K_α radiation.[208] The satellite components ($\underline{c}4f^1\underline{L}$ bonding and antibonding) in the residual spectra arise due to charge transfer to $4f^0$ orbital of core ionized lanthanum atom. The fitting was performed for La 3d spectrum with a spin-orbit splitting of 16.78 eV for the main peak ($\underline{c}4f^0$), satellite peaks ($\underline{c}4f^1\underline{L}$ bonding and antibonding) and plasmons. The obtained main peak ($\underline{c}4f^0$) position, separation from $\underline{c}4f^0$ to $\underline{c}4f^1\underline{L}$ bonding satellite and separation from $\underline{c}4f^1\underline{L}$ bonding to anti bonding peak were 834.1 eV, 4.87 eV and 3.4 eV respectively and for both doping concentrations. The FWHM of the main and satellite peaks however increased by about 0.1 eV. Further quantification of lanthanum from the area of the peaks resulted in lanthanum concentration of 0 %, 7.8 % (0.03 Å/s) and 17.4 % (0.084 Å/s) with in an error of up to 15-20%, which are in reasonable agreement with the estimation using Vegard's law.

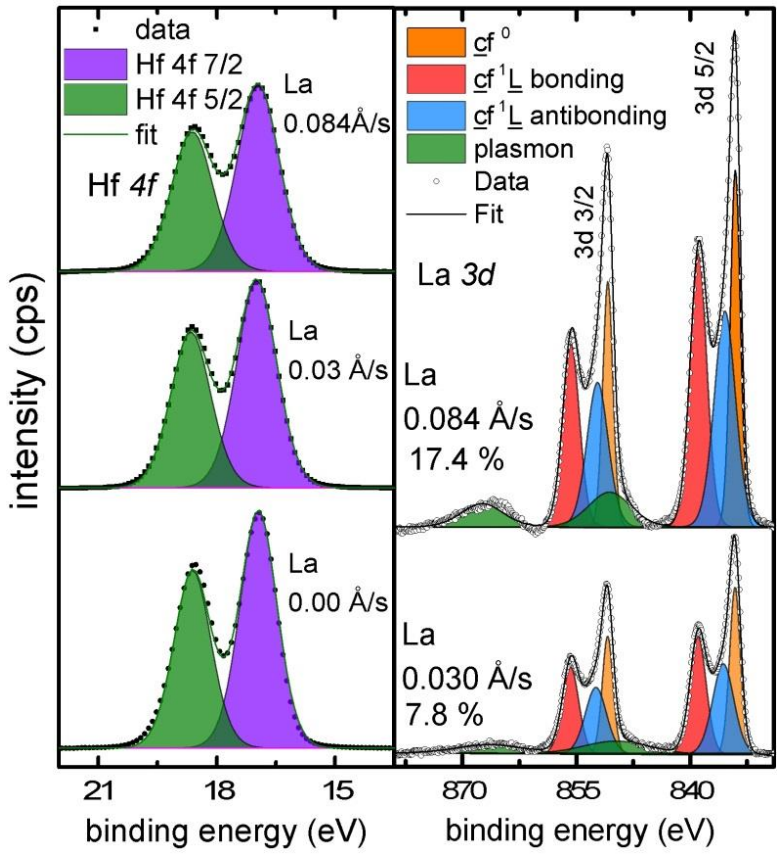

Figure 3.31: XPS spectrum and fitting of the Hf 4*f* and La 3*d* peaks for lanthanum doped hafnium oxide thin films grown on TiN electrodes with lanthanum evaporation rates of 0, 0.03, and 0.084 Å/s.

Similar to lanthanum doping, the growth of tantalum doped hafnium oxide thin films were carried out by co-evaporation of hafnium and tantalum on polycrystalline TiN films. The evaporation rate of Hf was fixed 0.2 Å/s, while that of Ta was varied as 0, 0.005, 0.015, 0.025 and 0.045 Å/s. The oxygen flow rate and the RF power applied to the radical source were fixed for all films at 2.5 sccm and 350 W respectively. Such high oxidation conditions were chosen to allow complete oxidation of tantalum. The films with thicknesses of ~20 nm were deposited with the substrate temperatures maintained at 440 °C. Figure 3.32 illustrates the XRD pattern of the as-grown tantalum doped HfO_2 films grown on polycrystalline TiN/Si substrates. Non-doped films crystallize in a monoclinic symmetry as indicated by the (-111) as well as (111) peaks. At a nominal tantalum doping rate of 0.005 Å/s, the peak shifts to slightly higher angles, possibly due to lattice compression due to the slightly smaller radii of the incorporated tantalum atom. On increasing the tantalum rate to 0.015 Å/s, there are extra peaks appearing at 30.46°and 35.3°, which can be attributed to the (101) and (110) peaks of the tetragonal structure of hafnium oxide (*t*-HfO_2), respectively. This is again consistent with the slightly smaller ionic radii of Ta^{5+} (0.69 Å under nearest neighbor coordination of seven) in comparison to Hf^{4+} (0.76 Å). Further increase in doping to 0.015 Å/s leads to a shift in

peak position to higher angle due to further compression of lattice. However, at the highest doping of 0.025 Å/s Ta, the peak was shifted to lower angles with lower peak intensity. Lower peak intensity is possibly due to higher crystallization temperature up on tantalum doping, thereby lowering the crystallinity of the film. It has to be pointed out that, it was difficult to maintain higher evaporation rates of tantalum and might have caused a non-uniform doping profile.

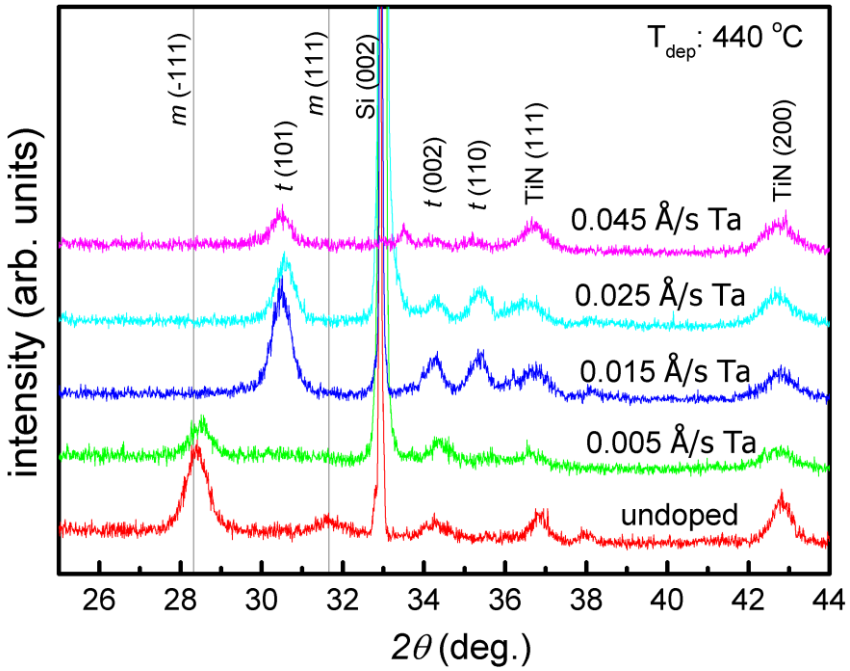

Figure 3.32: XRD pattern of tantalum doped hafnium oxide films grown on polycrystalline TiN/Si(100) substrates at 440°C by increasing the la evaporation rates, keeping a constant Hf evaporation rate and oxidation conditions.

In summary, higher dopant concentration of lanthanum and tantalum led to structural transformations in polycrystalline hafnium oxide from the monoclinic phase to higher symmetry cubic and tetragonal phases, respectively. The doped films were further electrically characterized, in a Pt/doped HfO_x/TiN configuration.

4. Electrical characterization and Analysis of RRAM

In this chapter, resistive switching characteristics of defect engineered oxide thin films are discussed. First, we consider the impact of oxygen stoichiometry engineering on electroforming in HfO_x/TiN and TaO_x/TiN devices. Then, the impact of oxygen stoichiometry on various resistive switching modes is discussed for Pt/HfO_x/TiN and Pt/TaO_x/TiN devices. Additionally, quantum conductance states have been investigated in Pt/HfO_x/TiN and high resistance states are analyzed using QPC model. Moreover, we have considered the impact of doping (La, Ta) on bipolar switching in Pt/HfO_x/TiN devices. All electrical measurements have been performed by applying bias to the top electrode and grounding the bottom TiN electrode. The devices considered were deposited on polycrystalline TiN electrodes, unless specified otherwise.

4.1. Electroforming in oxygen engineered HfO_x thin films

Usually, an initial electroforming step (high voltages) is required to obtain reliable and reproducible switching operation (at lower voltages). The forming voltage (V_F) is known to increase linearly with oxide thickness and decreases with increasing device area[209] and can be reduced to values very close to the operating set voltage (V_{SET}) in ultra-thin HfO_x devices with thicknesses approaching 3 nm.[210, 211] Such devices are sometimes characterized as forming-free. Forming-free operation or lower forming voltages have been suggested to reduce variability in RRAM devices. McKenna highlighted the necessity of sub-stoichiometric hafnium oxide for uniform nucleation and growth of conducting filaments during forming process.[72] As such, resistive switching observed in different non-stoichiometric metal oxides have exhibited improved device performances like low programming currents[212], better retention[213], forming free switching[214] and higher resistance ratio.[215] Engineering devices with an embedded oxygen deficient layer serving as an oxygen vacancy reservoir in TiO_x based devices is reported to improve switching performance which also leads to forming free switching.[216] Multilayer devices consisting of layers of TiO_x(2 nm)/HfO_x(5 nm) has also be used to induce oxygen vacancies by Ti doping in HfO_x thus obtaining a forming free switching and also presumably the controlled confinement of the filament.[217] In this study of oxygen stoichiometry engineering in hafnium oxide, we investigate electroforming in Pt/HfO_x/TiN devices (60 μm × 60 μm, lithography patterned), by comparing stoichiometric monoclinic-HfO_2 and highly oxygen deficient tetragonal like-$HfO_{1.5}$.

As shown in figure 4.1, we first consider **negative electroforming** in devices with (a) *m*-HfO_2 and (b) *t*-$HfO_{1.5}$, each with thicknesses of 20 nm. A quasi-static DC voltage ramp in steps of 25 mV was applied to the Pt top electrode and current compliance was applied to limit the

current to 100 μA, to avoid a hard-breakdown. In *m*-HfO_2, a higher electroforming voltage (V_F ~ -7.2 V) was required to form the filament, whereas the forming voltage was found to be reduced (V_F ~ -2.2 V) in oxygen deficient *t*-$HfO_{1.5}$. After negative electroforming, a first reset operation was possible in the positive polarity with a voltage up to +2.7 V in both *m*-HfO_2 and *t*-$HfO_{1.5}$. This positive reset is accompanied by a decrease in current by more than 2 orders of magnitude. There are also clear visible differences in the reset process. In *m*-HfO_2 devices, a high current of up to 30 mA was required to rupture the filament, suggesting a very high current overshoot, even though a current compliance was applied. This can be attributed to the delay (~300 μs) involved in the compliance circuit of the Keithley 4200-SCS to become active, during which the filament can be assumed to grow stronger. This current overshoot is further aided by the high breakdown voltages and the high Joule heating occurring during the process. In the case of oxygen deficient *t*-$HfO_{1.5}$ stack, the maximum reset current (~ 2 mA) required during the positive reset is an order of magnitude lower, due to lower forming voltages, which does not result in high current overshoots during the breakdown process. There is also a difference in the nature of the reset process in *t*-$HfO_{1.5}$, where we initially see a small sharp current increase which happens before the reset occurs. The nature of this set process will be discussed in detail in the section on resistive switching modes.

Now, we consider a **positive electroforming** where a positive bias is applied to Pt electrode, as shown in figure 4.1(c) and 4.1(d) for *m*-HfO_2 and *t*-$HfO_{1.5}$ device stacks, respectively. In the case of *m*-HfO_2, a positive electroforming process happening at V_F ~ +5.9 V can be followed up with a positive reset or rupture process. Therefore, the positive reset step can be considered to be present independent of the polarity of electroforming. It was observed that a negative reset process was usually not possible in *m*-HfO_2 devices, irrespective of the electroforming polarity. This suggests that the device asymmetry (TiN vs Pt electrodes) plays a role in the reset process, where TiN is the more active electrode. The variation in the break-down voltage is related to the device statistics, where device to device variations were present. For *t*-$HfO_{1.5}$ device stack, a positive electroforming process was found to be gradual in nature occurring at V_{F1} ~ +3.2 V (CC = 1 mA), where the leakage current is found to increase by more than four orders of magnitude. However, this gradual forming process is not accompanied by a current overshoot, and a reset process could not be obtained afterwards. In order to obtain a reset operation, a second negative electroforming process step showing sharp breakdown characteristics was additionally required. This negative electroforming process was found to occur at marginally lower voltages (V_{F1} ~ -1.8 V), in comparison to the direct negative electroforming step at V_F ~ -2.2 V. After the second negative electroforming step, a first reset operation in the positive polarity similar to that obtained after a direct

negative electroforming can be achieved (not shown). Moreover, it was additionally found that a negative reset was also possible in *t*-$HfO_{1.5}$ devices, which occurs gradually at lower voltages (V_{RESET} ~ -0.6 V) up to – 1.2 V. ´

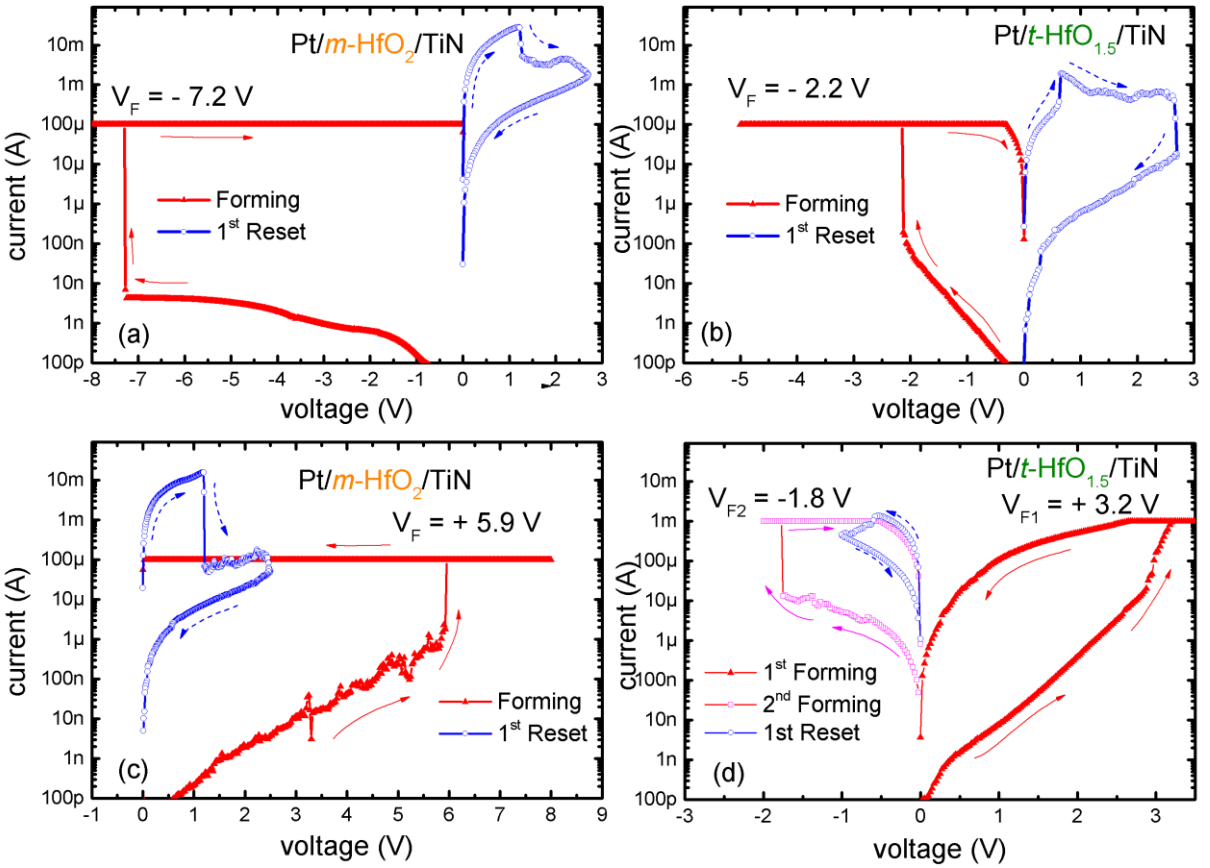

Figure 4.1: Electroforming followed by first reset operations in 60 μm × 60 μm Pt/HfO_x/TiN devices stacks by comparing stoichiometric monoclinic-HfO_2 (*m*-HfO_2) and highly oxygen deficient tetragonal like- $HfO_{1.5}$ (*t*-$HfO_{1.5}$); (a) *m*-HfO_2 with negative electroforming followed by positive reset, (b) *t*-$HfO_{1.5}$ with negative electroforming followed by positive reset, (c) *m*-HfO_2 with positive electroforming followed by positive reset, (d) *t*-$HfO_{1.5}$ with positive electroforming followed a necessary negative electroforming. Afterwards, in addition to a positive reset (not shown), a negative reset was also possible.

In the following section, we suggest a consistent **simplified model** required to account for the more stable **negative electroforming** in Pt/hafnium oxide/TiN. A typically high negative high-voltage electroforming step (V_F = -7.2 V) is required to activate resistive switching in stoichiometric *m*-HfO_2. The filament is most likely formed along grain boundaries which act as defect rich regions where preexisting oxygen vacancies ($V_{\ddot{O}}$) are energetically favored to segregate.[103] A lowered forming voltage compared to the dielectric strength is also expected in large area devices due to the larger breakdown probability at arbitrary defects.[209] Here, under a negative bias to the Pt electrode, the oxygen ions will be repelled towards the bottom TiN electrode, initiating the formation of filament growth. The oxygen ions finally accumulate at the TiN anode, and a conducting filament connects it to the Pt electrode. Even though, TiN and Pt electrodes are rather inert to oxidation, it has been suggested that TiN

could act as oxygen exchange interface[138] in the presence of defects like grain boundaries and nitrogen vacancies.[81]

As shown in figure 4.2, now the difference between *t*-$HfO_{1.5}$ and *m*-HfO_2 each with 20 nm thicknesses comes into play. In *m*-HfO_2, a large number of Hf-O bonds have to be broken to create oxygen vacancies and the resulting higher electroforming voltage ($V_F \sim$ -7.2 V) will create stronger filaments with more accumulation of oxygen ions near the TiN interface. Since immediate neighbor intimate Frenkel pairs (IFPs) are thermodynamically unstable,[124] well separated 'extended Frenkel pairs' (EFPs) arising from diffusion of oxygen interstitials is understood to play the major role in electrofroming.[125]

In case of unformed and pristine *t*-$HfO_{1.5}$, there already exists a homogeneous distribution of a large amount of oxygen vacancies, which are, however, below the threshold of creating a low-resistive state compared to a locally conducting filament. Therefore, also in this case, an electroforming step is required; however, in contrast, the filament formation in *t*-$HfO_{1.5}$ takes place under much lower electric fields ($V_F \sim$ -2.2 V) where only fewer Hf-O bonds are required to be broken due to the presence of pre-existing oxygen vacancies. This process has been suggested to be complemented by electron trapping in pre-existing vacancies which assists the formation of IFPs at adjacent sites, thereby leading to divacancies.[123] The formation energy of IFP is presumably further lowered near oxygen vacancy clusters due to a weak attraction of oxygen vacancies thus promoting easier clustering and filament growth.[123]

It is to be noted that, in *t*-$HfO_{1.5}$, this however does not exclude the conventionally accepted possibility of oxygen vacancy transport[126, 218] becoming more dominant compared to oxygen interstitials, as has been shown to be energetically favorable in the scenario when preexisting vacancies are induced by the presence of highly reactive electrodes.[125, 126, 219] The complex nature of electroforming in highly oxygen deficient HfO_x therefore requires more theoretical and experimental considerations. Overall, in contrast to *m*-HfO_2, it can be reasonably stated that the oxygen ion/vacancy redistribution during a negative electroforming is expected to be much less in *t*-$HfO_{1.5}$ due to intrinsically present oxygen vacancies; in particular, the accumulation of oxygen ions at the TiN interface will be much reduced as depicted in figure 4.2.

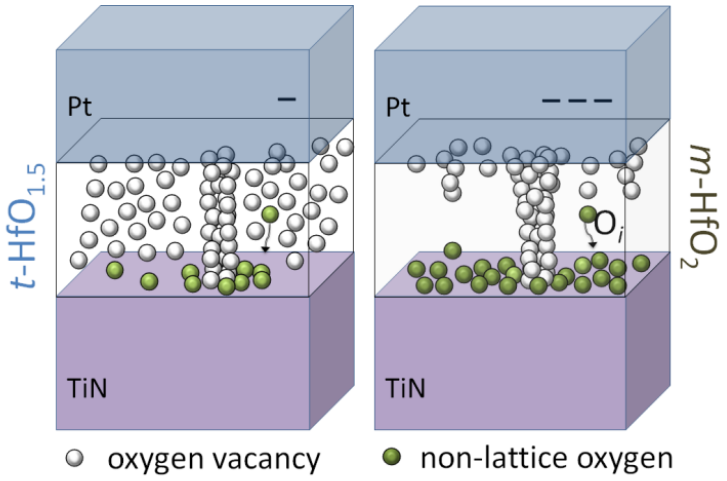

Figure 4.2: A schematic model of filament formation on applying negative voltages to the Pt electrode in Pt/ *t*-$HfO_{1.5}$/TiN (left) and Pt/ *m*-HfO_2/TiN (right).

To understand the gradual positive electroforming process in oxygen deficient *t*-HfO_x, we consider HfO_x/TiN devices in the absence of Pt top electrodes. For a comparative study, the thicknesses of the films (verified by fitting of grazing incidence X-ray reflectivity data) were varied in a wide range; *m*-HfO_2 (10, 20 and 50 nm) and *t*-HfO_x(10, 20, 50, 100 and 200 nm). After the thin film growth, the films were cooled down to room temperature and taken out of the deposition chamber, which resulted in the exposure of the surface of the films to ambient atmospheric conditions leading to the formation of an oxidized surface layer (as verified by angle dependent XPS in figure 3.25). The films were then contacted for electroforming and resistive switching directly using a rounded gold coated copper beryllium tip (top electrode) contacted with a force of 1.0 N was used to apply current compliant DC voltage sweeps directly on HfO_2 films, the TiN bottom electrode being grounded. The contact area of the gold electrode was ~ 50 μm in diameter. In all cases, reproducible switching characteristics could be obtained only after an initial electroforming step. Direct tip contact is expected to lead to oxygen exchange with the ambient during electroforming and switching. Both *m*-HfO_2 and *t*-HfO_{2-x} were electroformed by applying positive forming voltages (V_F) with a current compliance (CC) of 1 mA.

Figure 4.3(a) summarizes the **dependence of forming voltage on thicknesses** of stoichiometric (*m*-HfO_2) and oxygen deficient (*t*-HfO_{2-x}) films (for each thickness, 10 different devices were measured and an average value of forming voltage is plotted). The forming voltage increases linearly with thickness for the stoichiometric *m*-HfO_2 films with about 4.7 V required for a thickness 10 nm and about 15.4 V required for 50 nm. The linear increase of forming voltage (V_F) with thickness (t) is in agreement with reported values in literature.[209]

For stoichiometric films, a linear fit was performed to obtain a slope of 2.05. In contrast, the oxygen deficient films required only lower forming voltages with about 2 V required for 10 nm and interestingly remained nearly constant at about 3.2 V for higher thicknesses up to 200nm. It is noteworthy that forming voltages and the initial switching characteristics of the direct pin contacted case is comparable to Pt top electrode RRAM structure with similar contact area. Also, the forming voltage for 20 nm stoichiometric films *m*-HfO_2 with top Pt electrodes was about 7.5 V. Post electroforming, all the films exhibited bipolar resistive switching irrespective of the thickness and phase of HfO_2 with a negative set (I_{CC} =1 mA) and gradual positive reset and yielded a resistance ratio of ~ 5 between the HRS and LRS. Figure 4.3c depicts a typical switching cycle obtained for 50 nm *t*-HfO_x film after the forming step. In the endurance plot (figure 4.3(d)) of the same device acquired with Au tips, a gradual decline in resistance ratio was observed for cycles up to 100, staring with near 5.3 and reaching 1.5 after 100 cycles. This can be explained by the gradual depletion of oxygen vacancies due to ambient atmospheric conditions and absence of top deposited electrode.[151]

The observation of an almost thickness independent forming voltage for the oxygen deficient hafnium oxide samples raises the question of a probable scenario that oxygen deficient films after growth were conducting due to high oxygen vacancy concentration and when exposed to atmospheric conditions resulted in the oxidation of the surface layer (up to a few unit cells as confirmed by angle dependent XPS shown in figure 3.25(b)). Moreover, a low resistance could not be obtained on the surface of the as-grown polycrystalline films by two probe measurements using ohmmeter. This is unlike the highly textured oxygen deficient hafnium oxide films grown at higher temperature from previous studies, which were found to be highly conducting even after exposure to ambient conditions.[99,100] A lowered crystal quality can be understood to lead to easier surface oxidation by providing diffusion pathways. Therefore, these results of constant forming voltages confirm the presence of an oxidized surface layer independent of thickness of oxygen deficient polycrystalline *t*-HfO_x films which is responsible for the nearly same forming voltages in oxygen deficient films. In such a scenario, as shown in figure 4.3(b), one could imagine that only the top thin oxidized layer which is close to stoichiometric hafnium oxide needs the forming step and is independent of the film thickness as rest of the film is more conducting. The higher conducting matrix of thin film underneath the oxidized layer does not contribute to the required forming process, and hence the observed constant forming voltage independent of the film thickness. Thus, the gradual electroforming which was found to be independent of the oxide thickness of the tetragonal phase layer can be attributed to a progressive breakdown of the nominal oxidized surface passivation layer formed after exposure of the films to ambient atmosphere. This resistive

switching in 50 nm *t*-HfO_x is also a further indication that the switching occurs only at the oxidized surface top layer. Here, the exchange of oxygen with air as well as the oxygen deficient layer leads to quickly degradation of switching to very low resistance ratios (<2). This is different from the Pt/HfO_x/TiN devices, where switching could not be obtained directly after a positive electroforming process. The local nature of direct tip contact (Au), as well as possible oxygen exchange with atmosphere is likely to have assisted in a stronger filament formation as well as switching. In comparison, a positive electroforming in Pt/HfO_x/TiN devices induces oxygen ion motion across the entire Pt/oxidized t-HfO_x interface. This is reflected in the much gradual electroforming, which is less likely to have formed a strong filament.

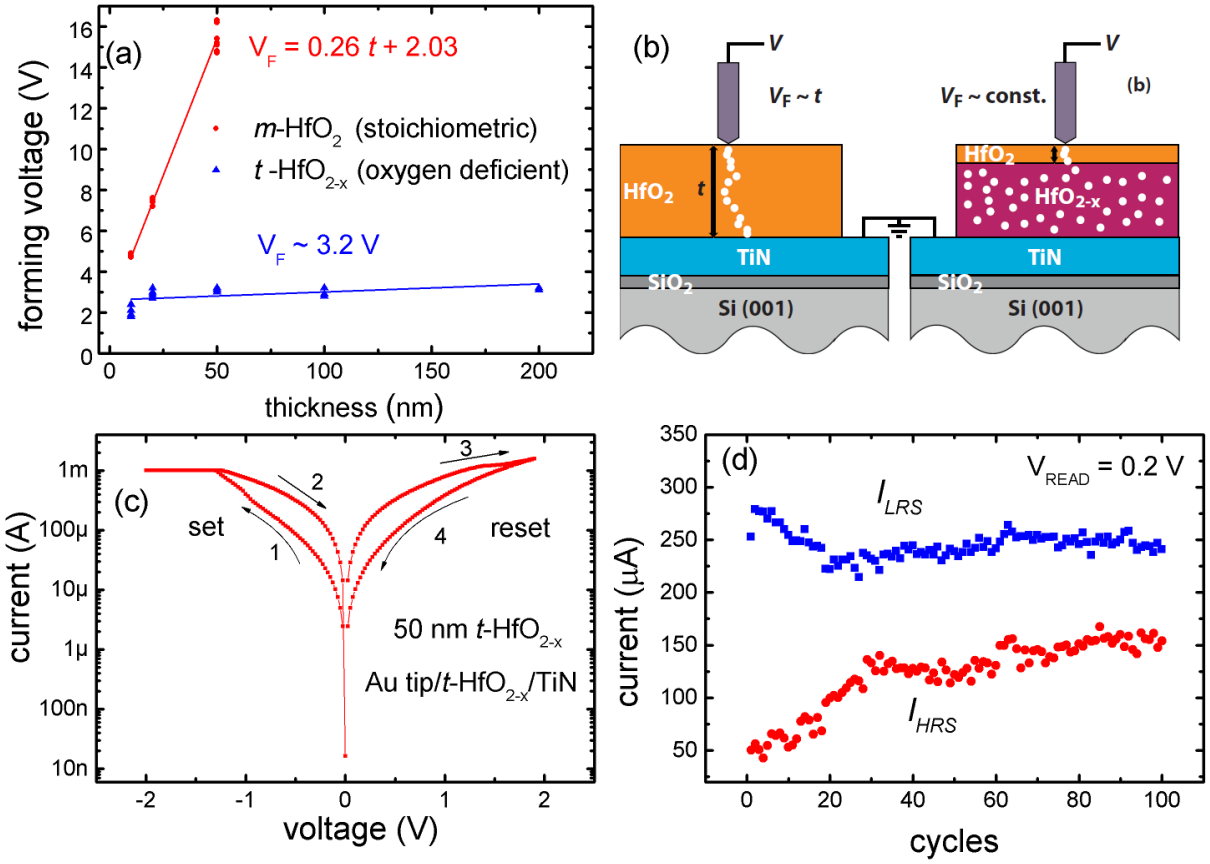

Figure 4.3: (a) Thickness dependence of positive electroforming voltages in stoichiometric (*m*-HfO_2) and oxygen deficient (*t*-HfO_{2-x}) films. (b) Schematic diagram of the thickness dependent electroforming process in stoichiometric (*m*-HfO_2) and oxygen deficient (*t*-HfO_{2-x}) films. b) Plot of the variation of average forming voltage with thickness for stoichiometric and oxygen deficient films c) Bipolar resistive switching characteristics (V_{SET} < 0) of a typical oxygen-deficient *t*-HfO_x film deposited with a thickness of 50 nm with a current compliance of 1 mA; (d) Endurance up to 100 cycles of 50 nm *t*-HfO_x. Published results.[220]

To summarize, the oxygen-deficient HfO_{2-X} films do not completely suppress the electroforming but they drastically decrease the voltage required for this process. The presence of the defects states in the band gap (XPS) should be responsible of the change in the electroforming process, making it easier to establish. In consequence, thicker dielectric

films can be used, which are still presenting an acceptable forming voltage not too high for CMOS applications. This is extremely interesting for RRAM applications that should be used in low-power systems like wireless sensor networks.

Study of the dependence of forming voltage and switching characteristics of stoichiometric *m*-HfO_2/TiN devices shows a linear increase with increase in oxide thickness as expected; 4.8 V for 10 nm to 15.4 V for 50 nm *m*-HfO_2. In stoichiometric Pt/*m*-HfO_2/TiN devices, the polarity of electroforming was found to have negligible impact, where only a reset operation in the positive polarity was possible. In contrast, oxygen deficient hafnium oxide based Pt/*t*-HfO_x/TiN devices showed an almost thickness independent positive forming voltage which was nearly constant at about 3.2 V. Angle dependent XPS studies showed that the top surface layer in the oxygen deficient films which oxidized due to exposure to ambient is the only layer contributing to the positive forming process and hence the observed thickness independent forming voltage. An *in-situ* top electrode deposition on hafnium oxide films could lead to the realization of a forming free RRAM device which could have a huge impact in increasing RRAM reliability.

4.2. Electroforming in oxygen engineered TaO_x thin films

In TaO_x based VCM-RRAM, forming free devices have been achieved either by tuning the oxygen stoichiometry of the tantalum oxide layer[221] or using an annealing step post electrode deposition of a scavenger electrode.[222] The sub-stoichiometric tantalum oxide is understood to be a mixture of various stable and metastable oxides like Ta_2O_5, TaO_2, Ta_2O_3, TaO, Ta_2O as well as Ta metal, all of which have been suggested in literature.[204, 223-225] Additionally, bilayer configuration of Ta_2O_{5-y}/TaO_x consisting of an oxygen rich Ta_2O_{5-y} which acts as a switching layer and an oxygen deficient TaO_x playing the role of an oxygen reservoir and self-compliance layer have shown exceptional reliability.[226, 227] This high endurance is be understood to be due to the low reaction Gibbs energy (ΔG) for TaO_x and Ta_2O_5 redox pair, allowing bistable and non-interacting states under thermodynamic equilibrium.[50, 228] In contrast, lower density of the oxide matrix was found to be favorable for metal ion migration in TaO_x based ECMs like Cu/Ta_2O_5 and Ag/Ta_2O_5, also assisting in reducing the forming voltages.[229] Hence, it becomes necessary to be able to precisely control the oxygen content of the deposited tantalum oxide films to optimally tailor the properties of the ReRAM device.

In this study, the oxygen stoichiometry was engineered in TaO_x thin films by varying the oxygen flow (0.2-2.5 sccm) during RMBE growth. Exposure to ambient of the as-grown films led to formation of a thin oxidized surface layer, Ta_2O_{5-y} with a thickness less than 1.5 nm.

Further, Pt/Ta_2O_{5-y}/TaO_x/TiN cells of 30 μm × 30 μm was defined via deposition of Pt top electrode by DC sputtering after a standard photolithography and lift off process. The devices were electrically characterized by applying current compliant DC voltage sweeps on the top Pt electrode, while the bottom TiN electrode was grounded. Now, we compare the electroforming of the Pt/$Ta_2O_{5-\delta}$/TaO_x/TiN stacks with different oxygen contents (x). The electroforming was performed in a number of devices by applying a negative voltage to the Pt electrode and grounding the bottom TiN electrode. The results of average forming voltages obtained for different oxygen flow is summarized in figure 4.4(a).

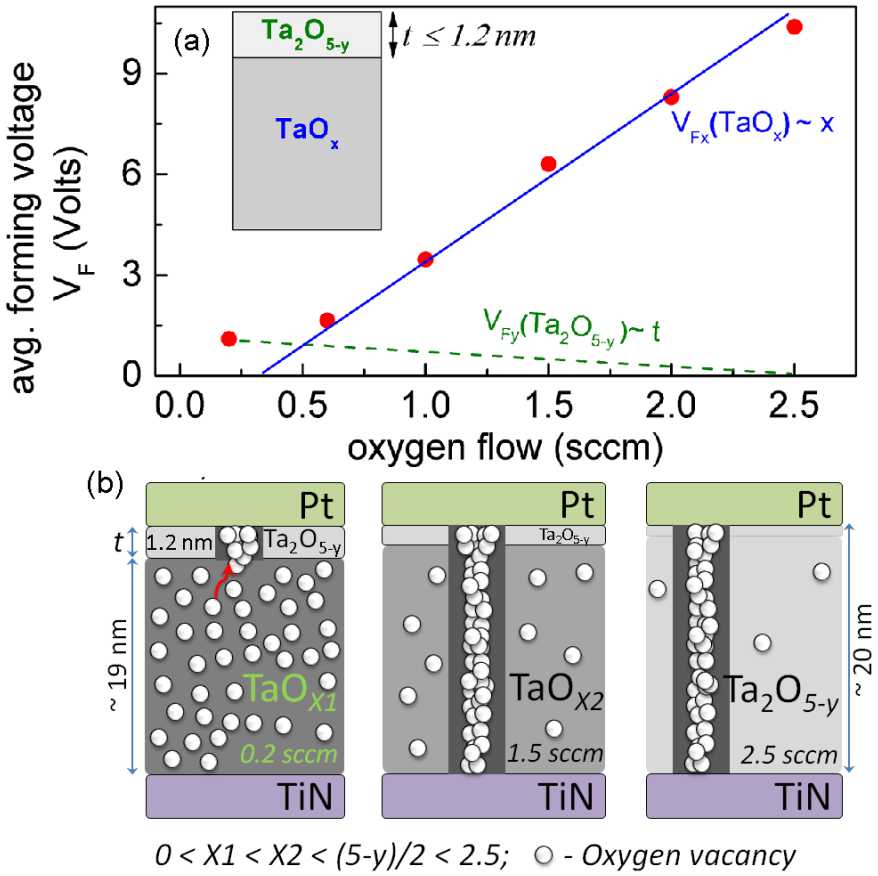

Figure 4.4: (a) Forming voltage dependence on oxygen flow in the devices. (b) The schematic of the filament formation in the Pt/$Ta_2O_{5-\delta}$/TaO_x/TiN based devices.

The forming voltage (V_F) was found to increase from 1.5 V in 0.2 sccm device to 10.5 V in the 2.5 sccm stack. The electroforming process is understood to be initiated in TaO_x based RRAM via electron hopping from oxygen vacancies to a neighboring tantalum atom, leading to the formation of positively charged oxygen vacancies.[230] These charged vacancies drift under the influence of electric filed towards the cathode, leading to the formation of filaments as shown in figure 4.4(b). Lowering of forming voltages could thus be attributed to a lowered

energy barrier for electron hopping in oxygen deficient TaO_x thin films. At 2.5 sccm, the corresponding electroforming field obtained of 0.49 V/nm is slightly lower than 0.54 V/nm obtained for stoichiometric $Ta_2O_{5-\delta}$ films reported in literature.[230] The electroforming process in the device can be modeled qualitatively by oxygen vacancy motion towards the cathode. The conducting filament thus formed, as shown in the figure 4.4(b) for the 2.5 sccm device, is represented by the darker region consisting of oxygen vacancies, lower valence states of tantalum, and its corresponding oxides.

At lower oxygen flow rates, the V_F as indicated in figure 4.4(a) depends on the breakdown of the surface passivation layer Ta_2O_{5-y} with varying thickness ($t < 1.2$ nm) and of the TaO_x layer. The contribution of the latter simply increases with higher oxidation 'x' in TaO_x and dominates under high oxidation conditions, which can be approximated by the bold line in figure 4.4(a). The contribution of the passivation layer scales with its thickness, which increases with decreasing oxygen flow as determined by XRR approximated by the dotted line. At less reducing conditions, the filament has to form through the entire Ta_2O_{5-y}/TaO_x bilayer, but the Ta_2O_{5-y} layer has a relatively minor contribution to V_F. (figure 4.4(b), right) Under highly reducing conditions (0.2 sccm), the effective contribution from the TaO_x layer underneath is negligible due to its relatively high conducting nature, as indicated by the presence of electronic states near the Fermi level observed in XPS measurements (see figure 3.27(a)). Therefore, the electroforming in the 0.2 sccm stack is primarily due to the breakdown of the 1.2 nm thick Ta_2O_{5-y} passivation layer. Here, the filament is expected to form only in the top oxidized Ta_2O_{5-y} layer, whereas the residual layer of TaO_x is sufficiently conducting (figure 4.4(b), left), similar to observations in oxygen deficient HfO_x. Recent scanning tunneling microscopy studies have shown that Ta ions within a very thin (2 nm) Ta oxide layer in the configuration Ta/Ta_2O_5 become mobile during electroforming.[51] The same work employed a very thin amorphous carbon layer at the Ta/Ta_2O_5 interface, inhibiting oxygen transport, therefore crossing-over from VCM to ECM switching. An ECM mode of switching involving large asymmetry in operating voltages and currents was not observed in the $Pt/Ta_2O_{5-y}/TaO_x/TiN$ devices used in this study. Therefore, the motion of Ta ions can be considered to be negligible in the absence of a layer inhibiting oxygen transport.

4.3. Resistive switching in $Pt/HfO_x/TiN$ devices

We have investigated the impact of oxygen stoichiometry on resistive switching in a $Pt/HfO_x/TiN$ model device stack, which has been reported to exhibit reliable switching in several publications.[56, 138, 150] As described in the introduction chapter, this device type is particularly interesting due to multiple coexisting switching modes and polarities,[56, 122, 148] as

well as a large possible resistance window of operation, making it promising as multi-bit synaptic devices in neuromorphic computing.[132, 133, 139, 149] The results detailed in this section were published in two papers.[152, 200]

4.3.1. Resistive switching modes (*f8/cf8*- BRS, CRS, TRS, URS)

In this section, we describe the different switching modes in Pt/*m*-HfO_2/TiN and Pt/*t*-$HfO_{1.5}$/TiN stacks, where the oxide thicknesses are 20 nm. Impact of oxygen stoichiometry on the different resistive switching modes is investigated for the first time in the same device configuration, expect for a change in oxygen stoichiometry. Figure 4.5 shows the various switching modes, which can be achieved in Pt/HfO_x/TiN, comparing *m*-HfO_2 and *t*-$HfO_{1.5}$. Unipolar, bipolar (counter-eightwise) and threshold switching was possible in *m*-HfO_2 based devices. Whereas, bipolar (counter-eightwise and eightwise) and complementary switching was observed in *t*-$HfO_{1.5}$ based devices.

A stable **counter-figure eightwise type bipolar resistive switching (*cf8*-BRS)** mode, with applied bias to Pt electrode has been most often reported in the Pt/***m*-HfO_2**/TiN device configuration. This *cf8*-BRS mode of operation is typically characterized by a sharp set under negative bias to Pt followed by a progressive reset process which allows for high resistance ratios ($> 10^3$). Figure 4.5(a) shows this typical *cf8* BRS operation obtained after a negative electroforming step. This *cf8* operation involves a sharp set of negative polarity (current compliance, I_{CC} = 5 mA), and a deep reset for which a voltage of +2.7 V was used to obtain a maximized ratio of the resistance in the high resistance state (HRS), R_{OFF}, and in the low resistance state (LRS), R_{ON}. This rather typical set and reset behavior was observed to be stable within the measured 1024 cycles.

A **unipolar resistive switching (URS)** sometimes coexists with *cf8*-BRS, where the reset process is possible only using Pt as the anode, which is common for both modes.[22] Such a URS operation as shown in figure 4.5(b) was also found to coexist with *cf8*–BRS in the Pt/***m*-HfO_2**/TiN device. The URS which was found to be stable only in the positive polarity and can be activated by using a forming step of either positive or negative polarity, followed by a positive reset in the *m*-HfO_2 based device. Such a hybrid operation which involves a negative electroforming and a positive unipolar set was reported by Goux *et al.* to yield stable operation.[56] In the current device, electroforming was performed in the positive polarity where a minimum current compliance of 10 μA was required to form a stable filament. Unipolar switching is obtained in these devices using a positive set with current compliance of 1 mA with a DC sweep up to 4.0 V followed by reset operation up to 2.7 V.

Occasional **threshold resistive switching (TRS)**, as also shown in figure 4.5(b), is found to coexist with the unipolar resistive switching mode on repeated cycling. Figure 4.5(c) shows the DC endurance plot with current read at 200 mV, where we see that unipolar switching recovers after intermittent threshold switching in the Pt/***m*-HfO$_2$**/TiN device. The coexistence of unipolar and threshold switching has been reported to occur in different cases depending on temperature,[43] current compliance,[231] oxygen stoichiometry[232] etc. This complex behavior has been attributed to improper heat dissipation[20] and/or instabilities due to local thermal fluctuations[21] in the conducting filaments, but remains a matter of debate.[21] This coexistence of unipolar and threshold switching is discussed further in the subsequent section on switching mechanisms.

We further describe the multiple switching behaviors obtained in a Pt/*t*-HfO$_{1.5}$/TiN stack. The negative electroforming for the *t*-HfO$_{1.5}$ device took place at a strongly reduced voltage of V_F = -2.2 V, where a more uniform conducting filament is expected. Interestingly, unipolar and threshold switching were completely absent in these devices, the reason for which is discussed later. The unconventional switching modes observed in the Pt/*t*-HfO$_{1.5}$/TiN device stack are described below.

Figure 4.5(d) shows a typical **coexistence of *f8*-BRS and c*f8*-BRS** in Pt/***t*-HfO$_{1.5}$**/TiN stack. Here, the device is operated at same high voltage bias and current compliance condition used for the *cf8* type operation in the stoichiometric *m*-HfO$_2$ device stack. We see several prominent differences in the set and reset behavior. Unlike the *m*-HfO$_2$ device stack, set operations were not completely sharp and were sometimes found to be two-step sets as seen for cycle #1 and cycle #30. The nature and cause of this intermediate step will be discussed in the next section. Additionally, the deep reset process in the positive polarity is often preceded by an initial set step at lower voltages (0.5 V to 1.0 V). This can be attributed to a coexisting *f8* type switching, where the low bias (< 1.0 V) set step in *f8*-BRS coexists in the higher bias (up to 2.7 V) reset step of the *cf8*-BRS. However, the negative reset process in the *f8*- BRS is hidden inside the IV-curve of the set process during *cf8* BRS operation due to the presence of a current compliance. The variation in positive set voltages of *f8*-BRS upon cycling (0.5 – 1.0 V) could therefore be due to an incomplete reset happening in the negative polarity due to the presence of this current compliance.

A **complementary resistive switching (CRS)** operation is typically present when set and reset can occur in the same polarity. It typically involves a set operation followed by reset upon increasing voltage in the same polarity. The degree to which the reset takes place, which can be controlled by the stop voltage, is used to operate the device in CRS mode. Such a

transition to a CRS behavior is shown in figure 4.5(e) on lowering of the operating voltage compared to *cf8*-BRS. This CRS mode was observed in the narrow regime of -1.2 V in the negative polarity and +1.1 V in the positive polarity, in agreement with other similar results, where a *f8* type bipolar switching was observed simultaneously.[122, 148] Any further increase in the positive bias voltage was found to lead to a deep reset behavior, thus, crossing over to a standard *cf8* type BRS, as described before.

The lower-bias voltage **figure eightwise type bipolar resistive switching** (***f8*-BRS**) operation (reset process with TiN as anode) with lower resistance ratios (~ 10) was also observed in similar devices and first reported in our paper.[152] The ***f8*-BRS** could be observed at the lowest operating voltages, as shown in figure 4.5(f). Chen *et al*. also suggested that this *f8* switching is stabilized by a two-step electroforming with opposite bias polarities.[148] Such a typical two-step positive and negative electroforming step, as shown before in figure 4.1(d), was used to improve the switching ON/OFF ratio. The positive electroforming was gradual in nature occurring at a voltage of V_F = 3.2 V with a current compliance of 1 mA. A positive forming does not result in a current overshoot and was followed by a second sharp negative forming step (V_F = -1.8 V and current compliance of 1 mA), which was found to be necessary to activate stable switching behavior. After the two-step forming, further switching operations were performed on the device. At low voltages, we then stabilize the *f8*-BRS, which involves a sharp positive set at around +0.6 V followed by a negative gradual reset step up to -1.0 V. In effect, appropriate choice of operation voltages can be used to switch between different operations modes in a Pt/*t*-$HfO_{1.5}$/TiN device. Interestingly, the set process during *f8*-BRS was found to exhibit self-compliance characteristics. When operated as such in the absence of current compliance, the switching was found to be stable up to 100 DC cycles with reduced R_{ON}/R_{OFF} ratios of nearly 10.

All the different switching modes which are reported to occur in MIM devices in literature have been found to be present in model Pt/HfO_x/TiN devices depending on the oxygen stoichiometry (x). These results of partial occurrence of switching modes, as summarized in table 4.1, would contribute to developing a unified switching model giving a deeper insight into the switching mechanism.

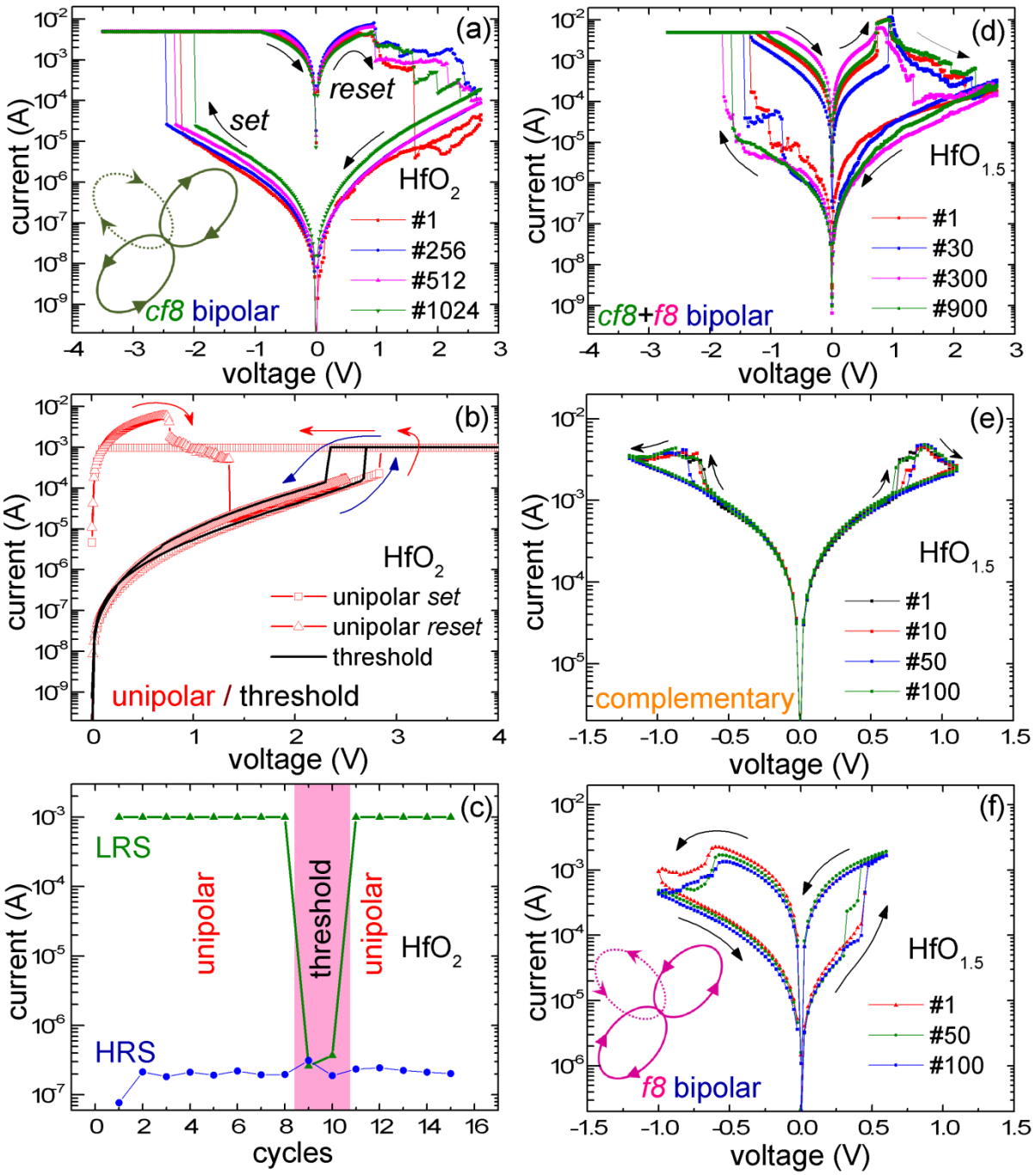

Figure 4.5: Comparison of resistive switching modes in Pt/HfO_x/TiN. (a) counter figure eightwise (*cf8*) bipolar resistive switching (BRS) behavior obtained using *m*-HfO_2 after a negative electroforming at -7.0 V (not shown); (b) coexisting unipolar resistive switching and threshold switching in *m*-HfO_2; (c) corresponding currents at low resistance (LRS) and high resistance states (HRS) read out at 200 mV for up to 15 cycles showing the coexistence of intermediate threshold switching cycles during unipolar operation due to insufficient heat dissipation. (d) counter figure eightwise (*cf8*) bipolar resistive switching behavior obtained using *t*-$HfO_{1.5}$ after a negative electroforming at -2.2 V; Note that *f8*-BRS is sometimes coexisting in the same cycle (e) and transition to complementary switching in *t*-$HfO_{1.5}$ on decreased bias of operation; (f) A stable exclusive *f8*-BRS behavior at lowest operation bias up to 100 dc cycles obtained after a multi-step positive and negative electroforming *t*-$HfO_{1.5}$ steps.

Table 4.1: Stoichiometry dependence of the partial occurrence of all resistive switching modes in Pt/HfO_x/TiN devices comparing, *m*-HfO_2 and *t*-$HfO_{1.5}$.

RS modes (bias to Pt TE)	**Pt/*m*-HfO_2/TiN**	**Pt/*t*-$HfO_{1.5}$/TiN**
Unipolar	✓ (set: +3.5 V/ 1mA, reset: +2.7 V)	X
Threshold	✓ (+3.5 V, only appears between URS cycles)	X
cf8-Bipolar (counter figure eightwise)	✓ (set:-2.7 V, reset:+2.7 V)	✓ (set:-2.7 V, reset:+2.7V) (*f8*-BRS may coexist)
f8- Bipolar (figure eightwise)	X	✓ (set: +0.6 V, reset: -1.0 V) (lower bias)
Complementary	X	✓ (-1.2 V, 1.1 V)

4.3.2. Endurance and Conduction mechanism

The endurance and conduction mechanisms in the most common bipolar switching operation modes (*f8* and cf8- BRS) are further considered. An *f8*-BRS operation for two devices with oxygen-deficient *t*-HfO_{2-X} films based first generation devices of TiN/Pt/HfO_x/TiN (100μm x 100μm), with oxide thicknesses of 20 nm and 50 nm are shown in figures 4.6(a) and 4.6(b), respectively. As discussed in the last section, both devices require an electroforming process prior to the obtained *f8*-BRS. As visible in the insets of the figures 4.6(a) and 4.6(b), voltage sweep was applied on the samples with 20 nm (50 nm) HfO_{2-X} down to -2 V (-5 V) with a current compliance equals to 0.3 mA (50 μA). Although the forming voltage is drastically reduced compared to stoichiometric films and is very close to the operating voltages during the switching, this step is still required. This is in agreement with the previously mentioned studies on the impact of very thin HfO_2 layers where the forming voltage values are reduced very close to the set values.[210] After electroforming, the 20 nm *t*-HfO_X based device shows a *f8*-bipolar resistive switching with a positive set around 0.8 V (CC = 0.5 mA) and a negative reset at -1.0 V. The corresponding endurance plot of figure 4.6(c) shows that the switching was stable over at least 120 cycles with a separation between the ON and OFF states around 3. The sample with 50 nm thick HfO_X also exhibits a *f8*- type bipolar resistive switching behavior with a positive set around 1.0 V (CC = 1 mA) and a negative reset at -1.5 V, as shown in figure 4.6(b). The corresponding endurance plot is shown in figure 4.6(d), where a stable resistive switching up to 128 cycles with a ratio between the ON and OFF states of around 5. Comparing the current levels in the ON-state between the 2 samples with oxygen-deficient HfO_{2-X} (figures 4.6(c) and 4.6(d)), it is found to

be rather similar. However, this *f8* type BRS could be stabilized only at lower resistance ratios (<10) in the presence of a current compliance in the set process. This is in agreement with a filamentary model where a conductive filament is built between the two electrodes, independently of the film thickness. It was also observed that the f8-BRS operation was difficult to stabilize and not operable for larger number of cycles (> 200), due to degradation in resistance ratios (<10).

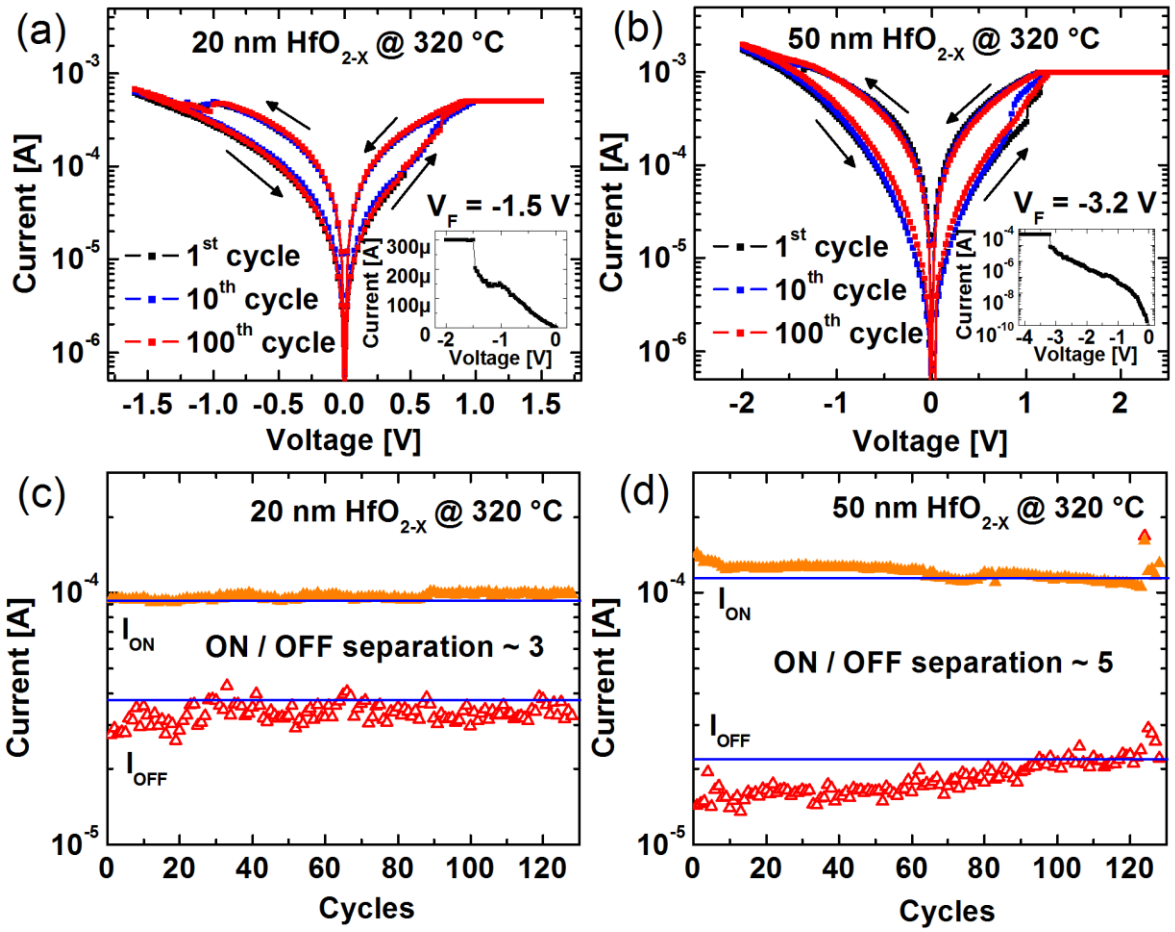

Figure 4.6: (a-b) f8 – type bipolar resistive switching characteristics (V_{SET} > 0) in Pt/HfO_x/TiN device stacks using oxygen-deficient *t*-HfO_x films deposited at 320 °C and with a thickness of 20 nm (a) and 50 nm (b). The insets show the forming processes which occur at V_F = -1.5 V with a current compliance of 0.3 mA with a linear scale in (a) and at V_F = -3.2 V with a current compliance of 50 μA in (b). (c-d) Endurance plots of the two systems, the ON and OFF states are read at 200 mV.

To better reveal the coexisting nature of the bipolar operations as well the nature of electronic conduction, figure 4.7(a) compares the high bias (-3.0 V, 2.7 V) bipolar operation in the linear scale for HfO_2 and $HfO_{1.5}$. A *cf8*-BRS operation as usually observed in the stoichiometric HfO_2 based device is plotted in comparison to a switching cycle in $HfO_{1.5}$ device where *f8*-BRS coexists with *cf8*-BRS. The low resistance state (LRS) for the *cf8* BRS operations, which is common to the LRS of *f8*-BRS is found to be ohmic in nature. The I-V characteristics for the high resistance state (HRS) of *f8* operation is best fitted using a Schottky emission

model as shown in figure 4.7(b), where *ln I*-$\sqrt{V}$ plot is linear at higher voltages, in agreement with literature.[148] The HRS for *cf8*-BRS in Pt/HfO_x/TiN devices was described by Yu *et al.* using a trap assisted tunneling model.[104] The endurance corresponding to *cf8*-BRS for *m*-HfO_2 and *t*-$HfO_{1.5}$ are shown in figure 4.7(c) and 4.7(d), respectively. The currents are read at 200 mV. The *cf8* bipolar operation in the *m*-HfO_2 based stack is found to be stable up to more than 1000 DC cycles with R_{ON}/R_{OFF} ratios of more than 5000. The *cf8* bipolar switching in *t*-$HfO_{1.5}$ based device stack shows a significant difference in the endurance. The current in the LRS state shows a wider spread and can be approximated as two distinct states: one higher current LRS arising only from a typical *cf8*-BRS operation, and the second lower current LRS due to the coexisting *f8*-BRS operation. The higher currents in the HRS of the *t*-HfO_x stack as compared to the *m*-HfO_2 stack can be attributed to the higher conductivity of the overall oxide matrix after filament rupture, also by the larger probability of tunneling in the tetragonal phase which has a higher concentration of oxygen vacancy traps.

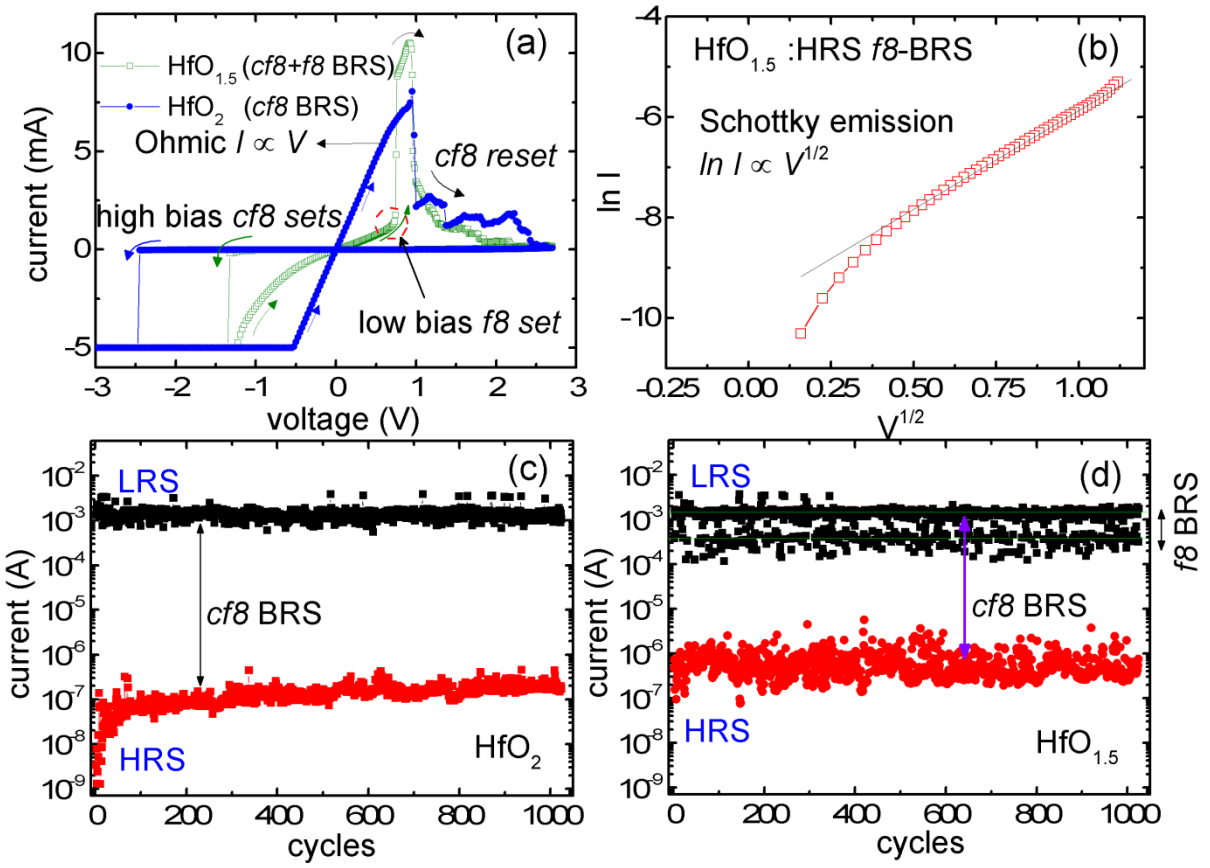

Figure 4.7: Analysis of bipolar resistive switching (BRS) operations in HfO_2 and $HfO_{1.5}$. (a) Comparison of typical I-V curves of high bias (-3.0 V, 2.7 V) bipolar operations showing only a counter figure eightwise (cf8) BRS for HfO_2 and a typical coexistence of cf8 BRS and low bias *f8*-BRS operations in *t*-$HfO_{1.5}$. Note that the low resistance state (LRS) for the *cf8* and *f8* operations are the same and is ohmic in nature. (b) Fitting of the I-V data for the high resistance state of f8 operation with Schottky emission model showing a linear fit for ln I - $\sqrt{V}$ plot. Corresponding DC endurance for the high bias *cf8*-BRS up to 1024 cycles read out at 200 mV is shown for (c) HfO_2 and (d) $HfO_{1.5}$. Distinct states appearing in the LRS of $HfO_{1.5}$ device is due to the presence or absence of *f8*-BRS.

4.3.3. Analysis of quantized conductance states

The deep reset step common to URS and *cf8*-BRS obtained by applying positive bias to the Pt electrode has been shown to exhibit gradual switching dynamics,[56] which is more desirable than the sharp set processes for adaptive learning in synaptic devices based on Pt/HfO_x/TiN.[133, 149] In other HfO_x based devices like Pt/HfO_2/Pt,[54] during unipolar reset, sharp transitions between discrete quantized conductance states were observed, where the resistance corresponds to a quantum of conductance ($G_0 = 2e^2/h = 12.9\ k\Omega^{-1}$). However, the practical application of quantized states for multibit memory remains elusive, also due to large fluctuations from cycle to cycle.[113]

Ideally, the observation of conductance quantization phenomenon is expected in the regime when the conductance is close to G_0. However, quantization is not very obvious in most cases and is only observed upon a statistical analysis of multiple switching cycles. We therefore analyzed the *cf8*-BRS cycles which undergoes transitions across G_0 for quantization. In *m*-HfO_2, quantization during set process could be ruled out due to its sharp dynamics. Interestingly, we also could not find any traces of conductance quantization steps in the reset process during *cf8*-BRS upon analysis of multiple cycles, even though the reset switching dynamics was neither fully sharp nor gradual in nature near the regime of G_0. Next, we analyzed the intermediate set steps occurring during the *cf8*-BRS, as shown in figure 4.8(a), which were observed only in the case of oxygen vacancy stabilized *t*-$HfO_{1.5}$ device stacks. It is notable that this behavior is unlike the sharp sets reported in all previous literature for devices based on Pt/HfO_2/TiN. All these intermediate set steps observed in consecutive 256 cycles were compared with quantized conductance states as shown in figure 4.8(b). The initial conductance (G) in the high resistance state is found to be less than 0.1 G_0. This is indicative of the presence of a spatial gap composed of at least one re-oxidized vacancy required in the case of $G << G_0$.[115] It is evident that large portion of the intermediate steps visibly correspond to multiples of quantum of conductance G_0 and $2G_0$. This implies the stable formation of an initial filament composed of few oxygen vacancies, as depicted in figure 4.8(a). More interestingly, there are no previous reports in literature regarding the observation of quantized conductance state during the set process in HfO_2 based VCM/TCM devices.[113] Also, in general, sharp sets reported in literature are typically controlled by the presence of a current compliance or self-compliant devices to stop a hard breakdown from happening. Possible reasons for the existence of this intermediate weak filament and its stability in a small voltage range are discussed in the subsequent sections.

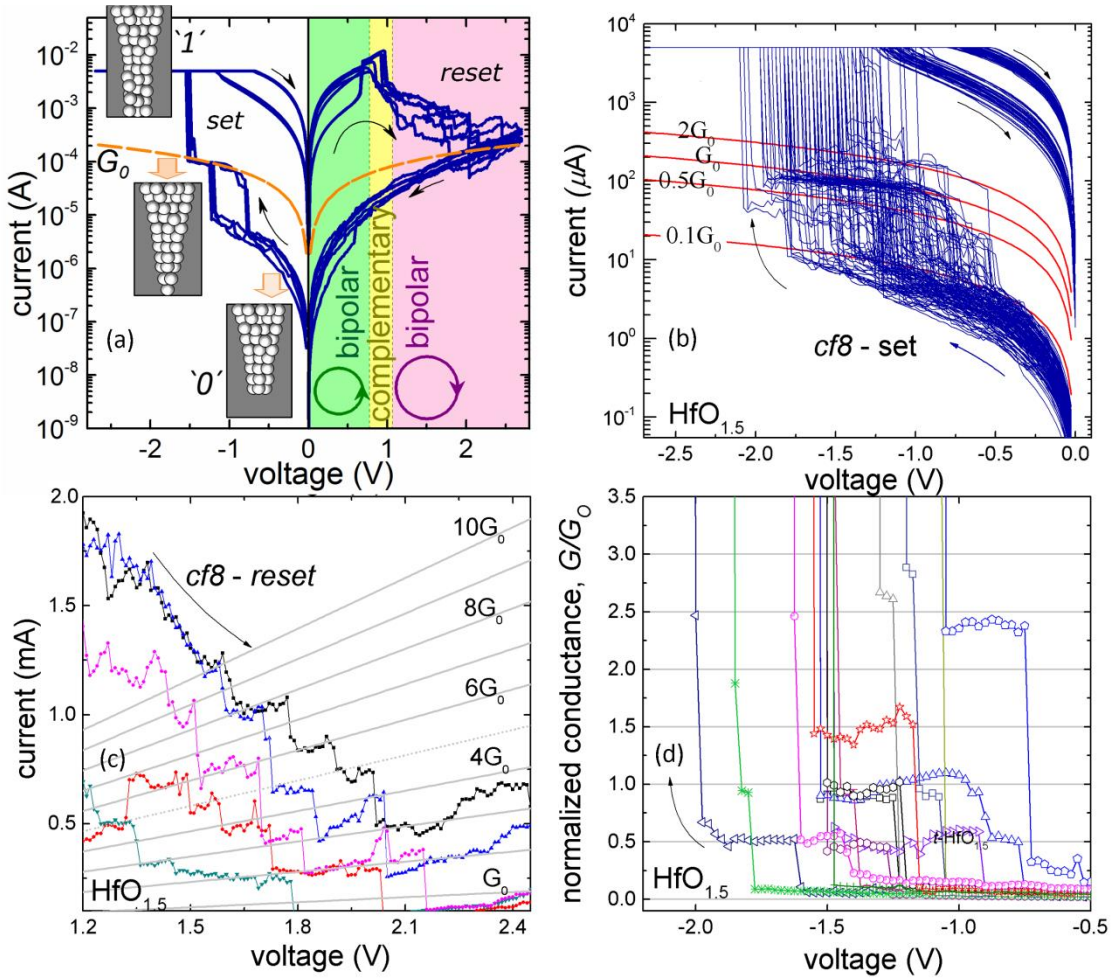

Figure 4.8: Analysis of quantized conductance states during cf8- bipolar resistive switching (BRS) operations in tetragonal like $HfO_{1.5}$. (a) Plot containing all the I-V curves which showed an intermediate step in set selected from 256 consecutive cycles. The intermediate sets are compared to arbitrary currents for quantized conductance levels for $0.5G_0$, G_0 and $2G_0$ (b) G-V plot corresponding to (a) for select cycles showing the existence of half integer multiples of G_0. (c) I-V plots of five representative *cf8*-reset data showing the presence of quantized conductance levels up to 10 G_0.

A more careful analysis of these intermediate steps corresponding to $G \sim G_0$ is shown in the G-V curves in figure 4.8(d), using selected data spanning the range of discrete conductance steps. Here, we see that current steps attributed to half-integer multiples of G_0 are also possible, though observed less frequently. In the presence of a weak filament, the current flowing through the device can be expressed as $I = N_{ch}\beta G_0$, where N_{ch} is the number of oxygen vacancy channels and β corresponds to the fraction of voltage that drops at the cathode.[113, 233] The existence of half integer multiples of G_0, more frequently observed in VCMs,[108, 113] has been suggested to be either due a difference in chemical potential of the electrodes[108] sometimes related to the symmetry (β) of voltage drop[113] or due to the absence of spin degeneracy arising from a weak magnetism in oxygen vacancies.[113] Recent theoretical study also suggest fractional quantum conductance levels in HfO_2 like 0.35 G_0 arising from definitive position of the first and second oxidized vacancy in the filament, which might explain the few conductance steps in between 0.1 G_0 and 0.5 G_0.[234] Further, the analysis of

multiple reset steps during the *cf8* reset in *t*-$HfO_{1.5}$ as shown for a few cycles in figure 4.8(c) also showed the presence of quantized conductance steps up to $10G_0$. The contrasting response of Pt/*m*-HfO_2/TiN in comparison to Pt/*t*-$HfO_{1.5}$/TiN, where no traces of quantization were found during the reset or set processes at room temperature, will be considered in more details in the next section.

To investigate the impact of lower temperature on the occurrence of quantum conductance states during switching, the cf8-BRS operation was performed at a lower temperature of 6 K, as shown in figure 4.9(a). The frequency of occurrence of intermediate steps at 6 K was much reduced with the initial set step leading to the intermediate conductance ($G \sim G_0$) are found to merge in to a single step. Interestingly, the set voltages for 128 cycles at 6 K were found to be increased in comparison to 128 cycles performed at 300 K before cool-down, as shown in figure 4.9(b). At 6K, the maximum set voltages were found to be ~ 3.0 V which is higher than the forming voltages of ~ -2.2 V at room temperature. This additionally suggests a link between the strength of the filament and the observation of quantum conductance states. Similar to intermediate steps during set, the occurrence of intermediate states during reset were also found to be decreased in frequency with less degree of adherence to multiples of G_0, as shown in figure 4.9(c). These results are not in agreement with other literature, where the occurrence and stability of quantum conductance steps were suggested to improve at 4 K in a Ti/HfO_2/TiN device. [116] This is perhaps related to a modified or strengthened filament due to higher set voltages at 6 K, which also is found largely suppresses the occurrence of coexisting f8-BRS (see figure 4.9(a) in comparison to 4.8(a)).

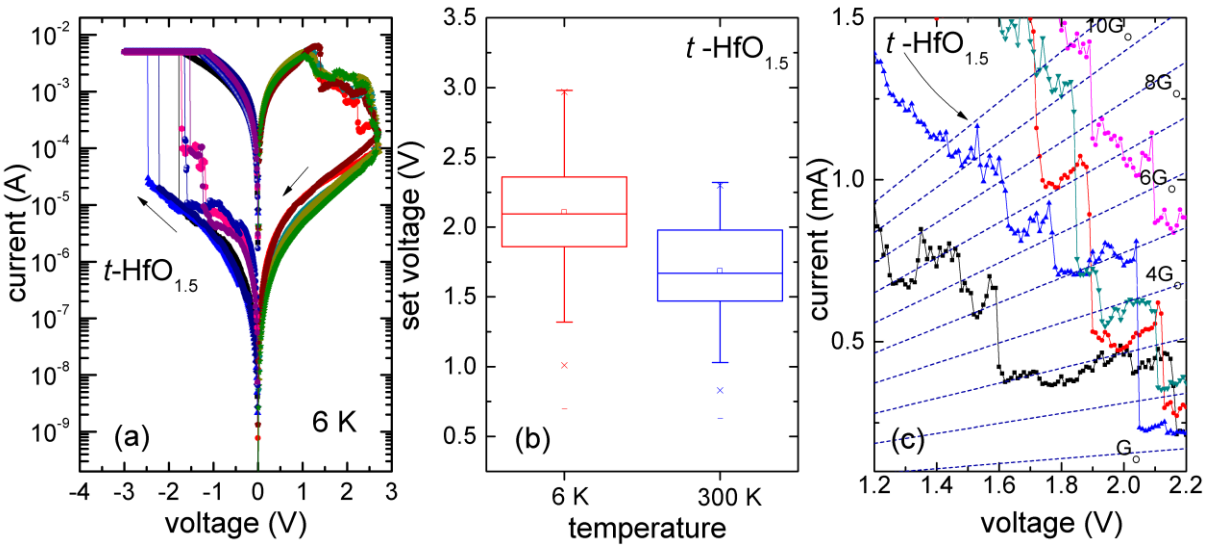

Figure 4.9: (a) cf8- BRS operation in Pt/*t*-HfO_x/TiN devices at 6K. (b) Box plots of set voltages for 128 cycles at 6 k and 300 K, (c) reset I-V plots of five representative *cf8*-reset data compared to quantized conductance levels up to 10 G_0.

4.3.4. Qualitative model of switching modes

Based on the differences in the strength of filament formation and initial oxygen vacancy concentration, we now discuss the partially occurring switching modes. In figures 4.10 and 4.11, a schematic model of the switching mechanisms is suggested to explain all the observed switching modes in Pt/*m*-HfO_2/TiN (depicted by *M1-M4*) and Pt/*t*-HfO_x/TiN (*T1-T4*), respectively. In general, in HfO_2, the switching is due to the transport of oxygen ions assisted by electric field and thermal effects related to Joule heating. The BRS is largely dominated by electric field driven migration of oxygen ions, indicated by vertical (blue) arrows. In URS, the Joule heating which is more dominant can lead to a concentration gradient driven diffusion (according to Fick's law) as well as a temperature gradient driven thermophoresis (Soret effect),[20, 118, 235] both represented by horizontal (red) arrows for simplicity. The competing Soret and Fick forces ultimately lead to the set and reset process, respectively during a unipolar switching. The direction of the arrows roughly represents the net force driving the migration of oxygen.

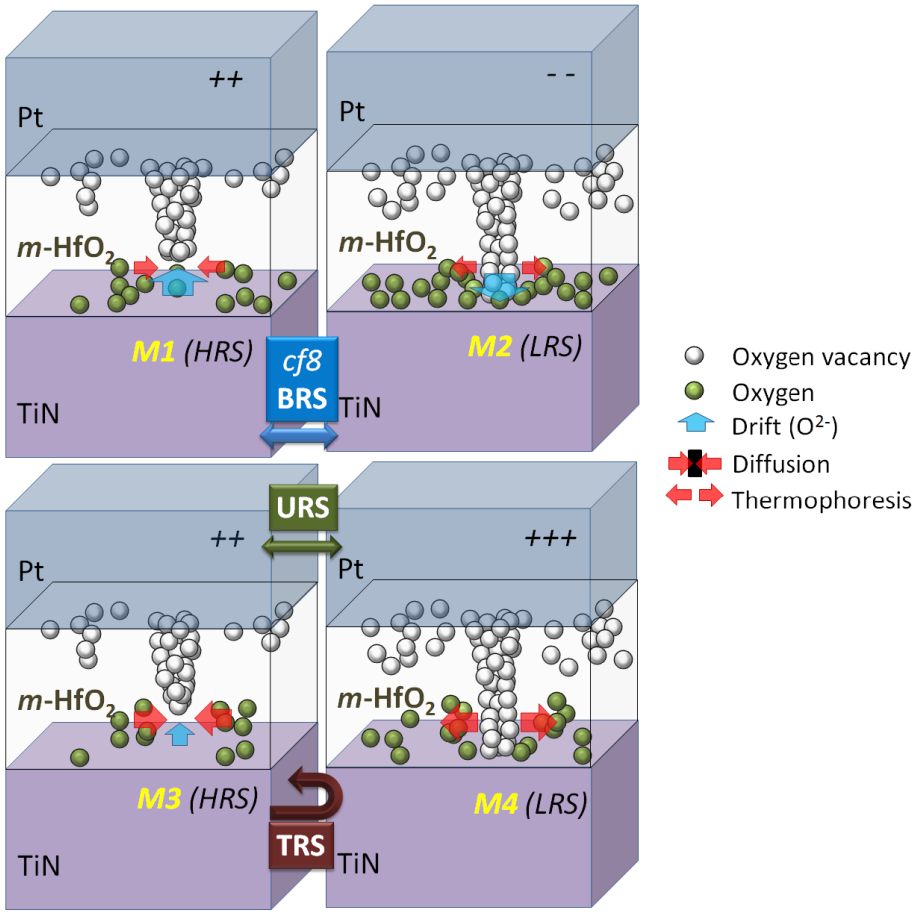

Figure 4.10: A schematic qualitative model of switching modes in Pt/*m*-HfO_2/TiN (depicted by *M1-M4*). The transition *M1* ⇔ *M2* corresponds to *cf8*-bipolar resistive switching (BRS); the transition *M3* ⇔ *M4* corresponds to unipolar resistive switching (URS), and *M3* ⇒ *M4* ⇒ *M3* to threshold resistive switching (TRS).

To understand the switching behavior in *m*-HfO_2, it is again worth noting that a similar reset process using Pt anode is found in the URS and *cf8*-BRS modes. URS operation is interestingly possible only in the positive polarity due to the presence of electrode asymmetry where TiN electrode is expected to act as the more active electrode. The CF rupture during this common reset using Pt anode can be aided by both the electric field and thermally driven Fick diffusion. The CF rupture location however remains a matter of debate. Goux *et al.* suggested that the reset behavior is due to an anodic re-oxidation process happening near the Pt anode.[56] This was supported by the argument that no reliable unipolar reset was possible in TiN/HfO_x/TiN devices unlike Pt/HfO_2/Pt devices, thereby concluding that Pt plays an essential role in the reset process.[150] However, Nardi *et al.* later reported a coexisting unipolar and complementary resistive switching in TiN/HfO_x/TiN devices.[40, 57] This anomaly might be related to the very delicate device symmetry which is easily broken during fabrication due to the higher reactivity of TiN in comparison to Pt as well as possibly the oxygen stoichiometry of HfO_x which is not well considered. On the other hand, Yu *et al.* ascribed the CF rupture to likely happen at the HfO_x/TiN interface,[104] citing a low electron occupation probability near the TiN cathode as the possible explanation, wherein a higher electron occupation near the Pt anode reduces the capture cross section of electron occupied V_O to O^{2-} interstitials.[236] Moreover, coexisting unipolar and bipolar switching in Pt/HfO_x/TiN devices have been well simulated assuming the reset process to proceed via recombination of $V_{\ddot{O}}/O^{2-}$ pair happening near the TiN cathode.[236] Therefore, the switching model in figures 4.10 and 4.11 are suggested on the premises that the reset process common to *cf8*-BRS and URS with positive bias to Pt happens at the anode (TiN)/oxide interface. The concept of dependence of thermal effects on oxygen stoichiometry suggested in the model is applicable regardless of the rupture location.

In the *m*-HfO_2 stack, the transition ***M1⇔M2*** corresponds to ***cf8*- BRS** as shown in figure 4.10. In the set process involving the negative bias on Pt (M2), electric field and Soret forces act symbiotically to cause oxygen vacancy clustering. During the URS mode (*M3 ⇔ M4*), on the other hand, the set process (M4) involves a positive polarity where the thermally driven Soret forces are more dominant over the electric field which acts against oxygen anions moving into the filament region. The filament rupture in the *cf8*-BRS/URS (M1,M3) modes will take place due to electron depletion in oxygen vacancies ($V_O \rightarrow V_{\ddot{O}} + 2e^-$) followed by recombination with O^{2-} ions migrating from TiN cathode as well as by thermal diffusion due to a concentration gradient of oxygen. The higher reset currents compared to set current compliance (I_{CC}) suggests that the process is dominated by electron depletion.[237] However, the reset dynamics during URS (figure 4.5(b)), is cumulatively sharper and more abrupt in

nature, in comparison to resets in *cf8*-BRS (figure 4.5(a)), hinting that the diffusion process dominates (larger horizontal arrows in figure 4.10) causing a more abrupt filament rupture during unipolar reset.

In addition to *cf8*-BRS and URS, threshold switching can also occur corresponding to the transition *M4⇒M3⇒M4*. For example, a change in behavior from unipolar switching operation to threshold switching has been observed on increasing the operation temperatures in NiO based RRAM.[43] The coexistence of unipolar and threshold operation on DC cycling could be explained by a reduced heat dissipation leading to further oxygen diffusion/drift back into the filament which becomes dominant at voltages slightly lower than the set voltage. The higher oxygen stoichiometric and insulating nature of *m*-HfO_2 probably leads to very low thermal conductivity. Under these circumstances, small variations in filament morphology from cycle to cycle might become sufficiently large for CF instability leading to the observed threshold switching which is reportedly favored under conditions of low heat dissipation.

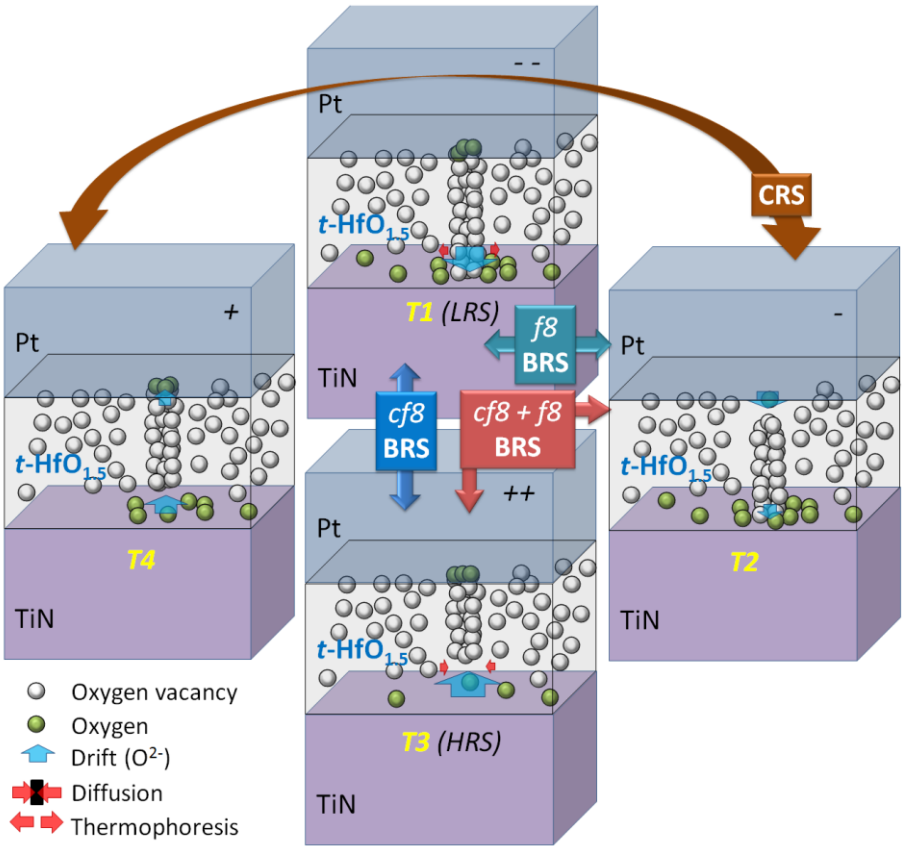

Figure 4.11: A schematic qualitative model of switching modes in Pt/ *t*-$HfO_{1.5}$/TiN (*T1-T4*). *cf8*-BRS is shown as *T1* ⇔ *T3, f8*- BRS as *T1* ⇔ *T2* and complementary resistive switching as *T4* ⇔ *T1* ⇔ *T2*.

Now we consider the switching operation in *t*-$HfO_{1.5}$ based devices, as depicted in figure 4.11. One can expect that the higher electrical conductivity of *t*-$HfO_{1.5}$ will translate to

higher thermal conductivity of the oxygen deficient matrix, similar to experimental observations in oxygen deficient tantalum oxide.[238] High thermal conductivity would lead to a larger heat dissipation which strongly reduces the Joule heating induced thermophoresis, thereby suppressing the occurrence of unipolar and threshold switching modes, which indeed is the case. In the *cf8*-BRS mode (*T1* ⇔ *T3*) which is analogous to that observed in *m*-HfO_2, the reset process involves CF rupture near the $HfO_{1.5}$/TiN interface, but is largely driven by field induced ionic drift with comparably lower contribution from Fick diffusion as shown in figure 4.11 in stack *T3*. Similarly, the set process (*T1*) involves field induced generation of Frenkel defect pairs followed and drift of oxygen interstitials expedited by Joule heating induced thermophoresis. This leads to the case of observation of intermediate quantized conductance states ($G \sim G_0$) during the set process in *cf8*-BRS, which can be attributed to stable atomic sized CF presumably a single oxygen vacancy chain. Such a multi-step set process was obtained in the model of CF evolution using a stochastic simulator for HfO_x based devices and further verified for devices with Pt and TiN electrodes.[239] The conducting filament evolution was then modelled to proceed via the formation of a thin fine filament followed by lateral expansion of the filament.[239] However, both the processes happen simultaneously in stoichiometric HfO_2 leading to a sharp set dynamics. In $HfO_{1.5}$, the initial filament formation is expected to happen at lowered voltages similar to electroforming due to the presence of pre-existing oxygen vacancies via field induced migration of oxygen ions. The lateral expansion which is largely due to thermophoresis presumably follows only at higher voltages when Joule heating is sufficiently high to overcome the heat dissipation. Such a fine single/few vacancy filaments thus formed at first is likely responsible for the quantized conductance states as observed during the set.

The existence of *f8*- BRS and CRS is presumably due to the lower forming voltage in *t*-$HfO_{1.5}$ ($V_F \sim$ -2.2 V), where the reset voltages during the *cf8*- BRS mode are in the same voltage range of operation (2.7 V). As mentioned before, this weak overall redistribution of oxygen ion profile in *t*-$HfO_{1.5}$ during electroforming likely leads to a more uniform filament geometry (more cylindrical than conical) in comparison to *m*-HfO_2, thereby allowing a weaker switching to occur simultaneously at the Pt/*t*-HfO_x interface which coexists with *cf8*-BRS. The reset process can therefore act as a positive forming process where oxygen ions migrate towards the top electrode interface. This allows a weaker (occurring at lower voltages) *f8* type BRS (*T1* ⇔ *T2*) arising from field driven oxygen ion migration close to the Pt/*t*-HfO_x interface, which translates to the modulation of Schottky interface. In this *f8* - BRS mode, the LRS to HRS ratio is much reduced. The better stability of *f8* type BRS using a dedicated positive electroforming might be due to driving more oxygen ions towards the Pt interface.

Since both interfaces now can play an active role, a complementary resistive switching operation (*T4* ⇔ *T1* ⇔ *T2*) becomes possible, as also observed in TiN/HfO_2/TiN and other back to back symmetric devices where by symmetry two active electrodes are present. In the CRS mode, the filament rupture occurs depending on the polarity at the cathode *and* anode. Therefore, in Pt/*t*-HfO_x/TiN devices, by adjusting the operating voltages, multiple and coexisting switching modes (CRS with *f8* and *cf8* types of BRS) can be achieved.

4.3.5. Quantum Point Contact modelling of HfO_x RRAM

The observation of discrete conductance steps is a strong evidence of atomic scale configuration of the filament occurring in the midst of the switching process. Therefore, the high resistance states during the *cf8*-bipolar operation, common to stoichiometric and oxygen deficient HfO_x, were further analyzed using the QPC model. The *I-V* characteristics of the HRS states up to a voltage of 1.1 V obtained during the endurance cycles (figure 4.7(c-d)) were fitted to obtain the barrier parameters related to the rupture region. In the high resistance state obtained after the deep reset (V_{reset} = 2.7 V), the conductance was found to be less than G_0, corresponding to more than one re-oxidized vacancy, as depicted in figure 4.12. The barrier thus formed can be assumed to have a width and thickness of r_B and t_B, respectively.

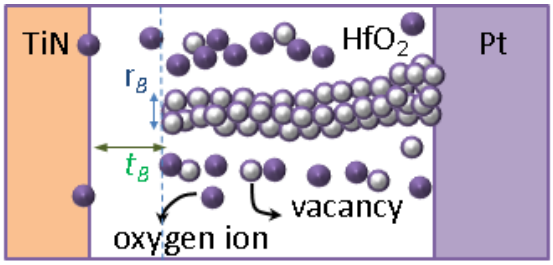

Figure 4.12: Schematic of filament ruptures during cf8-BRS showing the formation of barrier with a thickness (t_B) and radius (r_B).

As shown in figure 4.13(a), using equation 1.8, an iterative least squared error estimation based fitting was implemented using MATLAB to obtain the barrier height (Φ_B) and curvature parameter (α_B). Experimental fit of I-V was performed assuming an approximation of a single channel (N =1) and an asymmetric filament[240] rupture (β = 1). The scatter plot of the fit parameters, Φ_B and α_B over the first 128 cycles is shown in figure 4.13(b). The individual scatter region is similar to that observed by Lian *et al.*,[233] where the scatter in α-Φ plot was approximately captured by a region of $\alpha\Phi$ = constant. In figure 4.13(b), the region corresponding to stoichiometric *m*-HfO_2 is shifted to higher values of $\alpha\Phi$ with respect to the scatter region of *t*-$HfO_{1.5}$, suggesting different values of constants for the

devices. This is probably related to the different shape of the filament (more/less conical or cylindrical). The obtained range of values for the barrier height (0.5-2.5 eV) is consistent with values lower than the large band gap of hafnium oxide. Under the same reset conditions, higher leakage current in the HRS of oxygen deficient *t*-$HfO_{1.5}$ devices resulted in a lowered barrier height of 0.58 eV in comparison to 1.75 eV for *m*-HfO_2. This can be understood to be due to the larger oxygen vacancy concentration in oxygen deficient hafnium oxide, perhaps resulting in residual vacancies closer to the ruptured region. The surrounding vacancies would act as trap sites lowering the overall barrier by assisting in electronic transport via trap assisted tunneling. Further, equations 1.7 and 1.10 were used to obtain the barrier thickness (t_B) and radius (r_B), respectively. The effective electron mass, m* for hafnium oxide was assumed to be 0.11 m_0.[241] The average value of extracted fit parameters α and Φ, comparing *m*-HfO_2 and *t*-$HfO_{1.5}$ for the first 128 cycles is shown in table 4.2. Considering a separation of 0.26 nm between the nearest oxygen vacancies,[115] the barrier thickness of 0.71 or 0.62 nm in the HRS state can be assumed to be due to two to four oxidized vacancies in the rupture region. The barrier radius of 0.54 nm for *m*-HfO_2 device in comparison to 0.84 nm for *t*-$HfO_{1.5}$ likely represents a much broader tip of the conducting filament (more cylindrical) region in oxygen deficient devices.

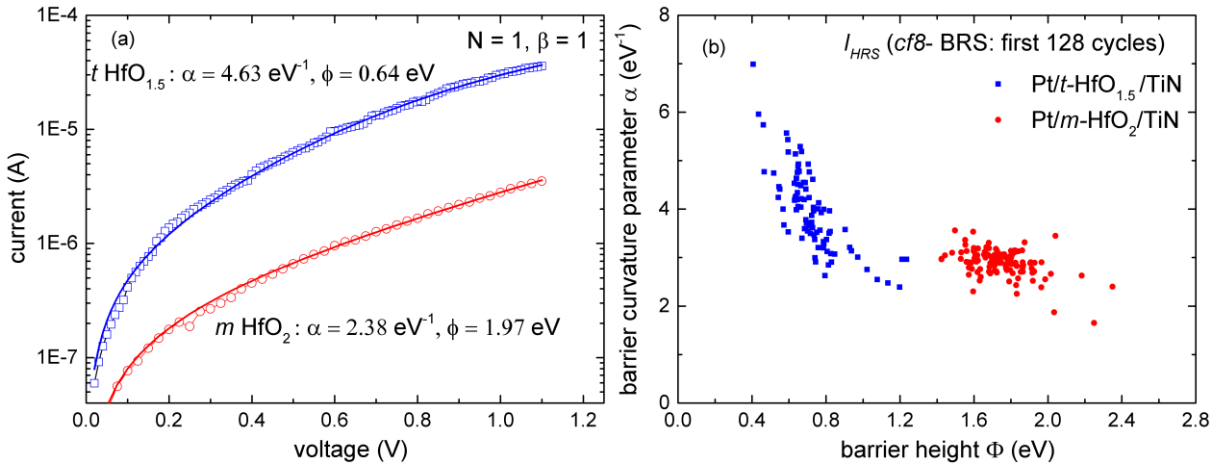

Figure 4.13: (a) Typical least squared estimation based fit (line) of the experimental data (hollow balls) of high resistance state after *cf8*-BRS using the QPC model for *m*-HfO_2 and *t*-$HfO_{1.5}$ based Pt/HfOx/TiN devices. Appropriate fitting yields the barrier height and (Φ) and curvature parameter (α),(b) The scatter plot of the fit parameters, Φ_B and α_B over the first 128 cycles.

Avg. 1st 128 cycles	HRS: *m*-HfO_2	HRS: *t*-$HfO_{1.5}$
ϕ (eV)	1.75	0.58
α (eV^{-1})	2.9	3.94
t_B (nm)	0.71	0.62
r_B (nm)	0.54	0.84

Table 4.2: Average values of extracted parameters for HRS after *cf8*-BRS using the QPC model for *m*-HfO_2 and *t*-$HfO_{1.5}$ based Pt/HfO_x/TiN devices

As indicated earlier from the endurance data (figure 4.7), the resistance of the HRS was found to drift upon switching for 1024 cycles. The nature of this drift can be related to cumulative movement of oxygen ions towards or away from the filamentary rupture region. QPC model was applied to extract the barrier parameters for up to 1024 cycles to better understand the impact of repeated voltage stress during endurance test. Figure 4.14 shows the box plots of extracted fit parameters forϕ, α, t_B and r_B from the QPC model. The 1024 cycles were grouped into eight consecutive regions of 128 cycles each. It is clear that the spread of the data is much larger for oxygen deficient *t*-$HfO_{1.5}$ for all the extracted parameters. This is related to the large concentration of pre-existing vacancies close to the filament leading to a larger variation in the HRS from cycle to cycle. It is interesting to note that mean value of ϕ, α, *and* r_B is found to converge towards each other. However, the mean value of barrier thickness is found to remain more or less constant. The constant barrier thickness suggest that the changes in barrier height (ϕ) arise due to local chemical changes in the defect density in the rupture region. Thus, the lowering of barrier height (ϕ) in stoichiometric *m*-HfO_2 can be assumed to take place from gradual loss of oxygen ions away from the filamentary region leading to a more conducting region, as reported by Kumar *et al.* as the eventual cause of failure of the HRS in a Pt/HfO_x/TiN device.[86] Conversely, the increase in the barrier height in oxygen deficient *t*-$HfO_{1.5}$ devices can be assumed to take place due to oxygen accumulation near the filamentary region. Here, repeated cycles can be understood to bring more oxygen ions near the filament due to thermophoresis.

These results of convergence of extracted barrier parameters in HfO_2 and $HfO_{1.5}$ based devices indicate that, at an intermediate oxygen stoichiometry, the drift related to oxygen accumulation or loss near the filamentary rupture region might be reduced. Therefore, it can be assumed that, an intermediate stoichiometry between x=1.5 and x=2 is perhaps the best suited for stable operation of a Pt/HfO_x/TiN device with reduced drift for high endurance

RRAM. This is in agreement with an optimal stoichiometry of x=1.5-1.75 reported for stable filament nucleation obtained by theoretical calculations.[72]

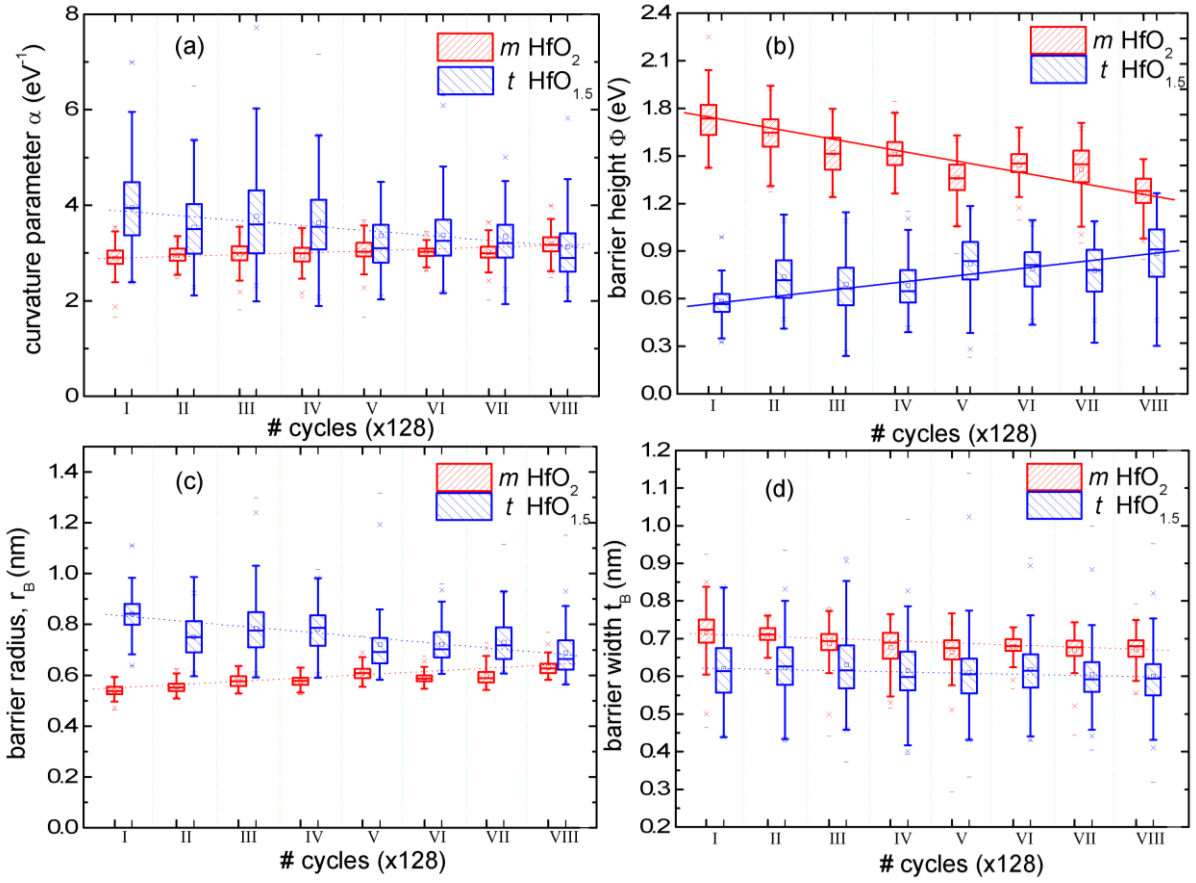

Figure 4.14: Evolution of of extracted parameters (a) curvature parameter (α_B), (b) barrier height (Φ_B), (c) barrier thickness (t_B) and (d) radius (r_B), for the HRS during *cf8*-BRS for 1024 cycles after using the QPC model for *m*-HfO_2 and *t*-$HfO_{1.5}$ based Pt/HfO_x/TiN devices. The 1024 cycles are grouped in to eight consecutive regions of 128 cycles each.

4.4. Resistive switching modes in Pt/TaO_x/TiN devices

Further, we describe the switching behavior of the oxygen engineered TaO_x devices. Here, the as-deposited devices of Pt/Ta_2O_{5-y}/TaO_x/TiN under different oxidation conditions (0.2-2.5 sccm) are considered. After a negative electroforming (I_{cc} =1 mA), *cf8*-type bipolar resistive switching could be realized in all the devices as shown in figure 4.15(a) for the 100th switching cycle in 0.2, 1.0, 1.5 and 2.5 sccm devices. The devices show stable bipolar resistive switching (BRS) up to 100 cycles with a sharp set (CC =5 mA) and a gradual reset starting at 0.8 V up to 2 V. In comparison to less reduced TaO_x devices, the set voltage dropped from around −1.0 V to −0.7 V in the 0.2 sccm device. This can be attributed to easier oxidation of the TaO_x, which acts as the electrode in the 0.2 sccm device in comparison to the TiN electrode in less reduced devices. On the other hand, the resistance ratio between the low

resistance state (LRS) and the high resistance state (HRS) during BRS operation was lowest in the 0.2 sccm device (~10) and highest in the 1.0 sccm device (~100).

In order to investigate the conduction mechanisms, the reset *I-V* curve is plotted double logarithmically as shown in figure 4.15(b) for 0.2 and 1.0 sccm devices showing the lowest and highest HRS resistances. The LRS conduction shows a simple ohmic behavior. In the HRS, the *I-V* curve shows ohmic like behavior at low voltages, and then crosses over to a quadratic behavior ($I \propto V^2$, Child's law) between 0.3 V and 1 V. This transport behavior can be described in terms of a trap-controlled space charge limited current (SCLC) conduction model.[242, 243] A third region of steep increase in current ($I \propto V^m$, m > 2) would then be due to trap filling. The traps are formed by the oxygen vacancies in the TaO_x layer. A trap filling transition (TFT) is found to occur at a voltage, V_{TFT}, of 1.3 V (0.2 sccm) and 0.98 V (1.0 sccm). A trend in the V_{TFT} was not observed with increasing oxygen flow and might be due to the inherent and competing nature of switching mechanisms, which affects the nature of the ruptured filament region, as described below.

Interestingly, only the 1.5 sccm and 2.0 sccm devices were found to exhibit unipolar RS (URS) as shown for the 2.0 sccm device in figure 4.15(c). This URS is characterized by a positive reset operation up to 2.0 V followed by a set operation up to 3.5 V (CC = mA) with resistance ratios as high as 200, and stable up to 100 DC cycles. On the URS operation, the LRS and HRS conduction showed a similar Ohmic and SCLC behavior, respectively. In the set operation, at bias voltages higher than 2 V, the slope of the double logarithmic *I-V* curve is decreasing to nearly 2 again ($I \propto V^2$). This can be explained by complete trap filling, which then leads to a trap free SCLC regime.[244] Figure 4.15(d) shows the effect of higher positive bias voltage and currents up to 50 mA on the devices where URS was not observed. Interestingly, a positive set was not possible in the 1.0 sccm devices, whereas the set in the 0.2 sccm device resulted in a hard breakdown. Similar to HfO_x, URS can be understood to be due to the greater contribution of Joule heating, where a temperature gradient assisted oxygen vacancy clustering and a concentration gradient induced thermal diffusion of vacancies are supposed to play the major role in the set and reset processes. The thermal conductivity of TaO_x thin films has been shown to increase with higher oxygen deficiency.[238] It can, therefore, be concluded that the unipolar switching in oxygen deficient thin films (at oxygen flows lower than 1.5 sccm) is impeded by a lower concentration gradient and higher heat dissipation. This, in turn suppresses the Soret force required to form a filament in the case of positive bias to Pt, as observed for the 1.0 sccm stack in figure 4.15(d). In the highest

oxidized films (2.5 sccm), the local Joule heating is maximum, and thus, an insufficient heat dissipation[20] causes a transition from unipolar to threshold resistive switching.

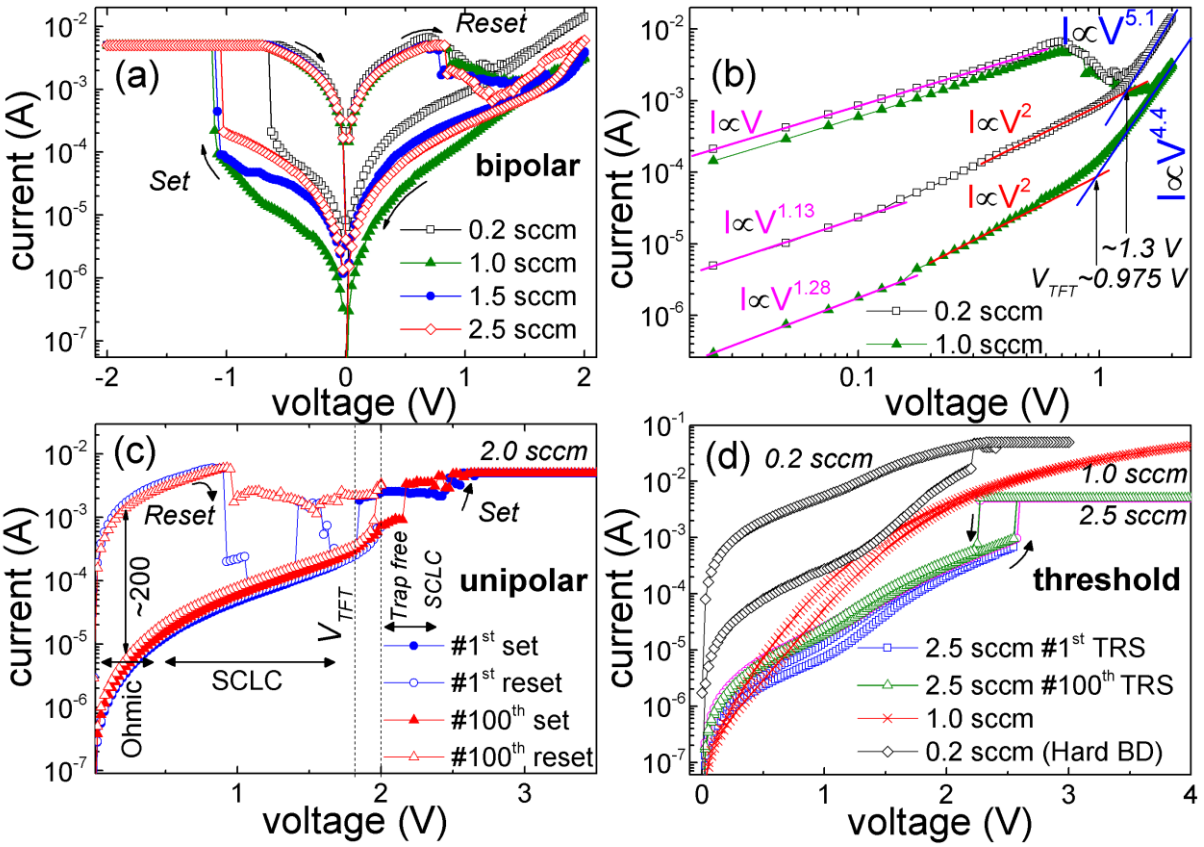

Figure 4.15: (a) Bipolar RS (100th cycle) at a CC of 5 mA of Pt/Ta_2O_{5-y}/TaO_x/TiN devices deposited at various oxygen flows. (0.2-2.5 sccm) (b) log I vs. log V plot of the reset process for 0.2 and 1.0 sccm. The upper and lower curves correspond to the LRS and HRS, respectively. (c) Unipolar RS at CC of 5 mA in the 2.0 sccm device up to 100 cycles (d) Threshold RS in the 2.5 sccm device; Note the absence of positive set in the 1.0 sccm device and a hard breakdown in the 0.2 sccm device. From published results.[245]

Summarizing, these observations in oxygen engineered Pt/Ta_2O_{5-y}/TaO_x/TiN devices are consistent with and similar to the Pt/HfO_x/TiN devices, where unipolar and threshold switching was observed at higher oxygen stoichiometry. These results of partial occurrence of switching modes depending on the oxygen stoichiometry (x), as summarized in table 4.3, would contribute to developing a unified switching model giving a deeper insight into the switching mechanism. A thin oxidized surface layer (~ 1.5 nm at 0.2 sccm flow) was sufficient to contribute to electroforming as well as stable bipolar switching. Interestingly, the *f8* (eight-wise) type BRS and complementary RS, were absent in the Pt/TaO_x/TiN devices. In addition to a stable bipolar RS, unipolar and threshold RS were found to coexist in the devices at higher oxygen contents. While the low resistance state displayed ohmic behavior, in the high resistance state, the current-voltage characteristics could be described by a trap controlled space charge limited conduction model with the oxygen vacancies acting as trap sites. These clear evidences of the dependence of multiple switching regimes on the oxygen

stoichiometry are significant to a better understanding for future design of TaO_x based RRAM devices with appropriate functionality.

During, the *cf8*-type BRS operation at 5 mA, the obtained maximum resistance ratio of ~ 100 led to HRS states with a conductance much higher than the quantum conductance (G_0). Therefore, quantum conductance states could not be observed. Quantum conductance states have been observed in TaO_x based devices in literature.[246] It is expected that smaller device sizes in future would allow operation at lower currents, allowing to possibly investigating the impact of oxygen stoichiometry on quantum conductance.

Table 4.3: Oxygen stoichiometry dependence of the partial occurrence of resistive switching modes in devices of $Pt/Ta_2O_{5-y}/TaO_x/TiN$.

$Pt/Ta_2O_{5-y}/TaO_x/TiN$ x ~ oxygen flow	**Bipolar**	**Unipolar**	**Threshold**	**Remarks**
0.2 sccm	✓	X	X	CF forms only in Ta_2O_{5-y} surface layer, Hard breakdown on URS attempt, TaO_x is highly conducting
0.6 sccm	✓	X	X	CF forms across the oxide bilayer
1.0 sccm	✓	X	X	High thermal conductivity suppresses URS and TRS at flows ≤ 1.0 sccm
1.5 sccm	✓	✓	X	
2.0 sccm	✓	✓	X	Low thermal conductivity
2.5 sccm	✓	X	✓	Very Low thermal conductivity

4.5. Bipolar resistive switching in La and Ta doped HfO_x based devices

Various defect engineering approaches are typically used to lower the vacancy formation energy and enhance the stability of the filament. In addition to direct oxygen stoichiometry engineering in HfO_2 based RRAM as described in the previous sections, impurity doping[139, 247] is another approach reported in literature. Ab-initio calculations of the filament-oxygen vacancy interaction suggest that weak p-type as well as n-type dopants play a role in reducing the forming voltages as well as stabilizing the filaments.[248] The better uniformity achieved in switching parameters have been reported to occur at the cost of a reduced ON/OFF ratio.[248] Substitutional dopants can also cause phase transitions in HfO_2 from its monoclinic phase to higher symmetry structures,[73] where oxygen vacancies play a stabilizing role in the new structure.[249, 250] However, most of the studies reported in literature have been for amorphous

hafnium oxide. In this study of impurity doping, the impact of p-type (La) and n-type (Ta) dopants have been investigated in polycrystalline hafnium oxide based devices with observed structural transformations.

Among various deposition techniques in literature for doping, chemical vapor deposition techniques like ALD usually involve the use of functionalized precursors and growth of multilayers via alternating cycles.[251 252] However, the residual impurities from precursors like carbon can act as dopants, and might change the switching dynamics and even interact with and adversely affect the oxygen deficient filament.[253, 254] Physical vapor deposition techniques like sputtering and reactive molecular beam epitaxy or ion implantation can therefore be effective in isolating and understanding the intrinsic effect of dopants due to the absence of other impurities. Moreover, the MBE deposition employed in this work has the advantage of co-deposition of the dopant and hafnium cations allowing control over the dopant concentration to a greater extent.

The model Pt-oxide-TiN electrode configuration used in this work is particularly interesting due to their large resistance window of operation. The typical dc bipolar resistive switching (BRS) dynamics as observed experimentally in Pt/HfO_x/TiN involves a sharp set process followed by a deep progressive reset process. The sharp nature of the set is due to a positive feedback to the current increase from Joule heating thus accelerating the process.[138] Therefore, a gradual transition during the reset due to a negative feedback has sometimes been preferably used for adaptive learning in synaptic devices based on Pt/HfO_x/TiN.[133] Though completely gradual nature of this reset has been reported before in such devices typically using multilayers or ion-implantation,[139, 255] material aspects responsible for the dynamics of such gradual/sharp transitions during reset require further investigations for reliable operation. Therefore, this study additionally aims at investigating the role of lanthanum (trivalent) and tantalum (pentavalent) dopants on the dynamics of set and reset in polycrystalline HfO_x based devices using the model Pt-oxide-TiN electrode configuration

After a negative bias electroforming process to the Pt electrode, all the devices (Ta, La doped) showed *cf8*-BRS switching behavior. Obtained trends of electroforming voltages with doping are not considered in detail, due to the many effects which contribute towards affecting it. Both lanthanum and tantalum leads to increased crystallization temperature of hafnium oxide. Therefore, the as-deposited films at same deposition temperatures lead to decreased crystallinity with increasing doping concentration. The forming voltage is therefore dependent on doping concentration as well as crystallinity. Also, it was recently reported that sub stoichiometry is necessary to activate the effect of dopants in lowering the forming

voltages.[256] However, the as-deposited films in this study were deposited under high oxidation conditions. Moreover, minor decrease or increase in forming voltages with doping was not obvious and fell in the range of the intrinsic variability of forming voltages in polycrystalline HfO_x and needs further investigation.

First, we consider the lanthanum doped hafnium oxide films of 17 nm thicknesses which were electrically analyzed in the Pt/oxide/TiN configuration. After electroforming under a negative polarity to Pt electrode with a current compliance (CC) of 0.1 mA, a cf8 type bipolar resistive switching (BRS) was observed for the non-doped device monoclinic phase of hafnia (*m*-HfO_2) as shown in figure 4.16(a). The *cf8*-BRS for the non-doped device involved a negative sharp set in the range of -1.5 to -2.5 V (CC = 10 mA) followed by a progressive positive reset starting at 0.8 V up to 2.7 V. The device was subject to an endurance of 512 cycles with cycles 1, 50, 100 and 500 shown in the figure with slight reduction in the resistance ratio. The reset process varies from cycle to cycle and can be characterized by series of progressive reset steps with increasing voltage interrupted by sharp transitions. In comparison, the BRS in the device with highest lanthanum concentration (~17.8%) with a cubic structure is shown in figure 4.16(b) under the same CC during set and reset voltage of 2.7 V. Here, the set process involved a similar sharp transition. However, the reset process was found to be gradual in nature in the entire range starting from 0.9 V to 2.7 V, which remained so for 512 consecutive cycles. Interestingly, a lower slope of reset induced current decrease up to 2.0 V transitions to a higher slope beyond 2.1 V. This might be due to the increased contribution of thermally induced Fick diffusion at higher voltages (< 2.1 V). Figure 4.16(c) shows the cumulative probability distribution of the low and high resistance states for 512 cycles of the devices with La doping concentrations of 0, ~8, ~12 and ~18 %. The resistances were taken at a read voltage of -0.2 V. It is evident that the ON/OFF ratio increases with increased concentration of lanthanum doping. A five-fold increase in the resistance ratios from ~435 (non-doped) to ~2500 (17.8% La) can been observed. However, theoretical calculations have generally predicted a decrease in ON/OFF ratio upon doping due to higher defect concentration in the high resistance state.[248] This anomaly might be related to the different crystallinity of the films deposited at same temperature. At higher lanthanum concentration, a lower crystallinity is expected to lead to a lowered contribution of grain boundaries to the current in the HRS. The transition from a sharp to gradual reset behavior might be related to filament stabilization arising from La doping. As shown in figure 4.16(d), the oxygen vacancies near the filament can be understood to be pinned to lanthanum ions. Thus, the uniformly distributed dopants would induce a uniform oxidation of vacancies

during the rupture process. This effectively allows all the intermediate resistance states to be observed during the reset step, thus enabling the transition to a gradual reset process.

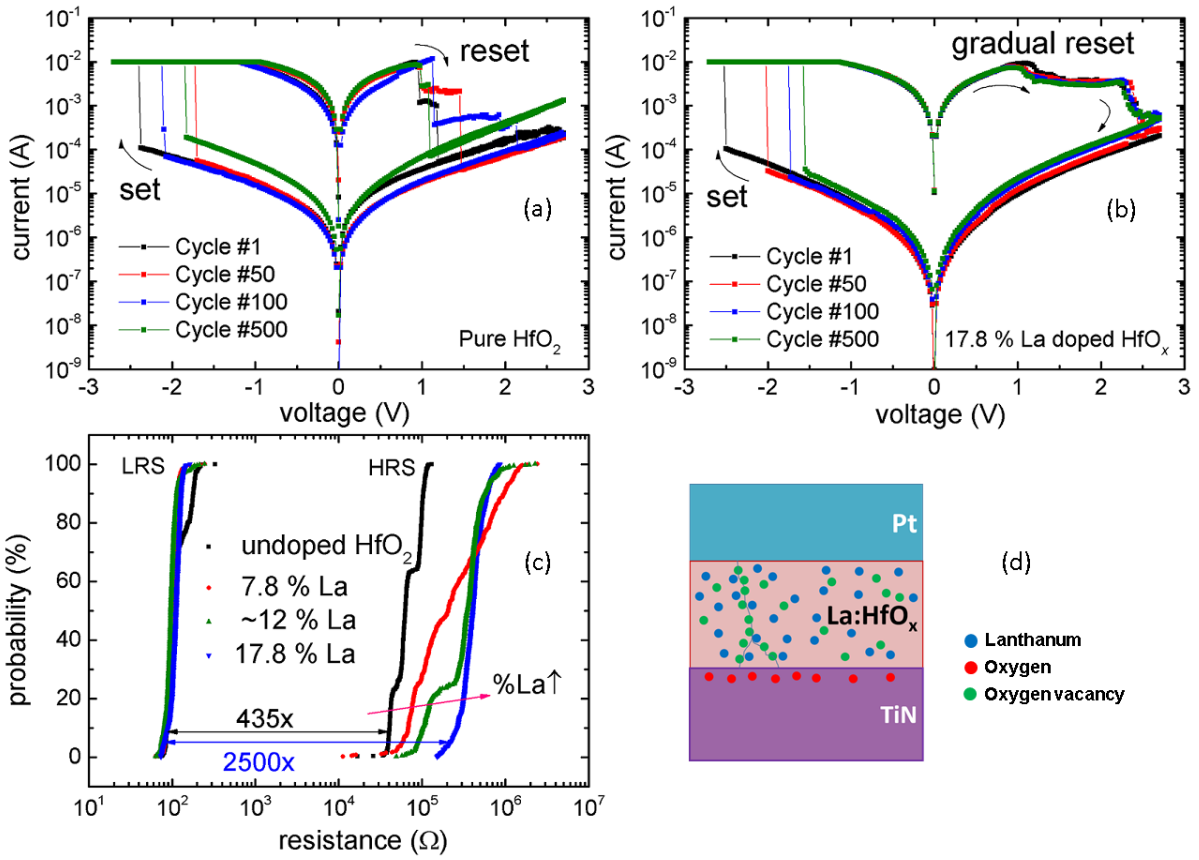

Figure 4.16 : *Cf8*-type bipolar resistive switching characteristics (V_{SET} < 0) up to 500 cycles with a current compliance of 10 mA of DC quasi-static switching response in Pt/ HfO_x/TiN based devices grown by MBE for (a) pure and stoichiometric monoclinic phase of hafnia (*m*-HfO_2) showing single sharp sets and mixed sharp/gradual reset. (b) Gradual reset dynamics achieved using an oxygen vacancy stabilized cubic phase of c-La:HfO_{2-x} by doping up to 17.8% lanthanum. (c) Cumulative probability distribution of resistances in the HRS and LRS for 512 cycles. (d) Schematic diagram of the filament formation in La doped HfO_{2-x} with oxygen vacancies near the La sites, aiding in the uniform or gradual reset.

Next, we consider the tantalum doped hafnium oxide films of 22 nm thicknesses in the Pt/oxide/TiN configuration. After electroforming, the *cf8* type bipolar resistive switching (BRS) was analyzed for the non-doped device monoclinic phase of hafnia (*m*-HfO_2) as shown in figure 4.17(a). The *cf8*-BRS for the non-doped device involved a negative sharp set in the range of -1.8 to -2.5 V (CC = 5 mA) followed by a progressive positive reset starting at 0.8 V up to 2.7 V. The reset process varies from cycle to cycle and can be characterized by series of progressive reset steps with increasing voltage interrupted by sharp transitions. The device was subjected to endurance up to 256 cycles with cycles 1, 50, 100 and 200 shown in the figure. It is to be noted that, the tantalum doping study was performed at much higher oxidation conditions (2.5 sccm, 350W) to allow for complete oxidation of tantalum in

comparison to oxidation conditions (1.2 sccm/200W) for lanthanum doping. This can explain the increased ON/OFF ratio of ~ 1000 for the non-doped device in figure 4.17(a) compared to ~ 435 for the non-doped device in figure 4.16(a). At a higher Ta concentration obtained at 0.25 Å/s, the *cf8*-BRS in the device is shown figure 4.17(b) under the same CC during set and a reset voltage of 2.7 V. In the endurance study of DC switching up to 256 cycles, it was observed that the ON/OFF ratio is reduced quickly beyond 50^{th} cycle. At the highest Ta concentration obtained at 0.45 Å/s, the *cf8*-BRS in the device is shown figure 4.17(c) under similar operating current and voltage. More interestingly, the switching behavior is similar to $Pt/TaO_x/TiN$ devices, where a SCLC type conduction mechanism is observed in the HRS state. The ON/OFF ratio is found to be lowest at the highest Ta concentration. Similar to La doping, the reset process was found to change from sharp transitions to a gradual behavior, which remained so for 256 consecutive cycles.

Figure 4.17(d) shows the cumulative probability distribution of the current levels at low and high resistance states of the devices with Ta rates of 0, 0.15, 0.025 and 0.045 Å/s. The currents were obtained at a read voltage of -0.2 V. The highest ON/OFF ratio is obtained in the device deposited at 0.015 Å/s rate of tantalum evaporation, corresponding to the nominal Ta concentration required for a transition to tetragonal structure. This is similar to La doping, where the lowered crystallinity likely plays a role in slightly increasing the ON/OFF ratio. However, at higher concentration of tantalum doping (0.025 and 0.045 Å/s), it is evident that the distribution of HRS currents is found to show a region with gradually increasing currents (lowered ON/OFF ratio) corresponding to the first few cycles $<50^{th}$. This is typically followed by a sharp transition to higher current levels typically up on further endurance ($>50^{th}$ cycle). After this sharp transition region is reached, the reduced ON/OFF ratio is found to remain more or less constant. The nature of this gradual decrease in ON/OFF ratios until a more stable ratio is reached is not very clearly understood. This might perhaps be related to mixed nature of tantalum oxide and tantalum oxide occurring at higher Ta concentration. This was reflected in the XRD results in previous chapter, where higher Ta concentration was associated with a much reduced intensity of the peaks. This suggests that beyond a certain dopant concentration where the tetragonal transition takes place, a much reduced crystallinity or mixed amorphous phases of individual oxides of hafnium and tantalum oxide may be present. This would lead to competing conduction mechanisms of TAT and SCLC, as was observed in the $Pt/HfO_x/TiN$ and $Pt/TaO_x/TiN$ devices, respectively. It can therefore be assumed that a TAT type conduction mechanism dominated by traps occurs at lower Ta concentration (0.015 Å/s). At higher Ta concentration (0.025 Å/s and 0.045 Å/s), the SCLC type conduction mechanism in TaO_x type devices is found to be dominant.

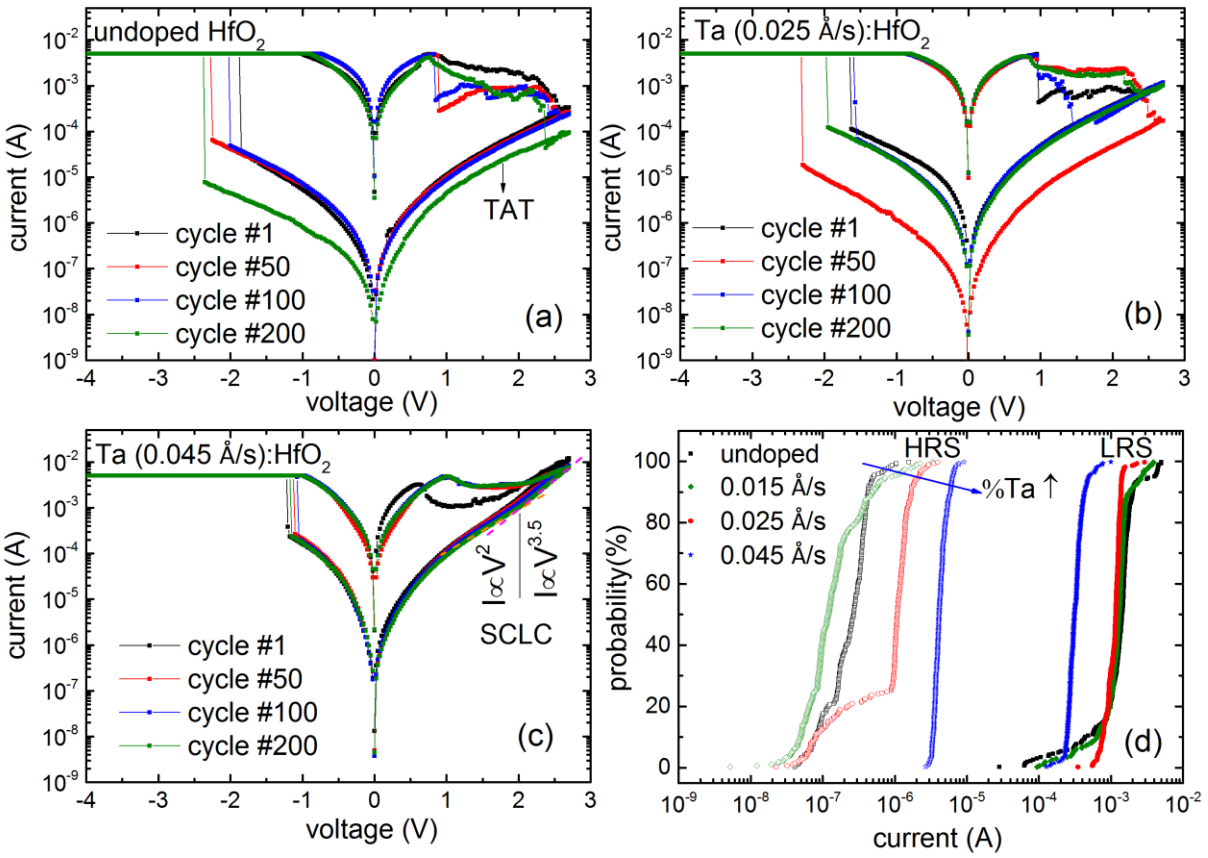

Figure 4.17: *Cf8*-type bipolar resistive switching characteristics (V_{SET} < 0) up to 200 cycles with a current compliance of 5 mA of DC quasi-static switching response in Pt/ HfO_x/TiN based devices grown by MBE for (a) pure and stoichiometric monoclinic phase of hafnia (*m*-HfO_2) showing single sharp sets and mixed sharp/gradual reset; DC quasi-static switching for predominantly tetragonal phase of *t*-Ta:HfO_x at Ta doping of (b) 0.025 Å/s and (c) 0.045 Å/s. (d) Cumulative probability distribution of resistances spanning 256 cycles in the HRS and LRS for various Ta doping concentrations.

4.5.1. Resistive switching dynamics in La doped HfO_x devices

A gradual or analog switching dynamics during this filament formation/rupture can also be exploited as an electronic synapse for application in neuromorphic computing.[134, 149] Here, synaptic plasticity is emulated in the RRAM devices through the application of pulses of increasing amplitudes or using trains of identical pulses.[136, 149] In order to study the viability of multilevel switching, preliminary electrical characterization was carried out in the ~18 % La doped hafnium oxide devices exhibiting gradual reset characteristics. Figure 4.18(a) show the BRS operation of the device at different operating voltages, keeping the current compliance during set at 10 mA. The device in the low resistance state was initially reset at a lower voltage (+1.0 V) followed by the set operation (up to -2.7 V at CC =10 mA). At lower operating stop voltages for reset, the dynamics of the set operation was also found to be gradual in nature. This is likely due to the largely electric field driven set operation taking place at lower voltages, corresponding to a VCM type operation. The set operation was found to exhibit abrupt characteristics after reset at higher reset stop voltages, suggesting the larger

role of thermal effects and coexistence of VCM and TCM. Owing to the gradual nature of the reset, the reset voltages could be progressively increased up to 2.7 V to obtain intermediate resistance states. As shown in the figure 4.18(a), up to seven different resistance states have been stabilized in the device. This suggests that multi-level switching can be achieved in the Pt/La-doped HfO_x/TiN devices with intermediate resistances spanning more than three orders of magnitude.

In addition to finite multi-level states achieved using DC switching, more number of intermediate resistance states can be stabilized by application of voltage pulses for exploitation as a synaptic device. Therefore, voltage pulses with a time width of 5 μs were applied on the top electrode to modulate the device resistances. In the case of the set process, the transition was found to be abrupt, when the pulse amplitudes were increased in steps of 0.5 V. Figure 4.18(b) shows the abrupt transition from a resistance of 2 MΩ to 200 Ω, obtained after applying a train of five identical pulses of -2.1 V amplitude. At voltages lower than -2.1 V, as shown for -2.05 V, no significant switching was observed on applying a train of 20 voltage pulses. This is similar to DC switching, where a sharp set is obtained due to the positive feedback of Joule heating to the increase in current. Therefore, the abrupt nature of set prevents the use of set operation for synaptic applications. However, Brivio *et al.* reported the possibility of gradual set operation using a train of pulses, in the resistance range spanning from 10 kΩ to 1 kΩ.[149] The gradual set operation was obtained in Pt/HfO_x/TiN devices, where complementary switching was additionally observed. It is notable that, in our work, intermediate resistance states corresponding to quantum conductance states were obtained during the set process in highly oxygen deficient $HfO_{1.5}$ based devices, where complementary switching was also observed. It is therefore expected that a gradual set dynamics can therefore be obtained in the oxygen deficient $HfO_{1.5}$ devices up on appropriate pulse train induced switching operations.

Unlike the set process, the reset process was more responsive to pulses of increasing amplitudes. As shown in figure 4.18(c), an increase in the pulse amplitudes from 1.2 V to 2.7 V gradually increased the resistance by up to four orders of magnitude. The reset operation (or synaptic depression) could also be achieved by using a train of identical pulses as shown in figure 4.18(d), for pulse trains with amplitudes of 2.4 V and 2.45 V. However, it was found that the resistance could only be increased by up to two orders of magnitude in the range 1-100 kΩ by applying a pulse train of constant amplitude. These results are in agreement with that reported by Yu *et al.* using Pt/HfO_x/TiO_x/HfO_x/TiO_x/TiN devices, where a gradual reset operation using pulse trains was exploited to implement synaptic functionality for

neuromorphic visual systems.[133] The gradual nature of reset in Pt/La:HfO_x/TiN devices used in this study can also be similarly utilized for synaptic applications. The combination of highly oxygen deficiency and lanthanum doping may lead to ideal synaptic devices with concurrent set as well as reset operations.

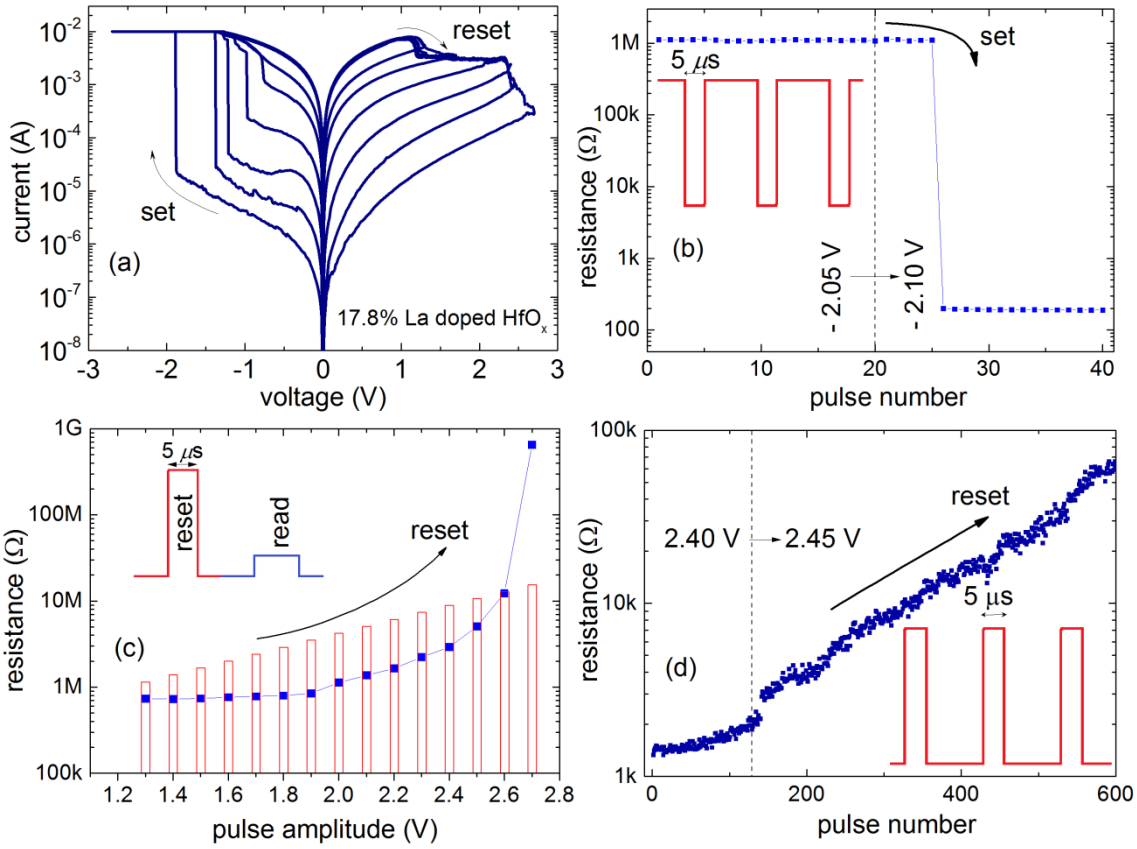

Figure 4.18: (a) DC Bipolar resistive switching characteristics in in Pt/La-doped HfO_x/TiN devices showing multilevel swicthing capability obtained at different reset stop voltages; Pulse switching with pulse widths of 5 μs using (b) pulse trains (20x) of amplitudes -2.05 V and -2.1 V leading to a set operation during the -2.1 V pulse train, (c) Pulse amplitude ramp from 1.2 V to 2.7 V leading to a reset operation and (d) pulse trains (20x) of amplitudes 2.40 V and 2.45 V leading to a gradual reset operation.

5. Conclusions and Outlook

HfO_x/TiN based RRAM devices have huge potential as next generation non-volatile memories and in neuromorphic electronics. This thesis mainly deals with two defect engineering approaches: (1) oxygen engineering in HfO_x and TaO_x and (2) impurity doping (La, Ta) in HfO_x, as realized by reactive molecular beam epitaxy (RMBE), and its impact on resistive switching behavior in the Pt/oxide/TiN device configuration. Oxygen stoichiometry engineering studies in TaO_x based devices, helped to establish oxidation condition for further Ta doping in HfO_x, and additionally served to study the impact of oxygen stoichiometry in RRAM devices. The work also includes the epitaxial growth of TiN electrodes by RMBE. The major results of this thesis are summarized below.

5.1. Summary

5.1.1. TiN thin films by reactive molecular beam epitaxy

1. TiN films were grown on the commercially relevant sapphire and silicon substrates by RF plasma assisted reactive MBE. In spite of a high lattice mismatch, epitaxial growth with smooth surfaces (streaky RHEED and XRR oscillations) as well as low resistivity (<150 $\mu\Omega$.cm) were achieved, thus making them suitable for application as epitaxial electrodes for many applications.
2. Epitaxial TiN(100) [100]||Si(100) [100] thin film growth on Si (001) substrates was aided by a thin Ti buffer layer which was quickly exposed to nitrogen to form TiN, to minimize any interface reaction. At the deposition temperature of 650 °C, high titanium and nitrogen flux rates were found to be necessary to achieve 2D film growth characterized by a streaky RHEED pattern as well as reduced interface reaction leading to smooth interfaces.
3. Epitaxial TiN (111) films grown on Al_2O_3(0001) substrates were found to grow with twin domains corresponding to TiN[110],[101] twins||Al_2O_3 [10-10]. A transition from 3D to 2D growth was achieved by increasing the Ti/N flux ratio, resulting in a streaky RHEED pattern in slightly nitrogen deficient TiN films, at a deposition temperature of 760 °C. Even higher Ti/N flux ratio during growth led to reaction at the interface with the substrate.
4. Higher superconducting transition temperature was obtained at low Ti/N flux ratios in TiN films. A highest T_C onset of 5.32 K and lowest resistivity of 21 $\mu\Omega$.cm was achieved in the case of polycrystalline TiN/Si(001). For both epitaxial TiN(100) and TiN(111) films, the resistivity was an order of magnitude higher with T_C typically lower than 4 K.. This

suggests that nitrogen incorporation by diffusion during growth was reduced in TiN films of higher crystalline quality.

5.1.2. Oxygen engineering in HfO_x and TaO_x

1. Defects have been introduced intrinsically in polycrystalline HfO_x thin films, via oxygen stoichiometry engineering using reactive molecular beam epitaxy (MBE). The films were deposited at a CMOS compatible temperature of 320 °C in contrast to an earlier work of oxygen engineering performed at 700 °C. Stoichiometric films crystallize in a monoclinic symmetry (*m*-HfO_2). With reducing oxidation condition in RMBE, the as-grown films grown at deposition temperature showed a transition to a predominantly oxygen vacancy stabilized tetragonal-like phase of hafnium oxide (*t*-HfO_x). Further reduction of the oxidation conditions resulted in the hexagonal structure of Hf metal with interstitial oxygen (*hcp*-HfO_x). An empirical phase diagram was suggested accounting for the phase formation under different oxidation conditions and temperature.
2. By oxygen stoichiometry engineering, the density of the as-grown HfO_x thin films could be tuned in a wide range from 9.6 g cm^{-3} (close to bulk density of HfO_2) to 12.12 g cm^{-3} (less than the metal Hf density of 13.3 g cm^{-3}). The stoichiometry of predominantly tetragonal hafnium oxide thin films was determined by EDS based quantification to be close to x = 1.5-1.6. Hard X-ray photoelectron spectroscopy confirmed the presence of sub-stoichiometric hafnium oxide and defect states near the Fermi level in *t*-HfO_x films. Angle dependent XPS studies confirm that the deficient layer is conducting and capped by a thin oxidized surface layer (< 3 nm), presumably developed after exposure to ambient conditions.
3. Tantalum oxide thin films (TaO_x) with engineered oxygen contents grown by RF-plasma assisted molecular beam epitaxy were found to be amorphous at a deposition temperature of 440 °C. The density of the TaO_x films change consistently with oxygen contents in the range of 12.4 to 9.0 g/cm^3. When exposed to atmosphere, an oxidized Ta_2O_{5-y} surface layer forms with a maximal thickness of 1.2 nm depending on the initial oxygen deficiency of the film, as confirmed by XRR. X-ray photoelectron spectroscopy studies show that multiple sub-stoichiometric compositions occur in oxygen deficient TaO_x thin films, where all possible valence states of Ta including metallic Ta were observed.

5.1.3. Electroforming in HfO_x/TiN and TaO_x/TiN devices

1. The presence of intrinsic oxygen vacancies is responsible for the large reduction of electroforming voltages to close to operating voltages in *t*-HfO_x based devices compared to *m*-HfO_2. Electroforming process of polycrystalline HfO_x/TiN devices by directly contacting

and applying positive bias to an Au coated tip showed that the forming voltage of stoichiometric *m*-HfO_2 layers increases linearly with layer thickness (~ 7.5 V for 20 nm thickness). Using strongly reduced oxygen deficient *t*-HfO_x thin films grown on polycrystalline TiN/Si(001) substrates, the thickness dependence of the forming voltage is strongly suppressed. Instead, an almost constant forming voltage of about 3 V is observed up to 200 nm layer thickness. This is related to filament formation in the surface layer of *t*-HfO_x/TiN formed up on using a Au tip contacted directly. After direct tip forming, switching occurs for all samples in the oxidized HfO_2 surface layer of a few nanometer thickness while the highly oxygen deficient thin film itself merely serves as an oxygen vacancy reservoir. Such a thickness independent forming voltage would offer technological advantages in terms of flexibility relaxed to requirements in thickness variation. A similar positive electroforming in Pt/*t*-HfO_x/TiN devices was more gradual in nature and reliable switching could not be obtained. This suggests uniform oxygen depletion across the interface of the oxidized surface layer in the presence of a deposited top electrode of Pt in comparison to an Au tip.

2. Similar to HfO_x, the forming voltage of TaO_x/TiN devices can be tuned in a large range according to the chosen amount of oxygen deficiency. A thin oxidized surface layer was sufficient to contribute to electroforming. Devices of the form Pt/Ta_2O_{5-y}/TaO_x/TiN exhibit highly tunable forming voltages of 10.5 V to 1.5 V with decreasing oxygen contents in TaO_x.

5.1.4. Resistive switching modes in oxygen engineered Pt/oxide/TiN devices

1. A comparative study of the resistive switching (RS) behavior for *t*-$HfO_{1.5}$ and *m*-HfO_2 based Pt/HfO_x/TiN devices were undertaken. All different switching modes (figure and counter figure eight types of bipolar RS, unipolar RS, threshold RS and complementary RS) were found to depend on the degree of oxygen deficiency and can be chosen by appropriate operating voltages in the same Pt/HfO_x/TiN device configuration. So far, this was previously realized only in different stacks or materials combinations. Thus, these observations open up the possibility of understanding and theoretical modelling of the various switching modes in a single device configuration.
2. The most stable bipolar (counter-eightwise) RS was possible in *m*-HfO_2 as well as in *t*-$HfO_{1.5}$ based devices for up to more than 1000 tested DC cycles. Similarly, the stable *cf8*-bipolar RS occurs in all the TaO_x devices irrespective of oxygen content (0.2-2.5 sccm).
3. Unipolar RS and threshold RS was found to coexist up on endurance tests only in the stoichiometric *m*-HfO_2, which were found to be completely absent in in *t*-$HfO_{1.5}$ based

devices. Similarly, unipolar RS was found to coexist with BRS only at moderately high oxidation conditions (1.5 sccm and 2.0 sccm), which transforms to a threshold switching behavior in the devices grown under highest oxidation condition (2.5 sccm). This suggests that thermochemical switching or Joule heating is dominant only at higher oxygen stoichiometry.

4. Bipolar (counter-eightwise and eightwise) RS and complementary RS was observed only in the *t*-$HfO_{1.5}$ based devices. This can be attributed to a weaker filament formation in *t*-$HfO_{1.5}$ devices, allowing the switching to occur at both interfaces in the oxygen deficient device. The bipolar (eightwise) RS in oxygen deficient *t*-$HfO_{1.5}$ occurs at low operating voltages and currents with self-compliance characteristics during set, thus suitable for low-power applications.
5. Based on oxygen ion transport, a simplified model was developed accounting for all types of switching modes Pt/HfO_x/TiN devices. The oxygen vacancy concentration is the key factor in manipulating the balance between electric field and Joule heating during formation, rupture (reset), and reformation (set) of the conductive filaments in the dielectric. The model is discussed for samples which are limiting cases (close to stoichiometric and highly oxygen deficient HfO_x), and therefore allow a clear distinction of the different cases. Additionally, it can be applied to understand and classify the switching behavior of a large variety of similar RRAM devices produced under different (and intermediate) oxidation condition.

5.1.5. Quantum effects and switching dynamics in defect engineered Pt/HfO_x/TiN

1. The bipolar (*cf8*) RS operation in Pt/HfO_x/TiN devices, occurring independent of oxygen stoichiometry typically consists of a single sharp set process and a progressive deep reset process with large abrupt decrease in current, due to dominant thermal effects in stoichiometric *m*-HfO_2. By using ~18% La-doped HfO_x based device, a completely gradual *reset* behavior with a higher ON/OFF ratio (~2500) could be achieved during the bipolar reset operation. The switching was found to be stable up to 500 DC cycles. This is likely related to filament stabilization around the dopant sites allowing a uniform rupture during *reset*.
2. In case of oxygen deficient *t*-$HfO_{1.5}$ devices, the presence of higher vacancy concentration and lowered thermally driven ionic/vacancy motion leads to the observation of intermediate steps occurring during the set process corresponding to integer and half-integer multiples of quantum conductance states at room temperature. The progressive reset process was also found to consist of relatively smaller abrupt jumps, corresponding to multiple discrete of quantum conductance states near the region of $G_0 < G < 10G_0$.

These are related to the better stabilization of intermediate atomic size filament constrictions during the switching process. Occurrence of these intermediate quantum conductance states, especially during the typically abrupt *set* process, is likely aided by a weaker filament and better thermal dissipation in the highly oxygen deficient devices. The possibility to stabilize intermediate states ($G \approx N.G_0$) composed of single (or few) vacancies in the filament at room temperature opens up further pathways to control the switching at an atomic scale via oxygen engineering.

RMBE in general is a great tool for oxygen stoichiometry engineering in oxides, which would in turn allow to better understand the switching mechanism and tailor the switching behavior of RRAM devices. Moreover, oxygen engineering and impurity doping thus shows great promise towards design of devices for reliable multi-level switching and synaptic applications.

5.2. Outlook

It was shown that studies on oxygen engineering in transition metal oxide has great potential in revealing the various phenomena occurring during resistive switching in resistive switching devices, and thus pave the way for realizing multiple potential applications of RRAM devices in the future.

As of now, all the as-grown films after deposition have been transferred from the deposition unit for top electrode deposition via the ambient resulting in surface oxidation. Surface oxidation of oxygen deficient films in ambient can be prevented by *in-situ* deposition of top electrode by MBE itself. However, such a case needs device fabrication via lithography and etching to form true forming free devices, and needs investigation in the continued work. Moreover, smaller area ($< 1\ \mu m^2$) devices have to be realized using oxygen deficient hafnium oxide in view of practical applications. The impact of oxygen deficient devices with reduced forming voltages on the device to device variability has to be studied as well.

Since the switching dynamics can be influenced by a combination of factors like defect concentration, thermal conductivity, crystallinity etc., appropriate defect engineering is the key towards control over the switching dynamics as well as enhancement of yield in HfO_x-RRAM. In a recent work, based on ab initio calculations, Zhao et al. suggested that, oxygen non-stoichiometry is necessary to activate the dopant effect to significantly reduce the forming voltages.[256] This was suggested to be the reasons for inconsistent results observed in literature where doping was sometimes found to increase forming voltages. Therefore, it is important to study the impact of doping by changing the oxygen radical flow rate during deposition. This could lead to ideal devices for synaptic applications combining the intermediate multiple states obtained during the set (in oxygen deficient devices) and gradual reset obtained in

lanthanum doped HfO_2 devices. The next step would be to realize potentiation and depression via pulse switching operations in RRAM devices with optimized synaptic functionality.

List of figures

List of tables

Bibliography

1. D. J. Wouters, R. Waser and M. Wuttig, Proceedings of the IEEE **103** (8), 1274-1288 (2015).
2. C. S. Hwang, Advanced Electronic Materials **1** (6) (2015).
3. D. Ielmini, Semiconductor Science and Technology **31** (6), 063002 (2016).
4. ITRS, http://www.itrs2.net/itrs-reports.html (2015).
5. D. S. Jeong, R. Thomas, R. S. Katiyar, J. F. Scott, H. Kohlstedt, A. Petraru and C. S. Hwang, Rep. Prog. Phys. **75** (7) (2012).
6. H. S. P. Wong and S. Salahuddin, Nat. Nanotechnol. **10** (3), 191-194 (2015).
7. R. Waser and M. Aono, Nat. Mater. **6** (11), 833-840 (2007).
8. B.-E. Park, H. Ishiwara, M. Okuyama, S. Sakai and S.-M. Yoon, *Ferroelectric-Gate Field Effect Transistor Memories*. (Springer, 2016).
9. H.-S. P. Wong, C. Ahn, J. Cao, H.-Y. Chen, S. B. Eryilmaz, S. W. Fong, J. A. Incorvia, Z. Jiang, H. Li, C. Neumann, K. Okabe, S. Qin, J. Sohn, Y. Wu, S. Yu, X. Zheng, (https://nano.stanford.edu/stanford-memory-trends, accessed February 10, 2017.).
10. M.-J. Lee, C. B. Lee, D. Lee, S. R. Lee, M. Chang, J. H. Hur, Y.-B. Kim, C.-J. Kim, D. H. Seo, S. Seo, U. I. Chung, I.-K. Yoo and K. Kim, Nat Mater **10** (8), 625-630 (2011).
11. A. Kawahara, R. Azuma, Y. Ikeda, K. Kawai, Y. Katoh, Y. Hayakawa, K. Tsuji, S. Yoneda, A. Himeno, K. Shimakawa, T. Takagi, T. Mikawa and K. Aono, IEEE Journal of Solid-State Circuits **48** (1), 178-185 (2013).
12. T. Y. Liu, T. H. Yan, R. Scheuerlein, Y. Chen, J. K. Lee, G. Balakrishnan, G. Yee, H. Zhang, A. Yap, J. Ouyang, T. Sasaki, S. Addepalli, A. Al-Shamma, C. Y. Chen, M. Gupta, G. Hilton, S. Joshi, A. Kathuria, V. Lai, D. Masiwal, M. Matsumoto, A. Nigam, A. Pai, J. Pakhale, C. H. Siau, X. Wu, R. Yin, L. Peng, J. Y. Kang, S. Huynh, H. Wang, N. Nagel, Y. Tanaka, M. Higashitani, T. Minvielle, C. Gorla, T. Tsukamoto, T. Yamaguchi, M. Okajima, T. Okamura, S. Takase, T. Hara, H. Inoue, L. Fasoli, M. Mofidi, R. Shrivastava and K. Quader, presented at the 2013 IEEE International Solid-State Circuits Conference Digest of Technical Papers, 2013 .
13. G. Molas, G. Piccolboni, M. Barci, B. Traore, J. Guy, G. Palma, E. Vianello, P. Blaise, J. Portal and M. Bocquet, presented at the VLSI Technology, Systems and Application (VLSI-TSA), 2016 International Symposium on, 2016 .
14. P. Ranganathan, Computer **44** (1), 39-48 (2011).
15. E. J. Marinissen, B. Prince, D. Keltel-Schulz and Y. Zorian, presented at the Design, Automation and Test in Europe, 2005 .
16. S. Kimura, presented at the VLSI Technology, 2016 IEEE Symposium on, 2016 .
17. J. Borghetti, G. S. Snider, P. J. Kuekes, J. J. Yang, D. R. Stewart and R. S. Williams, Nature **464** (7290), 873-876 (2010).
18. S. Park, J. Noh, M.-l. Choo, A. M. Sheri, M. Chang, Y.-B. Kim, C. J. Kim, M. Jeon, B.-G. Lee and B. H. Lee, Nanotechnology **24** (38), 384009 (2013).
19. R. Waser, R. Dittmann, G. Staikov and K. Szot, Adv. Mater. **21** (25-26), 2632-+ (2009).
20. J. J. Yang, D. B. Strukov and D. R. Stewart, Nat. Nanotechnol. **8** (1), 13-24 (2013).
21. J. S. Lee, S. Lee and T. W. Noh, Applied Physics Reviews **2** (3) (2015).
22. S. Bagdzevicius, K. Maas, M. Boudard and M. Burriel, J. Electroceram. (2017).

23. Y. Zhou and S. Ramanathan, Critical Reviews in Solid State and Materials Sciences **38** (4), 286-317 (2013).
24. A. Asamitsu, Y. Tomioka, H. Kuwahara and Y. Tokura, Nature **388** (6637), 50-52 (1997).
25. G. I. Meijer, U. Staub, M. Janousch, S. L. Johnson, B. Delley and T. Neisius, Phys. Rev. B **72** (15), 155102 (2005).
26. E. Y. Tsymbal and H. Kohlstedt, Science **313** (5784), 181-183 (2006).
27. A. N. Shipway, E. Katz and I. Willner, in *Molecular Machines and Motors*, edited by J.-P. Sauvage, V. Amendola, R. Ballardini, V. Balzani, A. Credi, L. Fabbrizzi, M. T. Gandolfi, J. K. Gimzewski, M. Gómez-Kaifer, C. Joachim, A. E. Kaifer, E. Katz, T. R. Kelly, J. Liu, C. Mangano, P. Pallavicini, A. R. Pease, L. Raehm, M. Sano, J. P. Sauvage, J. P. Sestelo, A. N. Shipway, J. F. Stoddart, M. Venturi and I. Willner (Springer Berlin Heidelberg, Berlin, Heidelberg, 2001), pp. 237-281.
28. T. W. Hickmott, J. Appl. Phys. **33** (9), 2669-2682 (1962).
29. S. Jin, T. H. Tiefel, M. McCormack, R. A. Fastnacht, R. Ramesh and L. H. Chen, Science **264** (5157), 413 (1994).
30. S. Q. Liu, N. J. Wu and A. Ignatiev, Appl. Phys. Lett. **76** (19), 2749-2751 (2000).
31. A. Beck, J. G. Bednorz, C. Gerber, C. Rossel and D. Widmer, Appl. Phys. Lett. **77** (1), 139-141 (2000).
32. M. N. Kozicki, W. C. West, US Patent No. 5914893 (1999).
33. D. B. Strukov, G. S. Snider, D. R. Stewart and R. S. Williams, Nature **453** (7191), 80-83 (2008).
34. L. Chua, IEEE Transactions on circuit theory **18** (5), 507-519 (1971).
35. S. Vongehr and X. Meng, Scientific reports **5** (2015).
36. A. Sawa, Materials Today **11** (6), 28-36 (2008).
37. F. A. Kröger and H. J. Vink, J. Phys. Chem. Solids **5** (3), 208-223 (1958).
38. J. J. Yang, I. H. Inoue, T. Mikolajick and C. S. Hwang, MRS Bull. **37** (2), 131-137 (2012).
39. G. W. Burr, R. S. Shenoy, K. Virwani, P. Narayanan, A. Padilla, B. Kurdi and H. Hwang, J. Vac. Sci. & Technol. B **32** (4) (2014).
40. F. Nardi, S. Balatti, S. Larentis and D. Ielmini, presented at the Electron Devices Meeting (IEDM), 2011 IEEE International, 2011 .
41. M. Son, J. Lee, J. Park, J. Shin, G. Choi, S. Jung, W. Lee, S. Kim, S. Park and H. Hwang, IEEE Electron Device Lett. **32** (11), 1579-1581 (2011).
42. E. Linn, R. Rosezin, C. Kugeler and R. Waser, Nat Mater **9** (5), 403-406 (2010).
43. S. H. Chang, J. S. Lee, S. C. Chae, S. B. Lee, C. Liu, B. Kahng, D. W. Kim and T. W. Noh, Physical Review Letters **102** (2), 4 (2009).
44. C. Funck, S. Menzel, N. Aslam, H. Zhang, A. Hardtdegen, R. Waser and S. Hoffmann-Eifert, Adv. Electronic Materials **2** (7), 1600169-n/a (2016).
45. J. M. Goodwill, A. A. Sharma, D. Li, J. A. Bain and M. Skowronski, ACS Applied Materials & Interfaces **9** (13), 11704-11710 (2017).
46. S. Slesazeck, H. Mahne, H. Wylezich, A. Wachowiak, J. Radhakrishnan, A. Ascoli, R. Tetzlaff and T. Mikolajick, RSC Advances **5** (124), 102318-102322 (2015).
47. B. Govoreanu, G. S. Kar, Y. Y. Chen, V. Paraschiv, S. Kubicek, A. Fantini, I. P. Radu, L. Goux, S. Clima, R. Degraeve, N. Jossart, O. Richard, T. Vandeweyer, K. Seo, P. Hendrickx, G. Pourtois, H. Bender, L. Altimime, D. J. Wouters, J. A. Kittl and M.

Jurczak, presented at the Electron Devices Meeting (IEDM), 2011 IEEE International, 2011 .
48. H. Y. Lee, Y. S. Chen, P. S. Chen, T. Y. Wu, F. Chen, C. C. Wang, P. J. Tzeng, M. J. Tsai and C. Lien, Electron Device Letters, IEEE **31** (1), 44-46 (2010).
49. C. Walczyk, D. Walczyk, T. Schroeder, T. Bertaud, M. Sowinska, M. Lukosius, M. Fraschke, D. Wolansky, B. Tillack, E. Miranda and C. Wenger, IEEE Trans. Electron Devices **58** (9), 3124-3131 (2011).
50. Z. Wei, Y. Kanzawa, K. Arita, Y. Katoh, K. Kawai, S. Muraoka, S. Mitani, S. Fujii, K. Katayama, M. Iijima, T. Mikawa, T. Ninomiya, R. Miyanaga, Y. Kawashima, K. Tsuji, A. Himeno, T. Okada, R. Azuma, K. Shimakawa, H. Sugaya, T. Takagi, R. Yasuhara, K. Horiba, H. Kumigashira and M. Oshima, IEEE Int. Electron Dev. Meet. Tech. Dig. **293**, 5671467 (2008).
51. A. Wedig, M. Luebben, D.-Y. Cho, M. Moors, K. Skaja, V. Rana, T. Hasegawa, K. K. Adepalli, B. Yildiz, R. Waser and I. Valov, Nat. Nanotechnol. **11** (1), 67-+ (2016).
52. Y. Wang, Q. Liu, S. Long, W. Wang, Q. Wang, M. Zhang, S. Zhang, Y. Li, Q. Zuo, J. Yang and M. Liu, Nanotechnology **21** (4), 045202 (2010).
53. G. Du, C. Wang, H. Li, Q. Mao and Z. Ji, AIP Advances **6** (8), 085316 (2016).
54. S. B. Long, X. J. Lian, C. Cagli, X. Cartoixa, R. Rurali, E. Miranda, D. Jimenez, L. Perniola, M. Liu and J. Sune, Appl. Phys. Lett. **102** (18) (2013).
55. D. S. Jeong, H. Schroeder and R. Waser, Electrochem Solid-State Lett **10** (2007).
56. L. Goux, Y. Y. Chen, L. Pantisano, X. P. Wang, G. Groeseneken, M. Jurczak and D. J. Wouters, Electrochem Solid-State Lett **13** (2010).
57. F. Nardi, S. Balatti, S. Larentis, D. C. Gilmer and D. Ielmini, IEEE Trans. Electron Devices **60** (1), 70-77 (2013).
58. J. H. Yoon, S. J. Song, I.-H. Yoo, J. Y. Seok, K. J. Yoon, D. E. Kwon, T. H. Park and C. S. Hwang, Adv. Funct. Mater. **24** (32), 5086-5095 (2014).
59. M. Hasan, R. Dong, H. J. Choi, D. S. Lee, D.-J. Seong, M. B. Pyun and H. Hwang, Appl. Phys. Lett. **92** (20), 202102 (2008).
60. R. Muenstermann, T. Menke, R. Dittmann and R. Waser, Adv. Mater. **22** (43), 4819-4822 (2010).
61. A. Odagawa, H. Sato, I. H. Inoue, H. Akoh, M. Kawasaki, Y. Tokura, T. Kanno and H. Adachi, Phys. Rev. B **70** (22), 224403 (2004).
62. K. Kamiya, M. Y. Yang, T. Nagata, S.-G. Park, B. Magyari-Köpe, T. Chikyow, K. Yamada, M. Niwa, Y. Nishi and K. Shiraishi, Phys. Rev. B **87** (15), 155201 (2013).
63. J. Dean, Material and manufacturing process **5** (4), 687-688 (1990).
64. F. Pan, S. Gao, C. Chen, C. Song and F. Zeng, Materials Science & Engineering R-Reports **83**, 1-59 (2014).
65. J. Robertson, Rep. Prog. Phys. **69** (2), 327-396 (2006).
66. K. Hubbard and D. Schlom, J. Mater. Res.**11** (11), 2757-2776 (1996).
67. C. Walczyk, D. Walczyk, T. Schroeder, T. Bertaud, M. Sowinska, M. Lukosius, M. Fraschke, D. Wolansky, B. Tillack, E. Miranda and C. Wenger, IEEE Trans. Electron Devices **58** (9), 3124-3131 (2011).
68. T. S. Böscke, J. Müller, D. Bräuhaus, U. Schröder and U. Böttger, Appl. Phys. Lett. **99** (10), 102903 (2011).
69. T. D. Huan, V. Sharma, G. A. Rossetti and R. Ramprasad, Phys. Rev. B **90** (6), 064111 (2014).

70. X. Sang, E. D. Grimley, T. Schenk, U. Schroeder and J. M. LeBeau, Appl. Phys. Lett. **106** (16), 162905 (2015).
71. W. J. Zhu, T. Tamagawa, M. Gibson, T. Furukawa and T. P. Ma, IEEE Electron Device Lett. **23** (11), 649-651 (2002).
72. K. P. McKenna, Modelling and Simulation in Materials Science and Engineering **22** (2), 025001 (025012 pp.)-025001 (025012 pp.) (2014).
73. C. K. Lee, E. N. Cho, H. S. Lee, C. S. Hwang and S. W. Han, Phys. Rev. B **78** (1), 012102 (2008).
74. R. Ningthoujam and N. Gajbhiye, Progress in Materials Science **70**, 50-154 (2015).
75. W. Spengler, R. Kaiser, A. Christensen and G. Müller-Vogt, Phys. Rev. B **17** (3), 1095 (1978).
76. Y. Krockenberger, S.-i. Karimoto, H. Yamamoto and K. Semba, J. Appl. Phys. **112** (8), - (2012).
77. G. V. Naik, B. Saha, J. Liu, S. M. Saber, E. A. Stach, J. M. K. Irudayaraj, T. D. Sands, V. M. Shalaev and A. Boltasseva, Proceedings of the National Academy of Sciences of the United States of America **111** (21), 7546-7551 (2014).
78. V. Talyansky, S. Choopun, M. J. Downes, R. P. Sharma, T. Venkatesan, Y. X. Li, L. G. Salamanca-Riba, M. C. Wood, R. T. Lareau and K. A. Jones, J. Mater. Res.**14** (08), 3298-3302 (1999).
79. H. A. Wriedt and J. L. Murray, Bulletin of Alloy Phase Diagrams **8** (4), 378-388 (1987).
80. A. Kaloyeros and E. Eisenbraun, Annual review of materials science **30** (1), 363-385 (2000).
81. S. R. Bradley, K. P. McKenna and A. L. Shluger, Microelectronic Engineering **109**, 346-350 (2013).
82. B. O. Johansson, J. E. Sundgren, J. E. Greene, A. Rockett and S. A. Barnett, J. Vac. Sci. & Technol. A **3** (2), 303-307 (1985).
83. M. Bonholzer, M. Lorenz and M. Grundmann, Physica Status Solidi a-Applications and Materials Science **211** (11), 2621-2624 (2014).
84. G. A. Olson, University of Illinois at Urbana-Champaign, 2015.
85. J. Narayan, P. Tiwari, X. Chen, J. Singh, R. Chowdhury and T. Zheleva, Appl. Phys. Lett. **61** (11), 1290-1292 (1992).
86. S. Kumar, Z. Wang, X. Huang, N. Kumari, N. Davila, J. P. Strachan, D. Vine, A. D. Kilcoyne, Y. Nishi and R. S. Williams, Appl. Phys. Lett. **110** (10), 103503 (2017).
87. T. Bertaud, M. Sowinska, D. Walczyk, S. Thiess, A. Gloskovskii, C. Walczyk and T. Schroeder, Appl. Phys. Lett. **101** (14), 143501 (2012).
88. S. Z. Rahaman, Y.-D. Lin, H.-Y. Lee, Y.-S. Chen, P.-S. Chen, W.-S. Chen, C.-H. Hsu, K.-H. Tsai, M.-J. Tsai and P.-H. Wang, Langmuir **33** (19), 4654-4665 (2017).
89. P. Hua and D. Ning, Chin. Phys. Lett. **31** (10), 107303 (2014).
90. Y. Chen, H. Lee, P. Chen, P. Gu, C. Chen, W. Lin, W. Liu, Y. Hsu, S. Sheu and P. Chiang, presented at the Electron Devices Meeting (IEDM), 2009 IEEE International, 2009 .
91. B. Hudec, C.-W. Hsu, I.-T. Wang, W.-L. Lai, C.-C. Chang, T. Wang, K. Fröhlich, C.-H. Ho, C.-H. Lin and T.-H. Hou, Science China Information Sciences **59** (6), 061403 (2016).

92. H.-Y. Chen, S. Yu, B. Gao, R. Liu, Z. Jiang, Y. Deng, B. Chen, J. Kang and H. P. Wong, Nanotechnology **24** (46), 465201 (2013).
93. S. Yu, H.-Y. Chen, B. Gao, J. Kang and H. S. P. Wong, Acs Nano **7** (3), 2320-2325 (2013).
94. V. A. Gritsenko, T. V. Perevalov and D. R. Islamov, Physics Reports **613**, 1-20 (2016).
95. K. Xiong, J. Robertson, M. C. Gibson and S. J. Clark, Appl. Phys. Lett. **87** (18), 183505 (2005).
96. D. M. Ramo, J. L. Gavartin, A. L. Shluger and G. Bersuker, Phys. Rev. B **75** (20) (2007).
97. P. Broqvist and A. Pasquarello, Appl. Phys. Lett. **89** (26), 262904 (2006).
98. T. V. Perevalov, V. S. Aliev, V. A. Gritsenko, A. A. Saraev and V. V. Kaichev, Microelectronic Engineering **109**, 21-23 (2013).
99. E. Hildebrandt, J. Kurian, M. M. Muller, T. Schroeder, H. J. Kleebe and L. Alff, Appl. Phys. Lett. **99** (11), 112902 (2011).
100. E. Hildebrandt, J. Kurian and L. Alff, J. Appl. Phys. **112** (11), 114112 (2012).
101. E. Lim and R. Ismail, Electronics **4** (3), 586 (2015).
102. F.-C. Chiu, Advances in Materials Science and Engineering **2014**, 18 (2014).
103. G. Bersuker, D. C. Gilmer, D. Veksler, P. Kirsch, L. Vandelli, A. Padovani, L. Larcher, K. McKenna, A. Shluger, V. Iglesias, M. Porti and M. Nafria, J. Appl. Phys. **110** (12), 12 (2011).
104. S. M. Yu, X. M. Guan and H. S. P. Wong, Appl. Phys. Lett. **99** (6), 063507 (2011).
105. C. Ahn, S. Kim, T. Gokmen, O. Dial, M. Ritter and H.-S. P. Wong, presented at the VLSI Technology, Systems and Application (VLSI-TSA), Proceedings of Technical Program-2014 International Symposium on, 2014 .
106. R. Fang, W. Chen, L. Gao, W. Yu and S. Yu, IEEE Electron Device Lett. **36** (6), 567-569 (2015).
107. A. Padovani, L. Larcher, O. Pirrotta, L. Vandelli and G. Bersuker, IEEE Trans. Electron Devices **62** (6), 1998-2006 (2015).
108. A. Mehonic, A. Vrajitoarea, S. Cueff, S. Hudziak, H. Howe, C. Labbé, R. Rizk, M. Pepper and A. J. Kenyon, Scientific Reports **3**, 2708 (2013).
109. B. Van Wees, H. Van Houten, C. Beenakker, J. G. Williamson, L. Kouwenhoven, D. Van der Marel and C. Foxon, Physical Review Letters **60** (9), 848 (1988).
110. S. Datta, *Electronic transport in mesoscopic systems*. (Cambridge university press, 1997).
111. E. Miranda and J. Sune, Appl. Phys. Lett. **78** (2), 225-227 (2001).
112. E. A. Miranda, C. Walczyk, C. Wenger and T. Schroeder, IEEE Electron Device Lett. **31** (6), 609-611 (2010).
113. Y. Li, S. Long, Y. Liu, C. Hu, J. Teng, Q. Liu, H. Lv, J. Sune and M. Liu, Nanoscale research letters **10** (1), 420-420 (2015).
114. M. Brandbyge, J. Schio, M. So, P. Stoltze, K. W. Jacobsen, J. No, L. Olesen, E. Lægsgaard, I. Stensgaard and F. Besenbacher, Phys. Rev. B **52** (11), 8499 (1995).
115. X. Lian, X. Cartoixa, E. Miranda, L. Perniola, R. Rurali, S. Long, M. Liu and J. Sune, J. Appl. Phys. **115** (24) (2014).
116. Y.-E. Syu, T.-C. Chang, J.-H. Lou, T.-M. Tsai, K.-C. Chang, M.-J. Tsai, Y.-L. Wang, M. Liu and S. M. Sze, Appl. Phys. Lett. **102** (17) (2013).
117. D. B. Strukov and R. S. Williams, Applied Physics A **94** (3), 515-519 (2009).

118. D. B. Strukov, F. Alibart and R. Stanley Williams, Applied Physics A **107** (3), 509-518 (2012).
119. U. Celano, A. Fantini, R. Degraeve, M. Jurczak, L. Goux and W. Vandervorst, AIP Advances **6** (8), 085009 (2016).
120. U. Celano, L. Goux, R. Degraeve, A. Fantini, O. Richard, H. Bender, M. Jurczak and W. Vandervorst, Nano Letters **15** (12), 7970-7975 (2015).
121. C. Li, B. Gao, Y. Yao, X. Guan, X. Shen, Y. Wang, P. Huang, L. Liu, X. Liu, J. Li, C. Gu, J. Kang and R. Yu, Adv. Mater. **29** (10), 1602976-n/a (2017).
122. S. Brivio, J. Frascaroli and S. Spiga, Appl. Phys. Lett. **107** (2), 023504 (2015).
123. S. R. Bradley, A. L. Shluger and G. Bersuker, Physical Review Applied **4** (6), 064008 (2015).
124. A. O'Hara, G. Bersuker and A. A. Demkov, J. Appl. Phys. **115** (18) (2014).
125. B. Traoré, P. Blaise and B. Sklénard, The Journal of Physical Chemistry C (2016).
126. S. Menzel, U. Böttger, M. Wimmer and M. Salinga, Adv. Funct. Mater. **25** (40), 6306-6325 (2015).
127. S. Suzer, S. Sayan, M. M. B. Holl, E. Garfunkel, Z. Hussain and N. M. Hamdan, J. Vac. Sci. & Technol. A **21** (1), 106-109 (2003).
128. V. Aliev, A. Gerasimova, V. Kruchinin, V. Gritsenko, I. Prosvirin and I. Badmaeva, Materials Research Express **3** (8), 085008 (2016).
129. J. Zhang, A. R. Oganov, X. Li, K.-H. Xue, Z. Wang and H. Dong, Phys. Rev. B **92** (18), 184104 (2015).
130. K.-H. Xue, P. Blaise, L. R. C. Fonseca and Y. Nishi, Physical Review Letters **110** (6), 065502 (2013).
131. B. P. Burton and A. van de Walle, Calphad **37**, 151-157 (2012).
132. S. Yu, B. Gao, Z. Fang, H. Yu, J. Kang and H.-S. P. Wong, Frontiers in Neuroscience **7** (2013).
133. S. Yu, B. Gao, Z. Fang, H. Yu, J. Kang and H. S. P. Wong, Adv. Mater. **25** (12), 1774-1779 (2013).
134. J. Woo, J. Song, K. Moon, S. Lee, J. Park and H. Hwang, presented at the 2016 IEEE Silicon Nanoelectronics Workshop (SNW), 2016 .
135. S. H. Jo, T. Chang, I. Ebong, B. B. Bhadviya, P. Mazumder and W. Lu, Nano letters **10** (4), 1297-1301 (2010).
136. J. Woo, K. Moon, J. Song, S. Lee, M. Kwak, J. Park and H. Hwang, IEEE Electron Device Lett. **37** (8), 994-997 (2016).
137. E. Covi, S. Brivio, A. Serb, T. Prodromakis, M. Fanciulli and S. Spiga, Frontiers in neuroscience **10** (2016).
138. X. M. Guan, S. M. Yu and H. S. P. Wong, IEEE Trans. Electron Devices **59** (4), 1172-1182 (2012).
139. G. Bin, C. Bing, Z. Feifei, L. Lifeng, L. Xiaoyan, K. Jinfeng, Y. Hongyu and Y. Bin, IEEE Trans. Electron Devices **60** (4), 1379-1383 (2013).
140. D. Kuzum, S. Yu and H. S. P. Wong, Nanotechnology **24** (38) (2013).
141. A. Grossi, D. Walczyk, C. Zambelli, E. Miranda, P. Olivo, V. Stikanov, A. Feriani, J. Sune, G. Schoof, R. Kraemer, B. Tillack, A. Fox, T. Schroeder, C. Wenger and C. Walczyk, IEEE Trans. Electron Devices **62** (8), 2502-2509 (2015).

142. A. Fantini, D. Wouters, R. Degraeve, L. Goux, L. Pantisano, G. Kar, Y.-Y. Chen, B. Govoreanu, J. Kittl and L. Altimime, presented at the Memory Workshop (IMW), 2012 4th IEEE International, 2012 .
143. G. Niu, X. Cartoixà, A. Grossi, C. Zambelli, P. Olivo, E. Perez, M. A. Schubert, P. Zaumseil, I. Costina, T. Schroeder and C. Wenger, The Journal of Physical Chemistry C **121** (12), 7005-7014 (2017).
144. A. Kalantarian, G. Bersuker, D. Gilmer, D. Veksler, B. Butcher, A. Padovani, O. Pirrotta, L. Larcher, R. Geer and Y. Nishi, presented at the Reliability Physics Symposium (IRPS), 2012 IEEE International, 2012 .
145. C. Walczyk, M. Sowinska, D. Walczyk, P. Calka and T. Schroeder, ECS Transactions **61** (2), 315-321 (2014).
146. C. Yu-Sheng, L. Heng-Yuan, C. Pang-Shiu, W. Tai-Yuan, W. Ching-Chiun, T. Pei-Jer, F. Chen, T. Ming-Jinn and L. Chenhsin, Electron Device Letters, IEEE **31** (12), 1473-1475 (2010).
147. H. Y. Lee, P. S. Chen, T. Y. Wu, Y. S. Chen, C. C. Wang, P. J. Tzeng, C. H. Lin, F. Chen, C. H. Lien and M. J. Tsai, IEEE International Electron Devices Meeting: Technical Digest, 1-4 (2008).
148. X. Chen, W. Hu, Y. Li, S. Wu and D. Bao, Appl. Phys. Lett. **108** (5), 053504 (2016).
149. S. Brivio, E. Covi, A. Serb, T. Prodromakis, M. Fanciulli and S. Spiga, Appl. Phys. Lett. **109** (13), 133504 (2016).
150. L. Goux, P. Czarnecki, Y. Y. Chen, L. Pantisano, X. P. Wang, R. Degraeve, B. Govoreanu, M. Jurczak, D. J. Wouters and L. Altimime, Appl. Phys. Lett. **97** (24), 243509 (2010).
151. L. Goux, X. P. Wang, Y. Y. Chen, L. Pantisano, N. Jossart, B. Govoreanu, J. A. Kittl, M. Jurczak, L. Altimime and D. J. Wouters, Electrochemical and Solid State Letters **14** (6), H244-H246 (2011).
152. S. U. Sharath, T. Bertaud, J. Kurian, E. Hildebrandt, C. Walczyk, P. Calka, P. Zaumseil, M. Sowinska, D. Walczyk, A. Gloskovskii, T. Schroeder and L. Alff, Appl. Phys. Lett. **104** (6), - (2014).
153. D. Smith, *Thin-film deposition: principles and practice*. (McGraw Hill Professional, 1995).
154. A. Rockett, in *The Materials Science of Semiconductors* (Springer US, Boston, MA, 2008), pp. 455-503.
155. L. Alff, A. Klein, P. Komissinskiy and J. Kurian, in *Ceramics Science and Processing, Vol. 3: Synthesis and Processing*, edited by R. Riedel and I.-W. Chen (Wiley VCH, Weinheim, 2011), Vol. 3.
156. H. Brune, Surf. Sci. Rep. **31** (4-6), 125-229 (1998).
157. S. Kowarik, A. Gerlach and F. Schreiber, Journal of Physics: Condensed Matter **20** (18), 184005 (2008).
158. D. G. Schlom, APL materials **3** (6), 062403 (2015).
159. D. G. Schlom, J. H. Haeni, J. Lettieri, C. D. Theis, W. Tian, J. C. Jiang and X. Q. Pan, Materials Science and Engineering B **87** (3), 282-291 (2001).
160. Buckow, R. Retzlaff, J. Kurian and L. Alff, Superconductor Science and Technology **26** (1), 015014 (2013).
161. E-beam evaporator, From http://www.cleanroom.byu.edu/metal
162. HM2 E-gun. From http://www.thermionics.com/

163. Y. Shimazu, T. Okumura, E. Sakai, H. Kumigashira, M. Okawa, T. Saitoh and T. Higuchi, Japanese J. Appl. Phys. **53** (6S), 06JG01 (2014).
164. A. Blant, O. Hughes, T. Cheng, S. Novikov and C. Foxon, Plasma Sources Science and Technology **9** (1), 12 (2000).
165. D. Kearns, D. Gillen, D. Voulot, R. McCullough, W. Thompson, G. Cosimini, E. Nelson, P. Chow and J. Klaassen, J. Vac. Sci. & Technol. A **19** (3), 993-997 (2001).
166. R. Vaudo, J. Cook and J. Schetzina, Journal of crystal growth **138** (1-4), 430-436 (1994).
167. F. Tang, T. Parker, G. Wang and T. Lu, J. Phys. D-Appl. Phys. **40** (23), R427 (2007).
168. S. Hasegawa, *Reflection high-energy electron diffraction*. Characterization of Materials 1-14 (2012).
169. A. Ichimiya and P. I. Cohen, *Reflection high-energy electron diffraction*. (Cambridge Univ. Press, Cambridge, 2004).
170. W. Braun, *Applied rheed : reflection high energy electron diffraction during crystal growth*. (Springer, Berlin, 1999).
171. B. D. Cullity and S. R. Stock, *Elements of X-ray diffraction*, 3. ed. (Pearson/Prentice Hall, Upper Saddle River, NJ, 2001).
172. A. R. Verma and O. N. Srivastava, *Crystallography for solid state physics*. (Wiley, New York, 1982).
173. K. Inaba, Overview. Rigaku J **24** (1) (2008).
174. M. Yasaka, Overview. Rigaku J **24** (2) (2010).
175. P. Zaumseil, RCRefSim Software (2005).
176. J. Chastain, R. C. King and J. Moulder, *Handbook of X-ray photoelectron spectroscopy: a reference book of standard spectra for identification and interpretation of XPS data*. (Physical Electronics Division, Perkin-Elmer Corporation Eden Prairie, Minnesota, 1992).
177. H.-L. Lee and N. T. Flynn, Handbook of Applied Solid State Spectroscopy, 485-507 (2006).
178. CASA XPS manual, CASA XPS software Ltd (2009).
179. S. Tanuma, C. J. Powell and D. R. Penn, Surf. Interf. Anal.**35** (3), 268-275 (2003).
180. R. Champaneria, P. Mack, R. White and J. Wolstenholme, Surf. Interf. Anal.**35** (13), 1028-1033 (2003).
181. T. L. Barr and S. Seal, J. Vac. Sci. & Technol. A **13** (3), 1239-1246 (1995).
182. A. Gloskovskii, G. Stryganyuk, G. H. Fecher, C. Felser, S. Thiess, H. Schulz-Ritter, W. Drube, G. Berner, M. Sing, R. Claessen and M. Yamamoto, J. Electron Spectrosc. Relat. Phenom. **185** (1), 47-52 (2012).
183. M. Repoux, Surf. Interf. Anal.**18** (7), 567-570 (1992).
184. L. Reimer, *Transmission electron microscopy: physics of image formation and microanalysis*. (Springer, 2013).
185. R. Zaouk, B. Y. Park and M. J. Madou, Microfluidic Techniques: Reviews and Protocols, 5-15 (2006).
186. C.-S. Shin, S. Rudenja, D. Gall, N. Hellgren, T.-Y. Lee, I. Petrov and J. E. Greene, J. Appl. Phys. **95** (1), 356-362 (2004).
187. S. P. Chockalingam, M. Chand, J. Jesudasan, V. Tripathi and P. Raychaudhuri, Phys. Rev. B **77** (21), 2145503 (2008).

188. R. Chowdhury, R. D. Vispute, K. Jagannadham and J. Narayan, J. Mater. Res.**11** (06), 1458-1469 (1996).
189. P. R. Willmott, R. Timm and J. R. Huber, Appl. Surf. Sci. **127**, 105-110 (1998).
190. B.-H. Hwang, J. Phys. D-Appl. Phys. **34** (16), 2469 (2001).
191. R. Barabash, W. Donner and H. Dosch, Appl. Phys. Lett. **78** (4), 443-445 (2001).
192. D. Edström, D. Sangiovanni, L. Hultman, I. Petrov, J. Greene and V. Chirita, Thin Solid Films **589**, 133-144 (2015).
193. D. Sangiovanni, D. Edström, L. Hultman, V. Chirita, I. Petrov and J. E. Greene, Phys. Rev. B **86** (15), 155443 (2012).
194. L. Hultman, H. Ljungcrantz, C. Hallin, E. Janzén, J. Sundgren, B. Pécz and L. Wallenberg, J. Mater. Res.**11** (10), 2458-2462 (1996).
195. P. Å. Persson, C. Höglund, J. Birch and L. Hultman, Thin solid films **519** (8), 2421-2425 (2011).
196. R. R. Manory, T. Mori, I. Shimizu, S. Miyake and G. Kimmel, J. Vac. Sci. & Technol. A **20** (2), 549-554 (2002).
197. C. Morant, L. Galan and J. M. Sanz, Surf. Interf. Anal.**16** (1-12), 304-308 (1990).
198. V. Mironov, O. Udalov, B. Gribkov and A. Fraerman, J. Appl. Phys. **104** (6), 064301 (2008).
199. E. Hildebrandt, J. Kurian and L. Alff, J. Appl. Phys. **112** (11), 10 (2012).
200. S. U. Sharath, S. Vogel, L. Molina-Luna, E. Hildebrandt, C. Wenger, J. Kurian, M. Duerrschnabel, T. Niermann, G. Niu, P. Calka, M. Lehmann, H.-J. Kleebe, T. Schroeder and L. Alff, Adv. Funct. Mater. **27** (32), 1700432-n/a (2017).
201. G. Lucovsky, D. Zeller and J. L. Whitten, Microelectronic Engineering **88** (7), 1471-1474 (2011).
202. S.-j. J. Wu, B. Houng and B.-s. Huang, Journal of Alloys and Compounds **475** (1), 488-493 (2009).
203. D. A. Vermilyea, Acta Metallurgica **6** (3), 166-171 (1958).
204. M. T. Brumbach, P. R. Mickel, A. J. Lohn, A. J. Mirabal, M. A. Kalan, J. E. Stevens and M. J. Marinella, J. Vac. Sci. & Technol. A **32** (5), 051403 (2014).
205. S. Lecuyer, A. Quemerais and G. Jezequel, Surf. Interf. Anal.**18** (4), 257-261 (1992).
206. L. Chang Bum, L. Dong Soo, A. Benayad, L. Seung Ryul, C. Man, L. Myoung-Jae, H. Jihyun, K. Chang Jung and U. I. Chung, IEEE Electron Device Lett. **32** (3), 399-401 (2011).
207. B. Xiao and S. Watanabe, Nanoscale **6** (17), 10169-10178 (2014).
208. M. Sunding, K. Hadidi, S. Diplas, O. Løvvik, T. Norby and A. Gunnæs, J. Electron Spectrosc. Relat. Phenom. **184** (7), 399-409 (2011).
209. C. An, IEEE Electron Device Lett. **35** (1), 57-59 (2014).
210. K. Fröhlich, P. Jančovič, B. Hudec, J. Dérer, A. Paskaleva, T. Bertaud and T. Schroeder, ECS Transactions **58** (10), 163-170 (2013).
211. Y. S. Chen, H. Y. Lee, P. S. Chen, T. Y. Wu, C. C. Wang, P. J. Tzeng, F. Chen, M. J. Tsai and C. Lien, IEEE Electron Device Lett. **31** (12), 1473-1475 (2010).
212. H. ChiaHua, H. Cho-Lun, C. Chun-Chi, L. Jan-Tsai, W. Cheng-San, H. Chien-Chao, H. Chenming and Y. Fu-Liang, 2010 IEEE International Electron Devices Meeting (IEDM 2010), 4 pp.-4 pp. (2010).
213. T.-M. Pan and C.-H. Lu, Materials Chemistry and Physics **139** (2–3), 437-442 (2013).
214. J.-S. Huang, C.-Y. Lee and T.-S. Chin, Electrochimica Acta **91** (0), 62-68 (2013).

215. P. Zhou, H. B. Lv, M. Yin, L. Tang, Y. L. Song, T. A. Tang, Y. Y. Lin, A. Bao, A. Wu, S. Cai, H. Wu, C. Liang and M. H. Chi, Journal of Vacuum Science & Technology B **26** (3), 1030-1032 (2008).
216. J. P. Strachan, J. J. Yang, L. A. Montoro, C. A. Ospina, A. J. Ramirez, A. L. D. Kilcoyne, G. Medeiros-Ribeiro and R. S. Williams, Beilstein Journal of Nanotechnology **4**, 467-473 (2013).
217. Z. Fang, H. Y. Yu, X. Li, N. Singh, G. Q. Lo and D. L. Kwong, IEEE Electron Device Lett. **32** (4), 566-568 (2011).
218. S. Menzel and J.-H. Hur, in *Resistive Switching* (Wiley-VCH Verlag GmbH & Co. KGaA, 2016), pp. 395-436.
219. S. Clima, B. Govoreanu, M. Jurczak and G. Pourtois, Microelectronic Engineering **120**, 13-18 (2014).
220. S. U. Sharath, J. Kurian, P. Komissinskiy, E. Hildebrandt, T. Bertaud, C. Walczyk, P. Calka, T. Schroeder and L. Alff, Appl. Phys. Lett. **105** (7), 073505 (2014).
221. A. J. Lohn, J. E. Stevens, P. R. Mickel and M. J. Marinella, Appl. Phys. Lett. **103** (6), 063502 (2013).
222. Y. Jiang, C. C. Tan, M. H. Li, Z. Fang, B. B. Weng, W. He and V. Y. Q. Zhuo, Ecs Journal of Solid State Science and Technology **4** (12), N137-N140 (2015).
223. V. F. Surganov, A. M. Mozalev and V. A. Lastochkina, Journal of Applied Spectroscopy **67** (3), 412-417 (2000).
224. S. Steeb and J. Renner, Journal of the Less Common Metals **9** (3), 181-189 (1965).
225. S. Gnanarajan, S. K. H. Lam and C. P. Foley, J. Appl. Phys. **101** (6), 063535 (2007).
226. M.-J. Lee, C. B. Lee, D. Lee, S. R. Lee, M. Chang, J. H. Hur, Y.-B. Kim, C.-J. Kim, D. H. Seo, S. Seo, U. I. Chung, I.-K. Yoo and K. Kim, Nat. Mater. **10** (8), 625-630 (2011).
227. K. M. Kim, S. R. Lee, S. Kim, M. Chang and C. S. Hwang, Adv. Funct. Mater. **25** (10), 1527-1534 (2015).
228. K. Kawai, A. Kawahara, R. Yasuhara, S. Muraoka, Z. Wei, R. Azuma, K. Tanabe and K. Shimakawa, IC Design & Technology (ICICDT), IEEE International Conference on, Austin, TX,, 1-4 (2014).
229. T. Tsuruoka, I. Valov, S. Tappertzhofen, J. van den Hurk, T. Hasegawa, R. Waser and M. Aono, Adv. Funct. Mater. **25** (40), 6374-6381 (2015).
230. T. H. Park, S. J. Song, H. J. Kim, S. G. Kim, S. Chung, B. Y. Kim, K. J. Lee, K. M. Kim, B. J. Choi and C. S. Hwang, physica status solidi (RRL)-Rapid Research Letters **9** (6), 362-365 (2015).
231. L. He, Z.-M. Liao, H.-C. Wu, X.-X. Tian, D.-S. Xu, G. L. W. Cross, G. S. Duesberg, I. V. Shvets and D.-P. Yu, Nano Letters **11** (11), 4601-4606 (2011).
232. H. Y. Peng, Y. F. Li, W. N. Lin, Y. Z. Wang, X. Y. Gao and T. Wu, Sci Rep **2** (2012).
233. X. Lian, S. Long, C. Cagli, J. Buckley, E. Miranda, M. Liu, J. Su, x00F and x00E, presented at the 2012 13th International Conference on Ultimate Integration on Silicon (ULIS), 2012 .
234. X. Zhong, I. Rungger, P. Zapol and O. Heinonen, Phys. Rev. B **94** (16), 165160 (2016).
235. S. Kumar, C. E. Graves, J. P. Strachan, E. M. Grafals, A. L. D. Kilcoyne, T. Tyliszczak, J. N. Weker, Y. Nishi and R. S. Williams, Adv. Mater. **28** (14), 2772-2776 (2016).
236. B. Gao, B. Sun, H. Zhang, L. Liu, X. Liu, R. Han, J. Kang and B. Yu, IEEE Electron Device Lett. **30** (12), 1326-1328 (2009).

237. B. Gao, J. F. Kang, Y. S. Chen, F. F. Zhang, B. Chen, P. Huang, L. F. Liu, X. Y. Liu, Y. Y. Wang, X. A. Tran, Z. R. Wang, H. Y. Yu and A. Chin, presented at the Electron Devices Meeting (IEDM), 2011 IEEE International, 2011 .
238. C. D. Landon, R. H. Wilke, M. T. Brumbach, G. L. Brennecka, M. Blea-Kirby, J. F. Ihlefeld, M. J. Marinella and T. E. Beechem, Appl. Phys. Lett. **107** (2), 023108 (2015).
239. P. Huang, X. Y. Liu, B. Chen, H. T. Li, Y. J. Wang, Y. X. Deng, K. L. Wei, L. Zeng, B. Gao, G. Du, X. Zhang and J. F. Kang, IEEE Trans. Electron Devices **60** (12), 4090-4097 (2013).
240. X. J. Lian, X. Cartoixa, E. Miranda, L. Perniola, R. Rurali, S. B. Long, M. Liu and J. Sune, J. Appl. Phys. **115** (24) (2014).
241. S. Monaghan, P. Hurley, K. Cherkaoui, M. Negara and A. Schenk, Solid-State Electronics **53** (4), 438-444 (2009).
242. S. Maikap, D. Jana, M. Dutta and A. Prakash, Nanoscale Research Letters **9** (1), 1-6 (2014).
243. K. M. Kim, B. J. Choi, Y. C. Shin, S. Choi and C. S. Hwang, Appl. Phys. Lett. **91** (1), 012907 (2007).
244. A. Carbone, C. Pennetta and L. Reggiani, Appl. Phys. Lett. **95** (23), 233303 (2009).
245. S. Sharath, M. Joseph, S. Vogel, E. Hildebrandt, P. Komissinskiy, J. Kurian, T. Schröder and L. Alff, Appl. Phys. Lett. **109** (17), 173503 (2016).
246. W. Yi, S. E. Savel'Ev, G. Medeiros-Ribeiro, F. Miao, M.-X. Zhang, J. J. Yang, A. M. Bratkovsky and R. S. Williams, Nature communications **7** (2016).
247. Y. S. Chen, B. Chen, B. Gao, L. F. Liu, X. Y. Liu and J. F. Kang, J. Appl. Phys. **113** (16) (2013).
248. L. Zhao, S. W. Ryu, A. Hazeghi, D. Duncan, B. Magyari-Köpe and Y. Nishi, presented at the 2013 Symposium on VLSI Technology, 2013 .
249. J. Muller, U. Schroder, T. S. Boscke, I. Muller, U. Bottger, L. Wilde, J. Sundqvist, M. Lemberger, P. Kucher, T. Mikolajick and L. Frey, J. Appl. Phys. **110** (11), 114113 (2011).
250. S. Starschich, S. Menzel and U. Böttger, Appl. Phys. Lett. **108** (3), 032903 (2016).
251. B. Chakrabarti, R. V. Galatage and E. M. Vogel, IEEE Electron Device Lett. **34** (7), 867-869 (2013).
252. C.-S. Peng, W.-Y. Chang, Y.-H. Lee, M.-H. Lin, F. Chen and M.-J. Tsai, Electrochemical and Solid-State Letters **15** (4), H88-H90 (2012).
253. C. Rodenbücher, E. Hildebrandt, K. Szot, S. U. Sharath, J. Kurian, P. Komissinskiy, U. Breuer, R. Waser and L. Alff, Appl. Phys. Lett. **108** (25), 252903 (2016).
254. G. Niu, H.-D. Kim, R. Roelofs, E. Perez, M. A. Schubert, P. Zaumseil, I. Costina and C. Wenger, Scientific Reports **6**, 28155 (2016).
255. S. Yu, Y. Wu, R. Jeyasingh, D. Kuzum and H. S. P. Wong, IEEE Trans. Electron Devices **58** (8), 2729-2737 (2011).
256. L. Zhao, S. Clima, B. Magyari-Köpe, M. Jurczak and Y. Nishi, Appl. Phys. Lett. **107** (1), 013504 (2015).

Curriculum Vitae

PERSONAL INFORMATION

Name:	Sharath Sankaramangalam Ulhas
Date of birth:	13.04.1990
Place of birth:	Kerala, India

EDUCATION

10/2012 – 11/2017:	PhD Student, Department of Materials Science, Technische Universität Darmstadt, Germany.
06/2007 – 07/2012:	Master of Technology (Integrated), Department of Applied Physics, Indian Institute of Technology (BHU), Varanasi, India.
RESEARCH INTERESTS	Molecular Beam Epitaxy, Thin films, Oxide Electronics, Resistive Random Access Memories, Emerging Non-volatile Memories & Neuromorphic Electronics.

List of publications and scientific contributions

PUBLICATIONS RELATED TO THIS THESIS

1. "Control of switching modes and conductance quantization in oxygen engineered HfO_x based memristive devices"
   S. U. Sharath, S. Vogel, L. Molina-Luna, E. Hildebrandt, C. Wenger, J. Kurian, M. Duerrschnabel, T. Niermann, G. Niu, P. Calka, M. Lehmann, H-. J. Kleebe, T. Schroeder and L. Alff.
   Advanced Functional Materials, **27**, 1700432 (2017).

2. "Impact of oxygen stoichiometry on electroforming and multiple switching modes in TiN/TaO_x/Pt based ReRAM"
   S. U. Sharath, M.J. Joseph, S. Vogel, E. Hildebrandt, P. Komissiniskiy, J. Kurian, T. Schroeder, and L. Alff.
   Applied Physics Letters, **109**, 173503 (2016).

3. "Thickness independent reduced forming voltage in oxygen engineered HfO_2 based resistive switching memories"
   S. U. Sharath, J. Kurian, P. Kommissinskiy, E. Hildebrandt, T. Bertaud, C. Walczyk, P. Calka, T. Schroeder and L. Alff.
   Applied Physics Letters, **105**, 073505 (2014).

4. "Towards forming-free resistive switching in oxygen engineered HfO_{2-x}"
   S. U. Sharath, T. Bertaud, J. Kurian, E. Hildebrandt, C. Walczyk, P. Calka, P. Zaumseil, M. Sowinska, D. Walczyk, A. Gloskovskii, T. Schroeder and L. Alff.
   Applied Physics Letters, **104**, 063502 (2014).

5. "Modulation of DC resistive switching dynamics in HfO_2 based RRAM by defect engineering for synaptic applications" **S. U. Sharath** *et al.* (Manuscript under preparation)

6. "Flux dependent 3D to 2D growth mode transition in epitaxial TiN thin films grown on *c*-cut sapphire substrates by reactive MBE" **S. U. Sharath** *et al.* (Manuscript under preparation)

7. "Quantum point contact modelling of high resistance state evolution in HfO_2 & HfO_x RRAM" **S. U. Sharath** *et al.* (manuscript under preparation).

OTHER PUBLICATIONS

8. "FIB based fabrication of an operative Pt/HfO_2/TiN device for resistive switching inside a transmission electron microscope"
A. Zintler, U. Kunz, Y. Pivak, **S. U. Sharath**, S. Vogel, E. Hildebrandt, H.-J. Kleebe, L. Alff and L. Molina-Luna.
Ultramicroscopy, **181**, 144 (2017).

9. "Electron hologryphy on HfO_2/HfO_{2-x} bilayer structures with multilevel resistive switching properties"
G. Niu, M. Schubert, **S. U. Sharath**, P. Zaumseil, S. Vogel, C. Wenger, E. Hildebrandt, S. Bhupati, E. Perez, L. Alff, M. Lehmann, T. Schroeder and T. Niermann.
Nanotechnology, **28**, 215702 (2017).

10. "$YCo_{5\pm x}$ thin films with perpendicular anisotropy grown by molecular beam epitaxy"
S. Sharma, E. Hildebrandt, **S. U. Sharath**, I. Radulov and L. Alff.
Journal of Magnetism and Magnetic Materials, **432**, 382 (2017).

11. "Toward Enhanced Electronic and Ionic Conductivity in Olivine $LiCoPO_4$ Thin Film Electrode Material for 5 V Lithium Batteries: Effect of $LiCo_2P_3O_{10}$ Impurity Phase'
G. Cherkashinin, **S. U. Sharath** and W. Jaegermann.
Advanced Energy Materials, **7**, 1602321 (2017).

12. "Hafnium carbide formation in oxygen deficient hafnium oxide thin films"
C. Rodenbuecher, E. Hildebrandt, K. Szot, **S. U. Sharath**, J. Kurian, P. Komissinskiy, U. Breuer, R. Waser and L. Alff.
Applied Physics Letters, **108**, 252903 (2016).

13. "(001) and (111) Single-Oriented Highly Epitaxial CeO_2 Thin Films on *r*-cut Sapphire Substrates"
D.S. Bick, **S.U. Sharath**, I. Hoffman, M. Major, J. Kurian, L. Alff.
Journal of Electronic Materials, **44**, 2930 (2015).

14. "Intrinsic versus extrinsic ferromagnetism in HfO_{2-x} and Ni:HfO_{2-x} thin films."
E. Hildebrandt, M.B. Yazdi, J. Kurian, **S.U. Sharath**, F. Wilhelm, A. Rogalev and L. Alff.
Physical Review B, **90**, 134426 (2014).

15. "Influence of grain and grain-boundary resistances on dielectric properties of $KNbO_3$ under small DC bias field"
S. U. Sharath, R. K. Singh, Raghvendra, B. P. Singh, P. Kumar, and P. Singh.
Journal of the American Ceramic Society, **96**, 3127 (2013).

CONFERENCE CONTRIBUTIONS

1. *(Oral presentation)* "Oxygen stoichiometry controlled resistive switching modes in HfO_x and TaO_x based RRAM devices"
   S. U. Sharath, S. Vogel, E. Hildebrandt, J. Kurian, P. Komissinskiy, T. Schroeder and L. Alff.
   MRS 2017 Spring meeting, April 17-21, 2017, Phoenix, AZ, USA.

2. *(Oral presentation)* "HfO_x based RRAM by MBE: Oxygen Engineering and doping"
   S. U. Sharath, S. Vogel, E. Hildebrandt, J. Kurian, P. Komissinskiy, M. J. Joseph, G.Niu, T. Schroeder and L. Alff.
   European MRS 2016 Spring meeting, May 2- 6, 2016, Lille, France.

3. *(Poster presentation)* "Resistive switching in oxygen engineered TaO_x based RRAM devices grown by MBE"
   M. J. Joseph, **S. U. Sharath**, S. Vogel, E. Hildebrandt, P. Komissinskiy, T. Schroeder and Lambert Alff.
   European MRS 2016 Spring meeting, May 2- 6, 2016, Lille, France.

4. *(Oral presentation)* "Effect of Oxygen Engineering in HfO_2 by MBE for RRAM Applications"
   S. U. Sharath, S. Vogel, E. Hildebrandt, J. Kurian, P. Komissinskiy, C. Walczyk, P. Calka, G. Niu, T. Schroeder and L. Alff.
   MRS 2015 Fall meeting, November 29 - December 4, 2015, Boston, U.S.A.

5. *(Poster presentation)* "Resistive switching in oxygen engineered HfO_2 based resistive random access memory (RRAM) devices grown by MBE"
   S. U. Sharath, S. Vogel, E. Hildebrandt, J. Kurian, P. Komissinskiy, C. Walczyk, P. Calka, G. Niu, T. Schroeder and L. Alff.
   International Workshop on Oxide Electronics 22, October 7-9, 2015, Paris, France.

6. *(Oral presentation)* "Effect of Oxygen Engineering on Resistive Switching in HfO_2 based RRAM"
   S.U. Sharath, J. Kurian, E. Hildebrandt, P. Komissinskiy, S. Vogel, T. Bertaud, Ch. Walczyk, P. Calka, G. Niu, T. Schroeder, L. Alff.
   European MRS 2015 Spring meeting, May 11- 15, 2015, Lille, France.

7. *(Oral presentation)* "Effect of oxygen engineering and doping on resistive switching in HfO_2 based RRAM devices grown by MBE"
   S. U. Sharath, J. Kurian, E. Hildebrandt, P. Komissinskiy, T. Bertaud, C. Walczyk, P. Calka, T. Schroeder and L. Alff. (Talk)
   DPG Spring Meeting 2015, March 15 – March 20, 2015, Berlin, Germany.

8. *(Oral presentation)* "Resistive switching in oxygen engineered hafnium oxide"
   S. U. Sharath, J. Kurian, E. Hildebrandt, P. Komissinskiy, T. Bertaud, C. Walczyk, P. Calka, T. Schroeder and L. Alff. (Talk)
   Deutscher MBE Workshop, September 2014, Darmstadt, Germany.

9. *(Oral presentation)* "Towards forming free switching in HfO_{2-x}/TiN thin films grown by molecular beam epitaxy"
   S. U. Sharath, T. Bertaud, J. Kurian, E. Hildebrandt, Ch. Walczyk, P. Calka, P. Zaumseil, M. Sowinska, D. Walczyk, A. Gloskovskii, T. Schroeder and L. Alff.
   DPG Spring Meeting 2014, March 30 – April 4, 2014, Dresden, Germany.